博士研究生国家奖学金申请审批表

<table>
<tr><td rowspan="6">基本情况</td><td>姓名</td><td>邵希吉</td><td>性别</td><td>男</td><td>出生年月</td><td>1982.10</td></tr>
<tr><td>政治面貌</td><td>党员</td><td>民族</td><td>汉</td><td>入学时间</td><td>2018.09</td></tr>
<tr><td>学院</td><td>理学院</td><td>专业</td><td>物理学</td><td>学号</td><td>18B940022</td></tr>
<tr><td>学制</td><td>4</td><td>攻读学位</td><td>博士</td><td>学生类别</td><td>博士研究生</td></tr>
<tr><td colspan="6">是否在 2021 年 9 月 30 日前完成开题且未完成预答辩：是☑　　否☐</td></tr>
<tr><td>身份证号</td><td></td><td></td><td></td><td></td><td></td><td></td><td></td><td></td><td></td><td></td><td></td><td></td><td></td><td></td><td></td><td></td><td></td></tr>
<tr><td>申请理由</td><td colspan="17">各位老师好：
博士研究生期间，在导师的指导下，我一直在各方面严格要求自己，积极向上，不断进取，也取得了一定成绩，现总结如下：
德育方面，我时刻以一名共产党员的身份要求自己，热爱集体，乐于助人，科研中坚持严谨认真的作风。
科研方面，目前已经发表 17 篇 SCI 收录论文，包括第一作者论文 7 篇。其中博士在读期间（2018.9 至今）发表 10 篇，包括第一作者及共同第一作者论文 4 篇，分别在 Nanoscale(IF=7.79)， ACS Applied Materials and Interfaces(IF=9.229)， ACS Applied Electronic Materials(IF=3.314)和 Chemical Physics(IF=2.348)期刊上。 其他的合作文章中负责了部分实验和相关的计算工作，文章发表在 Chem（IF=22.0804）， ACS Applied Materials and Interfaces(IF=9.229)，International Journal of Hydrogen Energy（IF=5.816），Applied Physics Letters（IF=3.791）等杂志上。目前还有一篇正在回复审稿意见中（期刊：ACS Appied Nano Materials(IF=5.097)）。3 篇正在准备当中。详见附页。
科研项目方面，主持及参与项目 3 项，如下：
1) 参与在研项目，广东省自然科学基金面上项目，“空穴掺杂 Mott 绝缘态锡 R3×R3 相的超导转变机制研究”。项目编号：2021A1515012034，经费 10 万元，2021.1-2023.12；
2) 主持研究生创新实践项目，“磷在单晶硅表面电子结构和动力学性质的研究”。经费 5.98 万元，2019.1.1-2019.12.30；
3) 参与项目，国家自然科学基金面上项目，“掺杂多环芳烃类有机超导体的扫描隧道显微术研究”。项目编号：11574128，经费 87.6 万元，2016.1-2019.12。
以上是我的申请理由，敬请各位评委老师审核、批准。

申请人签名：邵希吉

2021 年 10 月 8 日</td></tr>
</table>

<table>
<tr><td>推荐意见</td><td colspan="2">邵希吉同学在本人实验室攻读博士学位，工作积极、努力，按时完成了博士培养过程的阶段任务，在材料表面性能、磁性原子与表面相互作用等研究方向获得了多项有意义的成果并发表 SCI 收录论文 10 篇。此外，还有多篇磁性原子与表面相互作用的第一作者文章正在整理中。鉴于邵希吉同学的表现，本人推荐其申请博士研究生国家奖学金。

推荐人（导师）签名：王克东
2021 年 10 月 8 日</td></tr>
<tr><td>审核意见</td><td>学生所在党支部意见：

（党支部填）
支部书记签名：
年　　月　　日</td><td>基层党委意见：

（学院党委填）
党委书记签名（公章）：
年　　月　　日</td></tr>
<tr><td>评审情况</td><td colspan="2">经评审，并在本单位内公示 5 个工作日，无异议，推荐该同学获得研究生国家奖学金。
（学院评审主任委员签名，不需盖公章）　　评审委员会主任委员签名：
年　　月　　日</td></tr>
<tr><td>基层单位意见</td><td colspan="2">经评审，并在本单位内公示 5 个工作日，无异议，本单位申报该同学获得研究生国家奖学金。现报请研究生国家奖学金评审领导小组审定。
基层单位主管领导签名：
（南科大研究生院填）　　（基层单位公章）
年　　月　　日</td></tr>
<tr><td>培养单位意见</td><td colspan="2">经审核，并在本单位公示＿＿＿个工作日，无异议，现批准该同学获得研究生国家奖学金。

（哈工大填）
（培养单位公章）
年　　月　　日</td></tr>
</table>

附页

博士在读期间发表论文（共 **10** 篇）：

第一作者和共同第一作者**:**

1) **Xiji Shao**, Lin Li, Xingqiang Shi, Yaping Ma, Xuefeng Wu and Kedong Wang. The shielding effects of a C_{60} cage on the magnetic moments of transition metal atoms inside the corner holes of Si(111)-(7×7). **Nanoscale**. 11, 6228–6234 (**2019**)
2) **Xiji Shao,** Xuhang Ma, Mingjing Liu, Tao Zhang, Yaping Ma, Chaoqiang Xu, Xuefeng Wu, Tao Lin, Kedong Wang. Comparing study of picene thin films on SnSe and Au (1 1 1) surfaces. **Chemical Physics.** 532, 110689 **(2020)**
3) Guowei Liu[#], **Xiji Shao**[#], Congrun Chen, Xixian Wang, Xuefeng Wu, Fangfei Ming, and Kedong Wang. Controlled Implantation of Phosphorous Atoms into a Silicon Surface Lattice with a Scanning Tunneling Microscopy Tip. **ACS Appl. Electron. Mater.** 3, 3338-3345 **(2021) (**共同一作**)**
4) Yu Zhou[#], **Xiji Shao**[#], Kwok-ho Lam, You Zheng, Lingzhi Zhao, Kedong Wang, Jinzhu Zhao, Fuming Chen, and Xianhua Hou. Symmetric sodium-ion battery based on dual-electron reactions of NASICON-Structured $Na_3MnTi(PO_4)_3$ material. **ACS Appl. Mater. Interfaces.** 12, 30328-30335 **(2020) (**共同一作**)**

其它参与论文**:**

5) Hao Tian, Yanling He, Qinglong Zhao, Jiaxin Li, **Xiji Shao**, Zhe Zhang, Xiang Huang, Chao Lu, Kedong Wang, Qichuan Jiang, A.M.C. Ng, Hu Xu, and S.Y. Tong. Avoiding Sabatier's conflict in bifunctional heterogeneous catalysts for the WGS reaction. **Chem**. 7, 1–13 **(2021)**
6) Yaping Ma, **Xiji Shao**, Jing Li, Bowei Dong, Zhenliang Hu, Qiulan Zhou, Haomin Xu, Xiaoxu Zhao, Hanyan Fang, Xinzhe Li, Zejun Li, Jing Wu, Meng Zhao, Stephen John Pennycook, Chorng Haur Sow, Chengkuo Lee, Yu Lin Zhong, Junpeng Lu, Mengning Ding, Kedong Wang, Ying Li, and Jiong Lu. Electrochemically exfoliated platinum dichalcogenide atomic layers for high-performance air-stable infrared photodetectors. **ACS Appl. Mater. Interfaces**. 13, 8518−8527 **(2021)**
7) Chun-Sheng Zhou, Xiang-Rui Liu, Yue Feng, **Xiji Shao**, Meng Zeng, Kedong Wang, Min Feng, and Chang Liu. Quantum-confinement-induced periodic surface states in two-dimensional metal-organic frameworks. **Applied Physics Letters.** 117. 191601 **(2020)**
8) Guowei Liu, **Xiji Shao**, Chaoqiang Xu, xuefeng Wu, Kedong Wang, STM studies of potassium doped picene films on Au(111) surface. **The Journal of Physical Chemistry C**. 124, 22025–22034 (**2020)**
9) Zhenjun Song, **Xiji Shao**, Generation of molybdenum hydride species via addition of molecular hydrogen across metal-oxygen bond at monolayer oxide/metal composite interface. **International Journal of Hydrogen Energy.** 45, 2975-2988 **(2020)**
10) Chaoqiang Xu, Kejie Bao, Yande Que, Yuan Zhuang, **Xiji Shao**, Kedong Wang, Junyi Zhu and Xudong Xiao. Two-dimensional $ErCu_2$ intermetallic compound on

Cu(111) with moiré-pattern-modulated electronic structures. **Phys. Chem. Chem. Phys.** 22, 1693-1700 **(2020)**

目前正在修订和准备的论文：

1) **Xiji Shao**, Lin Li, Sizhao Huang, Zhenjun Song, Kedong Wang. Magnetic moment modulation of 3d transition metal atoms on Si (100) surface. **ACS Appl. Nano. Mater.** 2021 **(Reply)**
2) **Xiji Shao**, et al. "Investigations of Residual Magnetic Moments of Fe, Co, and Ni Atoms in Various Chemical Environments" **(In preparation)**
3) **Xiji Shao**, et al. " Magnetic Moments of Fe, Co, and Ni Atoms Adsorption on WXY（X,Y=S, Se, Te）" (**In preparation)**
4) **Xiji Shao**, et al. " Magnetic Moments Modulation of 3*d* Transition Metal Atoms on surface of TaS_2" (**In preparation)**

攻读博士学位前发表的论文（共 9 篇）：

5) Qin Liu, **Xiji Shao**, Fangfei Ming, Kedong Wang, Xudong Xiao. Adsorption and spin-related properties of multi-Co-atoms assembled in the half unit cells of Si(111)-(7x7). **New Journal of Physics**. 19, 023048 **(2017)**
6) Qin Liu, Qiang Fu, **Xiji Shao**, Xuhang Ma, Xuefeng Wu, Kedong Wang, Xudong Xiao. Diffusion of single Au, Ag and Cu atoms inside Si(111)-(7×7) half unit cells: A comparative study. **Applied Surface Science.** 401, 225-231 **(2017)**
7) Detian Li, Haijun Luo, Jianqiu Cai, Yongjuncheng, **Xiji Shao**, Changkun Dong. First-principles study of H, O, and N adsorption on metal embedded carbon nanotubes. **Applied Surface Science.** 403, 654-651 **(2017)**
8) **Xiji Shao**, Detian Li, Jianqiu Cai, Haijun Luo, Changkun Dong. First-principles study of structural and work function properties for nitrogen-doped single-walled carbon nanotubes. **Applied Surface Science**. 368, 477-482 **(2016)**
9) Qin Liu, Yanhua Lei, **Xiji Shao**, Fangfei Ming, Hu Xu, Kedong Wang and Xudong Xiao. Controllable dissociations of PH_3 molecules on Si(001). **Nanotechnology**. 27135704 (13pp), (**2016)**
10) **Xiji Shao**, Kedong Wang, Rui Pang, Xingqiang Shi. Lithium intercalation in Graphene/MoS2 composites: First-Principles Insights. **The Journal of Physical Chemistry C**. 119(46), pp 25860–25867 (**2015)**
11) **Xiji Shao**, Haijun Luo, Jianqiu Cai, Changkun Dong. First principle study of single atom adsorption on capped single-walled carbon nanotubes. **International Journal of Hydrogen Energy**. 39, 10161-10168 **(2014)**.
12) **Xiji Shao**, Changkun Dong, Detian Li, Yongjun Cheng, Zhenghai Li. Study on the effect of nonmetallic element on structure and properties of carbon nanotubes. **Vacuum & Cryogenics** (Chinese), 4, 193-200 (**2014**).
13) **Xiji Shao**, Zhanglin Hou, Linli He. Transform resolution of the fourier in the quantum mechanics. **Theory and Practice of Contemporary Education** (Chinese). 11, 141-143 (**2013**).

南方科技大学 | 研究生院
SOUTHERN UNIVERSITY OF SCIENCE AND TECHNOLOGY
SUSTech Graduate School

南方科技大学
博士研究生成绩单

姓名	邵希吉	性别	男	出生日期	1982/10/21	
学号	11849474			入学时间	2018/09/03	
物理系		培养单位	物理学	学科		

课程代码	课程名称	学时	学分	考核方式	成绩	绩点	备注
GGC5003	科技论文检索与写作	32	2	考试	96	4	
GGC5016	博士英语	32	2	考试	88	3.7	
GGC5021	中国马克思主义与当代	32	2	考查	92	4	
PHY5005	物理实验仪器原理和应用	64	4	其它	80	3	
PHY5006	计算物理	48	3	考试	95	4	
PHY5028	凝聚态物理讲坛	48	3	考试	B+	3	
PHY5031	微纳结构加工	48	2	其它	87	3.7	
PHY5004	高等固体物理	64	4	考查	76	2.7	
PHY5024	低温物理	48	3	考查	83	3.3	
ACA6011	论文开题考核		2	考查	通过		
ACA6012	博士资格考核		2	考查	通过		

完成课程学分/完成总学分 25/29 学分

平均绩点 3.38

备注 1. GGC开头课程为公共课、ACA开头为必修培养环节，其余为专业课。
2. 该生为哈尔滨工业大学与南方科技大学联合培养，课程学习和必修环节在南方科技大学完成。

填表人 李爱晨

负责人：赵丹丹

南方科技大学研究生院（公章）

2021年10月08日

地址：中国广东省深圳市南山区学苑大道1088号
Address:No.1088 Xueyuan Avenue, Nanshan District, Shenzhen, Guangdong, P.R. China
邮编（Zip Code）：518055 邮箱（E-mail）：gradinfo@sustech.edu.cn
网址（Website）：https://gs.sustech.edu.cn/

PCCP

ROYAL SOCIETY OF CHEMISTRY

PAPER

View Article Online
View Journal | View Issue

Cite this: *Phys. Chem. Chem. Phys.*, 2020, **22**, 1693

A two-dimensional $ErCu_2$ intermetallic compound on Cu(111) with moiré-pattern-modulated electronic structures†

Chaoqiang Xu, [a] Kejie Bao,[a] Yande Que, [a] Yuan Zhuang,[a] Xiji Shao,[b] Kedong Wang,[bc] Junyi Zhu *[a] and Xudong Xiao *[a]

A rare-earth compound on a metal may form a two-dimensional (2D) intermetallic compound whose properties can be further modulated by the underlying substrate periodicity and coupling. Here, we present a combinational and systematic investigation using scanning tunneling microscopy/spectroscopy (STM/STS) and density functional theory (DFT) calculations on erbium (Er) on Cu(111). Experimentally, an intriguing growth mode transition from a branched island to a fractal-like island has been observed depending on whether the deposition process of Er is interrupted for a certain duration: post-deposition effects, such as nucleation and island growth controlled by diffusion, play an essential role in altering the Er island edge and its activity. Upon annealing, the branched Er islands become strands of amorphous surface alloy; in contrast, the fractal-like islands (with additional Er atoms on top) give rise to a monolayer thick 2D $ErCu_2$ intermetallic compound and display a moiré pattern. Theoretically, using DFT calculations, we found that the characteristic energy states, particularly the state in the unoccupied region around 582–663 meV, of the 2D $ErCu_2$ intermetallic compound are position-dependent, consistent with STS measurements. The moiré pattern originating from the mismatch of the periodicities of the $ErCu_2$ layer and the Cu(111) surface was identified to be responsible for the observed periodic modulation on the coupling interaction that affects the electronic structures. Our further DFT calculations on a free-standing $ErCu_2$ monolayer found it to be a 2D ferromagnet with topological band structures. Our work should stimulate further studies on such 2D rare-earth-based nanostructures and exploration of the use of the tunable electronic structures in such atomically-thin layers.

Received 14th October 2019,
Accepted 16th December 2019

DOI: 10.1039/c9cp05585a

rsc.li/pccp

1. Introduction

Originating from the lattice mismatch and/or misorientation, moiré superlattices have been found to be able to critically modulate the electronic structure[1–6] and optical properties of the materials,[7–9] especially the two-dimensional (2D) van der Waals materials. For example, the moiré superlattice formed by vertically stacking two sheets of graphene with a small twist angle can induce an isolated flat band near zero Fermi energy, resulting in the appearance of correlated insulating states and unconventional superconductivity.[5,6] In the twisted hetero-bilayer of tungsten diselenide/tungsten disulfide (WSe_2/WS_2), the in-plane moiré superlattice can apply periodic potentials to confine the interlayer valley excitons, leading to the circularly polarized interlayer exciton resonances.[10] Aside from the stacked monolayers of 2D materials, a 2D material on substrates can also give rise to the formation of a featured moiré pattern, which can tune the electronic structures of the 2D material as well. One recent example is hexagonal boron nitride (hBN) on a Cu(111) substrate, where the band gap and work function modulations in the hBN/Cu(111) heterostructure are found to be dependent on the moiré pattern periodicity.[4] Another example is a rare earth-based intermetallic compound on the corresponding metallic substrate. By deposition of rare-earth atoms onto hot noble metal substrates, Ormaza *et al.* have fabricated a structurally robust monolayer $GdAg_2$ intermetallic compound and observed a high temperature (85 K) ferromagnetic phase in this system.[11] Such rare-earth/metal intermetallic compound monolayers exhibit a moiré structure due to the atomic lattice mismatch, which effectively offers potential tunability to the electronic structure[12] as well as magnetic order[13,14] *via* the position-dependent coupling interaction with the underlying metal surface. Furthermore, possessing a stable interfacial structure, the moiré-patterned two-dimensional

[a] *Department of Physics, the Chinese University of Hong Kong, Shatin, Hong Kong, China. E-mail: jyzhu@phy.cuhk.edu.hk, xdxiao@phy.cuhk.edu.hk*
[b] *Department of Physics, Southern University of Science and Technology, Shenzhen, Guangdong 518055, P. R. China*
[c] *Shenzhen Key Laboratory of Quantum Science and Engineering, SUSTech, Shenzhen 518055, China*

† Electronic supplementary information (ESI) available. See DOI: 10.1039/c9cp05585a

rare-earth/metal heterostructures can also be used as nanotemplates, for example, for fabrication arrays of magnetic nanodots[15] and polymerization of organic nanowires.[16] As a rare-earth/metal compound, $ErCu_2$ renders a paradigmatic system. It crystallizes in the orthorhombic structure with space symmetry *Imma*[17] and is an antiferromagnetic material with a Néel temperature T_N = 11.3 K,[18] possessing intriguing magnetic properties such as metamagnetic transition.[19] Moreover, the properties of $ErCu_2$ in the two-dimensional form, namely, at the monolayer limit, remain scarcely explored.

In this paper, we mainly focus on studying the formation mechanism as well as the physical origin of the modulated electronic structure of $ErCu_2$/Cu(111) heterostructures at sub-monolayer coverage using low temperature scanning tunneling microscopy (STM) and density functional theory calculations (DFT). We first uncover a growth mode transition of Er on Cu(111) from flat branched islands to fractal-like islands with additional 3D growth by manipulating the deposition process and revealling the role of post-deposition effects in the epitaxial growth process. Interestingly, upon annealing treatment, the flat monolayer Er islands transform into an amorphous surface alloy, but in strong contrast, the fractal-like multilayer Er islands transform into a monolayer of well-ordered intermetallic compound. This $ErCu_2$ monolayer compound clearly demonstrates position-dependent electronic structures and modulated coupling interaction with the underlying Cu(111) surface with the moiré-pattern periodicity, as shown both by scanning tunneling spectroscopy (STS) measurements and DFT calculations. The calculation results also reveal that a free-standing $ErCu_2$ monolayer compound possesses 2D ferromagnetism and topological band structures, contrary to the anti-ferromagnetism of its bulk counterpart.

Details regarding sample preparation, STM/STS measurement methods, and DFT calculations are presented in the ESI.†

2. Results and discussion

2.1 Growth and formation of 2D $ErCu_2$ intermetallic compound

Deposition of Er on a Cu(111) surface at room temperature leads to the formation of branched or fractal-like Er islands. Fig. 1a presents an STM image of surface morphology of Er islands at sub-monolayer coverage of 0.3 ML. Most Er islands start to grow from the step edge of the substrate and preferentially spread out perpendicularly to the edge; only a few Er islands nucleate on the terrace and apparently branch along the three favorable orientations due to the three-fold symmetry of the underlying substrate. Practically, no corrugation is resolved on top of these branched islands, indicating the flatness and compactness of their high crystalline quality. The apparent height of these islands is measured to be 4.4 ± 0.2 Å, as seen in Fig. 1b (the step height of 2.1 Å of the Cu(111) surface is also presented as a reference). To increase the coverage of Er, one can choose either to

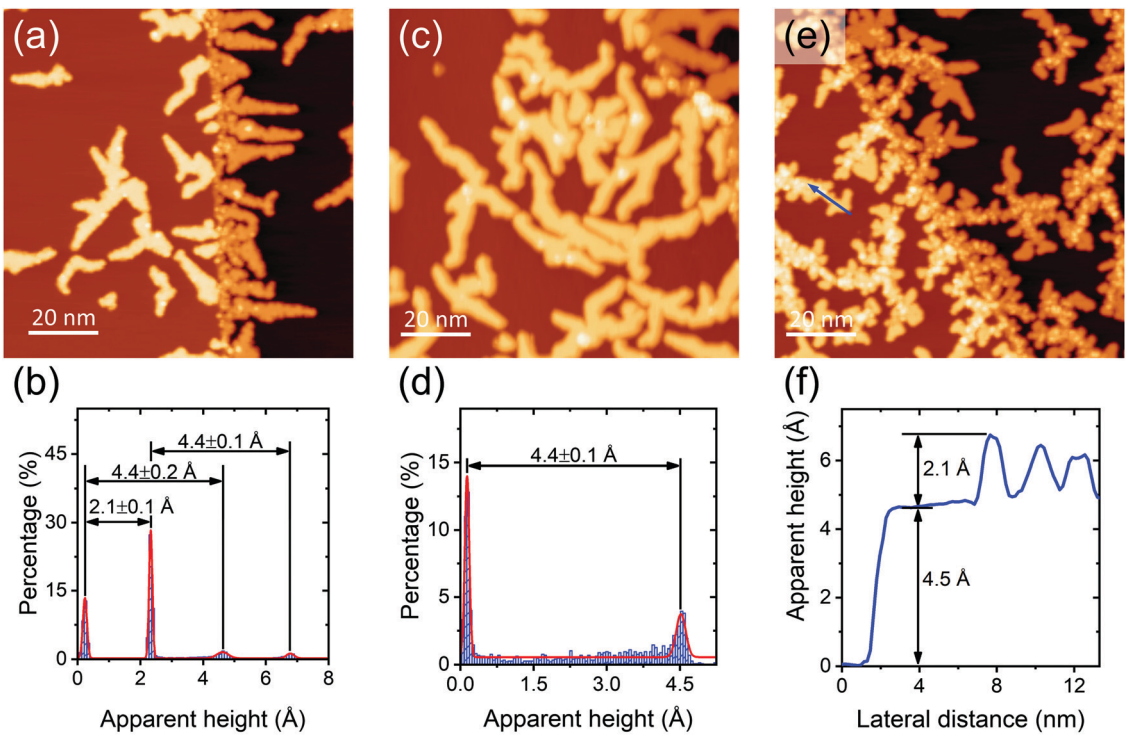

Fig. 1 (a) Constant-current STM image of about 0.3 ML Er on a Cu(111) surface. (b) Height histogram of Er/Cu(111) in (a). The Gaussian fit (red line) on height distribution (blue columns) is used to determine the step height of the Cu(111) surface and the thickness of Er islands. (c and e) Constant-current STM images of about 0.6 ML Er on Cu(111) surface, respectively, without and with interruption during deposition. (d) Height histogram of Er/Cu(111) in (c). (f) Line profile along the blue arrow in (e). Tunneling conditions for (a), (c) and (d) are 1.0 V and 100 pA.

simply increase the deposition time within the same dose or to make a second-round deposition onto the existing Er/Cu(111) surface at a later time. The main difference between these two procedures is whether the deposition process is interrupted or not. In the single prolonged deposition procedure, the growth process shows similar behavior as above, leading to wider and longer branched islands, and a higher island density as shown in Fig. 1c, without thickening the islands (Fig. 1d). However, in the interrupted deposition procedure, *e.g.*, depositing sub-monolayer Er, scanning the surface morphology using STM, and subsequently depositing more Er atoms, the growth mode is different and new branches are observed to grow along the direction perpendicular to the previous branches, resulting in a fractal-like pattern for the islands (Fig. 1e). Moreover, a significant amount of Er atoms now remain on top of the islands, forming Er clusters with varied apparent height about 2.1 Å, as shown in Fig. 1f. The completely different surface morphologies and growth modes shown in Fig. 1c and e with two different growth procedures with comparable Er coverage, at first sight, present a clear discrepancy despite being nearly the same amount. To understand this discrepancy, we must take the post-deposition effects, namely, nucleation and island growth after deposition, into account.[20] The island growth in a UHV environment is a non-equilibrium thermodynamic process. During deposition, collisions among the diffusing Er atoms take place to form small clusters, which further serve as the nucleation centers for island growth. When the deposition is stopped, nucleation and island growth will continue to proceed, which modifies the morphology and the chemical properties of the island edges. The time given to settle the edge structure, which controls the growth mode for additional Er atoms in the 2D structure, is obviously critical for the growth mode and thus determines the shape of the formed islands. Thus, interruption of deposition can indeed result in observable growth mode change.

The surface morphology of Er islands on Cu(111) further changes upon annealing treatment and the two kinds of precursor islands presented in Fig. 1c and e evolve into different structures. After 30 min UHV annealing at 473 K, the flat Er islands shown in Fig. 1c have disappeared and are replaced by rough and distorted islands, as now shown in Fig. 2a. The apparent height of the corrugated rough islands is 2.1 ± 0.2 Å (Fig. 2b), significantly smaller than that of the as-deposited flat branched islands, indicating that intercalation at the atomic level has taken place between the rare-earth Er islands and the underneath Cu(111) substrate. Further increase of the annealing temperature still fails to form ordered structures, suggesting the high stability of this intercalated structure. This observation is similar to a previous result, where a random surface alloy is formed after annealing of Ce/Pt(111) at low coverage (<0.7 ML).[21] When the same annealing condition is applied to the precursor shown in Fig. 1e, a well-ordered island phase surprisingly appears, as shown in Fig. 2c, forming a 2D intermetallic compound rather than a metal alloy. Similar structures have been observed elsewhere on the surface of rare earth/metal systems.[11,22–25]

The 2D intermetallic compound on Cu(111) substrate is featured with a long-range moiré periodicity of 24.7 ± 1.0 Å, as presented in Fig. 2d. The apparent height of the monolayer

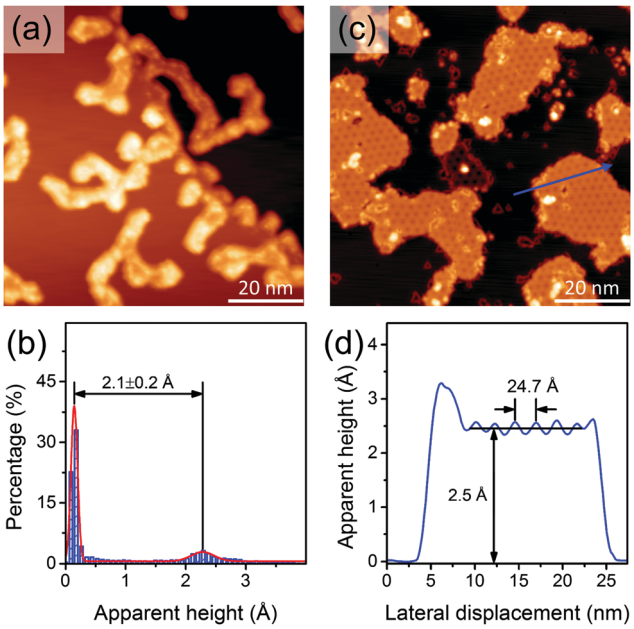

Fig. 2 (a and c) Constant-current STM images of Er/Cu(111) surfaces after the annealing treatment. The corresponding precursors of (a) and (c) are shown in Fig. 1(c) and (e), respectively. (b) Height histogram of Er/Cu(111) in (a). (d) Height profile taken along the blue arrow in (c). Tunneling conditions: (a) 1 V, 0.1 nA; (c) 0.5 V, 0.1 nA.

compound is measured to be about 2.46 Å. Fig. 3a and b display the atomically resolved STM images of this $ErCu_2$ monolayer taken at different sample bias voltages. At a bias voltage above the Fermi level, a honeycomb lattice of Cu is imaged with a lattice constant of 2.8 ± 0.1 Å (Fig. 2e), expanding 12% compared to the nearest neighbor distance of bulk Cu (2.5 Å). At a bias voltage below the Fermi level, a hexagonal lattice of Er is imaged with a lattice constant of 4.9 ± 0.2 Å ($\sqrt{3} \times 2.8$ Å, Fig. 2f). The moiré pattern arises from the lattice mismatch between the monolayer $ErCu_2$ lattice and the underlying Cu(111) surface. With the $ErCu_2$ lattice rotated by 30° from the Cu(111) surface lattice, the periodicity of the moiré pattern, 24.7 ± 1.0 Å, corresponding to the lattice of (8.7 × 8.7) of $ErCu_2$ and the lattice of (9.6 × 9.6) of Cu(111), suggests that the superlattice structure of the $ErCu_2$ monolayer is incommensurate with the Cu(111) substrate.

Based on the experimentally determined atomic structure, Fig. 3c and d present the calculated relaxed atomic structure of the moiré patterned $ErCu_2$/Cu(111). Here, an atomic modelling of one layer of (9 × 9) of $ErCu_2$ on top of two layers of (10 × 10) of Cu(111) is employed in the DFT calculations. We can see that the emergence of a moiré pattern is due to the reconstruction of the compound layer atoms, buckled along the *z* direction and non-uniformly strained in the *x*–*y* plane. We notice that the three high symmetry points, labelled as FCC, TOP, and HCP in the Fig. 3c, still preserve their in-plane C_3 symmetry. The atomic top sites of the Er atoms above the Cu atoms of the second layer, namely, the TOP sites, are lowered due to relatively strong coupling between Er and Cu, resulting in the valley image of the experimental results (Fig. 2a and b). Atoms at the FCC and

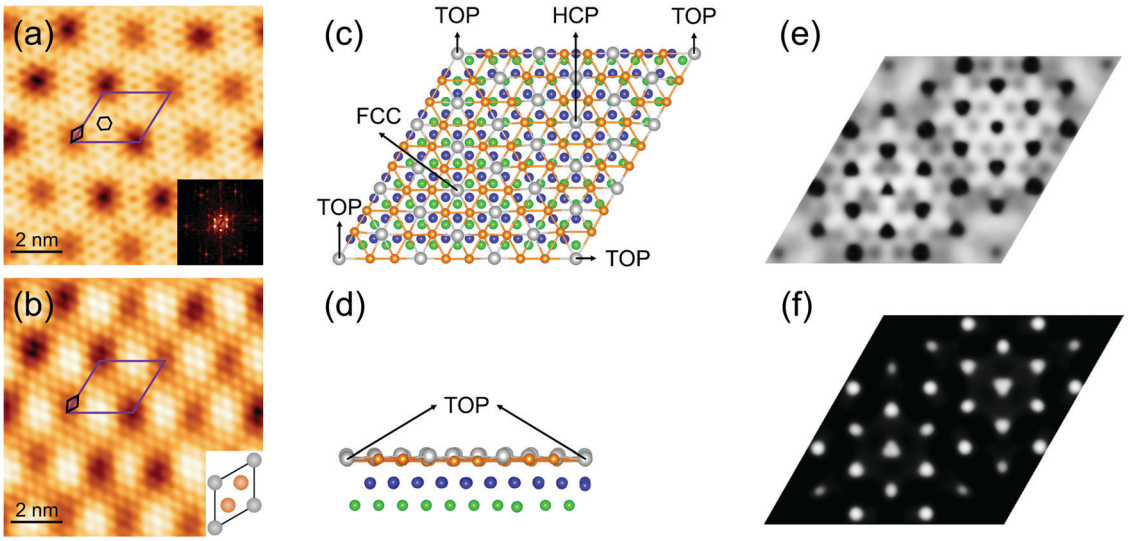

Fig. 3 (a and b) Zoomed-in constant-current STM images with atomic resolution taken on top of the $ErCu_2$ monolayer compound at various bias voltages, where Cu atoms in (a) and Er atoms in (b) are manifested as bright protrusions, respectively. The inset in (a) shows its FFT. The inset in (b) depicts the diamond unit cell of $ErCu_2$ with the silver and orange balls representing the Er and Cu atoms, respectively. The black hexagon in (a) denotes the Cu honeycomb lattice, while the black and purple diamonds in (a) and (b) delineate the unit cell and moiré superstructure, respectively. Tunneling conditions: (a) 1 mV, 0.6 nA; (b) −10 mV, 1.5 nA. (c) Top view and (d) side view of the calculated relaxed atomic structure of the moiré pattern of $ErCu_2$/Cu(111). Blue balls and green balls represent the Cu atoms in the second layer and third layer, and silver and orange balls represent the Er and Cu atoms in the $ErCu_2$ layer, respectively. The three kinds of top sites of Er atoms are denoted by FCC, TOP, and HCP, respectively. Simulated (e) empty- and (f) filled-state STM images of one moiré pattern of the $ErCu_2$ monolayer, where Er atoms are manifested as dark and bright spots in (e) and (f), respectively.

HCP sites are higher than the Er atom at the TOP sites, consistent with early literature results.[24] Simulated empty- and filled-state STM images (Fig. 3e and f) of one moiré pattern of the $ErCu_2$ monolayer agree well with the experimental results, *i.e.*, the Cu atoms are manifested as bright honeycomb lattices in the empty-state STM image, while the Er atoms are manifested as bright spots in the filled-state STM image. This main feature is shared among the calculated STM images at different empty or filled states near the Fermi level, as shown in the ESI,† Fig. S1. It is worth pointing out that the Er atoms at the TOP sites, above and below the Fermi level, are always imaged as big dark spots in both our simulated and experimental STM images, due to their strong bonding with the underlying Cu atoms as well as lower height.

It is interesting that obviously different structures (amorphous strands *versus* well-ordered moiré superstructure) have been formed after the annealing treatment on the two precursors. Similar results have been observed by Tang *et al.* when annealing Ce thin films deposited on Pt(111).[21] Tang *et al.* found that annealing of Ce/Pt(111) at low coverage resulted in the formation of a random surface alloy, while annealing of Ce/Pt(111) at high Ce coverage led to the emergence of a well-ordered intermetallic surface compound.[21] Despite the similarity, our results show that the surface morphology of the final products upon heating treatment mainly depends on the initial structure of the rare-earth film, rather than on the coverage. As stated before, nearly the same amount of Er is deposited onto the substrates in Fig. 1c and e, which evolves into different structures after annealing treatment. It should also be noted that the formation of the well-ordered monolayer $ErCu_2$ intermetallic compound is not only a physical thermodynamic equilibrium process, but also a chemical reaction process. In fact, compared to the sample in Fig. 1c, since the amount of copper atoms participating in the reaction at the same annealing conditions remains almost the same, from the point of view of chemical reaction, the presence of multilayer Er islands in Fig. 1e increases the Er concentration locally, which eventually induces a dramatic change in the resultant morphology. The suggested formation mechanisms of surface morphologies of different heterostructures are summarized in the ESI,† Fig. S2.

2.2 Electronic structures

To obtain the electronic structure information, we have performed scanning tunneling spectroscopy (STS) measurements. Fig. 4 presents the differential conductance dI/dV spectra taken on various Er/Cu(111) heterostructures, which reveal the local density of states (LDOS).

On the flat Er islands (inset in Fig. 4a), in addition to the feature at −262 meV originating from the well-known Cu(111) surface state, all the dI/dV spectra unveil a similar peak above the Fermi level at 696 meV (Fig. 4a), independent of the sampling position. The absence of position dependence as well as the absence of island size and shape dependence indicate the weak coupling between these flat islands and the supporting substrate. As already shown in Fig. 2a and the inset in Fig. 4b, annealing of these as-deposited Er islands significantly increases the surface roughness and forms a random alloy. Representative dI/dV spectra taken on both the dark area and the bright area of the Er–Cu alloy strands (Fig. 4b) demonstrate the disappearance of the pronounced peak feature observed on the as-deposited Er islands and the presence of a somewhat rectifying type I–V characteristic feature. In contrast, on the well-ordered $ErCu_2$

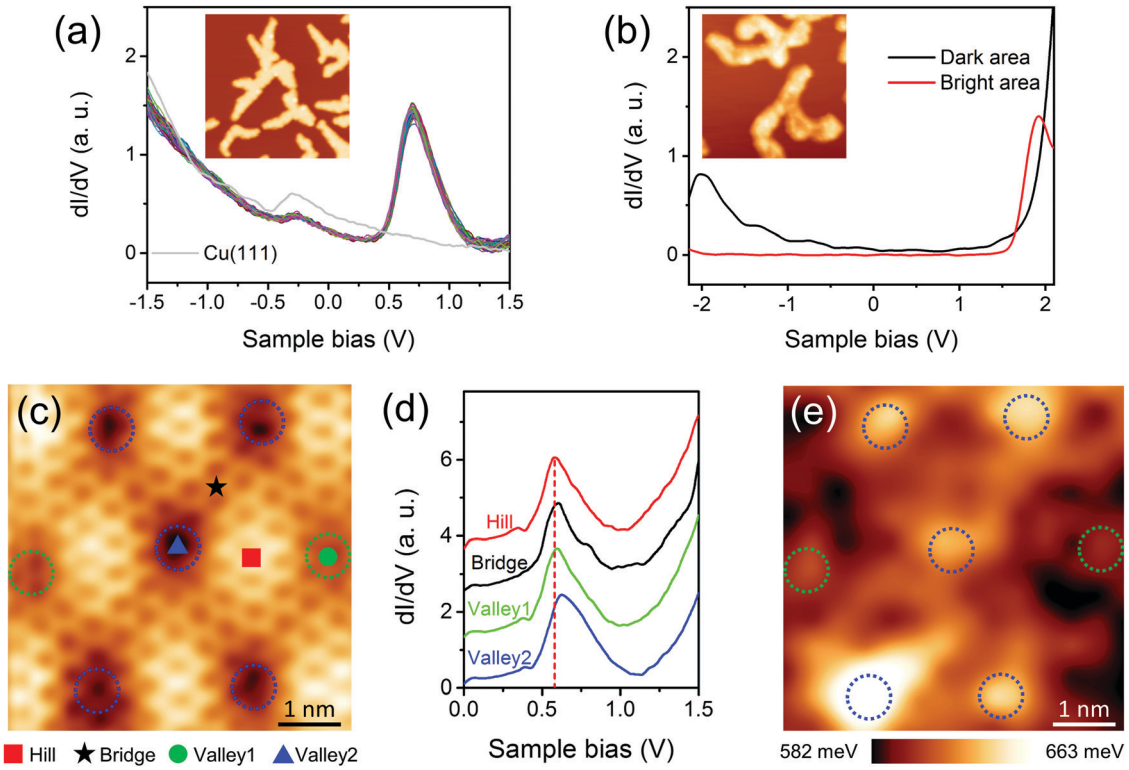

Fig. 4 (a) d*I*/d*V* spectra acquired at different positions on the flat Er islands shown in Fig. 1a, and on the bare Cu(111) surface. (b) d*I*/d*V* spectra acquired at different positions on the disordered rough Er–Cu alloy strands shown in Fig. 2a. Insets in (a) and (b) (image size: 50 × 50 nm^2) are as-deposited flat Er islands and amorphous alloy after annealing, respectively. (c) Atomically resolved constant-current STM image of $ErCu_2$ (10 mV, 0.3 nA) where four different sites are identified as the hill, bridge, valley-1, and valley-2, denoted by the red square, black star, green circle, and blue triangle, respectively. (d) d*I*/d*V* spectra acquired on these four sites. (e) Spatial map of the peak position of the d*I*/d*V* spectrum measured within the area shown in (c) (16 × 16 spectra are taken in total).

compound monolayer (Fig. 4c), the d*I*/d*V* spectra reveal sizable site dependence on the moiré pattern. As depicted in Fig. 4d, the peak position of d*I*/d*V* spectra not only show an overall "red shift" as compared to that shown in Fig. 4a but also exhibits a noticeable peak position shift from ~582 meV at sites of 'hill', 'bridge', and 'valley-1' to ~624 meV at 'valley-2'. It is noted that the LDOS at sites of valley-1 and valley-2 are surprisingly different which should be associated with noticeable difference in height, indicating a varied atomic environment, as shown in the STM image (Fig. 4c). This energy difference (~42 meV) is far larger than the characteristic thermal energy at 78 K (~7 meV) and the measurement uncertainty. Gridding a 5.6 × 5.6 nm^2 area on the $ErCu_2$ compound monolayer by 16 × 16 points and extracting the peak positions from the respective d*I*/d*V* spectra, a spatial map of the d*I*/d*V* peak can be obtained as shown in Fig. 4e. It is clear that the position of the d*I*/d*V* peak is strongly spatially dependent. The bright area in the peak map, which represents a relatively high energy of the peak position, coincides well with the dark area in the STM image (seven dotted circles in Fig. 4c and e serve as the reference), implying a position-dependent interaction between the 2D $ErCu_2$ compound layer and the underlying Cu(111) substrate.

In order to understand the origin of the observed moiré-pattern position-dependent electronic structure of $ErCu_2$/Cu(111), we have calculated the total density of states (tDOS) within the framework of DFT. Within the given energy window as shown in Fig. 5a and b, both the experimentally averaged d*I*/d*V* spectra over different sites in the moiré structure and the calculated tDOS have five states/peaks and their positions agree reasonably well. In particular, the calculated energy distance between the third state and the forth state is about 0.7 eV, almost identical to the experimental result. The noticeable discrepancy in the relative intensity of these 5 peaks between the measured d*I*/d*V* and calculated tDOS should be mainly attributed to the background of tip electronic states.

Furthermore, while the origin of these five states might be different, the calculated projected density of states (pDOS) shown in Fig. 5c and d suggest that the experimentally observed pronounced peak around 0.6 eV is the anti-bonding state above the Fermi level, mainly originating from the Er d state and Cu p and d states. Moreover, the calculated DOS (Fig. 5e) of Er atoms at the FCC and TOP sites, respectively, corresponding to the 'hill' and 'valley' areas of the moiré pattern, display a clear energy shift toward high energy for this antibonding state at ~0.6 eV from the FCC site Er atom to the TOP site Er atom. Therefore, we can safely conclude that the position-dependent electronic structure is attributable to the modulated coupling interaction between Er atoms and underlying Cu atoms.

2.3 Calculated band structure of a free-standing $ErCu_2$ layer

Single-layer $ErCu_2$ is possibly obtainable by co-evaporation of Er and Cu onto other substrates and peeling off experimentally.

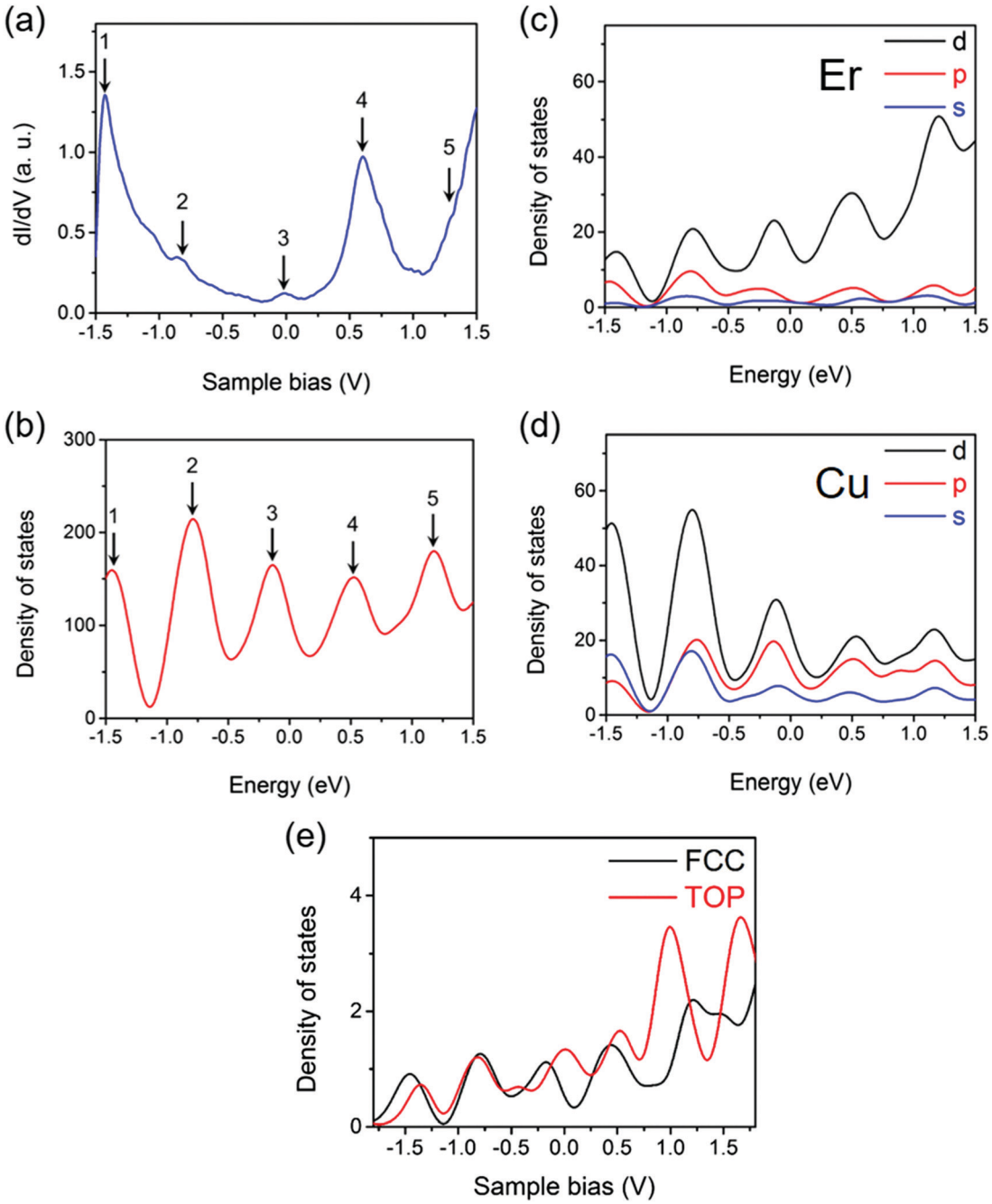

Fig. 5 (a and b) Comparison between experimentally averaged d*I*/d*V* spectrum and calculated total density of states of the $ErCu_2$ monolayer on Cu(111). (c and d) Calculated projected density of states of Er and Cu atoms, respectively, in the $ErCu_2$ compound layer. (e) Comparison between calculated DOS of Er atoms at FCC and TOP sites.

Therefore, it is worthwhile to compute the band structure of the isolated $ErCu_2$ layer by means of DFT calculations. As shown in Fig. 6a, without considering spin–orbit coupling (SOC), the spin-resolved band structures clearly demonstrate the 2D ferromagnetism in single-layer $ErCu_2$, similar to what has been experimentally observed in the rare-earth based 2D material, $GdAg_2$.[11] It is interesting to note that there are a number of band crossings near the Fermi level without opening any energy gaps, indicating the formation of three Dirac nodal loops around the K point.[26,27] On considering the SOC effect, while the in-plane magnetization will break the M_z symmetry and open an energy gap as wide as 78 meV in the nodal line labelled NL (Fig. 6b), the out-of-plane magnetization will preserve all the gapless nodal lines (Fig. 6c). Our calculation results suggest that altering the magnetization direction can open/close the energy gap near the band crossings and further experimental efforts should be stimulated to explore the exotic electronic structure of the $ErCu_2$ monolayer. We also notice that

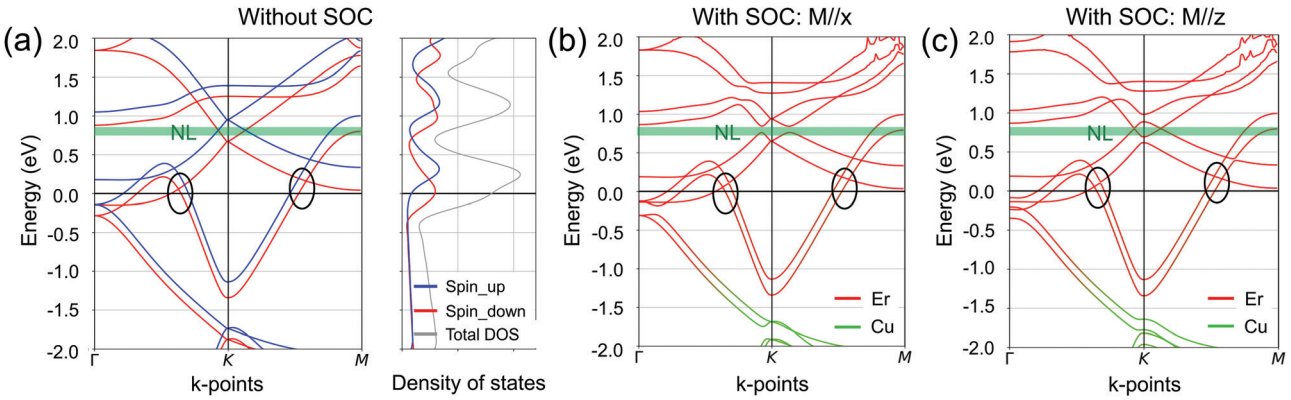

Fig. 6 Calculated band structure of a free-standing $ErCu_2$ monolayer. (a) (left) Spin-resolved band structures without considering SOC, where the spin-up and spin-down bands are displayed, respectively, by red and blue lines. The green area and black ovals denote three nodal lines. (right) Calculated total density of states. (b and c) Calculated band structures after taking into account SOC for in-plane and out-of-plane magnetization. Green area and black ovals denote the position of Dirac nodal loops.

a recent work on $GdAg_2$ has been published, which claims the discovery of Weyl nodal lines in such 2D ferromagnetic material by ARPES and first-principle calculations.[28]

3. Conclusions

To summarize, we have investigated the growth behaviors and the electronic properties of various Er/Cu(111) heterostructures. While the continuous deposition of Er on Cu(111) at room temperature leads to growth of branched islands, interrupted deposition induces in-plane fractal-like island growth and some degree of out-of-plane growth due to post-deposition effects. Further annealing of the flat branched Er islands results in amorphous alloy strands; in contrast, annealing the fractal-like islands with Er atoms or clusters on top gives rise to the formation of a uniform monolayer of $ErCu_2$ intermetallic compound featured with a moiré pattern. This moiré periodicity is found to be able to effectively modulate the electronic structure of the $ErCu_2$ monolayer on the Cu(111) surface, as also confirmed by the DFT calculations. Such a result provides a reliable method to tune the electronic structures of the atomically thin layers. The DFT calculations also reveal that a free-standing 2D $ErCu_2$ compound monolayer possesses a ferromagnetic phase and exotic band structures. Our work should stimulate further study on such 2D rare-earth-based nanostructures and exploration of the use of tunable electronic structures in such atomically-thin layers.

Conflicts of interest

There are no conflicts to declare.

Acknowledgements

This work was supported by the Research Grant Council of Hong Kong (Grant No. 404613), the Direct Grant for Research of CUHK (No. 4053306 and 4053348), the National Natural Science Foundation of China (Grant No. 11574128), the MOST 973 Program (Grant No. 2014CB921402), and the Science, Technology and Innovation Commission of Shenzhen Municipality (No. ZDSYS20170303165926217).

References

1 C. R. Dean, L. Wang, P. Maher, C. Forsythe, F. Ghahari, Y. Gao, J. Katoch, M. Ishigami, P. Moon, M. Koshino, T. Taniguchi, K. Watanabe, K. L. Shepard, J. Hone and P. Kim, *Nature*, 2013, **497**, 598–602.
2 K. Kim, A. DaSilva, S. Huang, B. Fallahazad, S. Larentis, T. Taniguchi, K. Watanabe, B. J. Leroy, A. H. MacDonald and E. Tutuc, *Proc. Natl. Acad. Sci. U. S. A.*, 2017, **114**, 3364–3369.
3 W. Yao, E. Y. Wang, C. H. Bao, Y. O. Zhang, K. A. Zhang, K. J. Bao, C. K. Chan, C. Y. Chen, J. Avila, M. C. Asensio, J. Y. Zhu and S. Y. Zhou, *Proc. Natl. Acad. Sci. U. S. A.*, 2018, **115**, 6928–6933.
4 Q. Zhang, J. Yu, P. Ebert, C. Zhang, C. R. Pan, M. Y. Chou, C. K. Shih, C. Zeng and S. Yuan, *ACS Nano*, 2018, **12**, 9355–9362.
5 Y. Cao, V. Fatemi, A. Demir, S. Fang, S. L. Tomarken, J. Y. Luo, J. D. Sanchez-Yamagishi, K. Watanabe, T. Taniguchi, E. Kaxiras, R. C. Ashoori and P. Jarillo-Herrero, *Nature*, 2018, **556**, 80.
6 Y. Cao, V. Fatemi, S. Fang, K. Watanabe, T. Taniguchi, E. Kaxiras and P. Jarillo-Herrero, *Nature*, 2018, **556**, 43.
7 C. Jin, E. C. Regan, A. Yan, M. Iqbal Bakti Utama, D. Wang, S. Zhao, Y. Qin, S. Yang, Z. Zheng, S. Shi, K. Watanabe, T. Taniguchi, S. Tongay, A. Zettl and F. Wang, *Nature*, 2019, **567**, 76–80.
8 K. Tran, G. Moody, F. Wu, X. Lu, J. Choi, K. Kim, A. Rai, D. A. Sanchez, J. Quan, A. Singh, J. Embley, A. Zepeda, M. Campbell, T. Autry, T. Taniguchi, K. Watanabe, N. Lu, S. K. Banerjee, K. L. Silverman, S. Kim, E. Tutuc, L. Yang, A. H. MacDonald and X. Li, *Nature*, 2019, **567**, 71–75.
9 K. L. Seyler, P. Rivera, H. Yu, N. P. Wilson, E. L. Ray, D. G. Mandrus, J. Yan, W. Yao and X. Xu, *Nature*, 2019, **567**, 66–70.

10 F. C. Wu, T. Lovorn and A. H. MacDonald, *Phys. Rev. Lett.*, 2017, **118**, 6.
11 M. Ormaza, L. Fernandez, M. Ilyn, A. Magana, B. Xu, M. J. Verstraete, M. Gastaldo, M. A. Valbuena, P. Gargiani, A. Mugarza, A. Ayuela, L. Vitali, M. Blanco-Rey, F. Schiller and J. E. Ortega, *Nano Lett.*, 2016, **16**, 4230–4235.
12 Q. Zhang, J. Yu, P. Ebert, C. Zhang, C.-R. Pan, M.-Y. Chou, C.-K. Shih, C. Zeng and S. Yuan, *ACS Nano*, 2018, **12**, 9355–9362.
13 J. Ren, H. Guo, J. Pan, Y. Y. Zhang, X. Wu, H.-G. Luo, S. Du, S. T. Pantelides and H.-J. Gao, *Nano Lett.*, 2014, **14**, 4011–4015.
14 F. Donati, L. Gragnaniello, A. Cavallin, F. Natterer, Q. Dubout, M. Pivetta, F. Patthey, J. Dreiser, C. Piamonteze and S. Rusponi, *Phys. Rev. Lett.*, 2014, **113**, 177201.
15 L. Fernandez, M. Blanco-Rey, M. Ilyn, L. Vitali, A. Magana, A. Correa, P. Ohresser, J. E. Ortega, A. Ayuela and F. Schiller, *Nano Lett.*, 2014, **14**, 2977–2981.
16 M. Abadia, M. Ilyn, I. Piquero-Zulaica, P. Gargiani, C. Rogero, J. E. Ortega and J. Brede, *ACS Nano*, 2017, **11**, 12392–12401.
17 A. Storm and K. Benson, *Acta Crystallogr.*, 1963, **16**, 701–702.
18 Y. Hashimoto, H. Kawano, H. Yoshizawa, S. Kawano and T. Shigeoka, *Phys. B*, 1995, **213**, 333–335.
19 K. Sugiyama, T. Yamamoto, N. Nakamura, A. Thamizhavel, S. Yoshii, K. Kindo, N. H. Luong and Y. Ōnuki, *Phys. B*, 2003, **327**, 423–426.
20 B. Müller, L. Nedelmann, B. Fischer, H. Brune and K. Kern, *Phys. Rev. B: Condens. Matter Mater. Phys.*, 1996, **54**, 17858.
21 J. Tang, J. Lawrence and J. Hemminger, *Phys. Rev. B: Condens. Matter Mater. Phys.*, 1993, **48**, 15342.
22 M. Corso, L. Fernández, F. Schiller and J. E. Ortega, *ACS Nano*, 2010, **4**, 1603–1611.
23 A. Correa, B. Xu, M. J. Verstraete and L. Vitali, *Nanoscale*, 2016, **8**, 19148–19153.
24 A. Correa, M. F. Camellone, A. Barragan, A. Kumar, C. Cepek, M. Pedio, S. Fabris and L. Vitali, *Nanoscale*, 2017, **9**, 17342–17348.
25 M. Ormaza, L. Fernández, S. Lafuente, M. Corso, F. Schiller, B. Xu, M. Diakhate, M. J. Verstraete and J. E. Ortega, *Phys. Rev. B: Condens. Matter Mater. Phys.*, 2013, **88**, 125405.
26 B. J. Feng, B. T. Fu, S. Kasamatsu, S. Ito, P. Cheng, C. C. Liu, Y. Feng, S. L. Wu, S. K. Mahatha, P. Sheverdyaeva, P. Moras, M. Arita, O. Sugino, T. C. Chiang, K. Shimada, K. Miyamoto, T. Okuda, K. H. Wu, L. Chen, Y. G. Yao and I. Matsuda, *Nat. Commun.*, 2017, **8**, 6.
27 L. Gao, J. T. Sun, J. C. Lu, H. Li, K. Qian, S. Zhang, Y. Y. Zhang, T. Qian, H. Ding, X. Lin, S. Du and H. J. Gao, *Adv. Mater.*, 2018, **30**, 7.
28 B. Feng, R.-W. Zhang, Y. Feng, B. Fu, S. Wu, K. Miyamoto, S. He, L. Chen, K. Wu and K. Shimada, 2019, arXiv preprint arXiv:1901.01429.

Chem

CellPress

Article

Avoiding Sabatier's conflict in bifunctional heterogeneous catalysts for the WGS reaction

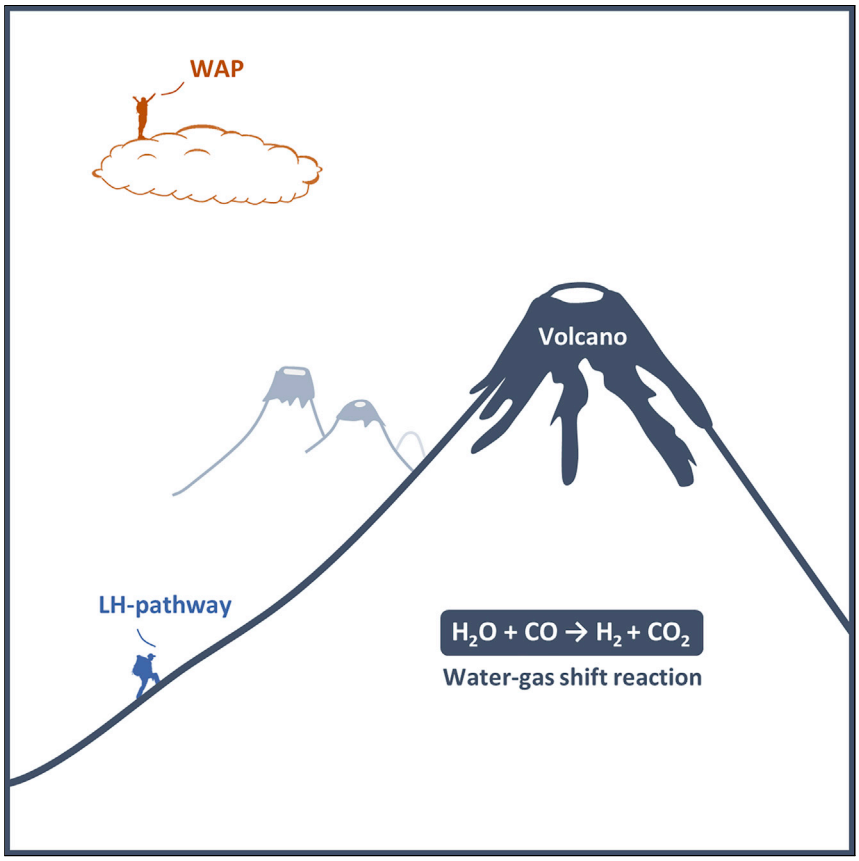

The WGS reaction is the industrial workhorse for removing CO and generating H_2. The prevailing thinking is that a highly reactive catalyst that readily dissociates water on its surface is key to the high efficiency of a WGS catalyst. We show that a new mechanism, WAP, using weakly reactive catalysts whose surface is oxygen covered, can achieve much higher efficiencies by avoiding the Sabatier conflict of the rate-limiting step and, thus, accelerating the kinetics of the reaction.

Hao Tian, Yanling He, Qinglong Zhao, ..., A.M.C. Ng, Hu Xu, S.Y. Tong

xuh@sustech.edu.cn (H.X.)
tongsy@cuhk.edu.cn (S.Y.T.)

HIGHLIGHTS

A new strategy for designing efficient heterogeneous catalysts is presented

The proposed WAP mechanism avoids the Sabatier conflict of the rate-limiting step

The WAP catalyst, Au/TiC(111), shows high efficiency and durability

A reactive substrate is no longer key to the high efficiency of a WGS catalyst

Tian et al., Chem 7, 1–13
May 13, 2021
https://doi.org/10.1016/j.chempr.2021.01.018

Please cite this article in press as: Tian et al., Avoiding Sabatier's conflict in bifunctional heterogeneous catalysts for the WGS reaction, Chem (2021), https://doi.org/10.1016/j.chempr.2021.01.018

Chem

CellPress

Article

Avoiding Sabatier's conflict in bifunctional heterogeneous catalysts for the WGS reaction

Hao Tian,[1,2,6] Yanling He,[1,2,6] Qinglong Zhao,[3,6] Jiaxin Li,[1] Xiji Shao,[1] Zhe Zhang,[1] Xiang Huang,[1] Chao Lu,[1] Kedong Wang,[1] Qichuan Jiang,[3] A.M.C. Ng,[1] Hu Xu,[1,*] and S.Y. Tong[1,4,5,7,*]

SUMMARY

A new strategy for designing efficient bifunctional heterogeneous catalysts for the water-gas-shift (WGS) reaction ($CO + H_2O \rightarrow CO_2 + H_2$) is presented. We avoid conflicting tasks that require *OH or *O from dissociated water to adsorb on and then desorb from the substrate of a catalyst. Instead, the CO on metal directly obtains OH from water that is connected by weak hydrogen bonds to the substrate. The task of the substrate is to efficiently channel *H on its surface and release them as H_2 gas. Experimental and theoretical results show that bifunctional catalysts with weakly reactive substrates have significantly higher CO conversion rates compared with highly reactive substrates that follow either the LH-associative or LH-redox process.

INTRODUCTION

The cardinal rule in heterogeneous catalysis, as stated by Paul Sabatier and others,[1–4] is that the interaction strength between a catalyst and the reactants should be "just right;" i.e., neither too strong nor too weak. This is because the reaction rate is limited by adsorption if the interaction strength is weak or by desorption if the interaction strength is strong. The efficiency of a catalyst is, thus, a result of compromise. In this work, we show that if we avoid assigning conflicting tasks to the substrate of a bifunctional catalyst, it is possible to greatly improve its efficiency.

To illustrate this idea, we use the water-gas-shift (WGS) reaction ($CO + H_2O \rightarrow CO_2 + H_2$) as an example, but the strategy is applicable to other catalytic reactions. WGS is the industrial workhorse for removing CO from the atmosphere and generating hydrogen in the process. The reaction is exothermic with the release of 41.1 kJ/mol, so the conversion of CO to CO_2 becomes less effective as the temperature increases. Catalysts that act efficiently below 450 K are much sought after in order to minimize CO that poisons electro-catalysts used in fuel cells.[5,6] Current front-runner catalysts are metal particles deposited on suitable substrates, the so-called bifunctional catalysts.[7–17] The traditional WGS process using bifunctional catalysts follows the Langmuir-Hinshelwood (LH) pathway,[18,19] where the reaction proceeds between CO adsorbed on metal and H_2O dissociatively adsorbed on the substrate. The substrate thus carries out two conflicting tasks: (1) to dissociate water, forming *OH and/or *O (* denotes the adsorption state) on its surface, and (2) to facilitate *OH or *O to desorb and bind with *CO on the metal. If *CO on metal binds with *OH to form *COOH on metal, the process is called LH-associative[5,20,21] (Figure 1A). If *CO on metal binds with *O to form CO_2, the process is called LH-redox. Prior studies have focused on using highly reactive catalysts that readily dissociate water. Numerous studies have reported that more *OH formed on the surface of a catalyst

The bigger picture

The cardinal rule in heterogeneous catalysis is the Sabatier Principle, believed to be ubiquitous and unavoidable in catalyst design. This paper points out that it is possible to avoid the inherent contradiction embedded in the principle and find catalysts with much higher efficiencies. For illustration, we use the water-gas-shift (WGS) reaction to reach conclusions. A new mechanism called water-assisted pathway (WAP) is proposed on two-component catalysts (metal + oxygen-covered substrate), and its high efficiency for WGS reaction is observed for the as-designed catalyst, Au/TiC(111). In WAP, the weakly reactive oxygen-covered substrate avoids the Sabatier conflict of the rate-determining step, in stark contrast to much studied highly reactive substrates that follow the LH-associative or LH-redox process.

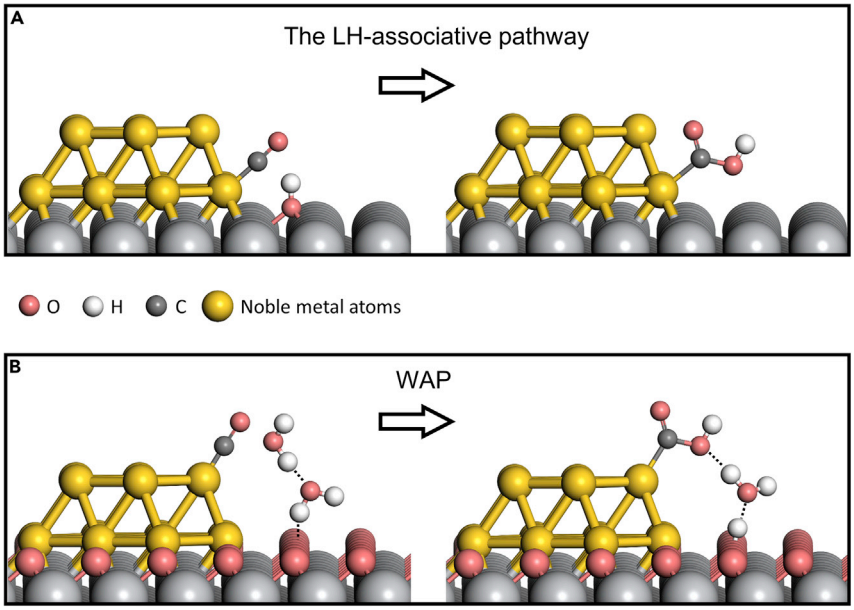

Figure 1. Schematic illustration of the WGS reaction on a bifunctional catalyst

(A) The LH-associative pathway in which *CO on metal obtains OH that are strongly adsorbed on the substrate.

(B) The WAP process in which *CO on metal obtains OH from water involving two water molecules that are linked by weak H-bonds to each other and to the oxygen-covered substrate. For the bifunctional catalyst, gray, pink, and yellow balls, respectively, represent bare substrate's M, surface O, and Au atoms. Small gray, pink, and white balls, respectively, represent C, O, and H atoms of CO and water. Solid double lines indicate covalent bonds; single dotted lines indicate H-bonds.

relates directly to higher efficiency of the WGS reaction.[13,15] However, these catalysts face an unavoidable obstacle: their efficiency is limited by the large desorption barrier of water components attached strongly on the surface of the catalysts. To obtain a breakthrough in the efficiency, a new avenue must be sought.

RESULTS AND DISCUSSION

We followed a different strategy. Instead of using substrates that react strongly with water, we looked for "substrates" that form H-bonds with water molecules. The strength of an H-bond is about 0.2 eV, much weaker than that of a covalent bond. The water molecule does not dissociate through this weak bond. The CO molecules adsorb exclusively on the metal and they extract OH from the water molecules that are H-bonded to the weakly interactive "substrate." This reaction has a very low reaction barrier, typically around 0.1 eV (Figure S1); however, the process quickly stops if the left-over hydrogen atom has no outlet. The reaction becomes sustainable if there is a suitable "substrate" on which the left-over hydrogen can channel away through hydrogen evolution from its surface. This, then, is the primary task of the "substrate." To date, the best "substrates" that fit this purpose are metal-carbides or 2D compounds whose surfaces are covered by an atomic layer of adsorbed *O (majority) and *OH (minority). These oxidized-hydroxylated substrates also guarantee that CO does not adsorb on them, thus avoiding their surfaces being poisoned by CO. In this design, there was clear separation of tasks that avoided conflict: *CO on metal was tasked to extract OH from H-linked water; oxidized-hydroxylated substrate was tasked to allow *H to migrate and escape as H_2 gas (Figure 1B). Suitable metals were chosen to maximize the efficiency of the

[1]Department of Physics, Southern University of Science and Technology, Shenzhen 518055, China

[2]Department of Physics, the University of Hong Kong, Hong Kong, China

[3]State Key Laboratory of Automotive Simulation and Control and School of Materials Science and Engineering, Jilin University, 5988 Renmin Street, Changchun 130025, China

[4]School of Science and Engineering, the Chinese University of Hong Kong, Shenzhen 518172, China

[5]Institute of Materials Science and devices, Suzhou University of Science and Technology, Suzhou 215009, China

[6]These authors contributed equally

[7]Lead contact

*Correspondence: xuh@sustech.edu.cn (H.X.), tongsy@cuhk.edu.cn (S.Y.T.)

https://doi.org/10.1016/j.chempr.2021.01.018

Please cite this article in press as: Tian et al., Avoiding Sabatier's conflict in bifunctional heterogeneous catalysts for the WGS reaction, Chem (2021), https://doi.org/10.1016/j.chempr.2021.01.018

first task, and suitable "substrates" were chosen to maximize the efficiency of the second task.

We call the new catalyst design water-assisted pathways (WAP). Water is known to regulate reaction rates and facilitate proton transfer in enzyme catalysts[21] and heterogeneous catalysts;[22,23] however, WAPs in WGS have never been studied. Our calculation shows that many compounds are suitable WAP "substrates," for example, the oxidized-hydroxylated (0001) surface of M_nAX_{n+1} (also known as MAX compounds) or the oxidized-hydroxylated (111) surface of carbon-deficient MC_x. In MAX compounds, M = Ti, Mo, Nb, etc.; X = C, N; and A = Si, Al, Ga, etc., and the (0001) surface has the lowest energy.[24,25] For MC_x compounds, the (111) surface has the lowest energy under carbon-deficient conditions[26,27] (Note S1; x is less than 1.0 and denotes the C/M number ratio). Schematic diagrams of the (0001) surface of MAX compounds and (111) surface of carbon-deficient MC_x are shown in Figures S2 and S3. The (0001) or (111) surface of these compounds are terminated by a hexagonal array of metal atoms, and they are electron rich. According to our calculations, on these bare Ti_3SiC_2(0001) and α-MoC_x(111) surfaces, the optimal *O coverage was 75% and 88%, respectively, and the remaining sites were covered by *OH (Note S2 and Figures S4 and S5). These results are in good agreement with experimental observations.[26,27] For the metal in the bifunctional catalyst, we chose Au clusters deposited on the bare substrates. Theory shows that Au atoms occupy *fcc* sites on top of the metal layer, forming epitaxial islands two to three layers high. Figure S6 shows NAP-XPS (near ambient pressure XPS) data of Au/TiCx(111)Oy(OH)z. The spectra at 120°C show the Au 4f core-level peak (upper panel) in UHV, (middle panel) after exposure to 1.5 mbar of H_2O, and (lower panel) after exposure to 1.5 mbar of H_2O and 1.5 mbar of CO gas, respectively. The peak profiles reveal that CO adsorbs on Au leading to a side peak (arrow). As water and CO are introduced in the NAP cell, the Au 4f peak reduces in intensity. This is a known fact attributed to the scattering of photoelectrons by the gas molecules in the cell, thus reducing the number of photoelectrons that are collected. Factors affecting the level of attenuation include the type of gas, pressure, temperature, kinetic energy and travel distance of the photoelectrons, etc.[28] The calculated binding energy of CO on Au is between −0.6 to −0.8 eV, depending on the location of the Au atom in the cluster (Figure S7). The adsorbed CO has a small migration barrier of 0.33 eV on the Au cluster, indicating that it can move to find favorable sites to react with H-bonded water molecules (Figure S8). On the bare MAX(0001) and α-MC_x(111) surfaces, CO binds strongly at the top site with large binding energy of −2.11 and −1.44 eV, respectively (Figure S7). This means that CO exposure to the bare surface quickly populates it and poisons it. Calculations show that CO does not bind to the oxidized-hydroxylated substrate. For nomenclature, we shall use the following convention: if the metal particles are gold, we express the metal-oxidized-hydroxylated substrate catalyst as Au/$M_{n+1}AX_n$(0001)$O_x(OH)_y$ for MAX compounds and Au/α-MC_x(111)$O_y(OH)_z$ for MC_x compounds. Yao et al.[26] recently reported remarkably high efficiency for the catalyst Au/α-MoC_x(111)$O_y(OH)_z$. This catalyst is a member of the WAP family, belonging to the carbon-deficient MC_x(111) group. In the following, we explain how WAP catalysts work, particularly how the reaction barrier of the task assigned to *CO on metal and that assigned to the oxidized-hydroxylated substrate are independently maximized without conflict. The main text also contains experimental results of the performance of the WAP catalyst Au/TiC_x(111)$O_y(OH)_z$, compared with that of catalysts that follow the LH-pathways. Au/TiC_x(111)$O_y(OH)_z$ was chosen because it is the most stable in the WAP family for the WGS reaction. Earlier, Yao et al.[26] used the Au/α-MoC_x(111)$O_y(OH)_z$ catalyst, but that catalyst is not stable under WGS conditions. Furthermore, those authors explained the

Please cite this article in press as: Tian et al., Avoiding Sabatier's conflict in bifunctional heterogeneous catalysts for the WGS reaction, Chem (2021), https://doi.org/10.1016/j.chempr.2021.01.018

catalytic process using traditional LH-pathways.[26] The rate-limiting barrier under LH is 4.6 times bigger and cannot explain the measured high efficiency of the catalyst. Differences between results and models of our work and that of Yao et al.[26] are given in Note S3.

In the WAP process, one or more water molecules can participate, depending on the location of adsorbed CO in relation to the oxidized-hydroxylated substrate. In a single-water participation event, the oxidized-hydroxylated substrate anchors water molecules through H-bonds and gathers them near Au clusters. The calculations showed that H-bonded water near an Au cluster had binding energy ~2 times stronger than that at sites far from Au (Figure S9). Similar strengthening of H-bonding near Au clusters was reported by Saavedra et al.[22] in their work of gold-titania bifunctional catalyst for CO oxidation. As depicted in Figure 2A, the "linked" water directly supplies an OH to *CO on metal to form *COOH, while simultaneously depositing an H on the oxidized-hydroxylated substrate. Assisted by additional H-bonded water molecules, the deposited H migrates on the substrate until at some location, two *H come together to release a H_2 gas. As the bare substrate is covered by an optimal mix of *O and *OH, the deposition of H shifts the substrate away from equilibrium. The energy shift is several meV per deposited H near equilibrium and is tenable at the reaction temperature. When there is sufficient concentration of H deposited on the substrate, the release of ($*H \rightarrow 1/2H_2(g)$) brings the system back to equilibrium. The calculated Gibbs free energy change for hydrogen release ($*H \rightarrow 1/2H_2(g)$) on oxidized-hydroxylated substrates is small and not rate limiting (Figure S10). Separately, the *COOH formed on Au encounters little resistance to leave as CO_2 gas, simultaneously depositing its H on the substrate. The reaction is exothermic, and the reaction barrier is small and not rate limiting (Figures S11 and S12). As before, this second *H migrates along the surface, finding another *H to release a H_2 gas.

If CO is adsorbed at a higher site on the Au cluster, more than one water molecule can participate in the WAP process. In Figure 2B, we show the case involving two water molecules. The adsorbed CO binds with an OH from a higher water molecule, while a lower water molecule receives an H from the higher water molecule and deposits an H on the oxidized-hydroxylated substrate. Through this chain process, the reaction barrier is further reduced (Figure S12, red curves versus blue curves). For Au/α-$MoC_x(111)O_y(OH)_z$, the calculated two-water reaction barrier (rate limiting) is 0.27 eV, compared with LH-associative barrier of 1.25 eV and LH-redox barrier of 1.29 eV, respectively (Table S1; Figure S13). The calculated WAP barrier of 0.27 eV is in excellent agreement with the measured apparent activation energy of ~0.23 eV.[26] The reduction in reaction barrier between WAP with single and multiple water participation also explains the experimental observation of increased efficiency between using single Au atoms and Au clusters for the catalyst.[26] For single Au atoms, the proximity of the adsorbed CO to the oxidized-hydroxylated substrate favors the process involving a single water molecule. For Au clusters, many adsorbed CO are farther away from the capped substrate, because the Au cluster is two to four atomic layers high.[26] For the higher CO, the process involves pathways that follow Figure 2B, with the participation of two or more water molecules. We have calculated reaction pathways involving three and four water molecules on oxidized-hydroxylated Au/α-$MoC_x(111)O_y(OH)_z$. The reaction barrier continued to decrease, approaching values of 0.05 and 0.07 eV, respectively (Figure S14). Although long water chains have lower barriers, the probability to form long chains also decreases, and hence their contribution to the WGS reaction decreases.

Please cite this article in press as: Tian et al., Avoiding Sabatier's conflict in bifunctional heterogeneous catalysts for the WGS reaction, Chem (2021), https://doi.org/10.1016/j.chempr.2021.01.018

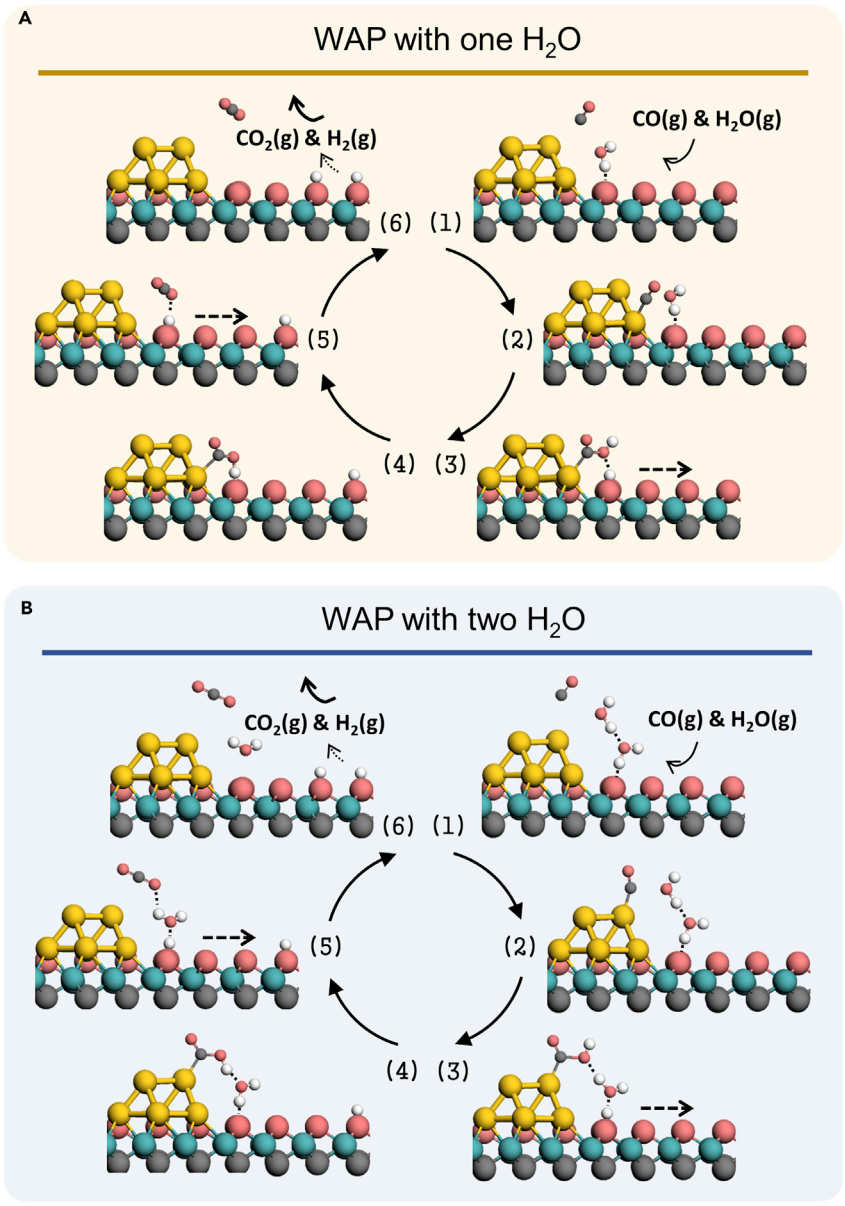

Figure 2. Schematic illustration of the WGS reaction under WAP

(A and B) The WAP process involving (A) one H_2O and (B) two H_2O are shown. For the bifunctional catalyst, cyan, gray, pink, and yellow balls, respectively, represent bare substrate's M, X, surface O, and Au atoms. Small gray, pink, and white balls, respectively, represent C, O, and H atoms of CO and water. The process follows (clockwise [1] … [6]) and the broken arrow indicates *H migration on the oxidized-hydroxylated substrate. Solid double lines indicate covalent bonds; single dotted lines indicate H-bonds.

In Figure 3, we show experimental results of the WGS reaction run at 423 K to measure the percent of CO conversion (2% CO/6% H_2O in Ar; total space velocity: 12,000 mL/[g_{cat}·h]) for different samples. These are: the WAP catalyst comprising mostly Au/$TiC_x(111)O_yOH_z$ with 2 wt % Au loading; LH-catalysts Au/TiO_2 and Au/Mo_2C also with 2 wt % Au loading; and mostly $TiC_x(111)O_yOH_z$ without Au loading. We can make TiC nano-crystals bounded by majority (111) facets by controlling the Ti:C ratio: heat a mixture of 50Al-43.5Ti-6.5C (wt %) at 1,400°C for 15 s and quench in

Please cite this article in press as: Tian et al., Avoiding Sabatier's conflict in bifunctional heterogeneous catalysts for the WGS reaction, Chem (2021), https://doi.org/10.1016/j.chempr.2021.01.018

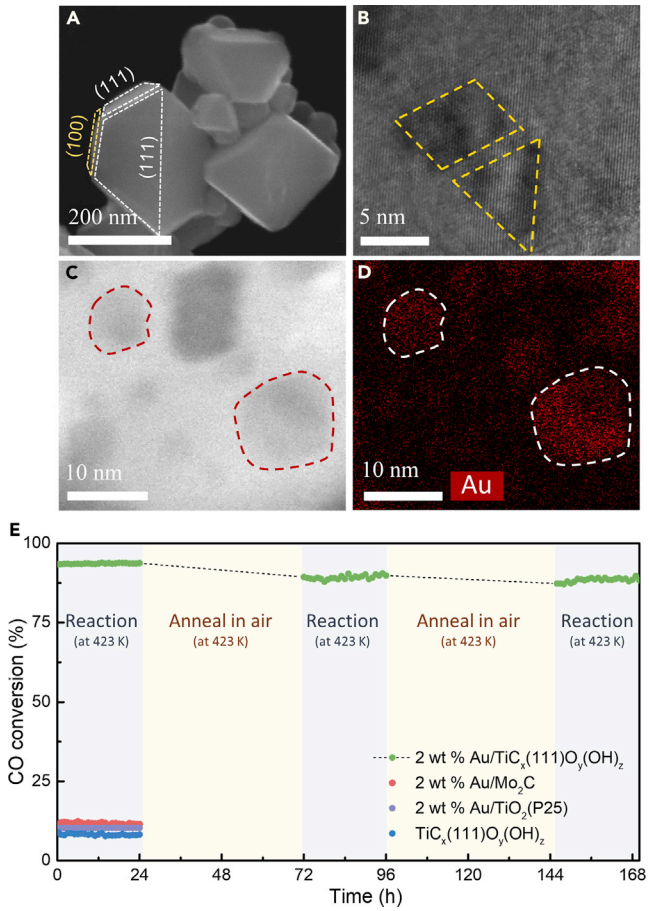

Figure 3. Electron microscopy characterization of the mostly Au/$TiC_x(111)O_yOH_z$ sample and its performance in the WGS reaction compared with other catalysts

(A) SEM image of the sample showing mostly (111) facets and some (100) facets.

(B) HRTEM image showing crystallinity of the sample with well-ordered lattice. The gold trapezoid highlights epitaxial gold clusters.

(C and D) (C) Low-magnification STEM image and (D) EDX mapping of Au with dashed lines highlighting gold clusters grown on TiC_x substrates.

(E) CO conversion percentage by different catalysts at 423 K (2% CO/6% H_2O in Ar; total space velocity: 12,000 mL/[g_{cat}·h]) in cycles totaling 168 h.

oil (Methods: experiment). Scanning electron microscopy (SEM) image (Figure 3A) shows that mostly (111) bounded crystals have near-octahedral shapes.[29] Upon Au loading, the high-resolution transmission electron microscopy (HRTEM) image (Figure 3B) shows that Au clusters grow epitaxially on the TiC_x (111) surface. The size and distribution of gold clusters are captured in low-magnification scanning transmission electron microscopy (STEM) image (Figure 3C) and energy-dispersive X-ray spectroscopy (EDX) mapping (Figure 3D). The results show clear efficiency superiority of the mostly Au/$TiC_x(111)O_y(OH)_z$ sample (Figure 3E). In a continuous 24 h experiment, this sample reaches a steady CO conversion of 93%. By comparison, the benchmark samples Au/TiO_2, Au/Mo_2C, and $TiC_x(111)O_yOH_z$ without Au show CO conversions below 15%. The mass-specific activity of the mostly Au/$TiC_x(111)O_yOH_z$ sample at 423 K is calculated to be 4.3×10^{-5} $mol_{CO}/(g_{cat}\cdot s)$, which is among the highest reported activities to date.[26,30] More important is the fact that the Au/$TiC_x(111)O_yOH_z$ sample excels in its durability. After the first 24 h reaction, we annealed the sample at 423 K in air for 48 h and, without any reactivation process,

Please cite this article in press as: Tian et al., Avoiding Sabatier's conflict in bifunctional heterogeneous catalysts for the WGS reaction, Chem (2021), https://doi.org/10.1016/j.chempr.2021.01.018

ran the WGS reaction for a second time for 24 h. The CO conversion in the second 24 h remained above ~89%. The sample was annealed in air at 423 K for a second time, and without reactivation, the WGS reaction was run for a third time for 24 h. The CO conversion remained above ~87% (Figure 3E). We also did an experiment subjecting the catalyst under the WGS condition continuously for 600 h and, without reactivation, found that the CO conversion efficiency remained above 80% of its initial value. By comparison, the efficiency of Au/α-$MoC_x(111)O_y(OH)_z$,[24] the most efficient catalyst in the WAP family, decreased by nearly 50% in just 150 h at 473 K (compared with 423 K of this experiment). As metal carbides are prone to oxidation at their surfaces, stable metal carbide catalysts for WGS rely on preparing samples with a very low percentage of non-(111) facets. Furthermore, as shown by Roiaz et al.,[31] the stability of the catalyst and substrate before and after the reaction is an important issue. We have taken HRTEM data of Au clusters and the TiC(111) substrate before and after the reaction (Figure S15) and found no evidence that either have gone through structural or composition change. The work of Williams et al.[32] and Shekhar et al.[12] have shown that catalytic activity increases sensitively as the average size of Au clusters decreases. Thus, we need to assess the size of Au clusters on the three catalysts to ensure that size effect of Au is not responsible for the measured higher activity of the Au/TiCx(111)Oy(OH)z catalyst. In Figure S16, we show HRTEM results of Au clusters on the three catalysts. The results indicate that Au clusters on TiO_2 < Mo_2C < TiCx(111)Oy(OH)z. The cluster size of Au on TiCx(111)Oy(OH)z is the largest among the three substrates, because the growth is epitaxial due to the near commensurate lattice constants between TiC(111) and Au(111). Since smaller cluster size increases activity, the HRTEM results are definitive proof that the measured high activity of the Au/TiCx(111)Oy(OH)z catalyst is not caused by varying sizes of the Au clusters on the three substrates.

Earlier, Rodriguez et al.[14] studied the WGS reaction using catalyst Au/TiC(001). They found enhanced activity with Au coverages below 0.15 ML, where monolayer Au islands with average diameter ~0.6 nm are formed. They attributed the enhancement to monolayer Au islands receiving extra electronic charge from the TiC(100) substrate, becoming ultra-reactive with water to form a large amount of *OH and *H on its surface. This explanation follows the LH-associative model, where a highly reactive catalyst that readily dissociates water is key to its high efficiency. On the other hand, the Au/$TiC_x(111)O_y(OH)_z$ catalyst follows a different route, i.e., the WAP process. The oxidized-hydroxylated (111) surface of $TiC_x(111)$ is weakly reactive; it does not dissociate water, and CO gets the OH directly from water.

A central feature of the WAP process is the weak interaction between water and the oxidized-hydroxylated substrate. We seek an independent measurement to determine the interaction strength between water and the substrate. This can be done by measuring the apparent reaction order obtained from the relation between the reaction rate and partial pressure of the reactant. Prior studies show that the apparent reaction order n (i)has a range from −1 to 1.[12,33] If n (i) is negative and close to −1, the reactant i is strongly held by the substrate. For example, Shekhar et al.[12] measured the apparent reaction order of water and determined it to be −0.36 for the catalyst Au/TiO_2 with 3.8 nm average Au particle size in the WGS reaction. They conclude that the negative apparent reaction order points to strong interaction between water and the substrate, resulting in high coverage of dissociated water species on the surface of the catalyst. On the other hand,[12,33] a positive apparent reaction order indicates weak interaction between reactant *i* and the surface of the catalyst. We have measured the apparent reaction order of reactants and products of the WGS reaction for the catalyst Au/$TiC_x(111)O_yOH_z$ (Figure 4). The apparent

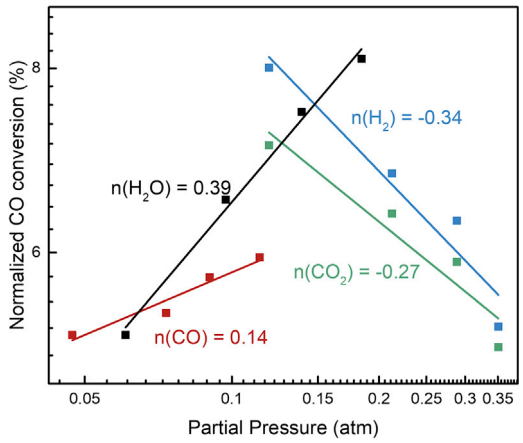

Figure 4. Apparent reaction order n (i) of reactants and products for Au/TiC$_x$(111)O$_y$OH$_z$

reaction order of water is 0.39, pointing to weak interaction between water and the oxidized-hydroxylated substrate. Interestingly, Yao et al.[26] also measured the apparent reaction order of water for catalyst Au/α-MoC$_x$(111)O$_y$(OH)$_z$ and found it to be 0.54, again indicating weak interaction. These are strong experimental evidence that for WAP catalysts, water interacts only weakly with the oxidized-hydroxylated substrate.

Another feature specific to WAP is that *CO does not obtain OH from the substrate. Thus, we expect the reaction barrier of *CO + H_2O → *COOH + *H to depend only mildly on the choice of the substrate. We investigated this idea by calculating the reaction barrier of *CO on five metals: Au, Ag, Cu, Pd, and Pt for two substrates: TiC$_x$(111)O$_y$(OH)$_z$ and α-MoC$_x$(111)O$_y$(OH)$_z$. The reaction barriers are listed in Table S2. The fractional change in reaction barrier on the two substrates is shown for each metal in Figure 5. It shows that the effect of the substrate is less than 30%. This is a major departure from the LH-associative pathway, where the substrate plays a highly sensitive role in the reaction barrier. From Table S2, the metal with the least reaction barrier is Au for both substrates. This is the metal used in our experiments and that of others.[26,29]

In summary, we have identified and explained the workings of a new class of bifunctional catalysts for the WGS reaction. The substrates of these catalysts react mildly with water, thus avoiding the limiting desorption barrier from highly reactive substrates. The high efficiency of WAP catalysts is due to role separation and conflict avoidance. The role of *CO is to form *COOH from water, while the role of the mildly reactive substrate is to channel *H on its surface, allowing them to desorb as H_2. We believe that this strategy can be applied to other catalytic systems with multiple materials or even to a single material but with different types of active sites.

EXPERIMENTAL PROCEDURES

Resource availability

Lead contact

Further information and requests for resources and reagents should be directed to the Lead Contact, S.Y.T. (tongsy@cuhk.edu.cn).

Materials availability

The materials generated in this study will be made available on request.

Please cite this article in press as: Tian et al., Avoiding Sabatier's conflict in bifunctional heterogeneous catalysts for the WGS reaction, Chem (2021), https://doi.org/10.1016/j.chempr.2021.01.018

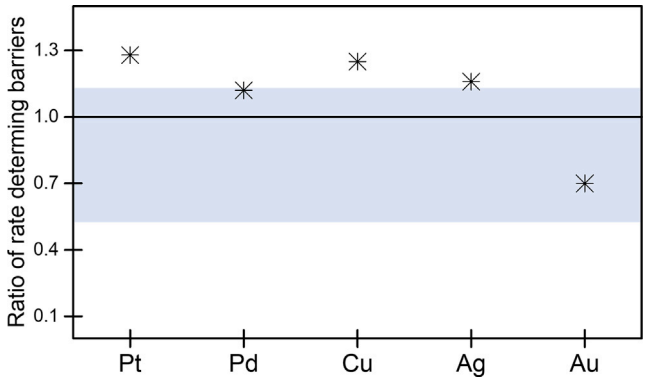

Figure 5. Fractional change in the reaction barrier (A/B) of *CO + H_2O → *COOH + *H for different metals on substrate A: $TiC_x(111)O_y(OH)_z$ and B: α-$MoC_x(111)O_y(OH)_z$
The reaction barriers are calculated for the two-water WAP process.

Data and code availability

All of the data are available from the corresponding author upon reasonable request.

Catalyst preparation

Au/TiO_2(P25)

The TiO_2(P25) was purchased from Evonik Industries with the purity of 99.5%. Au-loaded catalysts were prepared by the deposition precipitation method.[12] The Au precursor (99.99% $HAuCl_4 \cdot 4H_2O$ from Alfa Aesar) was added to deionized water to give a 0.0015 M gold solution. A solution of 0.1 M NaOH was added dropwise to the Au solution, so that the solution maintains a pH = 6 at 35°C for approximately 6 h. The support material was then added to the solution, and the mixture was heated to 85°C in 30 min. The mixture was maintained at 85°C for 1 h. It was then cooled, centrifuged, washed, and dried.

Au/Mo2C

The 2% wt Au loading Mo_2C was synthesized using a temperature-programmed reduction procedure.[34] An aqueous solution containing ($(NH_4)_6Mo_7O_{24} \cdot 4H_2O$, Energy Chemical) was mixed with the $HAuCl_4$ solution to achieve the desired loading at room temperature (RT). The mixed solution was stirred for 4 h and dried using a water bath at 353 K, followed by drying at 383 K in an oven overnight. The resulting material was calcined in air at 773 K for 4 h to obtain the precursor (Au/MoO_3). The Au/MoO_3 precursor was then carburized in a 20% CH_4/H_2 flow from RT to 973 K at 0.5 K/min and held at 973 K for 2 h at 2,000 Pa. The resulting material was cooled down to RT in a 20% CH_4/H_2 flow and then passivated in 1% O_2/Ar mixture for 8 h.

Carbon-deficient $Au/TiC_x(111)$

Micro/nano-crystalline carbon-deficient $TiC_x(111)$ was synthesized from precursors comprising commercial powders of Al (99.9%, ~48 μm), Ti (99.9%, ~29 μm), and carbon nanotubes. The powders of Al-Ti-C were mixed by ball milling and heated in a furnace under an Ar atmosphere. To obtain micro/nano-crystals of TiC_x bounded mostly by (111) faces, a mixture of 50Al-43.5Ti-6.5C (wt %) was heated at 1,400°C for 15 s and quenched in oil. The Au loading procedure was the same as described above. The Au-loaded $TiC_x(111)$ was treated in 15% CH_4/H_2 at 2000 Pa at 1,223 K for 2 h (heating rate from RT of 0.5 K/min). No additional pretreatment/reactivation was taken in subsequent experiments.

Please cite this article in press as: Tian et al., Avoiding Sabatier's conflict in bifunctional heterogeneous catalysts for the WGS reaction, Chem (2021), https://doi.org/10.1016/j.chempr.2021.01.018

Characterization of catalysts

Morphologies were investigated using a SEM equipped with an EDX analyzer (FEI, NovaNanoSEM operated at 30 kV), and HRTEM images were obtained on a FEI, Tecnai F30 microscope operated at an acceleration voltage of 300 kV. Crystal structures of the samples were analyzed by X-ray diffraction (Rigaku, Smartlab; operated at 45 kV and 200 mA, Cu Kα source). X-ray photoelectron spectra were taken in DeviSim NAP from Specs (base pressure 8E-10 mbar for sample chamber, 1E-9 mbar for analyzer), which consisted of an *in situ* NAP-cell (Max. operating pressure is 25 mbar). The XPS system was equipped with a multi-channel hemispherical electrostatic analyzer (PHOIBOS 150, SPECS) and an Al anode X-ray source (XR 50 MF, SPECS) using the Al Kα X-ray (1,486.6 eV). The high-resolution spectra were measured at 50 eV pass. The *ex situ* XPS measurement was performed in ESCALAB 250Xi from Thermo Fisher with the Al X-ray of 1,486.6 eV. The C(1s) binding energy (284.6 eV) of adventitious carbon was used as reference.

Catalytic performance evaluation

Catalytic performance of samples was evaluated in a continuous flow quartz reactor of Hiden QGA at atmospheric pressure and 150°C. The quartz tube was 4 mm in diameter in which the catalysts were sandwiched between quartz wool in the tube reactor. The catalysts (25 mg) were exposed to reformate gases (CO: 2%, H_2O: 6%, Ar: 92%). H_2O vapor was generated from a vaporizer maintained at 37°C carried by Ar without pretreatment. The gas composition was analyzed by a mass spectrometer (HAL 201-RC). The coefficients of CO and CO_2 were determined using standard CO gas. In the quantification, the conversion of CO was defined as: CO conversion = (CO (in)-CO (out))/CO (in) (V/V).

Evaluation of the catalysts' stability was carried out by a continuous product-free gas feed (CO: 2%, H_2O: 6%, Ar: 92%) for 24 h intervals described in the main text. The mass-specific reaction rate was obtained under low CO conversion rate (< 20%) by increasing CO concentration and reducing catalyst usage.

DFT calculations

Calculation details

First-principles calculations were performed by the Vienna *ab initio* simulation package (VASP)[35] based on density functional theory. The electronic exchange correlation was described using the Perdew-Burke-Ernzerhof (PBE) form[36] of the generalized gradient approximation (GGA). The projector augmented wave method[37,38] was used to treat electron–ion interactions with a plane-wave-basis cutoff of 500 eV. The vacuum region was set at ~12 Å to avoid interlayer interaction, and all structures were optimized by the conjugate gradient method until Hellmann−Feynman force convergence values were less than 0.02 eV/Å. The Gamma-centered sampling with 3 × 3 × 1 (for 4 × 4 supercell) and 7 × 7 × 1 (for 2 × 2 supercell) k meshes were used. The climbing image nudged elastic band (CI-NEB) method was used to investigate the minimum reaction pathways.[39] Vibrational frequencies were calculated at all stationary points, where only the adsorbates were relaxed. Corrections due to vdW forces (i.e., DFT-D3, Grimme, or Becke-Jonson) were checked and found that their contributions were largely cancelled in reaction barrier results.

Construction of the surface model

Cubic α-MoC with bulk lattice constant a = b = 4.37 Å (experimental = 4.27 Å[26]) was used to construct a (111) slab. The unreconstructed 1 × 1 α-MoC(111) structure was measured by the experiment.[26] The slab was bounded by two equivalent Mo-terminated (111) surfaces. In this geometry, the electrostatic dipole of the atomic layers is

cancelled. Similar slabs have been used to evaluate surface energies of other polar planes.[40,41] Au_{10} was used to represent the gold cluster in the bifunctional catalyst. In an Au_{10} cluster, all surface Au atoms were corner atoms. The corner Au atoms were found to be the most active site for the WGS reaction.[12] We used an Au_{10} cluster to evaluate reaction barriers to save computation time. However, we calculated CO adsorption energy and the reaction barrier of CO -> COOH using an Au_{15} cluster. The results are shown in Figures S17 and S18 and Table S3. They show that while CO adsorbs much stronger at corner sites,[12] the reaction barrier is about the same between corner-adsorbed CO and perimeter-adsorbed CO. The difference is only about ~0.05 eV.

Thermochemistry of surface termination and Gibbs free energy

Terminations of α-MoC(111) and Ti_3SiC_2(0001) were predicted under the relevant temperature and gas pressure. Cap species *OH and *H are assumed to be generated when the catalysts come in contact with the feeding steam and reaching thermodynamic equilibrium through the following steps:

$$H_2O + 2^* \rightarrow {}^*H + {}^*OH \quad \text{(Equation 1)}$$

$$2{}^*OH \rightarrow 2{}^*O + H_2. \quad \text{(Equation 2)}$$

The thermodynamic relation is as follows:

$$G^0 = H^0 - TS \quad \text{(Equation 3)}$$

For a given temperature larger than 0 K, the enthalpy term is expressed as follows:

$$H = H^0 + \int C_P dT \quad \text{(Equation 4)}$$

For solids and adsorbates, the $\int C_P dT$ integral has negligible contribution, and no thermal correction is considered for the enthalpy calculations. For gas molecules, their temperature-dependent heat capacities together with entropy S are directly obtained from standard thermodynamic database.[42] The entropy S for adsorbates was calculated using the harmonic approximation model, where only the vibrational contribution (S_v) is taken into account. The harmonic model was also used to estimate the zero-point energy (ZPE) for both gas molecules and adsorbates. The Gibbs free energy change between initial and final states of a reaction was computed from:

$$\Delta G = \Delta H^0 + \Delta ZPE + \Delta \int C_P dT - \Delta TS + 1/2\ kT \ln(p/p^0). \quad \text{(Equation 5)}$$

The logarithmic term gives the pressure dependence of the chemical potential of gas molecules.[43] Here, the pressure ratio p/p^0 of H_2O is taken as 0.21, in accordance with the experiment.[26] When a reaction exclusively involves adsorbed species for both initial and final states, the entropy change is minimal and can be neglected.

SUPPLEMENTAL INFORMATION

Supplemental information can be found online at https://doi.org/10.1016/j.chempr.2021.01.018.

ACKNOWLEDGMENTS

We thank the Center for Computational Science and Engineering of Southern University of Science and Technology for high performance computing resources and

the Core Research Facilities of Southern University of Science and Technology for the assistance in materials characterization. This work was supported by the National Natural Science Foundation of China (NSFC, grant nos. 11334003 and 11674148), Program for Guangdong Introducing Innovative and Entrepreneurial Teams (grant no. 2019ZT08L101), and the Guangdong Natural Science Funds for Distinguished Young Scholars (no. 2017B030306008).

AUTHOR CONTRIBUTIONS

Conceptualization, H.T., H.X., and S.Y.T.; formal analysis, H.T., Y.H., H.X., and S.Y.T.; investigation, Y.H., H.T., J.L., X.S., Z.Z., X.H., and C.L.; resources, Q.Z. and Q.J.; writing – original draft, H.T. and S.Y.T.; writing – review & editing, H.X. and S.Y.T.; visualization, Q.Z., K.W., Q.J., and A.M.C.N.; funding acquisition, H.X. and S.Y.T.; supervision, H.X. and S.Y.T.

DECLARATION OF INTERESTS

The authors declare no competing interests.

Received: June 30, 2020
Revised: September 13, 2020
Accepted: January 25, 2021
Published: February 25, 2021

REFERENCES

1. Sabatier, P. (1911). Hydrogénations et déshydrogénations par catalyse. Ber. Dtsch. Chem. Ges. *44*, 1984–2001.
2. Balandin, A. (1969). Modern state of the multiplet theor of heterogeneous catalysis. Adv. Catal. *19*, 1–210.
3. Medford, A.J., Vojvodic, A., Hummelshøj, J.S., Voss, J., Abild-Pedersen, F., Studt, F., Bligaard, T., Nilsson, A., and Nørskov, J.K. (2015). From the Sabatier principle to a predictive theory of transition-metal heterogeneous catalysis. J. Cat. *328*, 36–42.
4. Pérez-Ramírez, J., and López, N. (2019). Strategies to break linear scaling relationships. Nat. Cat. *2*, 971–976.
5. Gokhale, A.A., Dumesic, J.A., and Mavrikakis, M. (2008). On the mechanism of low-temperature water gas shift reaction on copper. J. Am. Chem. Soc. *130*, 1402–1414.
6. Ratnasamy, C., and Wagner, J.P. (2009). Water gas shift catalysis. Catal. Rev. *51*, 325–440.
7. Fu, Q., Saltsburg, H., and Flytzani-Stephanopoulos, M. (2003). Active nonmetallic Au and Pt species on ceria-based water-gas shift catalysts. Science *301*, 935–938.
8. Panagiotopoulou, P., and Kondarides, D.I. (2006). Effect of the nature of the support on the catalytic performance of noble metal catalysts for the water-gas shift reaction. Catal. Today *112*, 49–52.
9. Rodriguez, J.A., Ma, S., Liu, P., Hrbek, J., Evans, J., and Pérez, M. (2007). Activity of CeOx and TiOx nanoparticles grown on Au(111) in the water-gas shift reaction. Science *318*, 1757–1760.
10. Zhai, Y.P., Pierre, D., Si, R., Deng, W.L., Ferrin, P., Nilekar, A.U., Peng, G.W., Herron, J.A., Bell, D.C., Saltsburg, H., et al. (2010). Alkali-stabilized Pt-OHx species catalyze low-temperature water-gas shift reactions. Science *329*, 1633–1636.
11. Schweitzer, N.M., Schaidle, J.A., Ezekoye, O.K., Pan, X.Q., Linic, S., and Thompson, L.T. (2011). High activity carbide supported catalysts for water gas shift. J. Am. Chem. Soc. *133*, 2378–2381.
12. Shekhar, M., Wang, J., Lee, W.S., Williams, W.D., Kim, S.M., Stach, E.A., Miller, J.T., Delgass, W.N., and Ribeiro, F.H. (2012). Size and support effects for the water-gas shift catalysis over gold nanoparticles supported on model Al2O3 and TiO2. J. Am. Chem. Soc. *134*, 4700–4708.
13. Yang, M., Li, S., Wang, Y., Herron, J.A., Xu, Y., Allard, L.F., Lee, S., Huang, J., Mavrikakis, M., and Flytzani-Stephanopoulos, M. (2014). Catalytically active Au-O(OH)x species stabilized by alkali ions on zeolites and mesoporous oxides. Science *346*, 1498–1501.
14. Rodriguez, J.A., Ramírez, P.J., Asara, G.G., Viñes, F., Evans, J., Liu, P., Ricart, J.M., and Illas, F. (2014). Charge polarization at a Au-TiC interface and the generation of highly active and selective catalysts for the low-temperature water-gas shift reaction. Angew. Chem. Int. Ed. Engl. *53*, 11270–11274.
15. Yang, M., Liu, J.L., Lee, S., Zugic, B., Huang, J., Allard, L.F., and Flytzani-Stephanopoulos, M. (2015). A common single-site Pt(II)-O(OH)x-species stabilized by sodium on "active" and "inert" supports catalyzes the water-gas shift reaction. J. Am. Chem. Soc. *137*, 3470–3473.
16. Sabnis, K.D., Cui, Y.R., Akatay, M.C., Shekhar, M., Lee, W.S., Miller, J.T., Delgass, W.N., and Ribeiro, F.H. (2015). Water-gas shift catalysis over transition metals supported on molybdenum carbide. J. Cat. *331*, 162–171.
17. Xu, M., Yao, S.Y., Rao, D.M., Niu, Y.M., Liu, N., Peng, M., Zhai, P., Man, Y., Zheng, L.R., Wang, B., et al. (2018). Insights into interfacial synergistic catalysis over Ni@TiO2-x catalyst toward water-gas shift reaction. J. Am. Chem. Soc. *140*, 11241–11251.
18. Weinberg, W.H. (1996). Eley-Rideal surface chemistry: direct reactivity of gas phase atomic hydrogen with adsorbed species. Acc. Chem. Res. *29*, 479–487.
19. Langmuir, I. (1922). Part II. —"Heterogeneous reactions". chemical reactions on surfaces. Trans. Faraday Soc. *17*, 607–620.
20. Senanayake, S.D., Stacchiola, D., and Rodriguez, J.A. (2013). Unique properties of ceria nanoparticles supported on metals: novel inverse ceria/copper catalysts for CO oxidation and the water-gas shift reaction. Acc. Chem. Res. *46*, 1702–1711.
21. Li, G., Wang, B., and Resasco, D.E. (2020). Water-mediated heterogeneously catalyzed reactions. ACS Catal. *10*, 1294–1309.
22. Saavedra, J., Doan, H.A., Pursell, C.J., Grabow, L.C., and Chandler, B.D. (2014). The critical role of water at the gold-titania interface in catalytic CO oxidation. Science *345*, 1599–1602.
23. Liu, Z., Huang, E., Orozco, I., Liao, W., Palomino, R.M., Rui, N., Duchoň, T., Nemšák, S., Grinter, D.C., Mahapatra, M., et al. (2020). Water-promoted interfacial pathways in

methane oxidation to methanol on a CeO2-Cu2O catalyst. Science *368*, 513–517.

24. Zhang, H.Z., and Wang, S.Q. (2007). First-principles study of Ti3AC2 (A = Si, Al) (001) surfaces. Acta Mater. *55*, 4645–4655.

25. Medvedeva, N.I., and Freeman, A.J. (2008). Cleavage fracture in Ti3SiC2 from first-principles. Scr. Mater. *58*, 671–674.

26. Yao, S., Zhang, X., Zhou, W., Gao, R., Xu, W.Q., Ye, Y., Lin, L., Wen, X., Liu, P., Chen, B., et al. (2017). Atomic-layered Au clusters on alpha-MoC as catalysts for the low-temperature water-gas shift reaction. Science *357*, 389–393.

27. Lin, L., Zhou, W., Gao, R., Yao, S., Zhang, X., Xu, W., Zheng, S., Jiang, Z., Yu, Q., Li, Y.-W., et al. (2017). Low-temperature hydrogen production from water and methanol using Pt/alpha-MoC catalysts. Nature *544*, 80–83.

28. Nguyen, L., Tao, F.F., Tang, Y., Dou, J., and Bao, X.J. (2019). Understanding catalyst surfaces during catalysis through near ambient pressure X-ray photoelectron spectroscopy. Chem. Rev. *119*, 6822–6905.

29. Jin, S., Shen, P., Lin, Q., Zhan, L., and Jiang, Q. (2010). Growth mechanism of TiC x during self-propagating high-temperature synthesis in an Al– Ti– C system. Cryst. Growth Des. *10*, 1590–1597.

30. Dong, J., Fu, Q., Jiang, Z., Mei, B., and Bao, X. (2018). Carbide-supported Au catalysts for water-gas shift reactions: a new territory for the strong metal–support interaction effect. J. Am. Chem. Soc. *140*, 13808–13816.

31. Roiaz, M., Monachino, E., Dri, C., Greiner, M., Knop-Gericke, A., Schlögl, R., Comelli, G., and Vesselli, E. (2016). Reverse water-gas shift or Sabatier methanation on Ni(110)? Stable surface species at near-ambient pressure. J. Am. Chem. Soc. *138*, 4146–4154.

32. Williams, W.D., Shekhar, M., Lee, W.S., Kispersky, V., Delgass, W.N., Ribeiro, F.H., Kim, S.M., Stach, E.A., Miller, J.T., and Allard, L.F. (2010). Metallic corner atoms in gold clusters supported on rutile are the dominant active site during water– gas shift catalysis. J. Am. Chem. Soc. *132*, 14018–14020.

33. Bond, G.C. (2008). The use of kinetics in evaluating mechanisms in heterogeneous catalysis. Cat. Rev. *50*, 532–567.

34. Lee, J.S., Volpe, L., Ribeiro, F.H., and Boudart, M. (1988). Molybdenum carbide catalysts II. Topotactic synthesis of unsupported powders. J. Cat. *112*, 44–53.

35. Kresse, G., and Furthmüller, J. (1996). Efficient iterative schemes for ab initio total-energy calculations using a plane-wave basis set. Phys. Rev. B Condens. Matter *54*, 11169–11186.

36. Perdew, J.P., Burke, K., and Ernzerhof, M. (1996). Generalized gradient approximation made simple. Phys. Rev. Lett. *77*, 3865–3868.

37. Blöchl, P.E. (1994). Projector augmented-wave method. Phys. Rev. B Condens. Matter *50*, 17953–17979.

38. Kresse, G., and Joubert, D. (1999). From ultrasoft pseudopotentials to the projector augmented-wave method. Phys. Rev. B *59*, 1758–1775.

39. Henkelman, G., Uberuaga, B.P., and Jónsson, H. (2000). A climbing image nudged elastic band method for finding saddle points and minimum energy paths. J. Chem. Phys. *113*, 9901–9904.

40. Zhang, S.B., and Wei, S.H. (2004). Surface energy and the common dangling bond rule for semiconductors. Phys. Rev. Lett. *92*, 086102.

41. Dreyer, C.E., Janotti, A., and Van de Walle, C.G. (2014). Absolute surface energies of polar and nonpolar planes of GaN. Phys. Rev. B *89*, 081305(R).

42. Haynes, W.M. (2014). CRC Handbook of Chemistry and Physics (CRC Press).

43. Reuter, K., and Scheffler, M. (2002). Composition, structure, and stability of RuO2(110) as a function of oxygen pressure. Phys. Rev. B *65*, 035406.

Chemical Physics 532 (2020) 110689

Contents lists available at ScienceDirect

Chemical Physics

journal homepage: www.elsevier.com/locate/chemphys

Comparing study of picene thin films on SnSe and Au(1 1 1) surfaces

Xiji Shao[a,b,1], Xuhang Ma[a,1], Mingjing Liu[a], Tao Zhang[a], Yaping Ma[a], Chaoqiang Xu[d], Xuefeng Wu[a,*], Tao Lin[c,*], Kedong Wang[a,*]

[a] Department of Physics, Southern University of Science and Technology, Shenzhen 518055, China
[b] Harbin Institute of Technology, Harbin 150080, China
[c] College of New Materials and New Energies, Shenzhen Technology University, Shenzhen 518118, China
[d] Department of Physics, Chinese University of Hong Kong, Hong Kong, China

ARTICLE INFO

Keywords:
Picene
SnSe
STM
Structure
Electronic properties

ABSTRACT

Picene, as one representative of polycyclic hydrocarbons, represents an appealing application in hydrocarbon superconductors. Here, using scanning tunneling microscopy and spectroscopy combined with density functional theory calculations, we investigated the structural and electronic properties of picene thin films on p-type SnSe and Au(1 1 1) surfaces. For both substrates, at low coverage, the molecules present a flat-lying geometry, while at high coverage, the molecules exhibit alternating flat-lying and tilt-standing configurations. The diffusion of the molecules on SnSe and the splitting of lowest unoccupied molecular orbital state on Au(1 1 1) indicate that SnSe surface has a weaker interaction with the adsorbed molecules compared to other metallic substrate. Therefore, based on our study on structural and electronic properties, we conclude that a semiconductor substrate can maintain the intrinsic properties of picene films. The study of picene on different substrates may pave a way to unveil the structural and electronic properties of hydrocarbon superconductors on substrates.

1. Introduction

The first discovery of hydrocarbon superconductor in 2010 [1] has attracted significant interest since it may provide another approach towards fabrication of organic superconductors with higher superconducting transition temperature Tc. In such novel superconductors, metal atoms were introduced to be intercalated into solid polycyclic hydrocarbons, such as picene [1], coronene [2], phenanthrene [3], dibenzopentacene [4], etc. The intercalated metal atoms could range from alkali metals to alkali earth metals [1–5], especially potassium. However, due to the low shielding fraction of the hydrocarbon superconductors, the structure and the corresponding electronic states of these doped molecules remain mysterious [2,6]. On the other hand, the ferromagnetic phase rather than superconductivity was detected in the potassium doped aromatic hydrocarbons, which makes the existence of superconductivity questioning [7].

To this end, different alkali-doped polycyclic hydrocarbons thin films have been prepared on substrates and investigated by a series of advanced surface science techniques, including scanning tunneling microscopy and spectroscopy (STM/STS) [8–14], photoemission spectroscopy [8,15–18], low-energy electron diffraction [10,11], and electron energy-loss spectroscopy [19,20]. Meanwhile, with the aid of STM/STS, polycyclic hydrocarbon molecules can be studies at a single molecule level [21,22]. However, the experimental results from different groups unveil incompatible properties of the films, from insulating to metallic. For example, insulating states have been reported in the system of potassium doped picene thin films on a Ag substrate [13,17], while a metallic state was found on a graphite substrate [18]. One possible explanation to this discrepancy is that molecule-substrate interaction varies on different substrates. Therefore, a comprehensive understanding of structural and electronic properties of picene film on different substrates at molecular level is required. On the other hand, owing to the superconducting proximity effect, the superconductivity of a thin film could be suppressed by an underneath normal metal substrate [23]. Thus, an alkali-doped polycyclic hydrocarbons thin film decoupled from reactive metallic substrates by some insulating layers or on a weakly-coupled semiconductor/insulating substrate may hold the same superconducting feature as its bulk counterpart.

Previously, Xu et al. reported that molecule-substrate interaction is suppressed by some buffer layers, such as a flat initial layer of polycyclic hydrocarbons and KCl thin films [24]. However, until now, the study of polycyclic hydrocarbons thin films on semiconductor

* Corresponding authors.
E-mail addresses: wuxf@mail.sustech.edu.cn (X. Wu), lintao@sztu.edu.cn (T. Lin), wangkd@sustech.edu.cn (K. Wang).
[1] X. Shao and X. Ma contributed equally to this work.

https://doi.org/10.1016/j.chemphys.2020.110689
Received 21 September 2019; Received in revised form 1 January 2020; Accepted 22 January 2020
Available online 24 January 2020

substrates has not yet reported. Here, we applied STM/STS to investigate thin films of picene molecules on a semiconductor substrate, SnSe, under ultrahigh vacuum (UHV) conditions. By comparing the structural and electronic properties of picene films on SnSe and on Au (1 1 1), it is found that the interaction between picene thin film and SnSe is weakened. Our results provide another approach to reduce the interaction between polycyclic hydrocarbons thin films and the underneath substrate and it may pave the way toward a better understanding of hydrocarbon superconductor.

2. Experiments and methods

The STM experiments were performed in a commercial Unisoku UHV system with base pressure below 1×10^{-10} mbar. P-SnSe single-crystal was synthesized by the method described in ref. [25]. The SnSe crystal was introduced into the UHV chamber and cleaved by a piece of sticky tape inside the vacuum chamber. Clean Au(1 1 1) surface was prepared via cycles of Ar + sputtering and 500 °C annealing. The picene molecules (99.0%, International Laboratory USA) were sublimated by a homemade Knudsen cell from a Al_2O_3 crucible at around 370 K, which corresponds to an evaporating rate of 0.2 ML/min. During the deposition process, the substrate was held at room temperature. STM and STS measurements were performed at 78 K. The acquirement processes of dI/dV/(I/V) spectra are as follows: 1) average several individual I-V curves (around 10 curves); 2) numerical differential of the averaged I-V curves; 3) normalization by dividing smoothed I-V curves [26].

Density-functional theory (DFT) calculations are performed using the plane-wave basis set with the projector-augmented wave (PAW) [27] method as implemented in the Vienna ab initio simulation package (VASP) [28,29]. All the contact geometries of the picene (72 atoms) on the Au (1 1 1) (320 atoms) and SnSe (356 atoms) are used by the van-der-waals-corrected density functional (vdW-DF) calculations [30,31]. Considering the influence of the vdW interactions, the optB88-vdW-DF [30–32] is used, which yields accurate equilibrium interatomic distance and energies for a wide range of systems [33]. The kinetic energy cutoff is 500 eV. The vacuum space is set to be 15 Å, and Γ-point-only Brillouin zone sampling is used for structure optimization and electronic structure calculations with the Monkhorst − Pack scheme [34]. All atoms are fully relaxed until the residue force on each atom is less than 0.02 eV/Å.

3. Results and discussions

Fig. 1a shows the empty state STM image of a fresh cleaved SnSe along the bc-plane. A series of rows along the b-axis can be observed, which agrees well with the results in the previous study [35]. The rows of bright spot features are attributed to the Sn atoms according to the DFT calculations [35]. To identify the adsorption features of the picene molecules, around 1 monolayer (ML) of picene molecules were deposited onto the SnSe surface held at room temperature. The molecular coverage is defined in terms of the structure shown in Fig. 1c. As shown in Fig. 1b, the molecules form an ordered closed-packed network (phase I) and the corresponding density is around 1.06 molecules/nm^2. Within the network, a single molecule appears as a rod along the c-axis of the substrate. In the close-up STM image (Fig. 1c), a unit cell is labeled with a red parallelogram, and the lattice constants are approximately d1 = 0.72 nm, d2 = 1.38 nm and φ = 71°. Moreover, the zigzag edge at the longer side of the molecule can be clearly identified. By superimposing the chemical structure of picene molecules, a single picene molecule presents a flat-lying geometry and the zigzag edge can be attributed to the three phenyl rings at the longer side of a picene molecule. As demonstrated with the superimposed chemical structures, there exist two energy-favored configurations with mirror symmetry for picene molecules. Note that we couldn't determine which configuration is more energetically favored. Although in Fig. 1b most of molecules in this area adopt one configuration, the molecules shown in Fig. 2 display the opposite condition.

In order to have a better understanding of the adsorption configurations of the picene molecules, the DFT calculations were carried out. Fig. 1d shows the most energetically preferred adsorption configuration, demonstrating a flat-lying geometry parallel to the c-axis of the substrate, which agrees well with our experimental results. According to our calculation results, the adsorbed molecule stays 3.26 Å away from the surface and the corresponding adsorption energy of a single picene molecule is −1.81 eV. Moreover, three different kinds of molecular pairs which can be observed in the picene film were calculated. In Fig. 1e, the two molecules adopt the same configuration, while in Fig. 1f and g, the two molecules exhibit different configurations. The calculated absorption energies for the three molecular pairs are −2.17 eV, −2.17 eV and −2.15 eV, respectively, indicating that alternating to the other configuration don't affect the stability of the picene film. Moreover, a (2 × 4) supercell was examined to further investigate the proposed models. In calculation, the short and long sides of the unit cell correspond to 2 and 4 Se spacing of the substrate. Fig. 1h displays the energetically favored adsorption configuration and the corresponding simulated STM image obtained from DFT calculation. The simulated results reveal the intermolecular spacings varies along the row direction, indicating the molecules of phase 1 are slightly adjusted in order to be commensurate with the substrate.

As shown in Fig. 1b, some fuzzy features around the vacancies were frequently observed within the unsaturated monolayer, indicating that the adsorbed molecules are mobile even at 78 K. To further investigate this phenomenon, a series of consecutive STM images were acquired. The frame acquisition time is 8 min. As indicated by the yellow rectangles in Fig. 2b and c, three stable molecules (marked by black the dots in Fig. 2b) become mobile, resulting in fuzzy feature in Fig. 2c. Moreover, the blue rectangles in Fig. 2b and c display the reversible process: moving molecules fill the vacancies in the molecular network and become stable. The green rectangles highlight the area where the orientation of molecules (marked by the green arrows in Fig. 2a and b) changes. One may also speculate that the orientation change is due to a flipping process. The results unambiguously unveil the weak interaction between picene molecules and the SnSe substrate.

As shown in Fig. 3a, upon increase the molecular coverage to higher than 1 ML, a new phase (phase II) appears, which also exhibits a row feature. However, the rows align along a different direction (rotation angle ~9°) compared with phase I, as denoted by the black and yellow dotted line in Fig. 3a. In the close-up STM image (Fig. 3b), one can see that one unit cell contains two molecules with different postures, which are manifested as a bright and a dim protrusions, respectively. The bright one exhibits a short shape, indicating a tilted geometry with the short edge pointing upward. On the other hand, the dark one presents a long and flat feature which resembles the molecules in phase I, implying a flat-lying configuration. The unit cell of phase II is around 1.09×1.47 nm^2 with an angle of around 74°. The molecule density is about 1.30 molecule/nm^2, which is larger than that in phase I. Such tilted and flat-lying arrangement resembles the molecules in the bulk [1,2,8], which implies the intramolecular interaction plays a major role in phase II.

Indeed, there are contradictory explanations of the adsorption configuration of molecules in phase II. One interpretation involves a phase change from loose phase I to condensed phase II in the same layer driven by the increasing coverage [9,11,12]. In other words, both phases belong to the first layer, where part of molecules in phase I rotate in the out-of-plane direction. Recently, Hoffmann et al. demonstrated that the tilted molecules are adsorbed on the top of phase I in the systems of [7]phenacene and [9]phenacene. Thus, another model that the molecules in phase II adsorb on a wetting layer (phase I) is proposed recently [14]. The main evidence for the former interpretation is the low apparent height difference between phase II and phase I (~0.2 nm) [9], which is not high enough for one layer molecular film

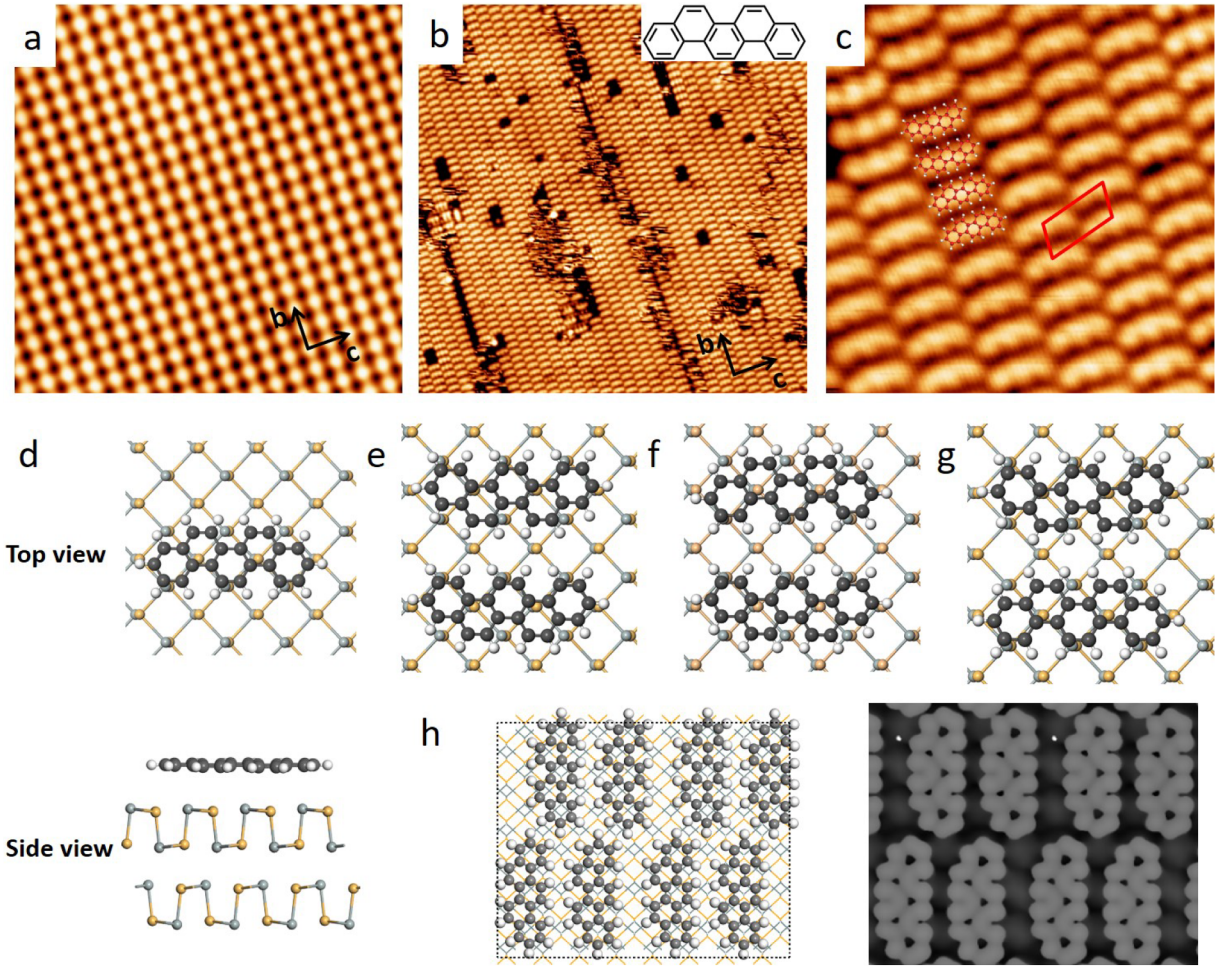

Fig. 1. Picene film grown on SnSe. (a) STM image of a cleaved SnSe surface. (Image size: 8 × 8 nm^2; imaging condition: $V_s = -1.5$V, $I_t = 50$pA). (b) STM image of ~1 ML picene on SnSe surface. (Image size: 40 × 40 nm^2; imaging condition: $V_s = 2$V, $I_t = 20$pA). Inset: Chemical structure of picene. (c) Close-up STM image of picene layer superimposed with chemical structures of picene molecules. The red parallelogram denotes the unit cell. (Image size: 7.5 × 7.5 nm^2; imaging condition: $V_s = 2$V, $I_t = 20$pA). (d) The most energetically favored adsorption geometry of a single picene molecule on SnSe surface obtained from DFT calculation. Color code: C, dark gray; H, white; Sn, light gray; Se, yellow. (e)-(g) Calculated model of three different molecular pairs. The adsorption energies per molecule are −2.17, −2.17, −2.15 eV, respectively. (h) One possible arrangement of molecules and the corresponding simulated STM image.

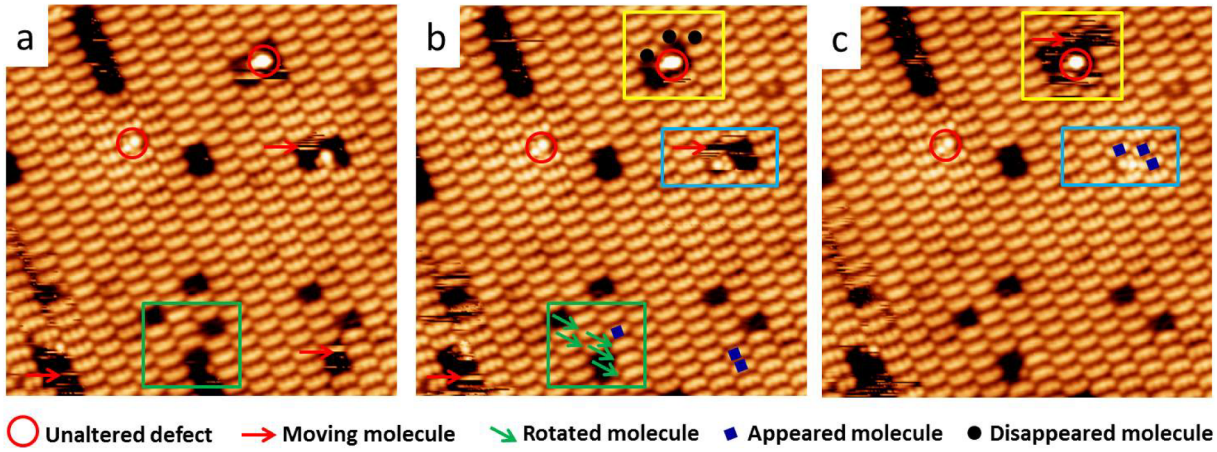

Fig. 2. Diffusion of picene molecules on SnSe. (a)-(c) Three consecutive STM images of the same area at 78 K. (image size: 25 × 25 nm^2; imaging condition: $V_s = 2$V, $I_t = 20$pA; timeinterval = 8min).

(usually several angstroms). On the other hand, some DFT simulation results reveal the former arrangement is more stable [11], providing another evidence for the former explanation. But the apparent height in STM image is strongly influenced by the localized density of states and usually does not reflect the real height in the systems with poor conductivity [14]. In fact, in our previous work of coronene films, where there is no phase change as thickness increases, the height difference between 1ML and 2ML is only 0.1 nm [13]. Thus, the explanation that

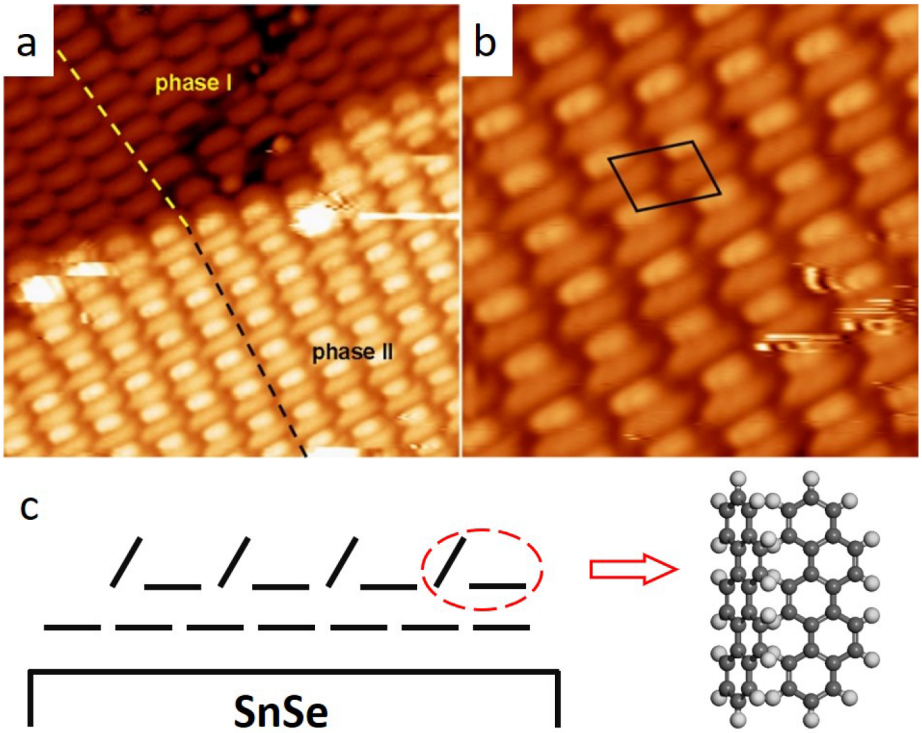

Fig. 3. (a) STM image of phase I and II (image size: 14 × 14 nm^2; imaging condition: V_s = 2.5V, I_t = 100pA). (b) STM image of Phase II. The black parallelogram denotes the unit cell. (Image size: 8 × 8 nm^2; imaging condition: V_s = 2.5V, I_t = 100pA). (c) A tentative structural model of phase II as the second layer on phase I.

the two phases belong to different layers of picene film is more plausible and a corresponding tentative structural model of phase 2 is provided in Fig. 3c. Here, we would like to point out that the elucidation of phase II requires further studies using other experimental methods and state-of-the-art simulations.

To further understand the electronic properties of the molecules on the semiconductor surface, STS were performed on different surfaces. The result of STS is presented as dI/dV/(I/V) spectra by differentiating of the averaged I − V spectra (10 acquired spectra) and then dividing by the corresponding I/V spectra [36]. The black curve shown in Fig. 4 is the spectrum taken on the bare SnSe surface, showing one shoulder and one peak located at −0.2 eV and 1.2 eV, respectively. It clearly proves p-type characteristics of the substrate since the Fermi level is located near the onset of the valence band. It also indicates that the band gap of the substrate is around 1.1 eV, determined by the energy difference between the onsets of the valence band and the conduction band. This is consistent with the previously reported STS on p-type SnSe [25,37].

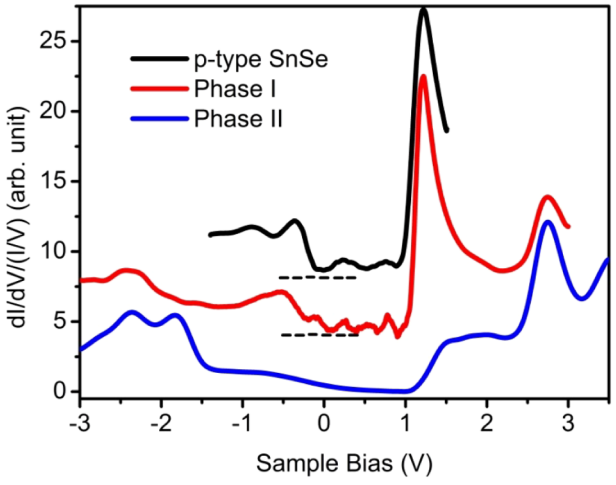

Fig. 4. Scanning tunneling spectra taken on bare SnSe surface (black), flat-lying molecules in phase I (red) and flat-lying/tilted molecules in phase II (blue). The tunneling condition for spectra of phase I and phase II is V_s = 2.5V, I_t = 20pA. The spectra are shifted for clearance. The dash lines indicate the shifted zero lines.

The spectrum (the red curve in Fig. 4) acquired on the flat-lying molecules in phase 1 shows two shoulders at −2.3 eV and −0.2 eV, and two peaks at 1.2 eV and 2.7 eV. Among them, the shoulder at −0.2 eV and the peak at 1.2 eV have a similar feature as the STS of SnSe, which indicates that these two states originate from the substrate. The shoulder at −2.3 eV and 2.7 eV, resulting a band gap around 4.5 eV. The blue curve in Fig. 4 shows the spectrum taken on the molecules in phase II. The corresponding spectrum indicates two shoulders at −1.8 eV and 1.2 eV, and one peak at 2.7 eV. The shoulder at 1.2 eV generated from the substrate is dramatically weakened, indicating the molecules in phase 2 are effectively decoupled from the SnSe substrate by the wetting layer. Meanwhile, the states originated from molecular orbitals are enhanced in phase II. The corresponding band gap of phase II is around 4.0 eV, determined as the energy difference between the onsets of the highest occupied molecular orbital (HOMO) and lowest unoccupied molecular orbital (LUMO) state. The band gap of molecules in both phase I and II are larger than that of the bulk sample 3.11 eV [38], which may attribute to less dispersion in the direction perpendicular to the substrate [9] and the structural difference between the thin film and its bulk counterpart.

To gain a comprehensive understanding of the influence of substrate in the growth process, we studied picene films on Au(1 1 1) surface as a comparison. On Au(1 1 1) surface, the molecules exhibit flat-lying geometry at low coverage (phase I, shown in Fig. 5a and b) and alternating flat-lying and tilt-standing configuration at high coverage (phase II, shown in Fig. 5c). Similar behaviors have been demonstrated other metallic substrates [9,11]. In Fig. 5a, the herringbone structure originating from Au(1 1 1) surface reconstruction is still visible in phase I of picene film, indicating the well-defined molecule-Au(1 1 1) interface.

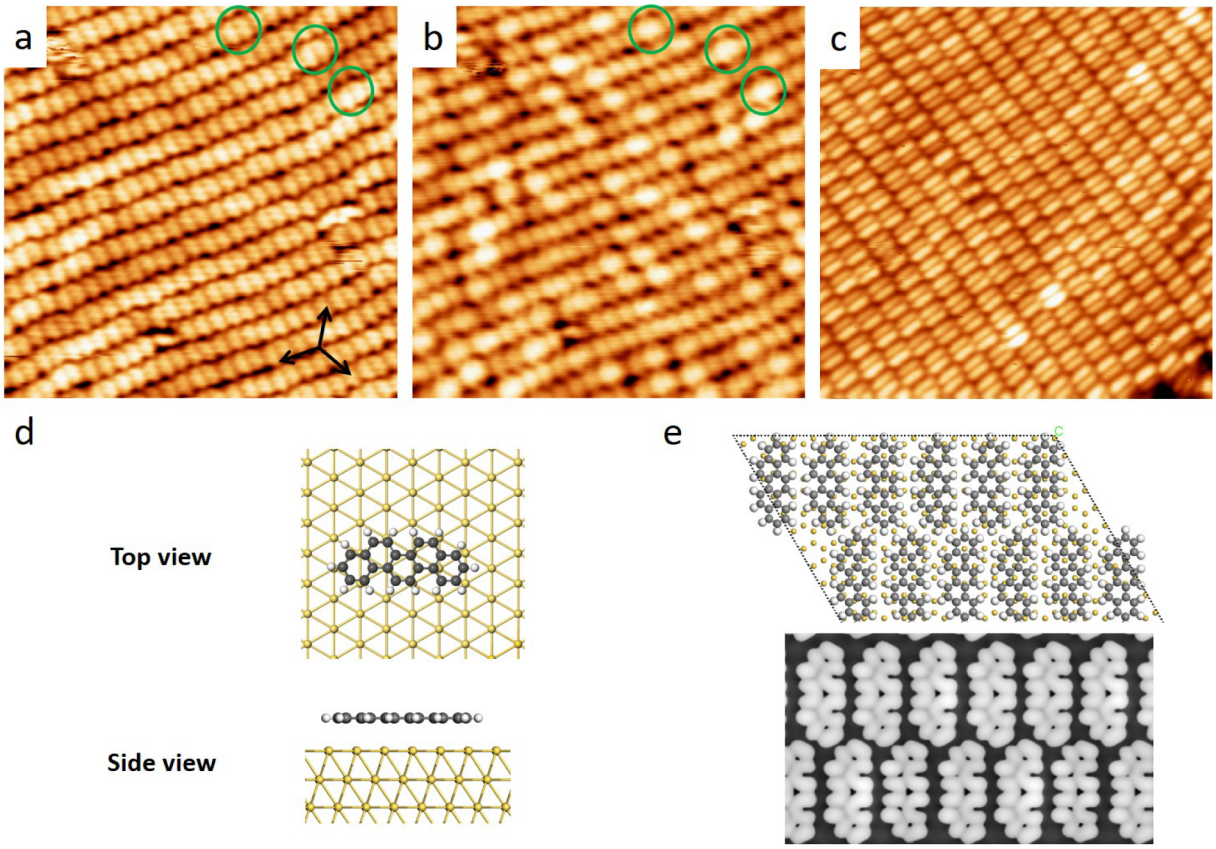

Fig. 5. STM images of picene film on Au(1 1 1). (a) STM images of phase I on Au(1 1 1) taken at $V_s = 1.0$V. The lattice directions of Au(1 1 1) are labeled in the image. (b) the same area as in (a) taken at $V_s = 2.5$V. (Image size: 20 × 20 nm^2). Sub-molecular structure of picene can be observed in (a). Some of molecular pairs which contain two molecules with mirror symmetric configurations are marked as green circles. The same molecular pairs are marked in (b). (c) STM image of phase II on Au(1 1 1) (image size: 20 × 20 nm^2; imaging condition: $V_s = 3.0$V, $I_t = 30$pA). (d) The most energetically favored adsorption geometry of a single picene molecule on Au(1 1 1) surface obtained by DFT calculation. (e) One possible arrangement of molecules and the corresponding simulated STM image.

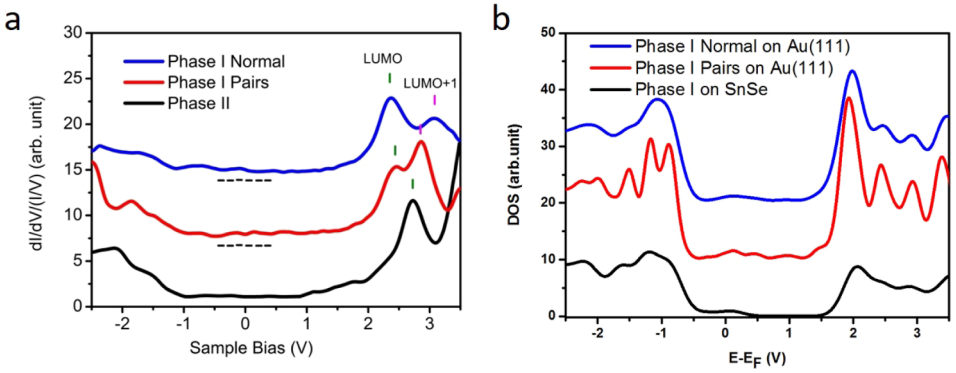

Fig. 6. (a) Scanning tunneling spectra of phase I, molecular pairs and phase II on Au(1 1 1). The spectra are taken at the tunneling condition of $V_s = 2.5$V, $I_t = 50$pA. The spectra are shifted for clearance. The dash lines indicate the shifted zero lines. (b) The simulated DOS of phase I on Au(1 1 1), molecular pairs in phase I on Au (1 1 1) and phase I on SnSe.

This herringbone structure is also a hint to determine the lattice direction of Au(1 1 1), as labeled in Fig. 5a. Thus, we can find molecules are perpendicular to one lattice direction of Au(1 1 1) and arranged into molecular rows along Au(1 1 1) lattice. Fig. 5d depicts the energetically preferred configuration of a single picene on Au(1 1 1) obtained by DFT calculation. The calculation results imply a lower adsorption height (3.03 Å) and lower adsorption energy (−2.36 eV), revealing a stronger interaction with Au(1 1 1) compared with SnSe. Moreover, as shown in Fig. 5e, a (2 × 6) supercell was examined and the corresponding simulated STM image fits the experimental image well, further confirming the proposed configuration. Similar to the case on SnSe, picene molecules in phase I on Au(1 1 1) possess two mirror symmetric configurations. Interestingly, it is frequently observed that two neighboring molecules adopt the two opposite configurations and form a molecular pair. Some of them are marked by green circles in Fig. 5a and 5b. When STM image is taken at 2.5 V, the molecular pairs appear as bright dots. The result is consistent with the measured higher density of states as shown in Fig. 6, which will be discussed below.

Although the structure of picene film is similar on two different substrates, there are still some key differences as follows. Firstly, no vacancy and movement of molecules were detected in Phase I on Au (1 1 1), indicates a stronger molecule-substrate interaction. Secondly,

unlike the straight rows in Phase I on SnSe, the molecular rows in phase I on Au(1 1 1) is slightly distorted. Since self-assembled molecular structures are determined by the intermolecular interaction as well as the interaction between molecules and substrates, two possible mechanisms contribute to this phenomenon: the weaker intermolecular interaction and better lattice matching between phase I and SnSe. Meanwhile, we noticed there is a higher image resolution for picene molecules of phase I on SnSe may due to the weak interaction with the substrate. Unlike Phase I, as being buffered by the underneath layer, for phase II, there is barely structural difference on both substrates. The flat-lying and tilt-standing arrangement is comparable to the bulk herringbone-like structure and is mainly determined by the intermolecular interaction.

Fig. 6a shows typical STS measured at phase I, molecular pairs in phase I and phase II, respectively. The measured STS exhibit that the density of state (DOS) of picene film is strongly dependent on the molecular configuration. For phase I, the LUMO and LUMO + 1 states are located at 2.3 V and 3.0 V, respectively. Although in the same layer, the mirror-symmetric molecular pairs show a narrow energy difference between LUMO and LUMO + 1, namely, LUMO at 2.5 V and LUMO + 1 at 2.9 V. However, in the given range, only LUMO state is detected in phase II, which is located at 2.7 V.

Neglecting the states originating from the substrate, the DOS measured in phase II on Au(1 1 1) exhibits similar positions of states with the one of phase II on SnSe. Due to the beneath phase I film acting as a buffer layer and its bulk-like structure, the DOS of phase II is more likely to represent the intrinsic DOS of bulk material. Although the difference in DOS between phase II on Au(1 1 1) and SnSe is negligible, the difference in DOS of phase I is much striking. As shown in Fig. 6b, the simulated DOS of phase I on SnSe and Au(1 1 1) is in good agreement with the experimental results, namely, several peaks exhibit on Au(1 1 1) while a single peak on SnSe in the region where E is larger than E_F. Because of weak substrate interaction, phase I on SnSe possess the same DOS as thick film. On Au(1 1 1), however, a stronger interaction between molecules and the substrate results in the different DOS. Moreover, the stronger interaction on Au(1 1 1) is also reflected by the calculated absorption energy and absorption distance. One interesting issue is that the LUMO state of phase II locates almost at the center of the LUMO and LUMO + 1 in phase I (Fig. 6a). We expect adsorption-induced splitting of LUMO in phase I, which usually takes place in the system of molecule adsorbed on metal surfaces [39]. The free picene molecule has a quasi-degenerate LUMO state as well [2]. After adsorbed on metal surfaces, a strong interaction with the substrate can break the intrinsic symmetry and cause the splitting of electronic state [39].

4. Conclusions

In summary, we report a comparing study of picene film on p-type SnSe and Au(1 1 1) by using STM, STS and DFT calculations. At different molecular coverage, a flat-lying phase and an alternating flat-lying and tilt-standing phase are observed on both substrates. The latter one resembles the bulk structure and barely dependent on the substrate interaction. The diffusion of picene molecules on SnSe surface at 78 K and the splitting of LUMO state of flat-lying layer on Au(1 1 1) indicate that SnSe has a weaker interaction with the adsorbed molecules. Therefore, we speculate that a semiconductor substrate can keep the intrinsic properties of picene films based on our studies. Our result may pave a new way to unveil the structures and electronic properties of hydrocarbon superconductors.

Author Statement

X.W., T.L. and K.W. conceived the experiments. X.M., M.L., T.Z., Y.M. C.X. and X.W. performed the STM measurements and analyzed the data. X.S. carried out the DFT calculations. X.S., X.W., T.L. and K.W. co-wrote the paper. All authors discussed the results and commented on the manuscript.

Acknowledgement

This work was supported by National Natural Science Foundation of China (Grant No. 11574128 and 21802067).

References

[1] R. Mitsuhashi, Y. Suzuki, Y. Yamanari, H. Mitamura, T. Kambe, N. Ikeda, H. Okamoto, A. Fujiwara, M. Yamaji, N. Kawasaki, Y. Maniwa, Y. Kubozono, Superconductivity in alkali-metal-doped picene, Nature 464 (2010) 76–79.
[2] Y. Kubozono, H. Mitamura, X. Lee, X. He, Y. Yamanari, Y. Takahashi, Y. Suzuki, Y. Kaji, R. Eguchi, K. Akaike, T. Kambe, H. Okamoto, A. Fujiwara, T. Kato, T. Kosugi, H. Aoki, Metal-intercalated aromatic hydrocarbons: A new class of carbon-based superconductors, Phys. Chem. Chem. Phys. 13 (2011) 16476–16493.
[3] X.F. Wang, R.H. Liu, Z. Gui, Y.L. Xie, Y.J. Yan, J.J. Ying, X.G. Luo, X.H. Chen, Superconductivity at 5 K in alkali-metal-doped phenanthrene, Nat. Commun. 2 (2011) 507.
[4] M. Xue, T. Cao, D. Wang, Y. Wu, H. Yang, X. Dong, J. He, F. Li, G.F. Chen, Superconductivity above 30 K in alkali-metal-doped hydrocarbon, Sci. Rep. 2 (2012) 389.
[5] X.F. Wang, Y.J. Yan, Z. Gui, R.H. Liu, J.J. Ying, X.G. Luo, X.H. Chen, Superconductivity in $A_{1.5}$phenanthrene (A = Sr, Ba), Phys. Rev. B 84 (2011) 214523.
[6] Y. Kubozono, R. Eguchi, H. Goto, S. Hamao, T. Kambe, T. Terao, S. Nishiyama, L. Zheng, X. Miao, H. Okamoto, Recent progress on carbon-based superconductors, J. Phys.: Condens. Matter 28 (2016) 334001.
[7] S. Heguri, M. Kobayashi, K. Tanigaki, Questioning the existence of superconducting potassium doped phases for aromatic hydrocarbons, Phys. Rev. B 92 (2015) 014502.
[8] M. Yano, M. Endo, Y. Hasegawa, R. Okada, Y. Yamada, M. Sasaki, Well-ordered monolayers of alkali-doped coronene and picene: Molecular arrangements and electronic structures, J. Chem. Phys. 141 (2014) 034708.
[9] Y. Yoshida, H.H. Yang, H.S. Huang, S.Y. Guan, S. Yanagisawa, T. Yokosuka, M.T. Lin, W. Bin Su, C.S. Chang, G. Hoffmann, Y. Hasegawa, Scanning tunneling microscopy/spectroscopy of picene thin films formed on Ag(111), J. Chem. Phys. 141 (2014) 114701.
[10] Y. Hasegawa, Y. Yamada, T. Hosokai, K.R. Koswattage, M. Yano, Y. Wakayama, M. Sasaki, Overlapping of frontier orbitals in well-defined dinaphtho[2,3-b:2′,3′-f] thieno[3,2-b]-thiophene and picene monolayers, J. Phys. Chem. C 120 (2016) 21536–21542.
[11] T. Huempfner, M. Hafermann, C. Udhardt, F. Otto, R. Forker, T. Fritz, Insight into the unit cell: Structure of picene thin films on Ag(100) revealed with complementary methods, J. Chem. Phys. 145 (2016) 174706.
[12] S.J. Kelly, D.C. Sorescu, J. Wang, K.A. Archer, K.D. Jordan, P. Maksymovych, Structural and electronic properties of ultrathin picene films on the Ag(100) surface, Surf. Sci. 652 (2016) 67–75.
[13] X. Wu, C. Xu, K. Wang, X. Xiao, Charge Transfer, Phase Separation, and Mott-Hubbard Transition in Potassium-Doped Coronene Films, J. Phys. Chem. C 120 (2016) 15446–15552.
[14] S.W. Chen, I.C. Sang, H. Okamoto, G. Hoffmann, Adsorption of Phenacenes on a Metallic Substrate: Revisited, J. Phys. Chem. C 121 (2017) 11390–11398.
[15] B. Mahns, F. Roth, M. Knupfer, Absence of photoemission from the Fermi level in potassium intercalated picene and coronene films: Structure, polaron, or correlation physics? J. Chem. Phys. 136 (2012) 134503.
[16] M. Caputo, G. Di Santo, P. Parisse, L. Petaccia, L. Floreano, A. Verdini, M. Panighel, C. Struzzi, B. Taleatu, C. Lal, A. Goldoni, Experimental study of pristine and alkali metal doped picene layers: Confirmation of the insulating phase in multilayer doped compounds, J. Phys. Chem. C 116 (2012) 19902–19908.
[17] A. Ruff, M. Sing, R. Claessen, H. Lee, M. Tomić, H.O. Jeschke, R. Valentí, Absence of metallicity in K-doped picene: Importance of electronic correlations, Phys. Rev. Lett. 110 (2013) 216403.
[18] H. Okazaki, T. Jabuchi, T. Wakita, T. Kato, Y. Muraoka, T. Yokoya, Evidence for metallic states in potassium-intercalated picene film on graphite, Phys. Rev. B 88 (2013) 245414.
[19] F. Roth, B. Mahns, B. Büchner, M. Knupfer, Dynamic response and electronic structure of potassium-doped picene investigated by electron energy-loss spectroscopy, Phys. Rev. B 83 (2011) 144501.
[20] F. Roth, J. Bauer, B. Mahns, B. Büchner, M. Knupfer, Electronic structure of undoped and potassium-doped coronene investigated by electron energy-loss spectroscopy, Phys. Rev. B 85 (2012) 014513.
[21] C. Zhou, H. Shan, B. Li, A. Zhao, B. Wang, Engineering hybrid Co-picene structures with variable spin coupling, Appl. Phys. Lett. 108 (2016) 171601.
[22] C.-S. Zhou, H. Shan, B. Li, A.-D. Zhao, Imaging molecular orbitals of single picene molecules adsorbed on Cu(111) surface: a combined experimental and theoretical study, Chin. J. Chem. Phys. 30 (2017) 29–35.
[23] X. Fei, W. Xiao, K. Yang, L. Liu, J. Pan, H. Chen, C. Zhang, C.K. Shih, S. Du, H. Gao, Tuning the proximity effect through interface engineering in a Pb/Graphene/Pt trilayer system, ACS Nano 10 (2016) 4520.
[24] C. Xu, Y. Que, Y. Zhuang, Z. Lin, X. Wu, K. Wang, X. Xiao, Growth behavior of pristine and potassium doped coronene thin films on substrates with tuned coupling

strength, J. Phys. Chem. B 122 (2017) 601–611.
[25] C. Chang, M. Wu, D. He, Y. Pei, C. Wu, X. Wu, H. Yu, F. Zhu, K. Wang, Y. Chen, L. Huang, J. Li, J. He, L. Zhao, 3D charge and 2D phonon transports leading to high out-of-plane ZT in n-type SnSe crystals, Science 783 (2018) 778–783.
[26] F. Ming, D. Mulugeta, W. Tu, T.S. Smith, P. Vilmercati, G. Lee, Y.-T. Huang, R.D. Diehl, P.C. Snijders, H.H. Weitering, Hidden phase in a two-dimensional Sn layer stabilized by modulation hole doping, Nat. Commun. 8 (2017) 14721.
[27] D. Joubert, From ultrasoft pseudopotentials to the projector augmented-wave method, Phys. Rev. B 59 (1999) 1758–1775.
[28] J. Hafner, Ab-initio simulations of materials using VASP: density-functional theory and beyond, J. Comput. Chem. 29 (2008) 2044–2078.
[29] G. Kresse, J. Furthmüller, Efficient iterative schemes for ab initio total-energy calculations using a plane-wave basis set, Phys. Rev. B 54 (1996) 11169–11186.
[30] M. Dion, H. Rydberg, E. Schroder, D.C. Langreth, B.I. Lundqvist, Van der waals density functional for general geometries, Phys. Rev. Lett. 92 (2004) 246401.
[31] G. Román-Pérez, J.M. Soler, Efficient implementation of a van der waals density functional: Application to double-wall carbon nanotubes, Phys. Rev. Lett. 103 (2009) 096102.
[32] J. Klime, D.R. Bowler, A. Michaelides, Van der Waals density functionals applied to solids, Phys. Rev. B 83 (2011) 195131.
[33] X. Li, J. Feng, E. Wang, S. Meng, J. Klime, A. Michaelides, Influence of water on the electronic structure of metal-supported graphene: Insights from van der Waals density functional theory, Phys. Rev. B 85 (2012) 085425.
[34] H.J. Monkhorst, J.D. Pack, Special points for Brillouin-zone integrations, Phys. Rev. B 13 (1976) 5188–5192.
[35] S.U. Kim, A.T. Duong, S. Cho, S.H. Rhim, J. Kim, A microscopic study investigating the structure of SnSe surfaces, Surf. Sci. 651 (2016) 5–9.
[36] J.A. Stroscio, R.A. Feenstra, A.P. Fein, Electronic Structure of the Si(111) 2 x 1 Surface by Scanning-Tunneling Microscopy, Phys. Rev. Lett. 57 (1986) 2579–2582.
[37] G. Duvjir, T. Min, T.T. Ly, T. Kim, A.-T. Duong, S. Cho, S.H. Rhim, J. Lee, J. Kim, Origin of p-type characteristics in a SnSe single crystal, Appl. Phys. Lett. 110 (2017) 262106.
[38] Q. Xin, S. Duhm, F. Bussolotti, K. Akaike, Y. Kubozono, H. Aoki, T. Kosugi, S. Kera, N. Ueno, Accessing surface Brillouin zone and band structure of picene single crystals, Phys. Rev. Lett. 108 (2012) 226401.
[39] W.H. Soe, C. Manzano, H.S. Wong, C. Joachim, Mapping the first electronic resonances of a Cu phthalocyanine STM tunnel junction, J. Phys.: Condens. Matter 24 (2012) 354011.

ACS APPLIED ELECTRONIC MATERIALS

pubs.acs.org/acsaelm Article

Controlled Implantation of Phosphorous Atoms into a Silicon Surface Lattice with a Scanning Tunneling Microscopy Tip

Guowei Liu, Xiji Shao, Congrun Chen, Xixian Wang, Xuefeng Wu,* Fangfei Ming,* and Kedong Wang*

Cite This: ACS Appl. Electron. Mater. 2021, 3, 3338−3345 Read Online

ACCESS | Metrics & More | Article Recommendations | Supporting Information

ABSTRACT: Controlling the position of dopants in a silicon lattice is a fundamental technique for future electronic devices with nanometer-sized components and for quantum applications in a Si platform, such as single-atom/defect-based qubits. Here, we demonstrate a controllable method to implant phosphorous (P) atoms into the Si surface lattice through a two-step atomic manipulation procedure using a scanning tunneling microscopy tip: first, P_4 molecules adsorbed on a Si(111)-7 × 7 surface are vertically picked up and dropped off at designated locations; second, a voltage pulse triggers a breakdown of the P_4 molecule, resulting in a stable P structure. First-principles calculations suggest that the manipulation product consists of a single covalently bonded P atom. Spectroscopic measurements reveal a local charge redistribution of the Si dangling bond states around the final P structure. This method will be applicable for innovation in Si-based devices with precisely spaced or patterned P dopants.

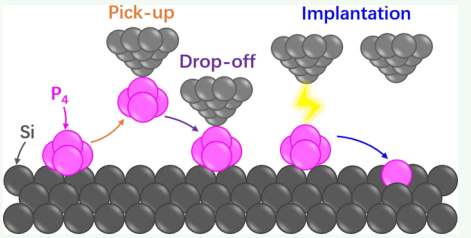

KEYWORDS: *dopant in silicon, tetraphosphorus, qubit, scanning tunneling microscopy, atomic manipulation, Si(111)-7 × 7*

INTRODUCTION

Controlling the position of single atoms is a critical technique for studying quantum physics in the atomic scale and making use of them in future devices. One of the most intriguing application is the realization of qubit and quantum computing based on the spin state of single atoms/defects. Significant progress has been made in fabricating such quantum devices in a silicon platform, where the qubit is realized by the single phosphorus (P) dopant in the Si crystal lattice (Si/P).[1−8] Incorporating the single P atom into the high-purity ^{28}Si lattice is the major challenge for fabricating such a Si/P qubit system.[9,10] Both top-down and bottom-up approaches have been demonstrated. For top-down methods, P ions are implanted into a Si crystal via ion implantation.[11,12] For bottom-up methods, P atoms are placed intentionally on designated locations with the help of scanning probe techniques.[4,13] The most well-known example of the bottom-up method is demonstrated by Simmons et al.,[13] who use scanning tunneling microscopy (STM) lithography[14] to selectively remove a few hydrogen (H) atoms on a H-passivated Si surface such that the exposed Si atoms could adsorb PH_3 molecules, while the rest of the surface remains inert during exposure to PH_3 gas. A single-P dopant could be formed after annealing at high temperatures.[3,15,16] Despite the great success of this method in fabricating single P atom-based qubits, the complex procedures involving gas molecule exposure and high-temperature annealing reduce the controllability and reproducibility on the production of single P dopants with controlled positions.[5,8,15,17,18] To simplify the procedure for implanting P atoms into the Si lattices, we had attempted to dissociate adsorbed PH_3 molecules on the Si(100) surface using voltage pulses with an STM tip; however, controlling the location of P atoms and removing the H atoms from the surface were not achieved.[19,20]

In this paper, we use a P_4 molecule source and demonstrate that the implantation of P atoms could be achieved by STM manipulation. P_4 molecules produced by heating a piece of black phosphorous (BP) are deposited onto a Si(111)-7 × 7 surface. The adsorbed P_4 molecules are stable upon adsorption, and their bonding to the surface is sufficiently weak such that the STM tip can pick up and drop off them at different locations; thus, it provides a control on their locations with atomic precision. The molecular state of the P_4 molecule could be broken by a voltage pulse again from the STM tip, and the P atoms then bond covalently to the Si surface. Possible atomic configuration for the manipulation product is investigated by density functional theory (DFT) calculations, which suggests that it contains only one P atom and the P_4 molecule dissociates during the voltage pulse. Spectroscopic measurements indicate that the final P structure induces local charge redistribution in the surrounding Si dangling bond (DB) states. This method for implanting P atoms into a Si surface lattice could produce identical P structures at designated locations and avoid the procedures to remove hydrogen atoms.

Received: March 19, 2021
Accepted: July 19, 2021
Published: July 27, 2021

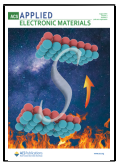

https://doi.org/10.1021/acsaelm.1c00266
ACS Appl. Electron. Mater. 2021, 3, 3338−3345

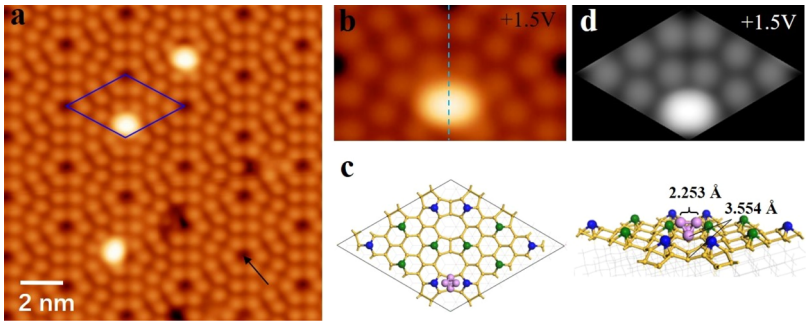

Figure 1. Adsorption of P_4 molecules on a Si(111)-7 × 7 surface. (a) Overview STM image taken after the adsorption of a small amount of P_4, which appear as bright oval features close to the corner holes of the 7 × 7 lattice. One surface unit cell with a P_4 molecule is labeled with a diamond. A corner hole is indicated by an arrow. (b) Magnified STM image of an adsorbed P_4 molecule taken at 1.5 V and 100 pA. The structure shows an apparent two-fold symmetry, as indicated by a dashed line, which is the boundary of two half unit cells (HUCs). (c) Top view of and the side view of a DFT-relaxed model. Si adatoms are represented with blue spheres (corner adatom) and green spheres (edge adatom), while P atoms are represented with purple spheres. Lower-layer Si atoms are shown with yellow balls. (d) Simulated STM image with a 1.5 V sample bias.

RESULTS AND DISCUSSION

Our experiments were performed in a commercial low-temperature STM instrument (Unisoku USM1300) installed in an ultrahigh vacuum chamber with a base pressure better than 1.0×10^{-10} mBar. The Si substrate was cut from a P-doped n-type Si(111) wafer with a room temperature resistivity of 0.026 Ω·cm. A clean Si(111)-7 × 7 reconstruction surface was obtained by degassing the substrate at 800 K overnight and flashing to 1480 K. A chunk piece of BP in an Al_2O_3 crucible heated to 500−600 K is used as the P source. The deposition lasts for ∼1 min, while the substrate is kept at ∼200 K and the chamber pressure is at $\sim 4.7 \times 10^{-10}$ mBar. The sample was immediately transferred to the STM chamber for measurement after deposition. A tungsten tip was cleaned using an e-beam bombardment heater before STM measurement. All STM measurements were performed at 78 K.

Figure 1a shows an STM image of the Si(111)-7 × 7 surface after the deposition of a small amount of P, which result in the bright oval-shaped features adsorbed close to the corner holes. Considering the threefold symmetry of the surface lattice, these oval-shaped features are identical. They are presumably P_4 molecules as it is known that P_4 is the dominating form of vapor for P elements.[21−23] Figure 1b shows a magnified STM image of one adsorbed P_4 molecule which straddles the boundary of a faulted half unit cell (FHUC) and an unfaulted half unit cell (UHUC) of the Si(111)-7 × 7 lattice. This image shows an apparent two-fold symmetry (half in FHUC and half in UHUC), as indicated by a dashed line, although it is expected to be broken by lower layer stacking fault of the surface reconstruction.[24] Considering the large number of unpaired Si DBs on the surface and a large energy gain by the P−Si covalent bond formation, one might expect the formation of a strong covalent P−Si bond between the molecule and the surface and/or a breakdown of the P_4 molecule. Surprisingly, these molecules keep their molecular structure intact and bond weakly to the Si(111)-7 × 7 surface. This is evident from the fact that they can be transferred as a whole between the tip and the surface without any damage, as will be shown later. Its molecular state is further supported by its wide energy gap in STS, as shown in Figure S1. The knowledge of its unchanged molecular structure and the oval shape in STM images provide a straightforward atomic configuration for the adsorbed P_4 molecule, which is further supported by DFT calculations. The relaxed atomic configuration is shown in Figure 1c, where a tetrahedron of four P atoms locates along the Si dimer row and near the corner hole, with two P atoms away from the surface aligning with the long axis of the oval feature seen in the STM image. The P_4 molecule keeps its tetrahedral structure and adsorbs at the middle of two corner adatoms, each from FHUC and UHUC. The simulated STM image in Figure 1d shows an oval-shaped feature consistent with the STM image in Figure 1b. In the relaxed model, two P atoms close to the Si surface and parallel to the Si dimer row are 2.203 Å apart, while the other two P atoms away from the surface and perpendicular to the dimer row are 2.253 Å apart. Both bond lengths are consistent with a P−P bond of 2.21 Å in the P_4 molecule.[25,26] On the other hand, the nearest P−Si distance is 3.554 Å, which is significantly longer than a P−Si covalent bond.[27] The adsorption energy of the P_4 molecule is found to be 0.567 eV, which is significantly smaller than P−Si bond formation energy[28] or the adsorption energy of K/Ag/Au/Cu atoms adsorbed on the same surface.[29] These bonding characters are in line with the experimental observations that the molecular structure of the P_4 molecule is largely unchanged and that there is no Si−P covalent bond formation upon adsorption on the Si surface.

Thanks to their weak bonding to the surface, the P_4 molecules could be manipulated vertically using an STM tip, meaning that the P_4 molecule could be transferred to the tip and dropped off to different locations on the surface. Sequential STM images shown in Figure 2a−c record the process of manipulating two P_4 molecules. Their initial locations are indicated in Figure 2a. In Figure 2b, the P_4 molecule highlighted by the yellow dashed circle is transferred to the location highlighted by a yellow solid circle, while in Figure 2c, another P_4 molecule labeled with a purple circle is transferred to a different location. After being dropped off onto the surface, the P_4 molecules still adsorb at positions close to corner holes that are nearest to the tip approaching location. As a result, the accuracy of such a vertical manipulation is limited by the size of a unit cell length of 2.7 nm. Although the adsorption location is almost identical to those naturally grown P_4 molecules, the apparent two-fold symmetry seems to be broken, which is likely a result of the molecules being frozen at a metastable adsorption configuration at 77 K. The vertical manipulation of the P_4 molecule consists of three consecutive steps: picking up, translation, and dropping off. To pick up a P_4 molecule, the tip approaches to the molecule for about 6 Å from the tunneling set point of −1.5 V and 100 pA. The

https://doi.org/10.1021/acsaelm.1c00266
ACS Appl. Electron. Mater. 2021, 3, 3338−3345

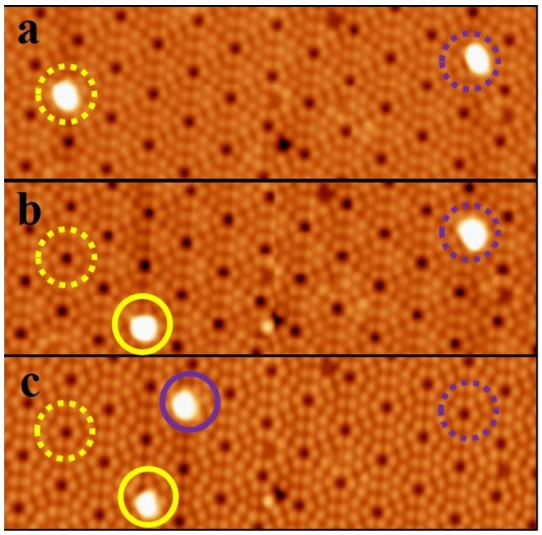

Figure 2. Vertical manipulation of P_4 molecules on a Si(111)-7 × 7 surface. (a–c) Consecutive STM images showing the relocation of two P_4 molecules. Dashed/solid line circles indicate the original/final locations. Two examples are labeled with yellow and purple.

molecule transfers to the tip apex at small tip sample separation when the tip slightly "touches" the molecule (a chemical bond likely forms at such a distance).[30] The dropping-off procedure is conducted with a similar "tip touching" procedure but with a reversed sample bias at +1.5 V. A successful transfer of the P_4 molecule is verified by subsequent STM imaging and is usually indicated by a changed tip height and image resolution (see Figure S2). A successful transfer depends on manipulation parameters. At the "tip touching" point, the P_4 molecule prefers to stay at the tip apex at negative sample bias, while it prefers to stay on the Si surface at positive bias. Although a freestanding P_4 molecule is electrically neutral, different charging states on the surface or at the tip apex might be responsible for the dependence of bias polarity. Similar to most studies of manipulation of single atom/molecules on surfaces, reposition of a P_4 molecule is a slow process. Since the success rate for a single vertical manipulation attempt is as low as a few percent (see Figure S3 for the bias voltage and the approaching distance dependence of the success rate), a successful reposition of a P_4 molecule normally requires performing multiple manipulation attempts on the same P_4 molecule. Typically, it could take about half an hour in total to finish one reposition work. Moreover, the tip apex condition is a critical factor for such a vertical manipulation which influences the manipulation parameters or even the feasibility to carry out such a manipulation at all. Getting a proper tip condition and the corresponding manipulation parameters is a trial and error process and usually takes hours or even days.

To break down the molecular state of an adsorbed P_4 molecule, a precisely controlled voltage pulse by the STM tip is applied on top of the molecule. Figure 3a shows three P_4 molecules. Their structures are stable under typical scanning conditions with a sample bias of +1.5 V and a tunneling current of 100 pA. After applying a pulse at 2.2 V with 1 s duration to each one of them, they all convert to identical structures, as indicated by blue triangles in Figure 3b. The manipulation product by the voltage pulse appears as a single bright spot at a corner Si adatom, showing a significantly smaller size and brightness in the STM image compared to the

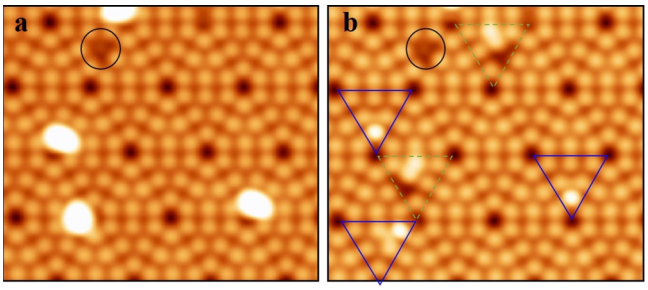

Figure 3. Voltage pulse manipulation of P_4 molecules on a Si(111)-7 × 7 surface. (a) STM image showing three adsorbed P_4 molecules. (b) STM image showing the same surface after applying a voltage pulse (+2.2 V, 1 s duration) to each one of the three P_4 molecules in (a). Three blue triangles indicate the HUC containing the manipulation product, while two dashed green triangles indicate two Si defects inducted during the voltage pulses. A circle marks an intrinsic Si defect.

P_4 molecule seen in Figure 3a. Rather than striding across two neighboring HUCs, the manipulation product locates within one HUC, predominately FHUC. Since a P_4 molecule locates at the boundary of FHUC and UHUC and the voltage pulse is applied to the center of a P_4 molecule, the preference of the FHUC suggests a lower reaction barrier for staying in FHUC than in UHUC. The pulse-induced transformation starts from voltages above 1.9 V and has a higher success rate at higher biases, for example, over 50% possibility at 2.2 V. See Figure S4 for the voltage dependence of the success rate of a pulse manipulation. An STM image is taken after each pulse manipulation to check whether the P_4 molecule is successfully cracked and the manipulation product is properly produced. Therefore, it usually takes a few minutes to finish one pulse manipulation work. The manipulation product is stable against further pulse or vertical manipulation attempts, suggesting that the covalent bonds are formed between the P atoms and the Si surface. Such a voltage pulse sometimes creates defects in nearby HUCs without P atoms (two cases labeled with dashed green triangles), which are attributed to Si defects and will recover later on during the STM scanning process (see Figure S5).

Figure 4a,b shows empty-state and filled-state STM images of a manipulation product, both showing a two-fold symmetry with a symmetry axis parallel to the *x*-axis. The empty-state STM image in Figure 4a shows a bright spot at a corner adatom ("CA" in the figure) and a slightly enhanced brightness at the two-neighboring edge adatoms ("EA" in the figure). The filled state image in Figure 4b shows that the two "EA" sites become significantly brighter, while the "CA" site becomes suppressed. The reversed contrast in empty- and filled-state images indicates a charge transfer from the "CA" atom to the "EA" adatom. For a companion of STM images between the clean Si(111)-7 × 7 unit cell and a unit cell with a manipulation product, see Figure S6.

In order to access the atomic structures of the manipulation product, we perform a systematic search for possible atomic configurations using first-principles calculations and compare them to the STM observations. In view of the relatively small size of the bright feature of the STM image and the fact that molecular dissociation could occur upon voltage pulses using an STM tip,[19,20,31,32] initial trial configurations with one or two P atoms are considered in our configuration search, in addition to four-P-atom models. Tested initial configurations include

https://doi.org/10.1021/acsaelm.1c00266
ACS Appl. Electron. Mater. 2021, 3, 3338–3345

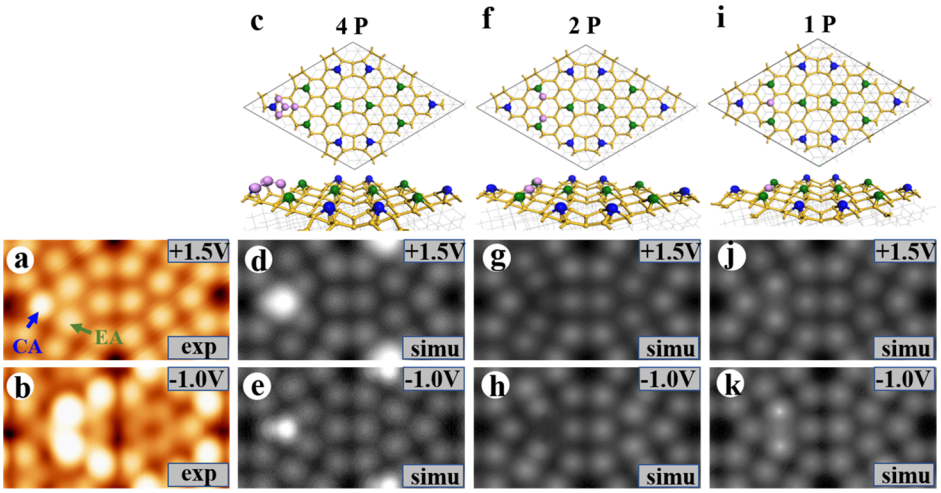

Figure 4. Comparison of experiment and simulation of the STM image of the manipulation product. (a) 1.5 V STM image. Two adatoms are labeled. "CA" represents a corner adatom site, and "EA" represents the edge adatom site. (b) −1.0 V STM image of the same structure. (c,f,i) Top and side views of DFT-relaxed models with four (c), two (f), and one (i) P atoms. Their corresponding simulated STM images at +1.5 V (d,g,j) and −1.0 V(e,h,k) are shown below their respective atomic models.

four configurations with four P atoms, five configurations with two P atoms, and five configurations with one P atom. Their initial and relaxed configurations are shown in Figure S7. Although all the initial configurations are set to possess the same two-fold symmetry as that in the STM image, most of them lose such symmetry after relaxation, which are excluded for further examination. The last three columns in Figure 4 show three relaxed configurations still possessing the two-fold symmetry, each with four P atoms, two P atoms, and one P atom. For the four-P-atom model shown in Figure 4c, the four P atoms form a nearly planer structure next to one of the corner adatoms within an HUC. Considering the corner Si adatom, the P atoms arrange in a compact structure. The closest Si−P distances are between 2.307 and 2.361 Å, indicating a covalent P−Si bond formation. For the two-P-atom model in Figure 4f and one-P-atom model in Figure 4i, the P atoms locates close to the edge adatoms in the FHUC, while the P−Si distances also indicate the formation of a covalent P−Si bond. STM images at both the empty state of +1.5 V and filled state of −1 V are simulated to compare with the experiment, their atomic models are shown below in Figure 4. For the simulated STM image from the four-P-atom model shown in Figure 4d,e, the bright spots are close to the center of the "CA" site and two equivalent "EA" sites and are largely unchanged in empty- and filled-state images. For the simulated STM image with the two-P-atom model shown in Figure 4g,h, suppressions rather than bright spots are observed at the edge adatom at both filled and empty states. For the simulated STM image from the one-P-atom model, the "CA" adatom becomes brighter in the empty-state image seen in Figure 4j, while two "EA" adatoms becomes brighter in the empty-state STM image shown in Figure 4k, which are qualitatively consistent with the STM images in Figure 4a,b. Based on the symmetry and STM image simulation, the one-P-model in Figure 4i agrees best with the experiment within all our tested models. Experimentally, to produce a structure with one P atom from the P_4 molecule, the P_4 molecule must dissociate and the extra three P atoms need to either desorb to the vacuum or to the STM tip, since no extra structure is observed around the manipulation product. It should be noted that the real atomic structure for the manipulation product could still be out of our search. Further experimental and theoretical work is needed to confirm the atomic structure and to reveal the reaction pathway for converting the P_4 molecule, which is beyond the scope of the current study.

The electronic structures of the pulse manipulation product are further characterized by scanning tunneling spectroscopy (STS), as summarized in Figure 5. Figure 5a shows the topography image ("z") of the manipulation product in an FHUC, as indicated by a triangle. In the "z" image, only the adatoms are resolved (blobs). Comparing it with the dI/dV images shown in Figure 5b−g, it is noticeable that most of the images show only the adatom character, except the "−0.8 V" image showing mostly the rest atom feature, which can be seen more clearly in the neighboring UHUC showing three bright blobs, consistent with previous experiments.[33] The manipulation product adsorbs close to the left corner of the FHUC and induces a local modulation of electronic structures, as compared to their equivalent sites in other unit cells away from the manipulation product. For an easy discussion, several adatom sites in the "z" image are labeled with numbers, as shown in Figure 5h. The most significant changes are at the nearby adatom sites 1 (brighter in the 0.7 V image), 2/2′ (brighter in −0.3 and +0.7 V images), 4 (brighter in the 0.5 V image), 7/7′ (darker in the 0.3 V image, compared with the equivalent site in other UHUC), and 8/8′ (brighter in 0.3 and −0.3 V images). STS spectra on these adatom sites are obtained to gain more insights into their DB states, shown in Figure 5i−m. Here, we show dI/dV spectra rather than $dI/dV/(I/V)$ to avoid data processing artifacts for the nearly semiconducting STS.[34] STS on adatom sites close to the manipulation product (1, 2, 3, 4, 7, 8, and 11) are compared to sites far away (5, 6, 9, 10, and 12), and equivalent sites in different unit cells are compared in the same panel. Despite the fact that sites 4, 7, and 8 show identifiable changes in dI/dV images in Figure 5b−g, their dI/dV curve shows minor changes, for example, site 4 versus site 6 in Figure 5j, site 7 versus site 9 in Figure 5l, and site 8 versus site 10 in Figure 5m. The DB at the corner hole [site 11 versus site 12 in Figure 5k] shows a minimal change as well. These minor changes indicate that the filling of the DBs at these sites are largely unchanged. On the other hand, STS at sites 1 and 2 show dramatic

https://doi.org/10.1021/acsaelm.1c00266
ACS Appl. Electron. Mater. 2021, 3, 3338−3345

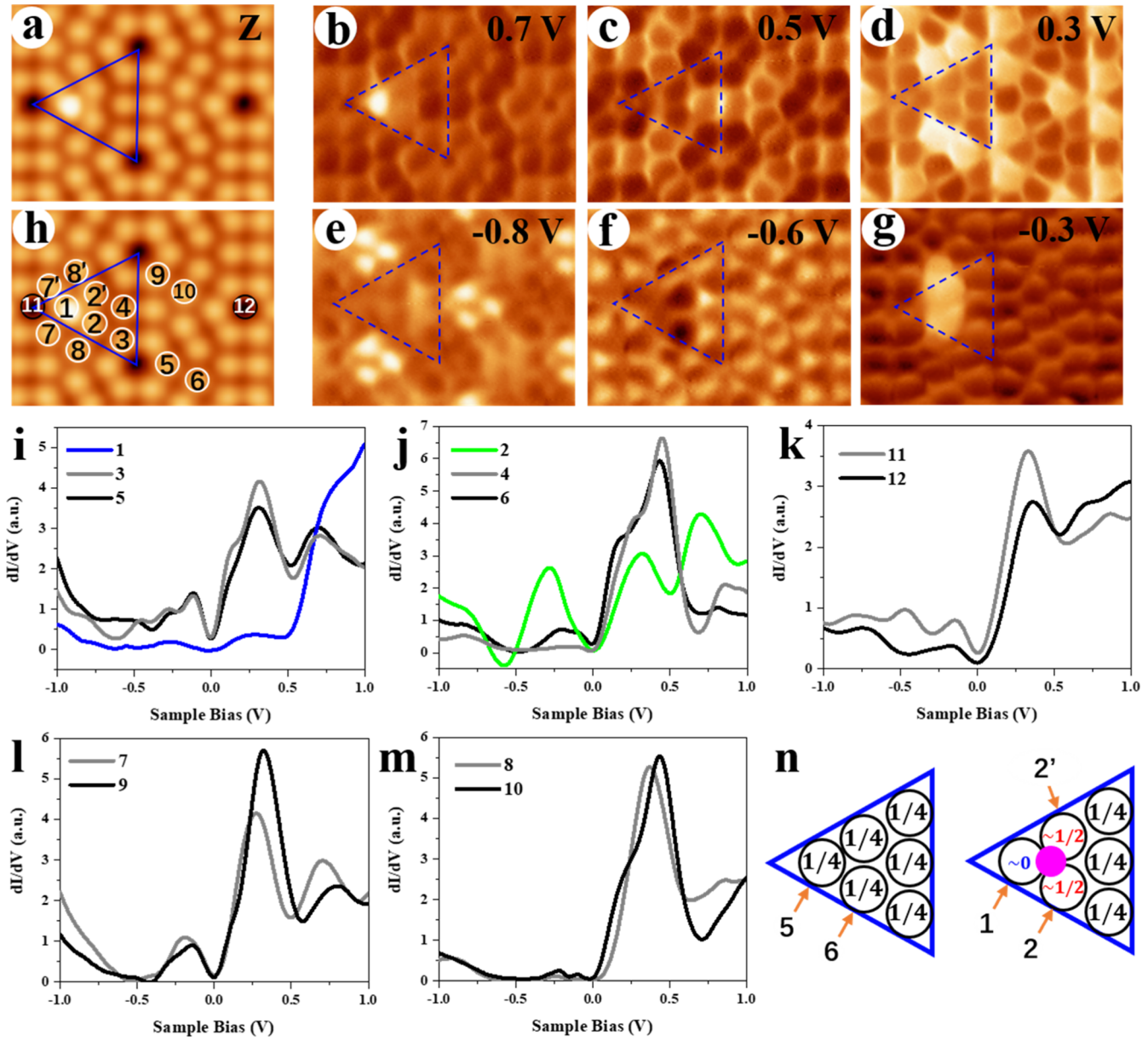

Figure 5. Spectroscopic measurements of a pulse manipulation product. (a) Topography of the manipulation product, scanned at 1.5 V, 100 pA. A triangle labels the FHUC containing the manipulation product. (b–g) dI/dV image of the manipulation product taken at various biases. (h) Same image as (a) with numbers indicating different adatoms sites, where dI/dV spectra are taken. (i–m) Selected dI/dV spectra. Each panel compares equivalent sites in different unit cells. Site 2′ is the equivalent location of site 2 and has identical STS and not shown here. (n) Sketch of a charging state model for the DBs on six adatoms within an FHUC. The left is for a clean FHUC, while the right is for an FHUC with an adsorbed P structure. Numbers in circles indicate the electron occupation of the corresponding adatom DBs. The purple circle indicates a P manipulation product. Arrows indicate the sites of 1,2,2′,5,6 labeled in (h).

changes, as evident from the site 1 versus site 5 in Figure 5i and 2 versus 6 in Figure 5j. STS at site 1 shows a nearly semiconducting state with a greatly reduced DOS around the Fermi level (−0.75 to 0.5 V). The minor states peaked near −0.25 and +0.25 V could even be states spilled from neighboring adatoms. The nearly semiconducting state and a strong state above 0.5 V suggest that the corresponding DB state at site 1 now becomes close to empty. Another significant change in STS is found at site 2. As seen in Figure 5j, spectral features around the Fermi level redistribute significantly from that on site 6, meaning that the filled states (−0.5 to 0 V) increase, while the empty states (0 to +0.5 V) decrease, indicating an increased electron filling but still away from full filling.

The abovementioned spectroscopic observations could be described by a simple charge redistribution picture around the manipulation product, as sketched in Figure 5n. On a clean Si(111)-7 × 7 surface, DB states on the six adatoms within an FHUC are expected to be 1/4 occupied (half electron), while DBs on the three rest atoms (not shown) are fully occupied.[35] The 1/4 filling converts to a ratio of 1:3 for filled and empty states, qualitatively consistent with their significantly stronger empty states (0 to +0.5 V) than the filled states (−0.5 to 0 V) seen in STS for unaffected DBs at site 5 (panel i) and site 6 (panel j). With the P structure sitting close to three of the six

https://doi.org/10.1021/acsaelm.1c00266
ACS Appl. Electron. Mater. 2021, 3, 3338−3345

adatom sites in the HUC, see the right part of Figure 5n, the DB at the nearest corner adatom (site 1) now becomes close to empty, as evident from its nearly semiconducting STS (panel i). On the other hand, the DBs of the two-neighboring edge adatoms (site 2 and 2′) gain more electrons. A naïve eyeball check of the STS on site 2 in panel (j) suggests a close-to-half filling of the DB as it has comparable spectral weight at filled (−0.5 to 0 V) and empty states (0 to +0.5 V). Other DB states are roughly unchanged from those on the clean Si surface. The rough electron filling numbers for the DBs are labeled at the right part of Figure 5n. A simple electron counting of the numbers would give ∼1/2 electron (1/4 filling of one DB orbital) in total gained by the three DBs after the adsorption of the P structure. It should be noted that these filling numbers are qualitative estimates from the spectral features observed in Figure 5i−m and are independent from the atomic models for the P structures. Since the dI/dV images in (b−g) do not show characteristic features for the P atoms/cluster in dI/dV images taken at energies close to the Fermi level, for example, between −0.8 and +0.7 V, the valence electrons of the P structure should all be paired. Considering the five valance electrons for a single P atom and that the P structure (with one, two, or four P atoms depending on the atomic model) should have paired valence electrons, one might expect three possible electron transfer pictures from the P structures to the three surrounding Si DBs: the P structure donates one electron (case A) if the P structure contains one P atom; it donates zero (case B) or two (case C) electrons if the P structure contains two or four P atoms. Assume that the DB "1" in Figure 5n is empty, the filling of the DB "2/2′" in the three scenarios will be 5/8 (case A), 3/8 (case B), and 7/8 (case C). Here, the case A or case B is close to the observation of nearly half-filled (∼1/2) DB for the DB 2/2′ in the dI/dV spectra, although this does not suggest a preference in the three atomic models with one, two, or four P atoms.

CONCLUSIONS

In summary, we have demonstrated a method to fabricate covalently bonded P atoms on the Si(111)-7 × 7 surface by depositing P_4 molecules and thereafter manipulating the molecule with an STM tip. The P_4 molecules adsorb weakly on the surface and could be vertically manipulated by the STM tip, while the P atoms covalently bond to the Si surface after a precisely controlled voltage pulse manipulation. This method of implanting P atoms with atomic precision could be executed consecutively without annealing at high temperatures. The atomic structure of the adsorbed P_4 molecule and the final product are fully characterized by STM and DFT calculations, which suggest that the final product contains a single P atom.

The current method of controllably positioning P atoms avoids the use of a hydrogen resist, offering the potential for new device fabrication strategies. It should be noticed that the Si(111) surface is not used in the existing studies[3,36] or making single/multiple P-dopant devices because in-vacuum hydrogen termination is extremely difficult and layer-by-layer silicon overgrowth is not as controlled as the Si(001) surface. The latter problem remains if similar devices are to be made starting from our work performed on the Si(111)-(7 × 7) surface. Moreover, the P structure produced here is not four-coordinated and is surrounded by a large density of DB states, which makes it unlikely to be used as qubits directly. To make an applicable device, such as a quantum bit, extra steps of capping the surface with layers of Si and recrystallization are needed. Considering the high stability of the Si(111)-(7 × 7) reconstruction, recrystallization is likely to require a high-temperature annealing process, which could cause unwanted P dopant diffusion.[36] To overcome these potential problems with the Si(111)-7 × 7 surface, one possible future work is to explore the applicability of our method in other clean Si surfaces, such as a clean Si(001)-(2 × 1) surface. The vertical manipulation of the P_4 molecule described here is likely to be applicable as the P_4 molecule is stable in a Si DB environment, while the pulse manipulation parameters and the product will need to be explored. Compared with previous methods of making P dopants on the H-terminated Si(001) surface, the possible advantage of using the new method is that the produced P structure will be identical with a certain number of P atoms and will have identical atomic structures.[3,36] On the other hand, its disadvantage might include the difficulty in making electrodes with a large amount of P dopants due to the slow speed of vertical manipulation of P_4 molecules. New methods of applying the current approach to make devices with single/several P dopants will need to be explored in the future. Our work will stimulate further effort to fabricate a complex P dopant structure with atomic precision, for example, multiple P-based qubit arrays for quantum computing applications.[3,37]

METHODS

Computational Details. In this work, first-principles calculations were performed by the Vienna Ab initio Simulation Package (VASP)[38,39] based on the density functional dispersion correction (DFT-D3).[40−42] Projector-augmented wave (PAW) pseudopotentials[43] were used with the PBE exchange correlation function[44] and a plane-wave cutoff of 450 eV. A supercell consisted of seven layers including 298 Si atoms and 49 hydrogen atoms passivating Si DBs of the bottom of the slab. The vacuum separation was built as 20 Å. The Γ-point-only Brillouin zone sampling was used for structural optimizations. The simulated STM images are produced using the Tersoff−Hamann scheme,[45] where the isovalue $\rho_{iso} = 10^{-5}$ e/Bohr^3 is used in all calculations.[46,47] All atoms were allowed to relax until each atom force was below 0.01 eV/Å.

ASSOCIATED CONTENT

Supporting Information

The Supporting Information is available free of charge at https://pubs.acs.org/doi/10.1021/acsaelm.1c00266.

dI/dV spectra and a typical picking-up process of a P_4 molecule on a Si(111)-7 × 7 surface; statistics of the success rate of vertical manipulation and products of pulse manipulation; comparison of STM images and DFT calculations about the products; and generation and recovery of Si defects during the manipulation of P_4 (PDF)

AUTHOR INFORMATION

Corresponding Authors

Xuefeng Wu − *Department of Physics, Southern University of Science and Technology, Shenzhen, Guangdong 518055, China*; Email: wuxf@mail.sustech.edu.cn

Fangfei Ming − *State Key Laboratory of Optoelectronic Materials and Technologies, School of Electronics and Information Technology and Guangdong Province Key Laboratory of Display Material and Technology, Sun Yat-sen University, Guangzhou 510275, China*; Email: mingff@mail.sysu.edu.cn

https://doi.org/10.1021/acsaelm.1c00266
ACS Appl. Electron. Mater. 2021, 3, 3338−3345

Kedong Wang − *Department of Physics, Southern University of Science and Technology, Shenzhen, Guangdong 518055, China*; orcid.org/0000-0003-1253-5603; Email: wangkd@sustech.edu.cn

Authors

Guowei Liu − *Department of Physics, Southern University of Science and Technology, Shenzhen, Guangdong 518055, China*; orcid.org/0000-0003-1283-788X

Xiji Shao − *Department of Physics, Southern University of Science and Technology, Shenzhen, Guangdong 518055, China*

Congrun Chen − *Department of Physics, Southern University of Science and Technology, Shenzhen, Guangdong 518055, China*

Xixian Wang − *Department of Physics, Southern University of Science and Technology, Shenzhen, Guangdong 518055, China*

Complete contact information is available at: https://pubs.acs.org/10.1021/acsaelm.1c00266

Author Contributions

G.L. and X.S. contributed equally to the work. K.W. supervised the experiments. G.L. and X.W. preformed the experiments. G.L. and X.S. performed the theoretical simulations. G.L. and F.M. analyzed the data and wrote the manuscript. All authors discussed the results thoroughly and provided the comments about the manuscript.

Notes

The authors declare no competing financial interest.

■ ACKNOWLEDGMENTS

This work was supported by the National Natural Science Foundation of China (grants no. 11574128), the MOST 973 Program (grants no. 2014CB921402), the Guangdong Basic and Applied Basic Research Foundation (grants no. 2021A1515012034), and the General Physics Teaching Steering Committee of the Ministry of Education Teaching Reform Project (DJZW201931zn). F.M. acknowledges the support by Guangdong Natural Science Foundation: Distinguished Young Scholar (grants no. 2020B1515020009). The DFT calculations were supported by the Center for Computational Science and Engineering at Southern University of Science and Technology.

■ REFERENCES

(1) Kane, B. E. A silicon-based nuclear spin quantum computer. *Nature* **1998**, *393*, 133−137.

(2) Zwanenburg, F. A.; Dzurak, A. S.; Morello, A.; Simmons, M. Y.; Hollenberg, L. C. L.; Klimeck, G.; Rogge, S.; Coppersmith, S. N.; Eriksson, M. A. Silicon quantum electronics. *Rev. Mod. Phys.* **2013**, *85*, 961−1019.

(3) Simmons, M. Y.; Schofield, S. R.; O'Brien, J. L.; Curson, N. J.; Oberbeck, L.; Hallam, T.; Clark, R. G. Towards the atomic-scale fabrication of a silicon-based solid state quantum computer. *Surf. Sci.* **2003**, *532*−*535*, 1209−1218.

(4) Clark, R. G.; Brenner, R.; Buehler, T. M.; Chan, V.; Curson, N. J.; Dzurak, A. S.; Gauja, E.; Goan, H. S.; Greentree, A. D.; Hallam, T.; Hamilton, A. R.; Hollenberg, L. C. L.; Jamieson, D. N.; McCallum, J. C.; Milburn, G. J.; O'Brien, J. L.; Oberbeck, L.; Pakes, C. I.; Prawer, S. D.; Reilly, D. J.; Ruess, F. J.; Schofield, S. R.; Simmons, M. Y.; Stanley, F. E.; Starrett, R. P.; Wellard, C.; Yang, C. Progress in silicon-based quantum computing. *Philos. Trans. R. Soc., A* **2003**, *361*, 1451−1471.

(5) Broome, M. A.; Gorman, S. K.; House, M. G.; Hile, S. J.; Keizer, J. G.; Keith, D.; Hill, C. D.; Watson, T. F.; Baker, W. J.; Hollenberg, L. C. L.; Simmons, M. Y. Two-electron spin correlations in precision placed donors in silicon. *Nat. Commun.* **2018**, *9*, 980.

(6) Hile, S. J.; Fricke, L.; House, M. G.; Peretz, E.; Chen, C. Y.; Wang, Y.; Broome, M.; Gorman, S. K.; Keizer, J. G.; Rahman, R.; Simmons, M. Y. Addressable electron spin resonance using donors and donor molecules in silicon. *Sci. Adv.* **2018**, *4*, No. eaaq1459.

(7) Muhonen, J. T.; Dehollain, J. P.; Laucht, A.; Simmons, S.; Kalra, R.; Hudson, F. E.; Dzurak, A. S.; Morello, A.; Jamieson, D. N.; McCallum, J. C.; Itoh, K. M. Coherent control via weak measurements in P-31 single-atom electron and nuclear spin qubits. *Phys. Rev. B* **2018**, *98*, 155201.

(8) Wang, X.; Hagmann, J. A.; Namboodiri, P.; Wyrick, J.; Li, K.; Murray, R. E.; Myers, A.; Misenkosen, F.; Stewart, M. D.; Richter, C. A.; Silver, R. M. Quantifying atom-scale dopant movement and electrical activation in Si:P monolayers. *Nanoscale* **2018**, *10*, 4488−4499.

(9) Tyryshkin, A. M.; Tojo, S.; Morton, J. J. L.; Riemann, H.; Abrosimov, N. V.; Becker, P.; Pohl, H.-J.; Schenkel, T.; Thewalt, M. L. W.; Itoh, K. M.; Lyon, S. A. Electron spin coherence exceeding seconds in high-purity silicon. *Nat. Mater.* **2011**, *11*, 143−147.

(10) Abrosimov, N. V.; Aref'ev, D. G.; Becker, P.; Bettin, H.; Bulanov, A. D.; Churbanov, M. F.; Filimonov, S. V.; Gavva, V. A.; Godisov, O. N.; Gusev, A. V.; Kotereva, T. V.; Nietzold, D.; Peters, M.; Potapov, A. M.; Pohl, H. J.; Pramann, A.; Riemann, H.; Scheel, P. T.; Stosch, R.; Wundrack, S.; Zakel, S. A new generation of 99.999% enriched (2)8(S)i single crystals for the determination of Avogadro's constant. *Metrologia* **2017**, *54*, 599−609.

(11) Jamieson, D. N.; Yang, C.; Hopf, T.; Hearne, S. M.; Pakes, C. I.; Prawer, S.; Mitic, M.; Gauja, E.; Andresen, S. E.; Hudson, F. E.; Dzurak, A. S.; Clark, R. G. Controlled shallow single-ion implantation in silicon using an active substrate for sub-20-keV ions. *Appl. Phys. Lett.* **2005**, *86*, 202101.

(12) van Donkelaar, J.; Yang, C.; Alves, A. D. C.; McCallum, J. C.; Hougaard, C.; Johnson, B. C.; Hudson, F. E.; Dzurak, A. S.; Morello, A.; Spemann, D.; Jamieson, D. N. Single atom devices by ion implantation. *J. Phys.: Condens. Matter* **2015**, *27*, 154204.

(13) He, Y.; Gorman, S. K.; Keith, D.; Kranz, L.; Keizer, J. G.; Simmons, M. Y. A two-qubit gate between phosphorus donor electrons in silicon. *Nature* **2019**, *571*, 371−375.

(14) Randall, J. N.; Lyding, J. W.; Schmucker, S.; Von Ehr, J. R.; Ballard, J.; Saini, R.; Xu, H.; Ding, Y. Atomic precision lithography on Si. *J. Vac. Sci. Technol., B: Microelectron. Nanometer Struct.–Process., Meas., Phenom.* **2009**, *27*, 2764−2768.

(15) Schofield, S. R.; Curson, N. J.; Simmons, M. Y.; Ruess, F. J.; Hallam, T.; Oberbeck, L.; Clark, R. G. Atomically precise placement of single dopants in si. *Phys. Rev. Lett.* **2003**, *91*, 136104.

(16) Petta, J. R. Atom-by-Atom Construction of a Quantum Device. *ACS Nano* **2017**, *11*, 2382−2386.

(17) Shlimak, I.; Vagner, I. Quantum information processing based onP31nuclear spin qubits in a quasi-one-dimensionalSi28nanowire. *Phys. Rev. B: Condens. Matter Mater. Phys.* **2007**, *75*, 045336.

(18) Wang, Y.; Tankasala, A.; Hollenberg, L. C. L.; Klimeck, G.; Simmons, M. Y.; Rahman, R. Highly tunable exchange in donor qubits in silicon. *npj Quantum Inf.* **2016**, *2*, 16008.

(19) Liu, Q.; Lei, Y.; Shao, X.; Ming, F.; Xu, H.; Wang, K.; Xiao, X. Controllable dissociations of PH3 molecules on Si(001). *Nanotechnology* **2016**, *27*, 135704.

(20) Miotto, R.; Srivastava, G. P.; Ferraz, A. C. Dissociative adsorption ofPH3on the Si(001) surface. *Phys. Rev. B: Condens. Matter Mater. Phys.* **2001**, *63*, 125321.

(21) Schlesinger, M. E. The thermodynamic properties of phosphorus and solid binary phosphides. *Chem. Rev.* **2002**, *102*, 4267−4302.

(22) Distowski, H.; Hofmann, T. In *Ullmann's Encyclopedia of Industrial Chemistry*, 5th ed.; Elvers, B., Hawkins, S., Schulz, G., Eds.; VCH: Berlin, 1985; Vol. *A19*, p 505.

(23) Raghavachari, K.; Haddon, R. C. Small Elemental Clusters - Theoretical-Study of P, P2, P4 and P8. *Abstr. Pap. Am. Chem. Soc.* **1985**, *190*, 186.
(24) Takayanagi, K.; Tanishiro, Y.; Takahashi, S.; Takahashi, M. Structure analysis of Si(111)-7 × 7 reconstructed surface by transmission electron diffraction. *Surf. Sci.* **1985**, *164*, 367−392.
(25) Cordero, B.; Gómez, V.; Platero-Prats, A. E.; Revés, M.; Echeverría, J.; Cremades, E.; Barragán, F.; Alvarez, S. Covalent radii revisited. *Dalton Trans.* **2008**, 2832−2838.
(26) Guest, M. F.; Hillier, I. H.; Saunders, V. R. Theoretical study of the bonding in P4 and N4. *J. Chem. Soc., Faraday Trans. 2* **1972**, *68*, 2070−2074.
(27) Baboul, A. G.; Schlegel, H. B. Structures and Energetics of Some Silicon−Phosphorus Compounds: SiHmPHn, SiHmPHnSiHo, and (SiH3)3P. An ab Initio Molecular Orbital Study. *J. Am. Chem. Soc.* **1996**, *118*, 8444−8451.
(28) Zachariah, M. R.; Melius, C. F. Theoretical calculation of thermochemistry for molecules in the Si-P-H system. *J. Phys. Chem. A* **1997**, *101*, 913−918.
(29) Zhang, C.; Chen, G.; Wang, K.; Yang, H.; Su, T.; Chan, C. T.; Loy, M. M. T.; Xiao, X. Experimental and theoretical investigation of single Cu, Ag, and Au atoms adsorbed on Si(111)-(7x7). *Phys. Rev. Lett.* **2005**, *94*, 176104.
(30) Binnig, G.; Rohrer, H. In touch with atoms. *Rev. Mod. Phys.* **1999**, *71*, S324−S330.
(31) Sloan, P. A.; Palmer, R. E. Tip-state control of rates and branching ratios in atomic manipulation. *Nano Lett.* **2005**, *5*, 835−839.
(32) Sloan, P. A.; Palmer, R. E. Two-electron dissociation of single molecules by atomic manipulation at room temperature. *Nature* **2005**, *434*, 367−371.
(33) Myslivecek, J.; Strozecka, A.; Steffl, J.; Sobotik, P.; Ost'adal, I.; Voigtlander, B. Structure of the adatom electron band of the Si(111)-7x7 surface. *Phys. Rev. B: Condens. Matter Mater. Phys.* **2006**, *73*, 161302.
(34) Ming, F.; Mulugeta, D.; Tu, W.; Smith, T. S.; Vilmercati, P.; Lee, G.; Huang, Y.-T.; Diehl, R. D.; Snijders, P. C.; Weitering, H. H. Hidden phase in a two-dimensional Sn layer stabilized by modulation hole doping. *Nat. Commun.* **2017**, *8*, 14721.
(35) Losio, R.; Altmann, K. N.; Himpsel, F. J. Fermi surface of Si(111)7×7. *Phys. Rev. B: Condens. Matter Mater. Phys.* **2000**, *61*, 10845−10853.
(36) Wyrick, J.; Wang, X.; Kashid, R. V.; Namboodiri, P.; Schmucker, S. W.; Hagmann, J. A.; Liu, K.; Stewart, M. D., Jr.; Richter, C. A.; Bryant, G. W.; Silver, R. M. Atom-by-Atom Fabrication of Single and Few Dopant Quantum Devices. *Adv. Funct. Mater.* **2019**, *29*, 1903475.
(37) Tettamanzi, G. C.; Hile, S. J.; House, M. G.; Fuechsle, M.; Rogge, S.; Simmons, M. Y. Probing the Quantum States of a Single Atom Transistor at Microwave Frequencies. *ACS Nano* **2017**, *11*, 2444−2451.
(38) Kresse, G.; Furthmüller, J. Efficient iterative schemes for ab initio total-energy calculations using a plane-wave basis set. *Phys. Rev. B: Condens. Matter Mater. Phys.* **1996**, *54*, 11169−11186.
(39) Kresse, G.; Furthmüller, J. Efficiency of ab-initio total energy calculations for metals and semiconductors using a plane-wave basis set. *Comput. Mater. Sci.* **1996**, *6*, 15−50.
(40) Klimes, J.; Bowler, D. R.; Michaelides, A. Van der Waals density functionals applied to solids. *Phys. Rev. B: Condens. Matter Mater. Phys.* **2011**, *83*, 195131.
(41) Grimme, S.; Antony, J.; Ehrlich, S.; Krieg, H. A consistent and accurate ab initio parametrization of density functional dispersion correction (DFT-D) for the 94 elements H-Pu. *J. Chem. Phys.* **2010**, *132*, 154104.
(42) Grimme, S.; Ehrlich, S.; Goerigk, L. Effect of the Damping Function in Dispersion Corrected Density Functional Theory. *J. Comput. Chem.* **2011**, *32*, 1456−1465.
(43) Blöchl, P. E. Projector augmented-wave method. *Phys. Rev. B: Condens. Matter Mater. Phys.* **1994**, *50*, 17953−17979.
(44) Perdew, J. P.; Burke, K.; Ernzerhof, M. Generalized gradient approximation made simple (vol 77, pg 3865, 1996). *Phys. Rev. Lett.* **1997**, *78*, 1396.
(45) Tersoff, J.; Hamann, D. R. Theory of the Scanning Tunneling Microscope. *Phys. Rev. B: Condens. Matter Mater. Phys.* **1985**, *31*, 805−813.
(46) Radilla, J.; Galván, M.; Trinidad-Reyes, Y.; Batina, N. STM Image Simulation: Effect of the Number of Tunneling States and the Isosurface Value. *MRS Proc.* **2011**, *838*, 1−6.
(47) Gustafsson, A.; Okabayashi, N.; Peronio, A.; Giessibl, F. J.; Paulsson, M. Analysis of STM images with pure and CO-functionalized tips: A first-principles and experimental study. *Phys. Rev. B* **2017**, *96*, 085415.

https://doi.org/10.1021/acsaelm.1c00266
ACS Appl. Electron. Mater. 2021, 3, 3338−3345

ACS APPLIED MATERIALS & INTERFACES

www.acsami.org

Research Article

Electrochemically Exfoliated Platinum Dichalcogenide Atomic Layers for High-Performance Air-Stable Infrared Photodetectors

Yaping Ma, Xiji Shao, Jing Li,* Bowei Dong, Zhenliang Hu, Qiulan Zhou, Haomin Xu, Xiaoxu Zhao, Hanyan Fang, Xinzhe Li, Zejun Li, Jing Wu, Meng Zhao, Stephen John Pennycook, Chorng Haur Sow, Chengkuo Lee, Yu Lin Zhong, Junpeng Lu, Mengning Ding, Kedong Wang,* Ying Li,* and Jiong Lu*

Cite This: *ACS Appl. Mater. Interfaces* 2021, 13, 8518–8527

Read Online

ACCESS | Metrics & More | Article Recommendations | Supporting Information

ABSTRACT: Platinum dichalcogenide (PtX_2), an emergent group-10 transition metal dichalcogenide (TMD) has shown great potential in infrared photonic and optoelectronic applications due to its layer-dependent electronic structure with potentially suitable bandgap. However, a scalable synthesis of $PtSe_2$ and $PtTe_2$ atomic layers with controlled thickness still represents a major challenge in this field because of the strong interlayer interactions. Herein, we develop a facile cathodic exfoliation approach for the synthesis of solution-processable high-quality $PtSe_2$ and $PtTe_2$ atomic layers for high-performance infrared (IR) photodetection. As-exfoliated $PtSe_2$ and $PtTe_2$ bilayer exhibit an excellent photoresponsivity of 72 and 1620 mA W^{-1} at zero gate voltage under a 1540 nm laser illumination, respectively, approximately several orders of magnitude higher than that of the majority of IR photodetectors based on graphene, TMDs, and black phosphorus. In addition, our $PtSe_2$ and $PtTe_2$ bilayer device also shows a decent specific detectivity of beyond 10^9 Jones with remarkable air-stability (>several months), outperforming the mechanically exfoliated counterparts under the laser illumination with a similar wavelength. Moreover, a high yield of $PtSe_2$ and $PtTe_2$ atomic layers dispersed in solution also allows for a facile fabrication of air-stable wafer-scale IR photodetector. This work demonstrates a new route for the synthesis of solution-processable layered materials with the narrow bandgap for the infrared optoelectronic applications.

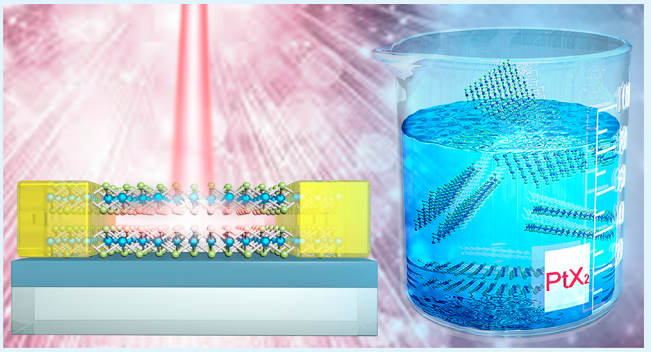

KEYWORDS: *IR photodetectors, electrochemical exfoliation, bilayer $PtSe_2$, bilayer $PtTe_2$, air-stable*

INTRODUCTION

Two-dimensional (2D) layered semiconductors have demonstrated great potential in future photonic and optoelectronic applications due to their flexible atomically thin structures and outstanding layer-dependent electronic and optical properties.[1−6] In particular, infrared (IR) photodetectors have been widely used in remote sensing, optical communications, and IR imaging.[7] Therefore, tremendous efforts have been devoted to search for promising 2D candidates for IR photodetection with high photoresponsivity and specific detectivity including graphene,[8−12] TMD,[13−16] and black phosphorus (BP).[17−20] For example, it has been reported that graphene exhibits an ultrawide band detection because of its semimetallic nature. Unfortunately, the photodetection performance of graphene is limited largely by its low absorption coefficient and short lifetime of the photogenerated carriers.[11,21,22] Alternatively, engineering graphene-based heterostructures has been exploited to further enhance the performance of graphene-based photodetection.[23] In contrast, semiconducting TMDs with sizable bandgaps and strong absorption at specific wavelengths are considered as appealing alternatives beyond graphene for photodetection. To date, most reports focus on the exploration of group-6 TMDs with bandgaps ranging between 1 and 2.5 eV, and thus their optoelectronic devices mainly work in the visible light regime.[24−26] In addition to TMDs, BP with a high carrier mobility demonstrates layer-dependent direct bandgaps ranging from the visible to infrared regime, which has sparked enormous research interest in the photodetection in near and mid-IR range. However, the extreme air-sensitivity of BP poses a formidable challenge for its practical application under ambient conditions.[19,20] Therefore, the development of new approaches for the synthesis of air-stable 2D semiconductors with suitable narrow bandgap for the infrared optoelectronic and photonic applications is highly desired.

Received: November 17, 2020
Accepted: February 2, 2021
Published: February 11, 2021

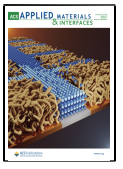

https://dx.doi.org/10.1021/acsami.0c20535
ACS Appl. Mater. Interfaces 2021, 13, 8518–8527

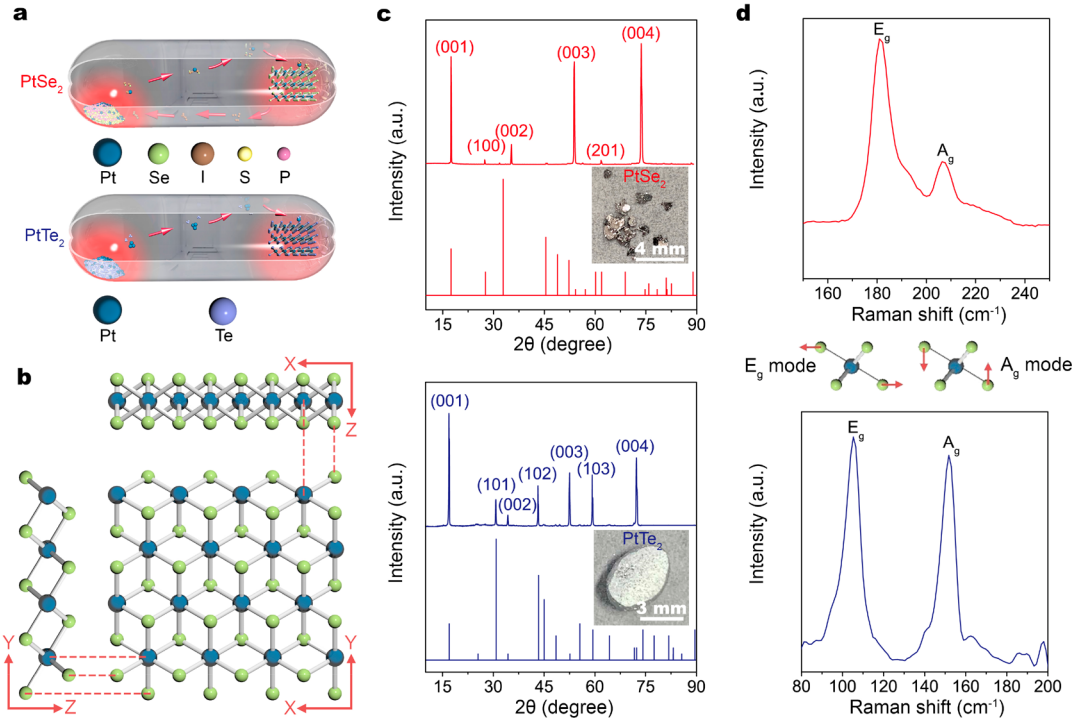

Figure 1. Synthesis of $PtSe_2/PtTe_2$ crystals through CVT method. (a) Schematic diagram of the experimental setup for the growth of $PtSe_2/PtTe_2$ crystals. (b) Top and side view of the crystal structure of 1T-$PtSe_2/PtTe_2$ (Blue: Pt, Green: Se/Te). (c) X-ray diffraction spectra of 1T-$PtSe_2/PtTe_2$ crystals (up) compared with the 1T-$PtSe_2/PtTe_2$ standard card of PDF#18−0970/PDF#18−0977 (bottom). Inset: the photograph of the synthesized $PtSe_2/PtTe_2$ crystals. (d) Raman spectra of $PtSe_2$ and $PtTe_2$ crystals.

Platinum dichalcogenide (PtX_2), a group-10 noble TMD, has been recently recognized as a remarkable candidate for the infrared photonic and optoelectronic applications owing to its environmental stability and unique layer-dependent electronic and optical properties.[27−33] Monolayer and bilayer $PtSe_2$ are predicted to have an indirect bandgap of ∼1.2 and ∼0.2 eV, respectively, while trilayer $PtSe_2$ and beyond have a zero-bandgap.[28,34] Similarly, monolayer $PtTe_2$ is predicted to possess an indirect bandgap of ∼0.4 eV, while bilayer $PtTe_2$ and beyond have a zero bandgap.[34] Recently, mechanically exfoliated bilayer $PtSe_2$ has been demonstrated as a photoactive material with a strong light absorption from visible to mid-IR range.[27] Interestingly, negative photoconduction is observed in ultrathin $PtSe_2$ film due to a photogating effect at Si/SiO_2 interface.[35] To further propel their practical application, a facile and scalable synthesis of 2D PtX_2 atomic flakes with controlled thickness is highly demanded. The current synthetic strategy mainly relies on chemical vapor deposition (CVD), or sonication-assisted liquid phase exfoliation (LPE) by probe sonication.[36−39] The mechanical exfoliation and chemical vapor deposition methods often yield multilayer structures, owing to their relatively larger interlayer binding energies as compared to other common TMD materials.[36,40−42] Sonication-assisted liquid phase exfoliation can produce few-layer PtX_2 flakes with small domain sizes that typically limit the performance of as-fabricated devices.[39] By contrast, a facile electrochemical exfoliation approach offers a rapid production of solution-processable few-layer 2D materials with micron lateral size at a large quantity and low cost.[17,43−46]

To this end, we report a facile electrochemical exfoliation approach for a rapid production of solution-processable high quality atomically thin $PtSe_2$ and $PtTe_2$ flakes. Bulky organic tetraalkylammonium (TAA) cations are used as the intercalant for the mild cathodic exfoliation of bulk $PtSe_2$ and $PtTe_2$ crystals to avoid the sample oxidation which would occur during the anodic exfoliation of 2D materials.[17,47,48] Under the optimized condition, bilayer $PtSe_2$ flakes can be readily exfoliated from bulk crystals with a yield of ∼44%. Furthermore, the photoresponse analysis based on as-exfoliated $PtSe_2$ and $PtTe_2$ bilayer flakes reveals outstanding performance with a high photoresponsivity of 72 mA W^{-1} and 1.62 A W^{-1} and decent specific detectivity of 1.44×10^9 and 2.11×10^9 Jones at zero gate voltage under the laser illumination of 1540 nm with a power density of 15.9 mW cm^{-2} and 0.16 W cm^{-2}, respectively.

RESULTS AND DISCUSSION

The Growth and Characterization of Bulk $PtSe_2$ and $PtTe_2$ Crystals. Figure 1a illustrates the growth process of the crystals in a quartz tube based on the chemical vapor transport (CVT) method (see details in the Experimental Section).[27,28,49] Representative PtX_2 single crystals with a lateral dimension of several mm are shown in the inset of Figure 1c. 1T-PtX_2 crystal possesses a typical hexagonal atomic structure under $P\bar{3}m1$ space group (Figure 1b).[27,30,50] X-ray diffraction (XRD) measurement of as-grown samples further confirms the crystal structure of $PtSe_2$ and $PtTe_2$ crystals (Figure 1c), consistent with the previous reports.[27,51] In addition, the presence of sharp peaks (001) indicates a good crystal quality of bulk $PtSe_2$ and $PtTe_2$ crystals. Raman spectrum acquired from the as-grown $PtSe_2$ ($PtTe_2$) crystals (Figure 1d) reveal two dominating features around 180 and 206.4 cm^{-1} (105.2 and 151.8 cm^{-1}), attributed to the E_g and the A_g modes corresponding to in-plane and out-of-plane phonon modes, respectively.[28,30,52,53] Therefore, both XRD data and Raman

https://dx.doi.org/10.1021/acsami.0c20535
ACS Appl. Mater. Interfaces 2021, 13, 8518−8527

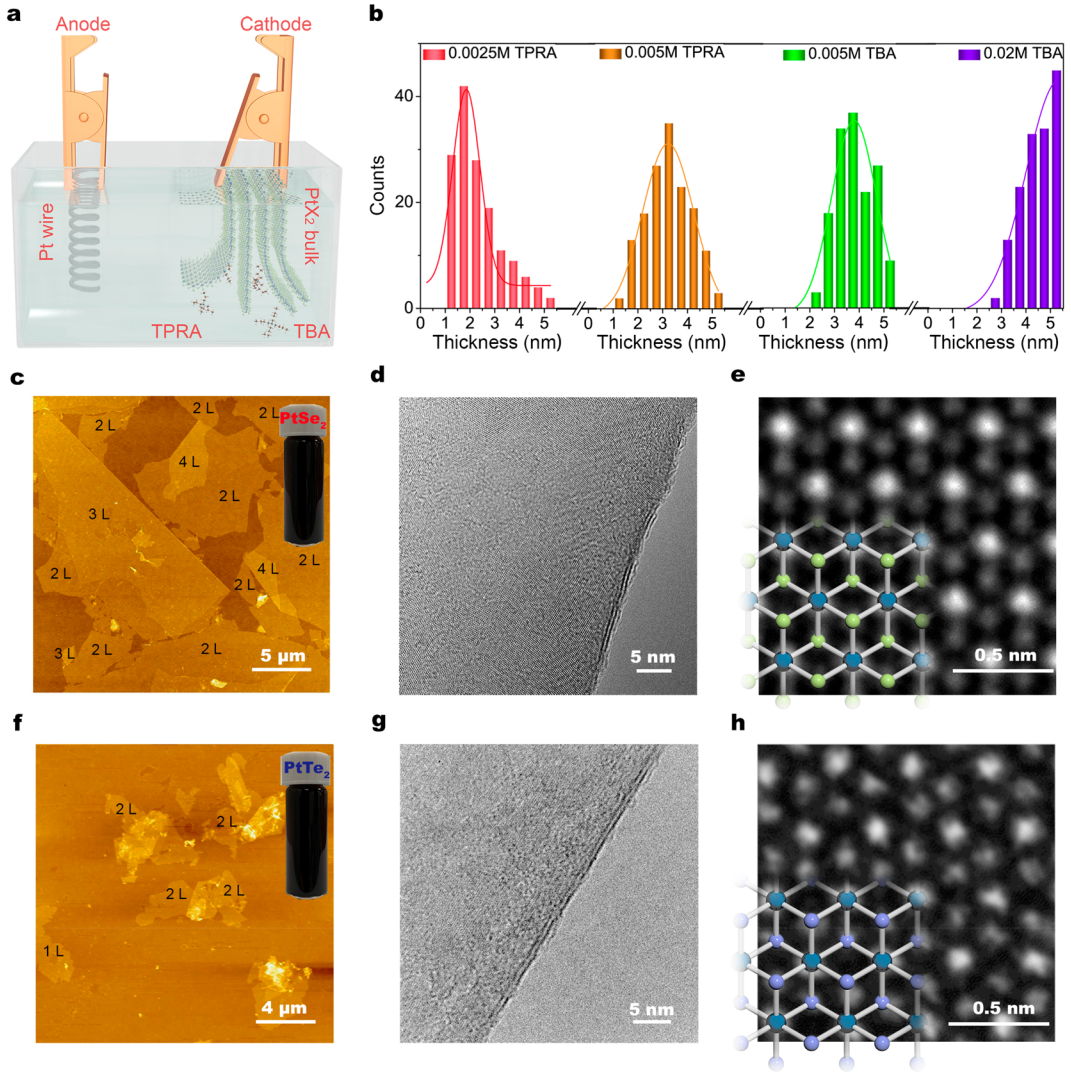

Figure 2. Characterization of the electrochemically exfoliated $PtSe_2/PtTe_2$ flakes. (a) Experimental setup for electrochemical exfoliation. (b) Statistics of the thickness of the $PtSe_2$ flakes exfoliated in DMSO solution under different conditions. (c,d) AFM image of the $PtSe_2$ (c) and $PtTe_2$ (f) flakes on SiO_2/Si substrate. The inset: photograph of the solution dispersion of exfoliated flakes. (d,e,g,h) TEM (d,g) and atomic resolution STEM-ADF (e,h) images of exfoliated $PtSe_2$ (d,e) and $PtTe_2$ (g,h).

spectrum demonstrate a good crystal quality of bulk $PtSe_2$ and $PtTe_2$.

The Electrochemical Exfoliation of $PtSe_2$ and $PtTe_2$ Bulk Crystals into Atomically Thin Flakes. Figure 2a illustrates the electrochemical exfoliation setup consisting of bulk $PtSe_2$ and $PtTe_2$ (cathode), Pt wire (anode), and organic TAA cations dissolved in dimethyl sulfoxide (DMSO) solvent (electrolyte).[17,54] It is noted that the thickness distribution of exfoliated $PtSe_2$ flakes can be controlled by tuning the length of alkyl chain of the TAA salts and their concentration as well as the solvent and cathodic voltage applied (Figure 2b). An optimal yield of bilayer $PtSe_2$ (~44%) can be achieved in electrolyte consisting of a 0.0025 M tetrapropylammonium (TPRA) in DMSO at the cathodic voltage of 6 V (refer to details in the Supporting Information (SI) Section 1 and Figure S2).[17] The thickness of the majority of as-exfoliated $PtSe_2/PtTe_2$ flakes is determined to be 1.2−1.5 nm by AFM imaging (Figure 2c,f and SI Figure S3), corresponding to the expected thickness of a bilayer $PtSe_2/PtTe_2$.[27] Raman spectra of different $PtSe_2$ and $PtTe_2$ flakes (SI Figure S4) reveal that E_g mode shows a blue shift when the flake becomes thinner.[39,50,52,53,55,56] The feature at ~230 cm^{-1} for bilayer-$PtSe_2$ flake is attributed to longitudinal optical (LO) modes.[52] The images of aberration-corrected scanning transmission electron microscopy−annular dark field (STEM-ADF) reveal a nearly perfect atomic crystal structure with each Pt atom (bright spot) surrounded by six dimmer Se/Te atoms, in agreement with the octahedral structure with the lattice constant of ~3.8 Å and ~4.0 Å expected for 1T-phase $PtSe_2$ and $PtTe_2$, respectively (Figure 2d,e,g,h).[27,51]

The Device Performance of a Bilayer $PtSe_2/PtTe_2$-Based Photodetector. As shown in Figure 3a−c, first-principles calculations predict the layer-dependent electronic structures of $PtSe_2$. Bilayer $PtSe_2$ possesses an indirect bandgap of ~0.23 eV, suitable for the infrared optoelectronics, in contrast to monolayer (an indirect bandgap of ~1.18 eV) and trilayer or above (semimetal).[34,57] We then fabricated a bilayer $PtSe_2$-based device to probe its photodetection performance in the IR regime (Figure 3g). The device adopts a typical field effect transistor configuration (Figure 3h) consisting of a heavily doped Si substrate as the back-gate and the Cr/Au (5 nm/60 nm) electrodes deposited by the electron-beam

https://dx.doi.org/10.1021/acsami.0c20535
ACS Appl. Mater. Interfaces 2021, 13, 8518−8527

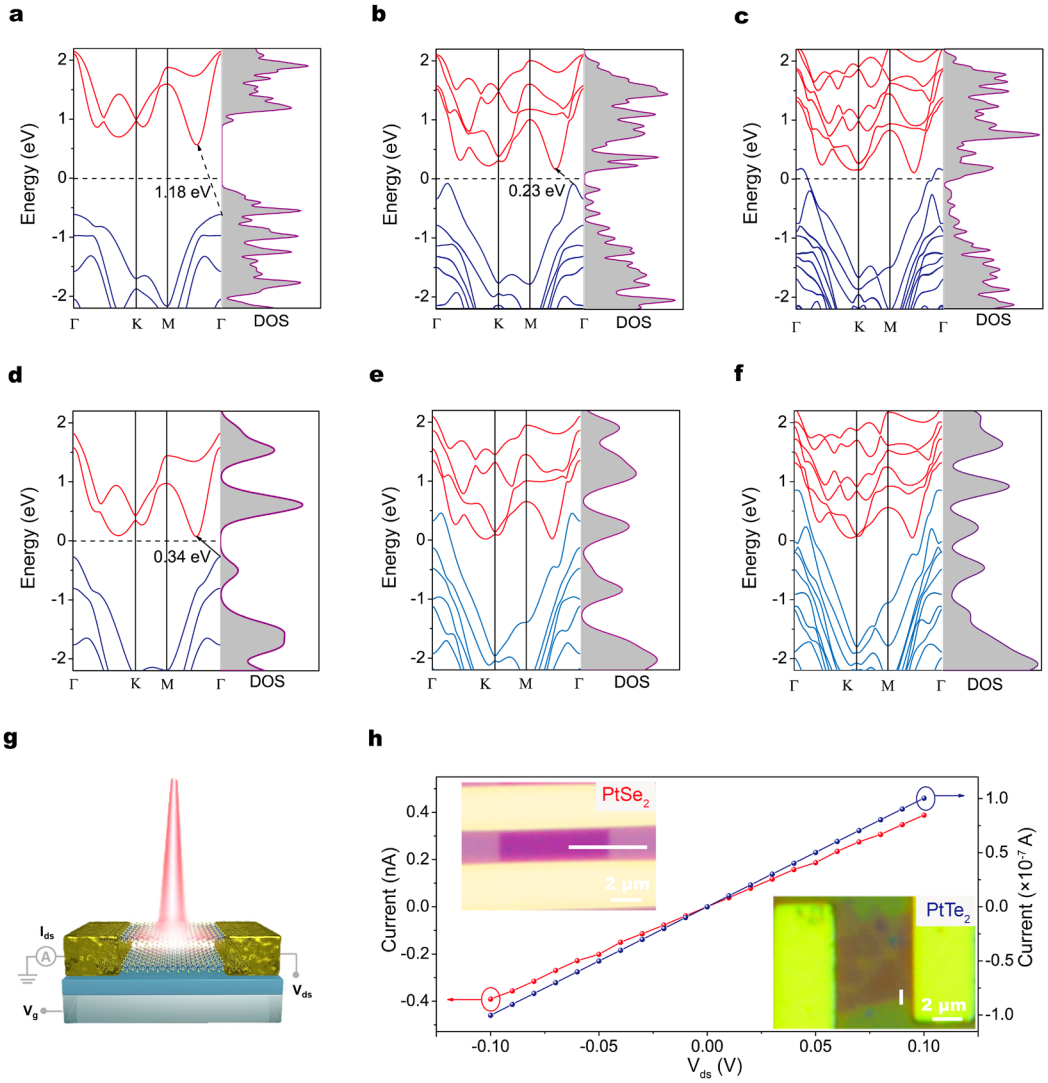

Figure 3. Theoretical calculations of band structure and density-of-states (DOS) of layered $PtSe_2$ and $PtTe_2$ and $I_{ds}-V_{ds}$ characteristics of bilayer-$PtSe_2$/$PtTe_2$ phototransistor devices. (a,b) Calculated band structure and DOS of (a) monolayer, (b) bilayer, and (c) trilayer $PtSe_2$ by first-principles calculations. (d–f) Calculated band structure and DOS of (d) monolayer, (e) bilayer, and (f) trilayer $PtTe_2$ by first-principles calculations. (g) Schematic diagram of the cross-section structure of the bilayer-$PtSe_2$/$PtTe_2$ device. (h) $I_{ds}-V_{ds}$ characteristics of the bilayer-$PtSe_2$/$PtTe_2$ FET under zero gate voltage and V_{ds} in the range of −0.1–0.1 V. Inset: Optical microscope images of the bilayer-$PtSe_2$/$PtTe_2$ devices.

evaporation. As depicted in Figure 3h, a linear $I_{ds}-V_{ds}$ curve measured in a small voltage range ($-0.1 < V_{ds} < 0.1$ V) implies an ohmic contact between bilayer $PtSe_2$ and metal electrodes. Furthermore, the contact resistance between the metal electrodes and the flake is determined to be $(5.8 \pm 0.5) \times 10^{-3}$ Ω cm^2 (SI Figure S5) according to the transmission line method (TLM).[58] The ohmic contact between the metal electrodes and the bilayer flake is beneficial for a high photodetection performance of bilayer $PtSe_2$-based device.[59]

Subsequently, the photodetection performance of a bilayer $PtSe_2$-based FET is investigated in the infrared region. First, the power density of a 1064 nm laser is modulated to record the photocurrent at V_{ds} = 0.5 V for the time-resolved photoresponse measurements as shown in Figure 4a (noted that $I_{ds}-V_{ds}$ characteristics are shown in SI Figure S6a). It is observed that the generated photocurrent (defined as $I_{ph} = I_{illum}-I_{dark}$) increases from ∼125 to ∼555 pA when the laser power density increases from 0.39 to 2.66 W cm^{-2} (Figure 4d and SI Figure S6a), which obeys a power law relationship($I_{ph} \propto P^{\alpha}$, where P is the incident power density).[14,27,60] The deviation from a linear relationship is possibly ascribed to the photogating dominated gain mechanism involving the generation, interaction, trapping and recombination of photocarriers.[10,24,61] Here, the power exponent α of the $PtSe_2$-based photodetector is extracted to be 0.781, consistent with the fact that low-dimensional materials-based photodetectors usually exhibit a power exponent α ranging from 0 to 1.[8,9,60]

The photoresponsivity and detectivity are considered as two important parameters for photodetectors.[14,27,60,62,63] The photoresponsivity and the detectivity can be defined using the following equations:[14,62,63]

$$R = \frac{I_{ph}}{P_{in}} \tag{1}$$

$$D^* = \frac{\sqrt{A}R}{\sqrt{2eI_d}} \tag{2}$$

where I_{ph}, P_{in}, A, e, I_d denote the photocurrent, the incident laser power, the effective device area, the electronic charge and

https://dx.doi.org/10.1021/acsami.0c20535
ACS Appl. Mater. Interfaces 2021, 13, 8518–8527

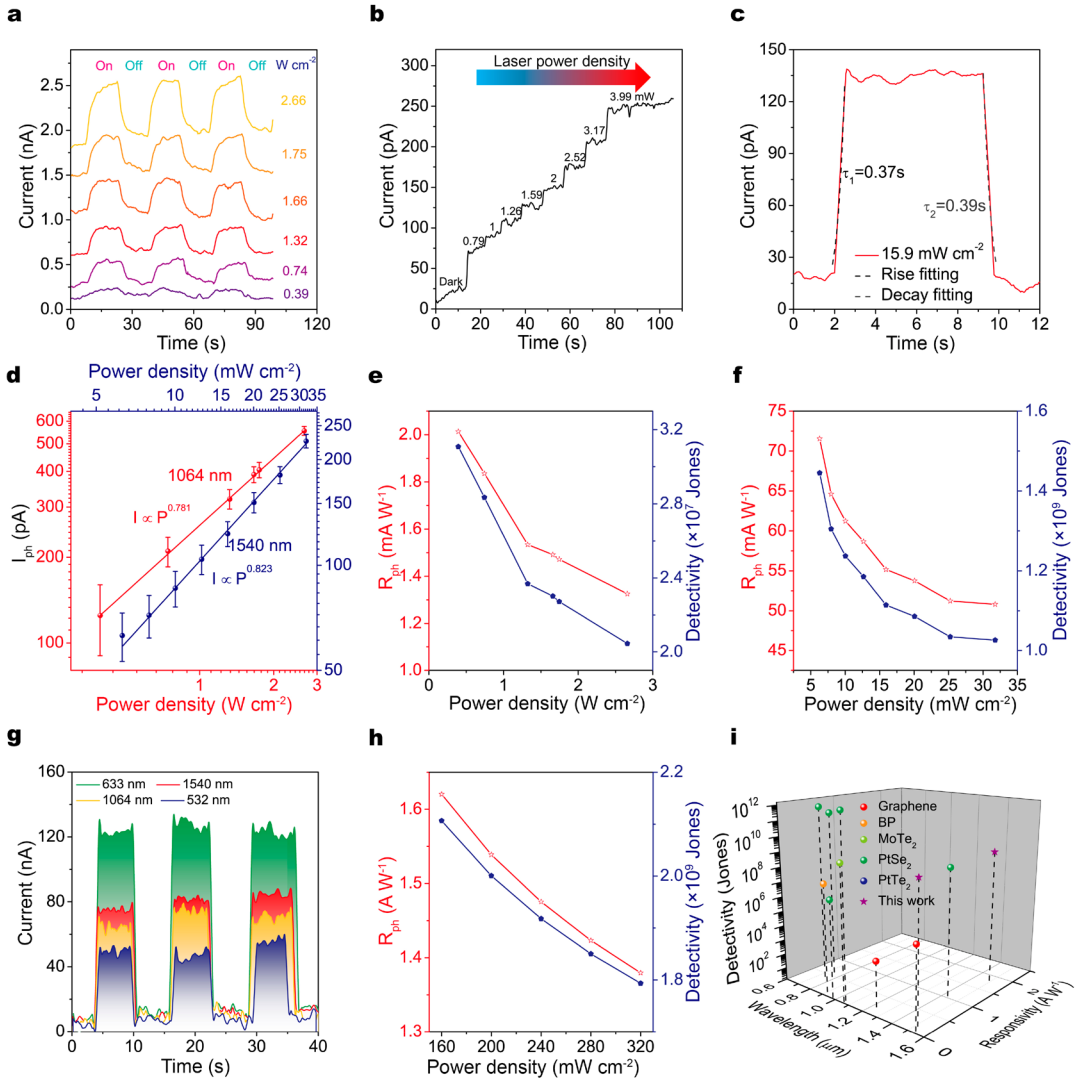

Figure 4. Optoelectronic properties of the bilayer-$PtSe_2$ and bilayer-$PtTe_2$ devices in the infrared region. (a,b) Time-resolved photocurrent of bilayer-$PtSe_2$ device for a bias voltage of 0.5 V and zero gate voltage excited by 1064 and 1540 nm laser illumination with different laser power density, respectively. (c) The rise and decay time of the photocurrent of bilayer-$PtSe_2$ device under the laser illumination with the wavelength of 1540 nm determined by fitting. (d) Power dependence of the photocurrent of the bilayer-$PtSe_2$ device recorded at V_{ds} = 0.5 V under 1064 and 1540 nm laser illumination. (e,f) Power dependence of the photoresponsivity and detectivity of the $PtSe_2$ device under 1064 and 1540 nm laser illumination, respectively. (g) Time-resolved photocurrent of bilayer-$PtTe_2$ device for a bias voltage of 0.5 V and zero gate voltage excited by 532 nm, 633 nm, 1064 nm, and 1540 nm laser illumination with a power density of 0.16 W cm^{-2}. (h) Power dependence of the photoresponsivity and detectivity of the $PtTe_2$ device under 1540 nm laser illumination. (i) Comparison with the reported infrared photodetector based on 2D materials.

the dark current, respectively. The laser power density dependent measurement reveals that both R and D^* decrease as the power density of incident laser increases (Figure 4e). The maximum of the photoresponsivity reaches 2 mA W^{-1} with a power density of 0.39 W cm^{-2}, much lower than other reported TMD-based photodetectors.[10,15,19] This is presumably due to a low light absorption coefficient at 1064 nm for the electrochemically exfoliated bilayer $PtSe_2$. The absorption measurement indeed reveals that the exfoliated $PtSe_2$ flakes exhibit a local absorption maximum between 1400 and 1600 nm (SI Figure S7 and S8), which suggests an increase of bandgap of the majority of bilayer flakes in the solution, presumably due to the presence of residual intercalated species in the interlayer space, consistent with the AFM height profile measured over bilayer flakes (SI Figure S9a). We then investigated the photodetection performance of the same device under the same laser power density (15.9 mW cm^{-2}) at the wavelength of 1540 nm, which reveals a dramatically enhanced photocurrent up to ~123 pA. Furthermore, the rise and decay time could be determined by fitting curves with the following equations:[64]

$$I_{rise} = I_0 + A_1 \exp\left(\frac{t - t_1}{\tau_1}\right) \quad (3)$$

$$I_{decay} = I_0 + A_2 \exp\left(-\frac{t - t_2}{\tau_2}\right) \quad (4)$$

where τ is the rise/decay time constant and t_1 or t_2 is the time of laser switching-on or switching-off, respectively. Here, τ_1 and τ_2 are determined to be ~0.37 s for rise time and ~0.39 s for decay time respectively (Figure 4c), superior to that at the wavelength of 1064 nm. In addition, the time period of the current range from 10% to 90% in rising and decaying is

https://dx.doi.org/10.1021/acsami.0c20535
ACS Appl. Mater. Interfaces 2021, 13, 8518−8527

determined to be ~0.38 s, consistent with the above fitted results (SI Figures S10 and S17 in Section 2). Figure 4d shows an apparent rise of the photocurrent against the laser power density. A standard fitting (based on $(I_{ph} \propto P^{\alpha})$ gives rise to a power exponent α of 0.823. This is probably due to the fact that high energy defect states cannot trap the photogenerated carriers at 1540 nm, leading to an enhanced photocurrent.[24,60] As depicted in Figure 4f, an increase of the incident laser power density reduces the photoresponsivity and detectivity, consistent with the previous report on other 2D materials based photodetectors.[29,60] The presence of trap states results in a higher carrier recombination rate under a larger laser power density, leading to a shorter average carrier lifetime and thus a lower photogain and photoresponsivity.[14,60] Moreover, the $PtSe_2$ device exhibits a high photoresponsivity of 72 mA W^{-1} under the laser power density of 6.29 mW cm^{-2} at 1540 nm, nearly 2 orders of magnitude higher than that at 1064 nm. Furthermore, as-fabricated $PtSe_2$ bilayer device shows a negligible decrease in the photocurrent after its storage in air for 3 months, suggesting a good stability (SI Figure S11). In addition, the structural anisotropy in $PtSe_2$ monolayer endows its properties with a polarization sensitive photodetection.[13,65] Indeed, the photocurrent varies with the change of polarization angle and reaches the maximum and minimum value at 0° and 90°, respectively (SI Figure S12). The linear dichroism properties of $PtSe_2$ will expand its potential application for future photonic and optoelectronic devices.

Apart from $PtSe_2$, monolayer $PtTe_2$ also possesses an indirect bandgap of ~0.34 eV, in contrast to bilayer and trilayer $PtTe_2$(zero bandgap). This suggests that $PtTe_2$ atomic layers may serve as another promising candidate for IR photodetection (Figure 3d–f and SI Figure S13).[66] Figure 3h shows a linear $I_{ds}-V_{ds}$ curve measured in a small voltage range $(-0.1<V_{ds} < 0.1\ V)$, implying an ohmic contact between bilayer $PtTe_2$ and metal electrodes in the bilayer-$PtTe_2$ device. Figure 4g shows that the bilayer-$PtTe_2$ photodetector demonstrates excellent photodetection performance in visible and infrared regime (SI Table S1). In detail, the bilayer-$PtTe_2$ device exhibits an excellent photoresponsivity of 1.62 A W^{-1} and the detectivity of 2.11×10^9 Jones under the laser power density of 0.16 W cm^{-2} at 1540 nm with excellent stability (Figure 4h and SI Figures S14 and S15). The photoresponsivity of bilayer-$PtTe_2$ device at 1540 nm is about 1 order of magnitude higher than that of bilayer-$PtSe_2$ device, while the detectivity of both devices lies in the same order of magnitude. The photoresponsivity and specific detectivity of the $PtSe_2$ and $PtTe_2$ devices in the IR regime is also superior or comparable to that of similar photodetectors made by graphene,[11,12] BP,[20] and TMD materials,[16,28,29,32,66,67] as shown in Figure 4i and SI Table S2. The photodetection performance of PtX_2-based photodetectors (e.g., rise/decay time and photoresponsivity) is comparable to that of the conventional IR photodetectors of PbS quantum dots (QDs).[68,69]

To further bridge the gap between the lab demonstration and practical applications, we utilize the high-solution processability of the exfoliated flakes to fabricate the large-scale and air-stable photodetectors on the quartz substrates. As shown in SI Figure S16a, the $PtSe_2$, and $PtTe_2$ thin film is deposited onto the substrate via drop-cast techniques. The time-resolved photoresponse measurement of the large-scale device (SI Figure S16) reveals that the photocurrent also increases, while the rise and decay time of the photoresponse decrease with an increase of the incident laser power. Furthermore, the large-scale photodetector shows a remarkable air-stability (>several months tested). However, the rise and decay time are much longer than that of the photodetector based on a single flake, which is presumably due to the weak penetrability of the infrared photons that influence the laser absorption of the underlying flakes.

CONCLUSIONS

In summary, a facile and general electrochemical approach is developed to exfoliate the $PtSe_2$ and $PtTe_2$ bulk crystals into high-quality atomically thin $PtSe_2$ and $PtTe_2$ flakes with a high bilayer yield under the optimized conditions. Furthermore, as-exfoliated bilayer $PtSe_2$ flake delivers an excellent photodetection performance with a high photoresponsivity of 0.072 A W^{-1} and the detectivity of 1.44×10^9 Jones at 1540 nm with a laser power density of 15.9 mW cm^{-2}, which can maintain its device performance more than 3 months. As-exfoliated $PtTe_2$ bilayer exhibits an excellent photoresponsivity of 1.62 A W^{-1} and the detectivity of 2.11×10^9 Jones at 1540 nm with a laser power density of 0.16 W cm^{-2}, about 4 orders of magnitude higher than the photoresponsivity of graphene-based device. In addition, the high solution-processability of exfoliated flakes allows for the fabrication of the large-scale $PtSe_2$ and $PtTe_2$ thin film devices with a high stability and a good photodetection performance. Therefore, this work offers a promising route for the scalable synthesis of air-stable PtX_2 atomic layers with controlled thickness for the superior photodetection performance in the IR regime under ambient conditions.

EXPERIMENTAL SECTION

Synthesis of $PtSe_2$ and $PtTe_2$ Crystals. The experimental set up shown in Figure 1a was used to grown bulk $PtSe_2$ though CVT method.[27,28,49] A mixture of Pt, Se, P, and S powders (the total weight of 350 mg) with a molar ratio of 1:2:1:3 plus iodine (17 mg, act as the transport gas) were sealed in a vacuum (10^{-6} Torr) quartz tube, which was placed into a muffle furnace subsequently. The temperature of the muffle furnace was fist kept at 900 °C for 40 h and then at 700 °C for 5 days. $PtSe_2$ bulk crystals are obtained after cooling to the room temperature. Bulk $PtTe_2$ crystal was also grown through CVT method. A mixture of Pt and Te powders with a molar ratio of 1:2.03 (the total weight is 301 mg) were sealed in quartz tube under the vacuum and put into the furnace. The temperature of the furnace was gradually increased to 1000 °C at the speed of 1 °C min^{-1} and kept at 1000 °C for 2 days, followed by a slow increase to 1150 °C (Kept for 60 min) at the speed of 1 °C min^{-1}. Finally, the furnace was cooled down to the room temperature at the speed of 1 °C min^{-1}.

Device Fabrication. Bulk $PtSe_2/PtTe_2$ crystals with typical dimensions of 2 × 2 × 1 mm^3 (length × width × thickness) were fixed on a Pt clip for a cathodic exfoliation at −6 V (vs Pt counter electrode) for 20 min (SI Figure S1). The bilayer yield was determined via AFM statistics. The bilayer yield was determined via the statistical analysis of the AFM height of as-exfoliated flakes. Specifically, exfoliated $PtSe_2/PtTe_2$ flakes in electrolyte were subjected to centrifugation at 3000 rpm (503.6 g) to separate them from unexfoliated bulks. The upper dispersion was dropped onto the SiO_2/Si substrates. We then measured the thickness of more than 150 individual flakes on the SiO_2/Si substrates by AFM imaging (SI Figure S2). The yield of bilayer flakes refers to the percentage of bilayer among all the flakes measured.[17] $PtSe_2/PtTe_2$ bilayer device: as-exfoliated $PtSe_2/PtTe_2$ flakes were first deposited onto the SiO_2/Si substrate via drop-casting and then were placed in DMSO to remove residual TAA salts and subsequently were dried in a vacuum tube. The target flakes were identified by the optical microscopy (Olympus BX51 microscope) and AFM (Park XE-100 system) imaging for device fabrications. After conducting the standard photolithography

https://dx.doi.org/10.1021/acsami.0c20535
ACS Appl. Mater. Interfaces 2021, 13, 8518−8527

procedures, we deposited Cr/Au (5 nm/60 nm) metal electrodes by the electron-beam evaporation method. Large-scale device fabrication: the exfoliated $PtSe_2/PtTe_2$ solution was subjected to centrifugation for 5 min at 3000 rpm (503.6 g) to remove thick unexfoliated flakes. The following two steps were repeated three times to remove the residual TAA salts in the exfoliated solution: (1) The solution was first centrifuged for 15 min at 12 000 rpm (8.057k g); (2) Remove the supernatant in the centrifuge tube and then shake the tube several times after adding the pure DMSO solvent. After the removal of the solvent via centrifugation, the concentrated $PtSe_2/PtTe_2$ inks can be obtained for large-scale device fabrication. Finally, Au (60 nm) electrodes were deposited by e-beam evaporation after placing a mask onto the $PtSe_2/PtTe_2$ flakes deposited on the quartz substrates.

Characterization. Optical images of the exfoliated $PtSe_2/PtTe_2$ flakes on the substrate were obtained via an Olympus BX51 microscope. XRD measurements of the grown bulk crystals were conducted by a Bruker X-ray diffractometer system. AFM (Park XE-100 system) was used to characterize the surface morphology and thickness of the $PtSe_2/PtTe_2$ flakes. An aberration-corrected ARM200F, equipped with a cold field-emission gun and an ASCOR corrector operating at 80 kV was utilized to obtain atomic-resolution STEM-ADF images. In addition, Raman spectra of the bulk crystals and exfoliated $PtSe_2/PtTe_2$ flakes were measured with a 532 nm laser excitation with the power of ~1 mW, 100× objective lens and a dispersive grating with 2400 l/mm at room temperature (WITec Alpha 300R Raman system). The absorption data of the exfoliated $PtSe_2$ flakes were collected using a UV−visible spectrophotometer. The photoresponse measurements of the $PtSe_2/PtTe_2$-based photodetector devices were conducted in the atmosphere with the illumination of different laser sources (a spot radius of 2 mm). The bias voltage across the channel and the drain-source current data were applied and collected respectively in a Keithley 4200 source meter system.

■ ASSOCIATED CONTENT

Supporting Information

The Supporting Information is available free of charge at https://pubs.acs.org/doi/10.1021/acsami.0c20535.

Additional information includes methods; electrochemical exfoliation current as the function of the applied electrochemical voltage; statistics histograms of the thickness of as-exfoliated $PtSe_2$ flakes; AFM image and line profiles of the $PtSe_2$ flakes on SiO_2/Si substrate; Raman spectra of few-layer and bulk $PtSe_2$ and $PtTe_2$, $I_{ds}-V_{ds}$ characteristics of the $PtSe_2$-based device, absorption spectrum of the $PtSe_2$ flakes from UV−visible spectrophotometer, photocurrent, and absorption results under laser illumination with different wavelength ranging from 1500 to 1600 nm; line profiles of $PtSe_2$ and $PtTe_2$ flakes; stability of bilayer-$PtSe_2$ device in atmospheric condition; linear polarization angle dependent photocurrent, UV−vis spectrum of as-exfoliated $PtTe_2$ flakes dispersed in DMSO; $I_{ds}-V_{ds}$ curves of the bilayer-$PtTe_2$ device; stability of bilayer-$PtTe_2$ device in atmospheric condition, photodetection performance of large-scale $PtSe_2$ and $PtTe_2$ devices, optoelectronic performance of $PtTe_2$-based device; optoelectronic performance of $PtTe_2$-based photodetector under the laser of various wavelength; a list of 2D materials based infrared photodetectors (PDF)

■ AUTHOR INFORMATION

Corresponding Authors

Jiong Lu − *Department of Chemistry and Centre for Advanced 2D Materials and Graphene Research Centre, National University of Singapore, Singapore 117543, Singapore*; orcid.org/0000-0002-3690-8235; Email: chmluj@nus.edu.sg

Ying Li − *SZU-NUS Collaborative Innovation Center for Optoelectronic Science & Technology, International Collaborative Laboratory of 2D Materials for Optoelectronics Science and Technology of Ministry of Education, College of Optoelectronic Engineering, Shenzhen University, Shenzhen 518060, China*; Email: queenly@szu.edu.cn

Jing Li − *Department of Chemistry and Centre for Advanced 2D Materials and Graphene Research Centre, National University of Singapore, Singapore 117543, Singapore*; orcid.org/0000-0002-5627-4153; Email: c2dlij@nus.edu.sg

Kedong Wang − *Department of Physics, Southern University of Science and Technology, Shenzhen 518055, China*; orcid.org/0000-0003-1253-5603; Email: wangkd@sustech.edu.cn

Authors

Yaping Ma − *SZU-NUS Collaborative Innovation Center for Optoelectronic Science & Technology, International Collaborative Laboratory of 2D Materials for Optoelectronics Science and Technology of Ministry of Education, College of Optoelectronic Engineering, Shenzhen University, Shenzhen 518060, China; Department of Chemistry, National University of Singapore, Singapore 117543, Singapore*; orcid.org/0000-0003-3907-6881

Xiji Shao − *Department of Physics, Southern University of Science and Technology, Shenzhen 518055, China*

Bowei Dong − *Department of Electrical and Computer Engineering, National University of Singapore, Singapore 117576, Singapore*

Zhenliang Hu − *Department of Physics, National University of Singapore, Singapore 117551, Singapore*

Qiulan Zhou − *Key Laboratory of Mesoscopic Chemistry, School of Chemistry and Chemical Engineering, Nanjing University, Nanjing 210023, China*

Haomin Xu − *Department of Chemistry, National University of Singapore, Singapore 117543, Singapore*; orcid.org/0000-0003-3704-1810

Xiaoxu Zhao − *Department of Materials Science and Engineering, National University of Singapore, Singapore 117575, Singapore*

Hanyan Fang − *Department of Chemistry, National University of Singapore, Singapore 117543, Singapore*

Xinzhe Li − *Department of Chemistry, National University of Singapore, Singapore 117543, Singapore*; orcid.org/0000-0001-6636-0496

Zejun Li − *Department of Chemistry, National University of Singapore, Singapore 117543, Singapore*; orcid.org/0000-0002-7582-0674

Jing Wu − *Centre for Advanced 2D Materials and Graphene Research Centre, National University of Singapore, Singapore 117546, Singapore; Institute of Materials Research and Engineering, Agency for Science, Technology and Research (A*STAR), Sigapore 138634, Singapore*

Meng Zhao − *Institute of Materials Research and Engineering, Agency for Science, Technology and Research (A*STAR), Sigapore 138634, Singapore*

Stephen John Pennycook − *Department of Materials Science and Engineering, National University of Singapore, Singapore 117575, Singapore*

https://dx.doi.org/10.1021/acsami.0c20535
ACS Appl. Mater. Interfaces 2021, 13, 8518−8527

Chorng Haur Sow − *Department of Physics, National University of Singapore, Singapore 117551, Singapore;* orcid.org/0000-0001-6385-3017

Chengkuo Lee − *Department of Electrical and Computer Engineering, National University of Singapore, Singapore 117576, Singapore;* orcid.org/0000-0002-8886-3649

Yu Lin Zhong − *Centre for Clean Environment and Energy, School of Environment and Science, Griffith University, Gold Coast, Queensland 4222, Australia;* orcid.org/0000-0001-6741-3609

Junpeng Lu − *School of Physics, Southeast University, Nanjing 211189, China;* orcid.org/0000-0002-7099-3162

Mengning Ding − *Key Laboratory of Mesoscopic Chemistry, School of Chemistry and Chemical Engineering, Nanjing University, Nanjing 210023, China;* orcid.org/0000-0001-6581-3385

Complete contact information is available at: https://pubs.acs.org/10.1021/acsami.0c20535

Author Contributions

J.Lu supervised the project. Y.M., Q.Z., and J.L. performed the sample growth and device fabrications. Y.M., J.L., B.D., and Z.H. performed photodetection performance measurements. Y.M. and H.F. performed AFM measurements. H.X. and X.Z. performed TEM characterization. X.S. and K.W. contributed to the first-principles calculations. Y.M. and J.L. wrote the paper. All authors took part in the discussion and preparation of the manuscript.

Notes

The authors declare no competing financial interest.

■ ACKNOWLEDGMENTS

J.L. acknowledges the support from MOE Tier 2 grant (MOE2019-T2-2-044 and R-143-000-A75-114) and NAMIC grant (R-143-000- B26-529). Y.M. acknowledges the financial support from the China Postdoctoral Science Foundation (2019M663033). J.L. acknowledges the support from the National Natural Science Foundation of China (21703143). K. Wang acknowledges the support from the General Physics Teaching Steering Committee of the Ministry of Education of China (Teaching Reform Project DJZW201931zn). M.Z. acknowledges the support from the Agency for Science, Technology and Research (A*STAR) (152700014 and H19H6a0025). Y.L.Z. acknowledges the support from the Australian Research Council (DP190100120). S.J.P. is grateful to the support from MOE Tier 2 grant (MOE2017-T2-2-139).

■ REFERENCES

(1) Sun, Y.; Gao, S.; Xie, Y. Atomically-Thick Two-Dimensional Crystals: Electronic Structure Regulation and Energy Device Construction. *Chem. Soc. Rev.* **2014**, *43*, 530−546.

(2) Hu, D.; Zhao, T.; Ping, X.; Zheng, H.; Xing, L.; Liu, X.; Zheng, J.; Sun, L.; Gu, L.; Tao, C. Unveiling the Layer-Dependent Catalytic Activity of $PtSe_2$ Atomic Crystals for the Hydrogen Evolution Reaction. *Angew. Chem.* **2019**, *131*, 7051−7055.

(3) Chang, K.; Mei, Z.; Wang, T.; Kang, Q.; Ouyang, S.; Ye, J. MoS_2/Graphene Cocatalyst for Efficient Photocatalytic H_2 Evolution under Visible Light Irradiation. *ACS Nano* **2014**, *8*, 7078−7087.

(4) Tsai, M.-L.; Su, S.-H.; Chang, J.-K.; Tsai, D.-S.; Chen, C.-H.; Wu, C.-I.; Li, L.-J.; Chen, L.-J.; He, J.-H. Monolayer MoS_2 Heterojunction Solar Cells. *ACS Nano* **2014**, *8*, 8317−8322.

(5) Jiang, H.; Ren, D.; Wang, H.; Hu, Y.; Guo, S.; Yuan, H.; Hu, P.; Zhang, L.; Li, C. 2D Monolayer MoS_2-Carbon Interoverlapped Superstructure: Engineering Ideal Atomic Interface for Lithium Ion Storage. *Adv. Mater.* **2015**, *27*, 3687−3695.

(6) Bie, Y.-Q.; Grosso, G.; Heuck, M.; Furchi, M. M.; Cao, Y.; Zheng, J.; Bunandar, D.; Navarro-Moratalla, E.; Zhou, L.; Efetov, D. K. A $MoTe_2$-based Light-Emitting Diode and Photodetector for Silicon Photonic Integrated Circuits. *Nat. Nanotechnol.* **2017**, *12*, 1124−1129.

(7) Michel, J.; Liu, J.; Kimerling, L. C. High-Performance Ge-on-Si Photodetectors. *Nat. Photonics* **2010**, *4*, 527−534.

(8) Konstantatos, G.; Badioli, M.; Gaudreau, L.; Osmond, J.; Bernechea, M.; De Arquer, F. P. G.; Gatti, F.; Koppens, F. H. Hybrid Graphene-Quantum dot Phototransistors with Ultrahigh Gain. *Nat. Nanotechnol.* **2012**, *7*, 363−368.

(9) Du, S.; Lu, W.; Ali, A.; Zhao, P.; Shehzad, K.; Guo, H.; Ma, L.; Liu, X.; Pi, X.; Wang, P. A Broadband Fluorographene Photodetector. *Adv. Mater.* **2017**, *29*, 1700463.

(10) Zhang, Y.; Liu, T.; Meng, B.; Li, X.; Liang, G.; Hu, X.; Wang, Q. J. Broadband High Photoresponse from Pure Monolayer Graphene Photodetector. *Nat. Commun.* **2013**, *4*, 1−11.

(11) Xia, F.; Mueller, T.; Lin, Y.-M.; Valdes-Garcia, A.; Avouris, P. Ultrafast Graphene Photodetector. *Nat. Nanotechnol.* **2009**, *4*, 839−843.

(12) Mueller, T.; Xia, F.; Avouris, P. Graphene Photodetectors for High-Speed Optical Communications. *Nat. Photonics* **2010**, *4*, 297−301.

(13) Zhang, E.; Wang, P.; Li, Z.; Wang, H.; Song, C.; Huang, C.; Chen, Z.-G.; Yang, L.; Zhang, K.; Lu, S. Tunable Ambipolar Polarization-Sensitive Photodetectors based on High-Anisotropy $ReSe_2$ Nanosheets. *ACS Nano* **2016**, *10*, 8067−8077.

(14) Zeng, L. H.; Wu, D.; Lin, S. H.; Xie, C.; Yuan, H. Y.; Lu, W.; Lau, S. P.; Chai, Y.; Luo, L. B.; Li, Z. J. Controlled Synthesis of 2D Palladium Diselenide for Sensitive Photodetector Applications. *Adv. Funct. Mater.* **2019**, *29*, 1806878.

(15) Wang, W.; Klots, A.; Prasai, D.; Yang, Y.; Bolotin, K. I.; Valentine, J. Hot Electron-based Near-infrared Photodetection using Bilayer MoS_2. *Nano Lett.* **2015**, *15*, 7440−7444.

(16) Huang, H.; Wang, J.; Hu, W.; Liao, L.; Wang, P.; Wang, X.; Gong, F.; Chen, Y.; Wu, G.; Luo, W. Highly Sensitive Visible to Infrared MoTe2 Photodetectors Enhanced by the Photogating Effect. *Nanotechnology* **2016**, *27*, 445201.

(17) Li, J.; Chen, C.; Liu, S.; Lu, J.; Goh, W. P.; Fang, H.; Qiu, Z.; Tian, B.; Chen, Z.; Yao, C. Ultrafast Electrochemical Expansion of Black Phosphorus toward High-yield Synthesis of Few-layer Phosphorene. *Chem. Mater.* **2018**, *30*, 2742−2749.

(18) Yuan, H.; Liu, X.; Afshinmanesh, F.; Li, W.; Xu, G.; Sun, J.; Lian, B.; Curto, A. G.; Ye, G.; Hikita, Y. Polarization-Sensitive Broadband Photodetector using a Black Phosphorus Vertical p-n Junction. *Nat. Nanotechnol.* **2015**, *10*, 707−713.

(19) Guo, Q.; Pospischil, A.; Bhuiyan, M.; Jiang, H.; Tian, H.; Farmer, D.; Deng, B.; Li, C.; Han, S.-J.; Wang, H. Black Phosphorus Mid-infrared Photodetectors with High Gain. *Nano Lett.* **2016**, *16*, 4648−4655.

(20) Buscema, M.; Groenendijk, D. J.; Blanter, S. I.; Steele, G. A.; Van Der Zant, H. S.; Castellanos-Gomez, A. Fast and Broadband Photoresponse of Few-Layer Black Phosphorus Field-Effect Transistors. *Nano Lett.* **2014**, *14*, 3347−3352.

(21) Sun, Z.; Chang, H. Graphene and Graphene-like Two-Dimensional Materials in Photodetection: Mechanisms and Methodology. *ACS Nano* **2014**, *8*, 4133−4156.

(22) Zhang, Q.; Jie, J.; Diao, S.; Shao, Z.; Zhang, Q.; Wang, L.; Deng, W.; Hu, W.; Xia, H.; Yuan, X. Solution-Processed Graphene Quantum Dot Deep-UV Photodetectors. *ACS Nano* **2015**, *9*, 1561−1570.

(23) Di Bartolomeo, A. Graphene Schottky Diodes: An Experimental Review of the Rectifying Graphene/Semiconductor Heterojunction. *Phys. Rep.* **2016**, *606*, 1−58.

(24) Koppens, F.; Mueller, T.; Avouris, P.; Ferrari, A.; Vitiello, M.; Polini, M. Photodetectors based on Graphene, Other Two-Dimen-

sional Materials and Hybrid Systems. *Nat. Nanotechnol.* **2014**, *9*, 780−793.
(25) Ye, L.; Li, H.; Chen, Z.; Xu, J. Near-infrared Photodetector based on MoS_2/Black Phosphorus Heterojunction. *ACS Photonics* **2016**, *3*, 692−699.
(26) Yin, J.; Tan, Z.; Hong, H.; Wu, J.; Yuan, H.; Liu, Y.; Chen, C.; Tan, C.; Yao, F.; Li, T. Ultrafast and Highly Sensitive Infrared Photodetectors based on Two-Dimensional Oxyselenide Crystals. *Nat. Commun.* **2018**, *9*, 1−7.
(27) Yu, X.; Yu, P.; Wu, D.; Singh, B.; Zeng, Q.; Lin, H.; Zhou, W.; Lin, J.; Suenaga, K.; Liu, Z. Atomically Thin Noble Metal Dichalcogenide: a Broadband Mid-infrared Semiconductor. *Nat. Commun.* **2018**, *9*, 1−9.
(28) Zhao, Y.; Qiao, J.; Yu, Z.; Yu, P.; Xu, K.; Lau, S. P.; Zhou, W.; Liu, Z.; Wang, X.; Ji, W. High-electron-mobility and Air-stable 2D Layered $PtSe_2$ FETs. *Adv. Mater.* **2017**, *29*, 1604230.
(29) Zeng, L. H.; Lin, S. H.; Li, Z. J.; Zhang, Z. X.; Zhang, T. F.; Xie, C.; Mak, C. H.; Chai, Y.; Lau, S. P.; Luo, L. B. Fast, Self-driven, Air-Stable, and Broadband Photodetector based on Vertically Aligned $PtSe_2$/GaAs Heterojunction. *Adv. Funct. Mater.* **2018**, *28*, 1705970.
(30) Zeng, L.; Lin, S.; Lou, Z.; Yuan, H.; Long, H.; Li, Y.; Lu, W.; Lau, S. P.; Wu, D.; Tsang, Y. H. Ultrafast and Sensitive Photodetector based on a $PtSe_2$/Silicon Nanowire Array Heterojunction with a Multiband Spectral Response from 200 to 1550 nm. *NPG Asia Mater.* **2018**, *10*, 352−362.
(31) Yim, C.; McEvoy, N.; Riazimehr, S.; Schneider, D. S.; Gity, F.; Monaghan, S.; Hurley, P. K.; Lemme, M. C.; Duesberg, G. S. Wide Spectral Photoresponse of Layered Platinum Diselenide-based Photodiodes. *Nano Lett.* **2018**, *18*, 1794−1800.
(32) Wu, D.; Wang, Y.; Zeng, L.; Jia, C.; Wu, E.; Xu, T.; Shi, Z.; Tian, Y.; Li, X.; Tsang, Y. H. Design of 2D Layered $PtSe_2$ Heterojunction for the High-Performance, Room-Temperature, Broadband, Infrared Photodetector. *ACS Photonics* **2018**, *5*, 3820−3827.
(33) Zhuo, R.; Zeng, L.; Yuan, H.; Wu, D.; Wang, Y.; Shi, Z.; Xu, T.; Tian, Y.; Li, X.; Tsang, Y. H. In-situ Fabrication of $PtSe_2$/GaN Heterojunction for Self-Powered Deep Ultraviolet Photodetector with Ultrahigh Current on/off Ratio and Detectivity. *Nano Res.* **2019**, *12*, 183−189.
(34) Villaos, R. A. B.; Crisostomo, C. P.; Huang, Z.-Q.; Huang, S.-M.; Padama, A. A. B.; Albao, M. A.; Lin, H.; Chuang, F.-C. Thickness Dependent Electronic Properties of Pt Dichalcogenides. *npj 2D Materials and Applications* **2019**, *3*, 1−8.
(35) Urban, F.; Gity, F.; Hurley, P. K.; McEvoy, N.; Di Bartolomeo, A. Isotropic Conduction and Negative Photoconduction in Ultrathin $PtSe_2$ Films. *Appl. Phys. Lett.* **2020**, *117*, 193102.
(36) Shawkat, M. S.; Chung, H.-S.; Dev, D.; Das, S.; Roy, T.; Jung, Y. Two-Dimensional/Three-Dimensional Schottky Junction Photovoltaic Devices Realized by the Direct CVD Growth of vdW 2D $PtSe_2$ Layers on Silicon. *ACS Appl. Mater. Interfaces* **2019**, *11*, 27251−27258.
(37) Wang, Z.; Li, Q.; Besenbacher, F.; Dong, M. Facile Synthesis of Single Crystal $PtSe_2$ Nanosheets for Nanoscale Electronics. *Adv. Mater.* **2016**, *28*, 10224−10229.
(38) Wang, Y.; Li, L.; Yao, W.; Song, S.; Sun, J.; Pan, J.; Ren, X.; Li, C.; Okunishi, E.; Wang, Y.-Q. Monolayer $PtSe_2$, a New Semiconducting Transition-Metal-Dichalcogenide, Epitaxially Grown by Direct Selenization of Pt. *Nano Lett.* **2015**, *15*, 4013−4018.
(39) Szydłowska, B. M.; Hartwig, O.; Tywoniuk, B.; Hartman, T.; Stimpel-Lindner, T.; Sofer, Z.; McEvoy, N.; Duesberg, G. S.; Backes, C. Spectroscopic Thickness and Quality Metrics for $PtSe_2$ Layers Produced by Topdown and Bottom-up Techniques. *2D Mater.* **2020**, *7*, 045027.
(40) Han, S. S.; Kim, J. H.; Noh, C.; Kim, J. H.; Ji, E.; Kwon, J.; Yu, S. M.; Ko, T.-J.; Okogbue, E.; Oh, K. H. Horizontal-to-Vertical Transition of 2D Layer Orientation in Low-Temperature Chemical Vapor Deposition-Grown $PtSe_2$ and Its Influences on Electrical Properties and Device Applications. *ACS Appl. Mater. Interfaces* **2019**, *11*, 13598−13607.
(41) Mounet, N.; Gibertini, M.; Schwaller, P.; Campi, D.; Merkys, A.; Marrazzo, A.; Sohier, T.; Castelli, I. E.; Cepellotti, A.; Pizzi, G. Two-Dimensional Materials from High-Throughput Computational Exfoliation of Experimentally Known Compounds. *Nat. Nanotechnol.* **2018**, *13*, 246−252.
(42) Kempt, R.; Kuc, A.; Heine, T. Two-Dimensional Noble-Metal Chalcogenides and Phosphochalcogenides. *Angew. Chem., Int. Ed.* **2020**, *59*, 9242−9254.
(43) Lu, J.; Yang, J.-X.; Wang, J.; Lim, A.; Wang, S.; Loh, K. P. One-Pot Synthesis of Fluorescent Carbon Nanoribbons, Nanoparticles, and Graphene by the Exfoliation of Graphite in Ionic Liquids. *ACS Nano* **2009**, *3*, 2367−2375.
(44) Parvez, K.; Wu, Z.-S.; Li, R.; Liu, X.; Graf, R.; Feng, X.; Mullen, K. Exfoliation of Graphite into Graphene in Aqueous Solutions of Inorganic Salts. *J. Am. Chem. Soc.* **2014**, *136*, 6083−6091.
(45) Abdelkader, A.; Cooper, A.; Dryfe, R.; Kinloch, I. How to Get between the Sheets: a Review of Recent Works on the Electrochemical Exfoliation of Graphene Materials from Bulk Graphite. *Nanoscale* **2015**, *7*, 6944−6956.
(46) Li, J.; Song, P.; Zhao, J.; Vaklinova, K.; Zhao, X.; Li, Z.; Qiu, Z.; Wang, Z.; Lin, L.; Zhao, M. Printable Two-Dimensional Superconducting Monolayers. *Nat. Mater.* **2021**, *20*, 1−7.
(47) Fang, Y.; Li, X.; Li, J.; Yao, C.; Hoh, H. Y.; Hai, X.; Lu, J.; Su, C. Janus Electrochemical Exfoliation of Two-Dimensional Materials. *J. Mater. Chem. A* **2019**, *7*, 25691−25711.
(48) Yang, S.; Zhang, P.; Nia, A. S.; Feng, X. Emerging 2D Materials Produced via Electrochemistry. *Adv. Mater.* **2020**, *32*, 1907857.
(49) Soled, S.; Wold, A.; Gorochov, O. Crystal Growth and Characterization of Several Platinum Sulfoselenides. *Mater. Res. Bull.* **1976**, *11*, 927−932.
(50) Yim, C.; Lee, K.; McEvoy, N.; O'Brien, M.; Riazimehr, S.; Berner, N. C.; Cullen, C. P.; Kotakoski, J.; Meyer, J. C.; Lemme, M. C. High-Performance Hybrid Electronic Devices from Layered $PtSe_2$ Films Grown at Low Temperature. *ACS Nano* **2016**, *10*, 9550−9558.
(51) Yan, M.; Wang, E.; Zhou, X.; Zhang, G.; Zhang, H.; Zhang, K.; Yao, W.; Lu, N.; Yang, S.; Wu, S. High Quality Atomically Thin $PtSe_2$ Films Grown by Molecular Beam Epitaxy. *2D Mater.* **2017**, *4*, 045015.
(52) O'Brien, M.; McEvoy, N.; Motta, C.; Zheng, J.-Y.; Berner, N. C.; Kotakoski, J.; Elibol, K.; Pennycook, T. J.; Meyer, J. C.; Yim, C. Raman Characterization of Platinum Diselenide Thin Films. *2D Mater.* **2016**, *3*, 021004.
(53) Yan, M.; Huang, H.; Zhang, K.; Wang, E.; Yao, W.; Deng, K.; Wan, G.; Zhang, H.; Arita, M.; Yang, H. Lorentz-violating Type-II Dirac Fermions in Transition Metal Dichalcogenide $PtTe_2$. *Nat. Commun.* **2017**, *8*, 1−6.
(54) Wang, C.; He, Q.; Halim, U.; Liu, Y.; Zhu, E.; Lin, Z.; Xiao, H.; Duan, X.; Feng, Z.; Cheng, R. Monolayer Atomic Crystal Molecular Superlattices. *Nature* **2018**, *555*, 231−236.
(55) Lee, C.; Yan, H.; Brus, L. E.; Heinz, T. F.; Hone, J.; Ryu, S. Anomalous Lattice Vibrations of Single-and Few-Layer MoS_2. *ACS Nano* **2010**, *4*, 2695−2700.
(56) Ma, H.; Chen, P.; Li, B.; Li, J.; Ai, R.; Zhang, Z.; Sun, G.; Yao, K.; Lin, Z.; Zhao, B. Thickness-Tunable Synthesis of Ultrathin Type-II Dirac Semimetal $PtTe_2$ Single Crystals and Their Thickness-Dependent Electronic Properties. *Nano Lett.* **2018**, *18*, 3523−3529.
(57) Ciarrocchi, A.; Avsar, A.; Ovchinnikov, D.; Kis, A. Thickness-Modulated Metal-to-Semiconductor Transformation in a Transition Metal Dichalcogenide. *Nat. Commun.* **2018**, *9*, 1−6.
(58) Wang, Y.; Kim, J. C.; Wu, R. J.; Martinez, J.; Song, X.; Yang, J.; Zhao, F.; Mkhoyan, A.; Jeong, H. Y.; Chhowalla, M. Van der Waals Contacts between Three-Dimensional Metals and Two-Dimensional Semiconductors. *Nature* **2019**, *568*, 70−74.
(59) Di Bartolomeo, A.; Pelella, A.; Liu, X.; Miao, F.; Passacantando, M.; Giubileo, F.; Grillo, A.; Iemmo, L.; Urban, F.; Liang, S. J. Pressure-Tunable Ambipolar Conduction and Hysteresis in Thin Palladium Diselenide Field Effect Transistors. *Adv. Funct. Mater.* **2019**, *29*, 1902483.
(60) Liang, Q.; Wang, Q.; Zhang, Q.; Wei, J.; Lim, S. X.; Zhu, R.; Hu, J.; Wei, W.; Lee, C.; Sow, C. High-Performance, Room

https://dx.doi.org/10.1021/acsami.0c20535
ACS Appl. Mater. Interfaces 2021, 13, 8518−8527

Temperature, Ultra-Broadband Photodetectors Based on Air-Stable $PdSe_2$. *Adv. Mater.* **2019**, *31*, 1807609.
(61) Urban, F.; Martucciello, N.; Peters, L.; McEvoy, N.; Di Bartolomeo, A. Environmental Effects on the Electrical Characteristics of Back-Gated WSe_2 Field-Effect Transistors. *Nanomaterials* **2018**, *8*, 901.
(62) Mao, J.; Yu, Y.; Wang, L.; Zhang, X.; Wang, Y.; Shao, Z.; Jie, J. Ultrafast, Broadband Photodetector based on MoSe2/Silicon Heterojunction with Vertically Standing Layered Structure using Graphene as Transparent Electrode. *Adv. Sci.* **2016**, *3*, 1600018.
(63) Choi, M. S.; Qu, D.; Lee, D.; Liu, X.; Watanabe, K.; Taniguchi, T.; Yoo, W. J. Lateral MoS_2 p-n Junction formed by Chemical Doping for Use in High-Performance Optoelectronics. *ACS Nano* **2014**, *8*, 9332−9340.
(64) Island, J. O.; Buscema, M.; Barawi, M.; Clamagirand, J. M.; Ares, J. R.; Sánchez, C.; Ferrer, I. J.; Steele, G. A.; van der Zant, H. S.; Castellanos-Gomez, A. Ultrahigh Photoresponse of Few-Layer TiS_3 Nanoribbon Transistors. *Adv. Opt. Mater.* **2014**, *2*, 641−645.
(65) Yang, Y.; Liu, S.-C.; Yang, W.; Li, Z.; Wang, Y.; Wang, X.; Zhang, S.; Zhang, Y.; Long, M.; Zhang, G. Air-stable In-plane Anisotropic GeSe2 for Highly Polarization-Sensitive Photodetection in Short Wave Region. *J. Am. Chem. Soc.* **2018**, *140*, 4150−4156.
(66) Xu, H.; Guo, C.; Zhang, J.; Guo, W.; Kuo, C. N.; Lue, C. S.; Hu, W.; Wang, L.; Chen, G.; Politano, A. $PtTe_2$-Based Type-II Dirac Semimetal and Its van der Waals Heterostructure for Sensitive Room Temperature Terahertz Photodetection. *Small* **2019**, *15*, 1903362.
(67) Zhang, Z.-X.; Zeng, L.-H.; Tong, X.-W.; Gao, Y.; Xie, C.; Tsang, Y. H.; Luo, L.-B.; Wu, Y.-C. Ultrafast, Self-driven, and Air-stable Photodetectors based on Multilayer $PtSe_2$/Perovskite Heterojunctions. *J. Phys. Chem. Lett.* **2018**, *9*, 1185−1194.
(68) Wei, Y.; Ren, Z.; Zhang, A.; Mao, P.; Li, H.; Zhong, X.; Li, W.; Yang, S.; Wang, J. Hybrid organic/PbS Quantum Dot Bilayer Photodetector with Low Dark Current and High Detectivity. *Adv. Funct. Mater.* **2018**, *28*, 1706690.
(69) Ren, Z.; Sun, J.; Li, H.; Mao, P.; Wei, Y.; Zhong, X.; Hu, J.; Yang, S.; Wang, J. Bilayer PbS Quantum Dots for High-Performance Photodetectors. *Adv. Mater.* **2017**, *29*, 1702055.

https://dx.doi.org/10.1021/acsami.0c20535
ACS Appl. Mater. Interfaces 2021, 13, 8518−8527

INTERNATIONAL JOURNAL OF HYDROGEN ENERGY 45 (2020) 2975–2988

Available online at www.sciencedirect.com

ScienceDirect

journal homepage: www.elsevier.com/locate/he

Generation of molybdenum hydride species via addition of molecular hydrogen across metal-oxygen bond at monolayer oxide/metal composite interface

Zhenjun Song [a,b,*], Xiji Shao [c,d], Qiang Wang [e], Chunxin Ma [f], Kedong Wang [c], Deman Han [a,**]

[a] School of Pharmaceutical and Materials Engineering, Taizhou University, Taizhou 318000, China

[b] Department of Chemistry, Key Laboratory of Advanced Energy Material Chemistry (MOE), Nankai University, Tianjin 300071, China

[c] Department of Physics, Southern University of Science and Technology, Shenzhen 518055, China

[d] Harbin Institute of Technology, Harbin 150080, China

[e] State Key Laboratory of Coal Conversion, Institute of Coal Chemistry, Chinese Academy of Sciences, Taiyuan 030001, China

[f] State Key Laboratory of Marine Resources Utilization in South China Sea, Hainan University, Haikou 570228, China

HIGHLIGHTS

- Generation of molybdenum hydride species on monolayer oxide/metal composite is investigated by employing DFT methods.
- Heterolytic dissociation of dihydrogen for obtaining molybdenum hydrides is energetically and dynamically favorable.
- Electronic properties for dihydrogen activation on monolayer oxide-metal interface are interpreted.
- The insulating oxide film shows high chemical activity by interface engineering.

GRAPHICAL ABSTRACT

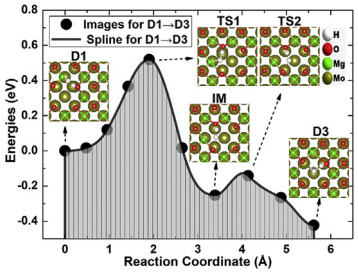

ARTICLE INFO

Article history:
Received 1 September 2019
Received in revised form
23 October 2019

ABSTRACT

Generation of molybdenum hydride species on monolayer oxide/metal composite via addition of molecular hydrogen across metal-oxygen bond is investigated for the first time utilizing periodic Van der Waals density-functional calculations. Lewis acid-base pair constructed by the interfacially defected oxide film and the metal support provides novel

* *Corresponding author*. School of Pharmaceutical and Materials Engineering, Taizhou University, Taizhou 318000, China.
** *Corresponding author*.
E-mail addresses: songzj@mail.nankai.edu.cn (Z. Song), hdm@tzc.edu.cn (D. Han).
https://doi.org/10.1016/j.ijhydene.2019.11.135

Accepted 18 November 2019
Available online 9 December 2019

Keywords:
Oxide-metal composite
Hydrogenation
Molybdenum hydride
Thermodynamics
Potential energy profile
Electronic properties

active sites for activating H_2. The produced heterolytic dissociative state exhibits negative dissociative adsorption energy of −0.315 eV which thermodynamically facilitate the dissociation process of H_2 on insulating oxide films. The penitential energy pathways are calculated to reveal the dynamics and reaction processes for H_2 splitting at the oxide-metal interface. The differential charge density contour, electronic density plots, particular occupied orbitals, work function and electron localization function of H_2 dissociation are interpreted to better understand the electronic properties of the unique dissociation behavior of H_2 at interfacially defected magnesia. It is anticipated that the results here could help understand the mechanism of hydrogenation reactions on nanostructured oxide film and provide useful clue for enhancing the reactivity of insulating oxide toward activating H_2.

Introduction

Metal oxides with myriad compositions, structures and bonding play an important role in heterogeneous catalysis and are often used as supports or active materials themselves [1–5]. Designing supported metal catalysts on metal oxides is an important strategy to achieve excellent catalysis performance. Metal particle/metal oxide interactions and charging/discharging of the metal particle strongly influences the energetics of redox processes in catalytic reactions [6–9]. The surface reactions are very sensitive to the oxide morphology and surface defects can greatly enhance the chemical activity [10–18]. Besides the metal oxide supported metal particles, the inverse model catalysts constructed by depositing ultrathin oxide films on metallic substrates has drawn researches' attention recently because of their great potential in catalytic applications. The reactivity and adsorption properties of oxide surface can be enhanced by introducing the suitable supports to form strong oxide-metal interactions (SOMI) [19,20]. Especially, the metal supported magnesia films is found to noticeably stabilize the dissociated form of water, methanol and peroxides to form surface hydroxyls while at the bulk magnesia (100) surface dissociated fragments can easily recombine [21–26].

H_2 is long considered as green energy storage medium and vital reagent in chemical and petrochemical engineering [27–30]. Activation of H_2 under ambient conditions is a significant and challenging task for exerting its key role in many catalytic processes such as hydrogenation and conversions of organic compounds and medicines. H_2 fragmentation on surfaces of reducible metal oxides has been explored extensively and productively by both experimental and theoretical methods. On the metal supported surface of lepidocrocite polymorph of titania, the H_2 splitting mode is found to depend closely on the metal substrate Pt(111) or Ag(100) [31]. Small activation energy barrier for H–H breaking on cerium-gallium hybrid oxides with gallia nanodomain can decrease the reduction potential efficiently [32], which is an important factor for initiating water gas shift reaction (WGSR). By HREEL experiments, temperature programmed reaction spectroscopy and scanning tunneling microscopy, the η^2-H_2 complexes and the dissociative hydride species are conclusively identified on different sites of RuO_2(110) surface [33–36]. The dissociative adsorption mode and reaction reversibility of H_2 chemisorption on metal oxide show a significant dependence upon exposed surface planes, and on the other hand the adsorption of surface hydrogen can induce surface reconstruction of metal oxides [37–39]. Reactivity of metal oxide is frequently dominated by the distribution and defect structure. Interaction of hydrogen with surface and subsurface defect structures deserves more research to identify active sites of oxide catalysts, and the defected metal oxide can be plausible method for building solid frustrated Lewis pairs (FLPs) toward splitting H_2 [40,41]. Recently, the first all-solid frustrated Lewis pair catalyst based on ceria is constructed with high concentration of surface defects, which can dissociate H_2 with energy barrier of 0.17 eV [42]. The results above provide deep insight into the coordination chemistry of H_2 on solid oxide surfaces.

Due to the chemical inertness, splitting H_2 on inert insulating oxide such as magnesia has been rarely investigated in the literature. However, as an important binary oxide with rock-salt structure, magnesia has many potential superiorities in industrial catalytic hydrogenation applications due to its abundance, high structural firmness and high temperature resistance. Magnesia is a representative model oxide and exhibits simple rock-salt structure and well-defined surfaces under conventional operating conditions. The slightly extended magnesia film (lattice mismatch within ~5%) can match pretty well with single-crystalline molybdenum, silver and gold substrate, with interfacial O atoms on top of metal atoms and interfacial Mg atoms falling in hollow positions. Magnesia is energetically stable even under high temperature and high pressure [43,44], and the chemical inertness makes magnesia suitable to investigate strain relief and atomistic details on the electronic property and reactivity of this material [45–48]. As the exposed face of a high-performance catalyst should be catalytically active and chemically stable under operating conditions, designing suitable nanostructured magnesia with geometric stability and enhanced reactivity should be an ideal strategy for activing and breaking H–H covalent bond.

In this contribution, we introduce the interfacially defected monolayer magnesia grown on crystalline molybdenum (100) support as inverse catalyst to reveal the fragmentation

behavior of H_2. The important role of metal-oxide interface with special electronic properties and local structural distortions is responsible for the energetically favorable heterolytic fragmentation of H_2. The Lewis acid-base pairs constructed by the interfacially defected oxide film and the metal support provide a novel category of active sites for enhancing the reactivity of insulating oxide toward splitting H_2.

Models and methodologies

We treat the core electrons with the PAW (projector augmented wave) approach [49], and the valence electrons are described explicitly. The DFT-D3 (Version 3.0, Rev1) scheme proposed by Grimme et al. [50] is utilized to accurately account for the dispersion forces. Employing the ab initio total energy method based on the gradient-corrected local density approximation [51] with the Perdew-Burke-Ernzerhof (PBE) exchange-correlation functional [52,53], we obtain the equilibrium geometries of dissociative adsorption structures. A large cutoff energy 500 eV is used to determine the size of plane-wave basis sets and maintain the accuracy of total energies as all plane waves with a kinetic energy smaller than cutoff energy are included in the basis set. To compute pair interactions and coordination number in vdW-energy expression, the corresponding cutoff radii is kept constant to be 50 and 20 Å, respectively. The Becke-Jonson (BJ) damping [54] is used to avoid the repulsive interatomic forces at short distances.

To eliminate interaction effects between periodic adsorbates, we construct the large supercell $(2\sqrt{2} \times 2\sqrt{2})$ R45° MgO (100). The lattice constants of bulk magnesia and molybdenum metal are calculated to be 4.249 Å and 3.152 Å at PBE theoretical level respectively, which agree very well with corresponding experimental values 4.22 Å [55] and 3.15 Å [56]. The p(4 × 4) metal substrate in (100) lattice plane is constructed using four atomic layers with 64 molybdenum atoms. The Mo(100) is used because of the suitability to form interfaces, and the convenience of calculations. Firstly, as a refractory transition metal, molybdenum can sustain very high annealing temperatures, which can produce metal-supported magnesia thin films with better structural quality and smaller roughness, although many first-principles calculations on magnesia–metal interfaces adopt silver and gold metal supports. Secondly, the lattice size and geometry of Mo(100) surface could agree well with the magnesia lattice. The lattice mismatch between molybdenum and magnesia is calculated to be 5%, and the molybdenum atoms in the top layer of Mo(100) could bond strongly with oxygen of magnesia film, which is suitable for producing well-structured oxide-metal interfaces. At DFT-D3 theoretical level, the oxide-metal binding energies (defined as the energy difference between composite and two isolated components, $E_b = E(\text{oxide/metal}) - E(\text{oxide}) - E(\text{metal})$) for Mo–MgO, Ag–MgO and Au–MgO composite structures are calculated to be −26.904, −13.381 and −13.276 eV, which confirms the high structural stability of Mo–MgO hybrid structure. Thirdly, the valence orbital for molybdenum includes six electrons, while valence orbital for silver or gold include eleven electrons. Thus the adoption of Mo(100) substrate can make the calculation converge more rapidly than Au(100) or Ag(100).

Even thicker molybdenum layers do not change the adsorption and reaction properties of the oxide films. One magnesium atom at neutral position is removed to generate interfacial defects. Adsorbates, oxide films and top two layers of metal slab are relaxed until the residual Hellmann-Feynman force acting on each atom is less than 0.02 eV $Å^{-1}$, while the bottom two layers of metal slab are fixed at their bulk positions. We use convergence criterion of 1.0×10^{-5} eV for energy minimization. The dissociative adsorption energies for H_2 on metal-supported monolayer magnesia are defined as:

$$E_{ad}(A) = E(A/S) - E(A) - E(S) \quad (1)$$

where A and S represent adsorbates and metal-supported monolayer magnesia. The negative dissociative adsorption energies indicate thermodynamically favorable fragmentation reaction.

The Gamma-centered (2 × 2 × 1) and (4 × 4 × 1) k-point samplings are used for the geometric relaxations and electronic properties for the adsorbates on oxide-metal hybrid structure supercells. The periodically repeated oxide-metal slabs are separated by a thick vacuum layer larger than 14 Å to avoid interactions between vertically repeated species. Bader charge population is computed utilizing the program developed by Henkelman and coworkers [57,58]. The transition states and minimum energy paths (MEP) are located using climbing image nudged elastic band (CI-NEB) method [59] implemented in VTST code [60], which is an improved way of estimating the local tangent and eliminating kinks on the elastic band. Less number of intermediate images is needed for finding the exact saddle point along the reaction path as CI-NEB method tries to maximize energy of potential highest-energy image along the band and minimize energy in all other directions. The periodic density functional calculations have been performed using Vienna Ab initio Simulation Package [61,62] to determine corresponding structural, energetic and electronic results. The reduced simplified models of dissociated states are generated using particle swarm optimization algorithm implemented in CALYPSO program [63–65] and finally optimized using hybrid B3PW91 functional [66–68] implemented in Gaussian 09 program [69]. The 6-311++G(3df,3pd) basis set is used for oxygen, hydrogen and Stuttgart-Dresden ECP plus DZ (SDD) basis set for molybdenum. The Multiwfn program [70], VASPMO program [71], VESTA program [72] and Visual Molecular Dynamics (VMD) program [73] are used to analyze and visualize the orbital and electronic properties.

Results and discussion

Geometric structures and adsorption sites for H_2 fragmentation on monolayer magnesia with interfacial defects

Dissociative adsorption energies E_{ads} for several motifs of H_2 fragmentation on different symmetry sites (adjacent O–Mg

site, diagonal adjacent O–O site and perpendicular adjacent O–Mo site, as shown in Fig. 1a–e) are calculated to determine the most stable adsorption site. The adsorption of H_2 on adjacent O–Mg site (Fig. 1a, D1 state) of monolayer magnesia/molybdenum with interfacial defects is calculated to be slightly unfavorable with adsorption energy of 0.109 eV at DFT-D3 theoretical level, which is energetically lower than previous reports (0.48 eV) [22] for H_2 fragmentation on corresponding perfect magnesia film. This result indicates that the surface engineering by introducing interfacial defects should enhance the probability of H_2 dissociation. The H1–H2 distance at D1 state is 1.417 Å, which is longer compared with its adsorption state A (Table 1). The O1–H1 and H2–Mg1 distances is calculated to be 1.026 and 1.790 Å, suggesting the possible formation of bonding interaction between H1H2 and surface O1Mg1 sites which could be further confirmed in the latter analysis of the projected density of states. The surface rumpling of relaxed first layer (i.e. the oxide layer) at D1 state is significantly more severe than those at isolated state (IS, bare magnesia film) or molecular adsorption state A. However, the relaxed inner metallic layers show less severe distortion than first layer.

It is particularly interesting and important for determination of dissociation structure of H_2 on surfaces from the viewpoint of their catalytic properties such as selective hydrogenation. In addition to the heterolytic fragmentation on adjacent O–Mg sites, we have also explored the homolytic fragmentation structures. The minimum-energy geometries for dissociation on two four-coordinated oxygen atoms (D2 state), as depicted in Fig. 1b, show energy increase of 0.608 eV compared with the isolated state. The relaxed structure for dissociative adsorption on a four-coordinated surface oxygen and a diagonally adjacent five-coordinated surface oxygen (Fig. 1c) corresponds to higher energy state D2′ with substantially positive adsorption energy of 0.889 eV, indicating the homolytic dissociation is thermodynamically unfavorable on interfacially defected metal-supported monolayer magnesia (001). The H1–H2 distance at D2 state is 2.553 Å, suggesting the complete splitting of H_2. The O1–H1 and O2–H2 distances are calculated to be 0.979 Å, indicating the possible formation of surface hydroxyl. The O1–Mg1 distances is lengthened to 3.096 Å, suggesting that surface bonds at the reaction sites are significantly broken. The rumpling value of the first layer at D2 state is 0.560 Å, which is obviously larger than those at D1 and A states. At the interface, the metallic substrate layer is also more strongly rumpled compared with D1 and A state. The surface structure of D2' (also a homolytic dissociation state) is more severely distorted than D2 with O1–Mg1 distance 3.745 Å. The H1–H2 distance is largest among considered structures, and the bond lengths of two hydroxyl (O1H1, O3H2) show slight difference as a result of the different bonding environment.

Table 1 – Geometries of H_2 adsorption on monolayer magnesia (100) supported on molybdenum at nondissociative (A) and dissociative (D1 and D2) adsorption states (in unit of angstrom).

	IS	A	D1	D2	D2′
H1–H2	0.750	0.761	1.417	2.553	3.385
O1–H1	–	2.286	1.026	0.979	0.971
O2(3)-H2	–	3.360	3.108	0.979	0.980
H2–Mg1	–	2.546	1.790	2.671	2.731
O1–Mg1	2.347	2.389	2.989	3.096	3.745

Due to the presence of interfacial defect, the hydrogen atoms could permeate into the interspace area to bond with surface oxygen and the molybdenum substrate underneath (Fig. 1d, D3 state). This dissociative adsorption state is uncovered for the first time, and very different from the significant energy cost of D1, D2 and D2', the dissociative adsorption

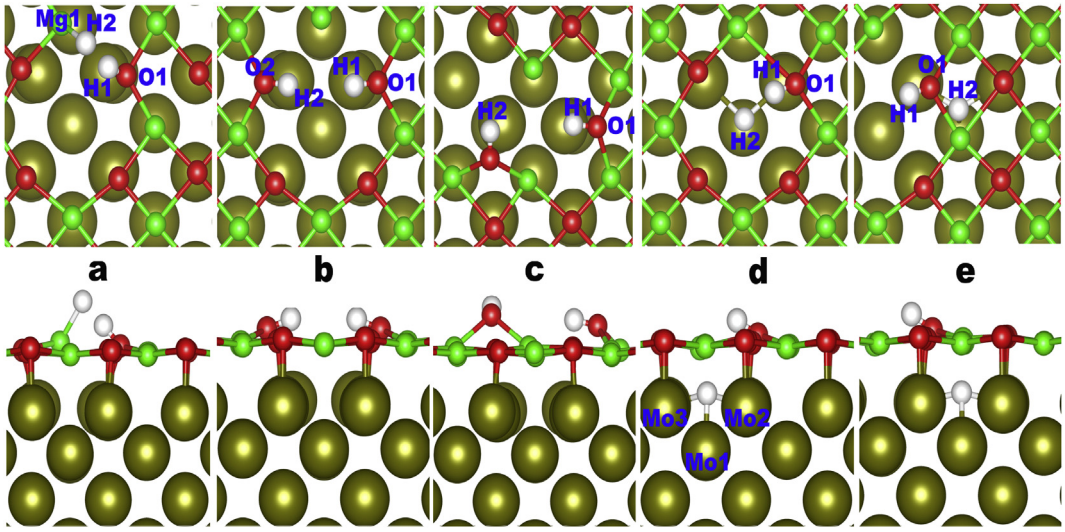

Fig. 1 – Relaxed atomic configurations (top and side views) for H_2 fragmentation on MgO(100)/Mo(100) hybrid film at D1(a), D2 (b), D2' (c), D3 (d) and D4 (e) states. The continuous thin lines denote the two-dimensional unit-cell of the supported magnesia. Large circles marked in olive color are the molybdenum atoms, circles marked in white, green and red colors are hydrogen, magnesium and oxygen atoms. The important atoms at the reaction sites are indicated. (For interpretation of the references to color in this figure legend, the reader is referred to the Web version of this article.)

state D3 exhibits negative adsorption energy of −0.315 eV which should facilitate the fragmentation process of H_2 on insulating oxide films. As listed in Table 2, the H1–H2 distance is calculated to be 2.799 Å indicating the dissociation of H–H covalent bond. The O1–H1, H2–Mo1, H2–Mo2 and H2–Mo3 distances are calculated to be 0.974, 1.914, 2.004 and 2.105 Å, which suggest the possible formation of a surface hydroxyl and a multiple (μ_3-H)-Mo bonding interaction. The Mo–H bond distance of molybdenum hydride is substantially longer than MoH_x compound reported in solid neon and argon matrixes [74,75], due to the multiple bonding interaction with metallic molybdenum slab. At this dissociative state, the surface structure of oxide film at the active site is partially broken with O1–Mg1 distance 2.970 Å. As listed in Table 3, although the hydrogen permeates into the oxide-metal interface, the calculated surface distortions are only 0.448, 0.092, 0.054 Å at D3 state, which are less severe than that at D2 state and decrease obviously with the depth of surface (the value of *x* in "x-th layer"). The translation of hydrogen at the interface could lead to the formation of D4 (Fig. 1e), which also possess surface hydroxyl and hydrogen-molybdenum bonds at the interface. However, comparing with the D3 state, D4 is energetically unfavorable by 0.395 eV. For the discussion of structures and properties of novel heterolytic splitting mode, we mainly focused on the D3 configuration.

Minimum energy pathway for H_2 fragmentation on monolayer magnesia with interfacial defect

The minimum energy pathway for splitting H_2 on interfacially defected monolayer magnesia (100) is calculated employing Climbing-Image Nudged Elastic Band method, as shown in Fig. 2. At the beginning isolated state (IS), the H_2 is 3.335 Å far away from the nearest surface oxygen atom. To form heterolytic D1 state, the H_2 on monolayer oxide film experiences an intermediate state (IM) with a slight energy release of 88 meV and a small activation energy barrier 0.332 eV, indicating the heterolytic dissociation on metal-supported ultrathin magnesia (100) is significantly further facilitated by interfacial defect (compared with previous important reports in Refs. [22,23]).

Intermediate state to obtain D1 state is characterized structurally with H1–H2 distance of 0.761 Å and O1–H1 distance of 2.286 Å, indicating the slight activation of H_2 during approaching to oxide film. At the transition state (TS), H1–H2, H2–Mg1 and O1–H1 distances are calculated to be 1.023, 1.872 and 1.231 Å, which is possibly due to the effective activation of H_2 and partial formation of hydride and hydroxyl. According to Hammond postulate [76] which is a general correlation between reaction rates and the positions of chemical equilibria, the total energy of transition state is more close to the D1 state (with energy difference of 76 meV) rather than the intermediate state (with energy difference of 0.332 eV), thus the structural geometry of transition state is very close to final D1 state.

Table 2 – Geometries of H_2 Adsorption on Monolayer Magnesia (100) Supported on Molybdenum at Dissociative (D3) Adsorption States (in unit of Angstrom).

H1–H2	2.799	O1–Mg1	2.970
O1–H1	0.974	H2–Mo1	1.914
O2(3)-H2	2.930	H2–Mo2	2.004
H2–Mg1	3.419	H2–Mo3	2.105

Table 3 – Rumpling (in Å) of the Relaxed xth-Layer before H_2 Adsorption (IS), at a Molecular Adsorption State (A) and at Dissociative Adsorption States (D1, D2, D3).[a]

x	IS	A	D1	D2	D3
1	0.210	0.215	0.334	0.560	0.448
2	0.067	0.114	0.210	0.215	0.092
3	0.012	0.076	0.113	0.096	0.054

[a] Rumpling in the Substrate is Defined as the Difference Between the z Coordinates of Highest and Lowest Atoms in the xth-Layer, While the Rumpling in the Oxide Film is Defined as max(z(O)-z(Mg)).

To obtain the homolytic D2 state with high relative energy, we can adopt heterolytically dissociative adsorption state D1 as reactant species. The transformation reaction exhibits one intermediate state (IM state) and two transition states (TS1 and TS2, as shown in Fig. 2b). Previous literatures also point out the requirement of more than one elementary processes and intermediate state to complete the transformation reaction or dissociation reactions of H_2 [77,78]. The reactant species firstly reach transition state TS1 with energy increase of 0.507 eV H2–Mg1 bond at TS1 configuration is lengthened to 1.790 Å, and the H1–H2 distance is shortened to 1.304 Å. The two unusual bonding distances indicate the TS1 is unstable, and the formation of (μ_4-η_3-OHH) ligand bonding with two surface magnesium and two molybdenum. The two newly formed H–Mo bonds with distances 2.691 and 2.725 Å facilitate the instantaneous existence of TS. Then TS1 can transform to an intermediate state IM with H2–Mo2 distance 1.830 Å, H2–Mo3 distance 2.126 Å and H2–Mg1 distance 2.050 Å. Although the formation of H2–Mo3 bonding interaction promotes the production of homolytic D2 state, the transformation from IM to D2 is an endothermic process by 0.749 eV and requires climbing an energy barrier 1.345 eV (TS2). At TS2 state, H2–Mo3 bonding interaction is significantly enhanced with distance 1.944 Å. The H2–Mg1 hydride species at TS2 state partially fragment with distance of 2.161 Å. The breaking of old chemical bonds is always accompanied by generation of new bonds. The H2–O2 distance is calculated to be 1.350 Å, which belongs to the strong hydrogen bonding interaction and forebodes the subsequent production of hydroxyl group.

Transformation reaction from D1 can produce heterolytically dissociative state D3 via another minimum energy pathway different from the generation of D2 (Fig. 2c). Firstly, the H2–Mg1 hydrides is fragmented to produce an intermediate state (IM) exothermic by −0.252 eV. At the IM state, the H2–Mo3, H2–Mo2 and H2–Mg1 distances is calculated to be 2.171, 1.826 and 2.051 Å, indicating the formation of H2–Mo hydride and the partial dissociation of H2–Mg bonding interaction. The transition structure (TS1) to yield IM state is 0.519 eV higher in energy than initial D1 state. At TS1 state, the H2–Mg1, H2–Mo2 and H1–H2 distance are calculated to be 1.766, 2.782 (shortened) and 1.296 Å (shortened), indicating the

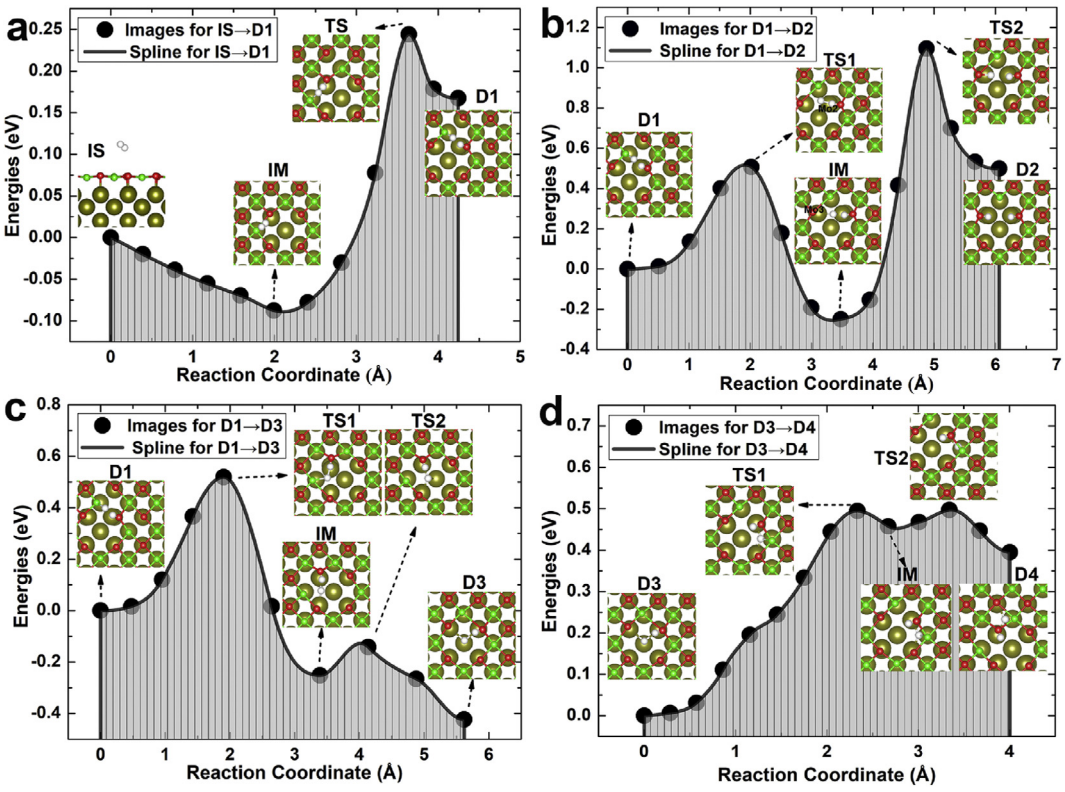

Fig. 2 – (a) Potential energy profile for fragmentation reaction from isolated states (IS) to D1 state; (b) potential energy profile for transformation reaction from D1 state to D2 state; (c) potential energy profile for transformation reaction from D1 state to D3 state; (d) Potential energy profile for transformation reaction from D3 state to D4 state. Structural geometries of isolated state (IS), intermediate states (IM), transition states TS are also illustrated. The curve is obtained from force-based interpolation between the images and the solid spheres are actual images in the nudged elastic band calculations.

possible partial formation of H–H and H–Mo bonding interaction. IM state should experience a transition state TS2 lying 0.110 eV higher in energy to acquire dissociative state D3. H2–Mo2 distance is prominently shortened to 1.821 Å, while the H1–H2 distance is lengthened to 2.118 Å suggesting the breaking of H–H chemical interaction. The H2–Mg1 distance at TS2 state is partially broken with distance of 2.141 Å. Although the D4 configuration presenting H–Mo bonds has structural similarity with D3 configuration, the D4 is 0.395 eV higher in energy than D3, and transformation from D3 to D4 state exhibits an activation energy barrier of 0.495 eV (Fig. 2d). The results suggest that the thermodynamically favorable hydrogen permeation could only occur at the defected interface regions.

H_2 fragmentation at oxide-metal interface with high coverages

The fragmentation of more H_2 molecules is explored extensively to reveal the influence of molecular coverage on the fragmentation behavior. The configurations for more than one H_2 molecules dissociated on the oxide-metal hybrid film, the averaged dissociative adsorption energy for H_2 and activation energy barrier for transformation reactions are depicted in Fig. 3. When the second H_2 reaches the interface, it can be dissociated heterolytically with structure similar to D1 (denoted as $D1_{2m}$) and shows small positive adsorption energy 0.11 eV. When the second H_2 is dissociated homolytically ($D2_{2m}$), the total energy is increased as large as 0.742 eV compared with the heterolytic state $D1_{2m}$. The $D3_{2m}$ state shows negative dissociative adsorption energy −0.128 eV, indicating the energetically favorable production of H–Mo and H–O bonds at the interface. When the third H_2 reaches the surface, it can be dissociated heterolytically at $D1_{3m}$ state with energy release of −0.262 eV, indicating that the D1 state become thermodynamically favorable for hybrid surface with higher coverage of H_2. The homolytic splitting state $D2_{3m}$ for the third H_2 is highly endothermic by 0.875 eV. The heterolytic splitting state $D3_{3m}$ for the third H_2 is remarkably exothermic by −0.462 eV. The heterolytic dissociative state $D1_{4m}$ with H–Mg bonds formation and energy release of −0.242 eV for the fourth H_2 maintains the exothermic feature as $D1_{3m}$. The homolytic dissociative state $D2_{4m}$ for the fourth H_2 is very difficult to occur showing large energy cost of 1.249 eV. The generation of H–Mo bonds for the fourth H_2 is thermodynamically favorable with energy release −0.244 eV. The averaged dissociative adsorption energies (adsorption energy per H_2) for dissociative states D1 and D3 which possess metal-hydrogen bonds are negative, while those for homolytic D2 states are substantially positive. In addition, the activation barriers for transformation from D1 to D2 are 1.55, 2.384 and 2.282 eV for reactions occurring at surfaces covered with two, three and four H_2, while corresponding activation barriers for D1 to D3 are only 0.528, 0.362 and 0.634 eV, verifying the

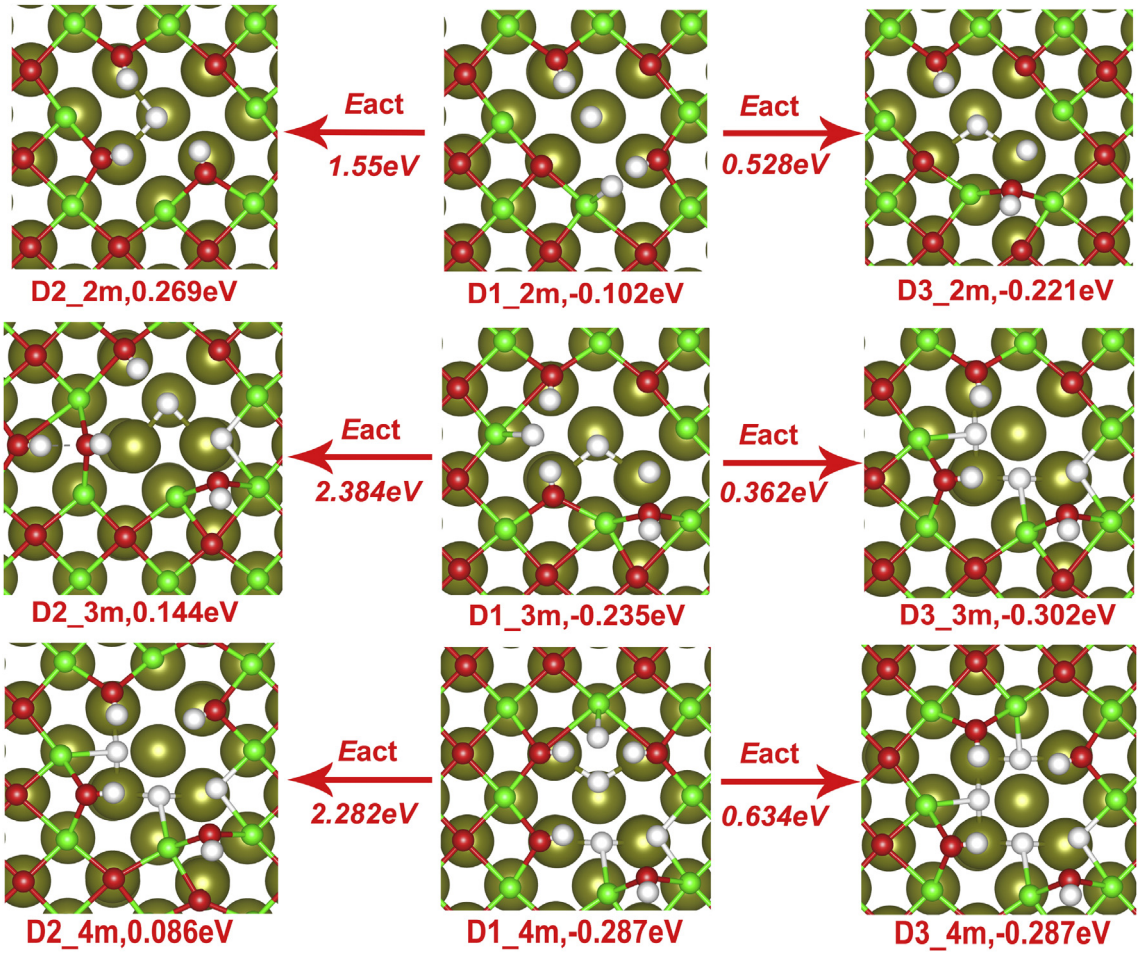

Fig. 3 – The configurations for more than one H_2 molecules dissociated on the oxide-metal hybrid film, the averaged dissociative adsorption energy for H_2 and activation energy barrier (E_{act}) for transformation reactions. The Dx_ym denotes the Dx state with y molecules adsorbed on the hybrid film.

feasibility of heterolytic splitting of H_2 with high coverage from the perspective of reaction dynamics.

When the coverage of H_2 become even larger, the ultrathin oxide surface will be structurally distorted and show characteristics of magnesium hydroxide. The majority of oxygen-molybdenum bonds are destroyed when the H_2 coverage is larger than 0.5 (eight H_2 per unit-cell, Fig. 4). The averaged dissociative adsorption energy for coverage 0.5 at D3 state is slightly positive, while that at D2 state is 1.136 eV, indicating the homolytic dissociative adsorption of H_2 with high coverage should be more difficult than corresponding reaction with low coverage. Majority of the oxygen-molybdenum bonds are replaced by hydrogen-molybdenum bonds at full coverage of H_2 (sixteen H_2 per unit-cell, Fig. 4), and the averaged dissociative adsorption energy is calculated to be −0.121 eV, demonstrating that the H_2 dissociation on the oxide-metal hybrid film with defects is thermodynamically feasible at high coverage.

The work functions and surface distortion for different coverages of H_2 are depicted in Fig. 5. The work functions reflect the chemical activity in the respect of how tightly the hydrogenated oxide film holds its electrons. At low coverages, the work function increase with the H_2 coverage, indicating the electrons tend to be more tightly bound at moderate coverage. However, when the coverage is larger than 0.25, the work function will be lower with the increase of coverage, which suggests the electron of the highly hydrogenated surface could travel readily to a potential oxidant. When the H_2 coverage increases, the surface rumpling values become larger indicating the surface distortion become more severe. This result can be ascribed to the structural damage of the oxide-metal hybrid structure via the permeation of hydrogen atoms and insertion of metal-hydrogen bonds.

Electronic properties for H_2 fragmentation behavior

At the heterolytic dissociative state D1, the local states of H1 is very weak which indicates 1s electrons of H1 is mainly transferred to surface oxygen, as shown in Fig. S1. Comparatively, the states of H2 show significantly large intensities suggesting the electron loss behavior doesn't occur on 1s orbital of H2. The interfacial molybdenum shows electronic occupation below 2.5 eV, suggesting the good electrical conductivity of the substrate material. Broad hybridization between $4d_z^2$ of interfacial Mo atoms and $2p_z$ of interfacial O atoms can be observed clearly with significant resonance of

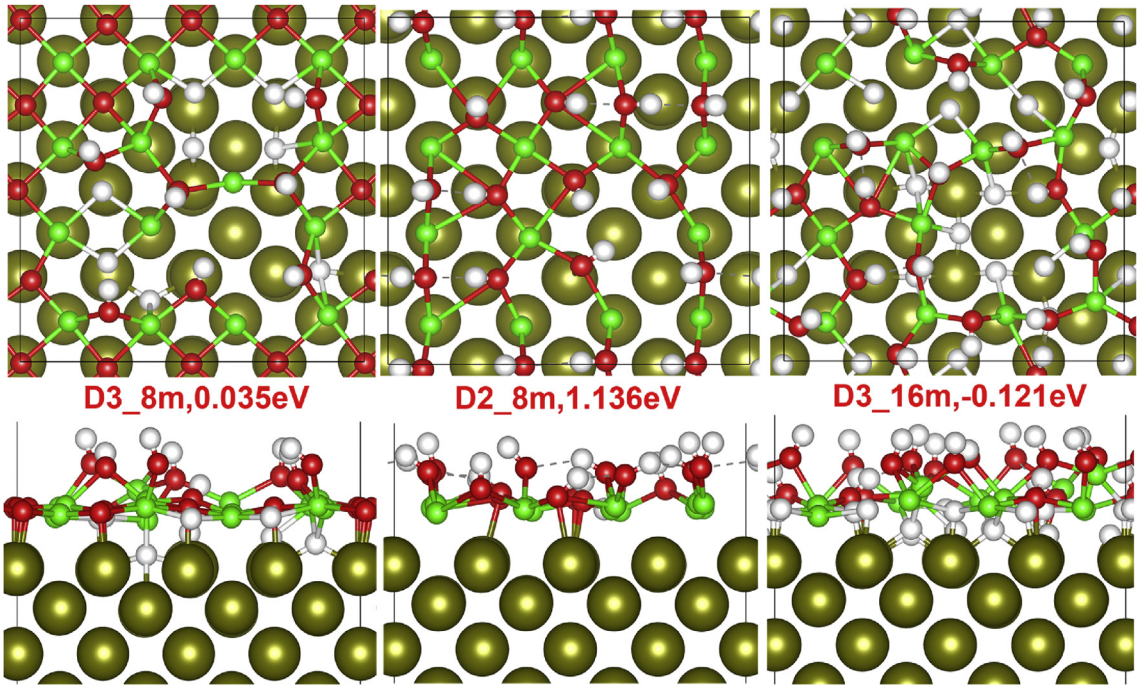

Fig. 4 – The configurations for eight and sixteen H_2 dissociated on one unit-cell of magnesia-molybdenum hybrid film. The averaged dissociative adsorption energies are denoted.

state peaks ranging from Fermi level to −6.3 eV, indicating sufficient covalent bonding interaction between Mo and O at the interface area. At energy level ranging from −2 to −3 eV, the local states of surface atoms O1 and Mg1 exhibit obvious hybridization with split species H1 and H2, respectively.

As shown in Fig. S2, at the homolytic fragmentation state D2, the local states of bonding orbitals of H1 and H2 exhibit sharp peaks distributed mainly at energy levels ranging from −8.5 to −9.0 eV below Fermi level. The shape and intensity of local states of H1 overlap with those of H2 at all the energy ranges. Apart from the superposition with O-2p_z orbital, the Mo-4d_z^2 orbital also shows hybridization with hydrogen adsorbates at energy range from −8.5 to −9 eV. The shapes of local density of states (LDOS) for O1 resemble those of O2, indicating these two surface oxygen have very similar atomic coordination surroundings. The state intensities of peaks of O1 and O2 show significant overlapping with fragmentation products H1 and H2 respectively at energy range from −8.5 to −9 eV, indicating the formation of surface hydroxyl with covalent bonding interaction.

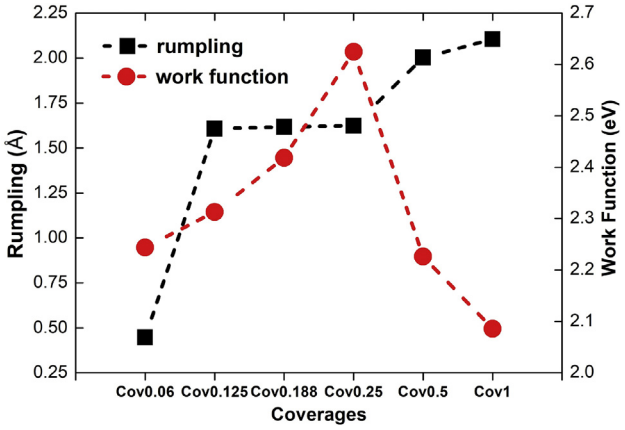

Fig. 5 – The work function and surface distortion for the magnesia-molybdenum composite structures with different H_2 coverages (rumpling value defined as the maximum distance projected in the z direction between atoms of the oxide film). The full coverage (Cov1) correspond to sixteen H_2 molecules adsorbed on one unit-cell.

For the heterolytic fragmentation state D3 with relatively low energy, H2 shows obvious LDOS peaks at -energy levels −3.5 eV to Fermi level indicating the activation and high reactivity of the adsorbate species, although the intensity of LDOS for H1 is weak in this particular energy range, as illustrated in Fig. 6. The orbital resolved LDOS of O1 and H2 exhibits significant hybridization. PDOS of interfacial molybdenum in z direction shows substantially overlap with those of interfacial oxygen at broad energy ranges. Surface magnesium Mg1 at the reaction site shows very weak LDOS and slight hybridization with O1 due to electrostatic pull. After transformation from D1 state to D3 state, the orbital hybridization between Mg1 and H2 is weakened, while obvious mixing of LDOS exists between the O1 and H1. The emergence of DOS peak of Mo-4d_z^2 at −6.7 eV indicates the newly formation of strong H–Mo interaction.

Using the computational methods developed by Henkelman group [57,58], we calculated the charge density grid partitioned into Bader volumes efficiently. The near-grid method can remove the lattice bias and make the dividing surface smooth. As listed in Table 4, H1 bonded to surface oxygen is positively charged (+0.552 e) while H2 bonded to surface magnesium is negatively charged (−0.664 e). The O1

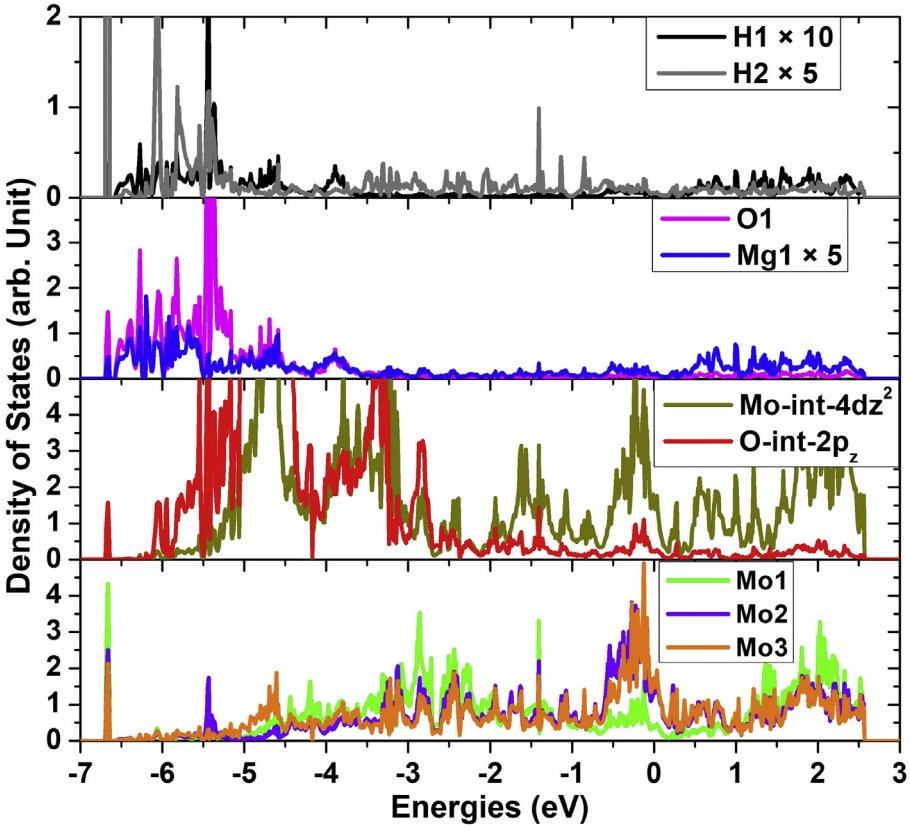

Fig. 6 – Local density of states of adsorbates hydrion and hydride ion; local density of states of particular interfacial molybdenum linked with hydrogen, Mo1, Mo2, Mo3; local density of states of surface atoms O1 and Mg1; projected density of states in the z direction of all the interfacial molybdenum and oxygen atoms at D3 state. The energy is given relative to the Fermi level ($E_f = 0$).

Table 4 – Bader Charge Populations (in electron) for H_2 Fragmentation at D1 State.

Species	Charge	Species	Charge
H1	+0.552	Oxide film	+1.073
H2	−0.664	Metal substrate	−0.961
O1	−1.413	Adsorbates	−0.112
Mg1	+1.591		

and Mg1 exhibit charge values (−1.413 and + 1.591) far less than their saturation oxidation numbers (+2 and −2). The charge transport should occur between oxide film and metal substrate because of the significant positive charge value in oxide thin film (+1.073 e). Adsorbate species show total charges of −0.112 e, indicating the overall electron-withdrawing effect of heterolytic fragmented H_2 at D1 state.

Table 5 – Bader Charge Populations (in electron) for H_2 Fragmentation at D2 State.

Species	Charge	Species	Charge
H1	+0.532	O2	−1.418
H2	+0.540	Oxide film	+0.715
O1	−1.410	Metal substrate	−1.787
Mg1	+1.445	Adsorbates	+1.072

As H2 is transferred to new adsorption site on top of surface oxygen O2, the adsorbate species show large positive charge +1.072 e at D2 state (Table 5). The charge value of Mg1 is decreased by 0.146 e due to the departure of electrophilic atom H2. The slight difference in charge value of O1 and O2 can be ascribed to minor variation in coordination environment due to introduction of interfacial defect. The magnesia film carries positive charge (+0.715 e) indicating it is oxidized considerably. The molybdenum slab acquires substantially more electrons (−1.787 e) compared with that at D1 state (−0.961 e).

H2 bonded with interfacial molybdenum at D3 state exhibits negative charge (Table 6), demonstrating that the D3 configuration is a unique heterolytic dissociative state. The H1 charge allocation at D3 state is larger than that at D1 and D2 states probably due to the significantly large H1…H2 distance

Table 6 – Bader Charge Populations (in electron) for H_2 Fragmentation at D3 State.

Species	Charge	Species	Charge
H1	+0.590	Mo2	−0.009
H2	−0.370	Mo3	+0.115
O1	−1.396	Oxide film	+0.875
Mg1	+1.615	Metal substrate	−1.095
Mo1	+0.102	Adsorbates	+0.220

and absence of H–H orbital overlapping. Generally, the adsorbates and the magnesia film are oxidized by the molybdenum substrate which acquires 1.095 e. The magnesium ion at reaction site ($Mg1^{\delta+}$) show substantially larger positive charge +1.615 e, indicating the ionic network O^{2-}-Mg^{2-} is firmer than those at D1 and D2 states.

We have also considered the electronic energies, bonding distances, Mulliken charge populations and stretching frequencies utilizing reduced model (Fig. S3, Table S1) at hybrid functional B3PW91/6-311++G(3df,3pd)/SDD theoretical level. The D3 dissociation state presents lowest total electronic energy, suggesting the special heterolytic dissociative state can maintain high stability even at nanoscale cluster model. The H-X (X = Mg, O, Mo) distances 1.713, 0.960 and 1.957 Å agree well with the parameters 1.790, 0.979 and 1.914 Å at D1, D2 and D3 states, respectively, demonstrating the main structural feature (H-X bonding interaction) could be reproduced even at the abbreviated model. Employing hybrid density-functional theory calculation, the H–Mg stretching and H–Mg–O wagging (with frequencies 1578 and 626 cm^{-1} respectively) are calculated to be the main vibration mode at D1 state. The H–O stretching and Mo–O–H wagging frequencies are calculated to be the main modes at D2 dissociative state with frequencies 3854 and 610 cm^{-1}, respectively. The largest vibration frequencies (1375 and 819 cm^{-1}) at D3 state are assigned to H–Mo stretching and Mo–O–H bending modes.

The real space function values and contour line diagrams of the Laplacian of the electronic density are calculated at critical point between H and X(Mg, O, Mo) at hybrid B3PW91 level (Fig. 7 and Table S2). The density of all electrons at H–Mo bonding critical point is much smaller than that those at H–Mg and H–O critical point, which can be ascribed to the influence of the high affinity and electron delocalization effect of the metallic molybdenum substrate at D3 state. The spin density of electrons defined as the difference between alpha and beta density at H–Mo critical point is largest compared with those at H–O and H–Mg critical points, due to the high multiplicity of 4d orbitals.

Potential energy density V(r) can be obtained by formula:

$$V(r) = -K(r) - G(r) = (1/4)\nabla^2\rho cp - 2G(r) \quad (2)$$

At the H–Mg critical point V(r) is positive while V(r) at H–Mo and H–O critical point is negative, which suitably reconfirm the high electron affinity of surface oxygen and molybdenum. Electron localization function and localized orbital locator at H–Mg and H–Mo critical points are significantly larger than those at H–O critical point, indicating the strong electron motion ability at the dissociation site of D1 and D3 state. However, at D2 state, the bonding electrons is significantly confined at regions around critical point. As Laplacian of electron density fluctuate violently and complicatedly near nuclei, the integration method based on mixed atomic-center and uniform grids is employed to obtain high accuracy. The Laplacian value could be obtained by formula:

$$\nabla^2\rho cp = 4 \times (G(r) - K(r)) \quad (3)$$

where the G(r) and K(r) are Hamiltonian kinetic energy density and Lagrangian kinetic energy density, respectively. The absolute value of Laplacian at H–Mo critical point is very small, which is another evidence for electron delocalization. On the contrary, the Laplacian at H–O and H–Mg critical point show large values, verifying the high affinity of oxygen and electron-donating feature of ultrathin magnesia.

In order to better understand the nature of the unique dissociation properties of H_2 at interfacially defected magnesia, we have calculated the differential charge density contour, electronic density plots, HOMO and particular orbitals with largest MO coefficiencies, and electron localization function of H_2 fragmentation state with lowest total energy (Fig. 8). Actually the related electronic property analysis is of significantly importance because local environment of the active centers may impact adsorption and dissociation activity greatly. The regions around H1 show obvious electron loss, and the areas around surface oxygen O1 show electron accumulation (Fig. S4). Generally the differential charge contour is consistent with the result of integrated projected density of

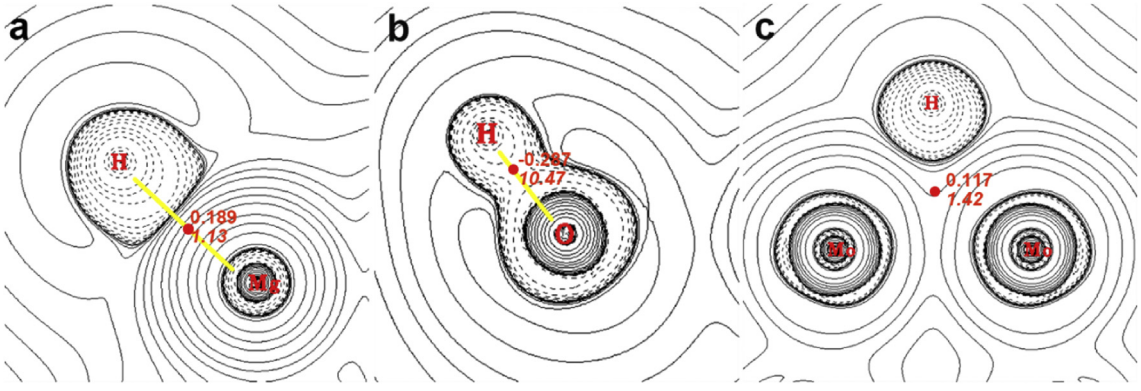

Fig. 7 – Contour line diagrams of the Laplacian of the electronic density of H–Mg (a), H–O (b) and H–Mo (c) bonding structure at hybrid B3PW91 level. Dotted lines represent regions of charge concentrations ($\nabla^2\rho(r) < 0$), and solid lines represent regions of charge depletion ($\nabla^2\rho(r) < 0$). The red spheres are (3, −1) type critical points between H-X (X = Mg, O, Mo) with $|V_{cp}|/G_{cp}$ values and Laplacian values in red regular and italic fonts respectively. (For interpretation of the references to color in this figure legend, the reader is referred to the Web version of this article.)

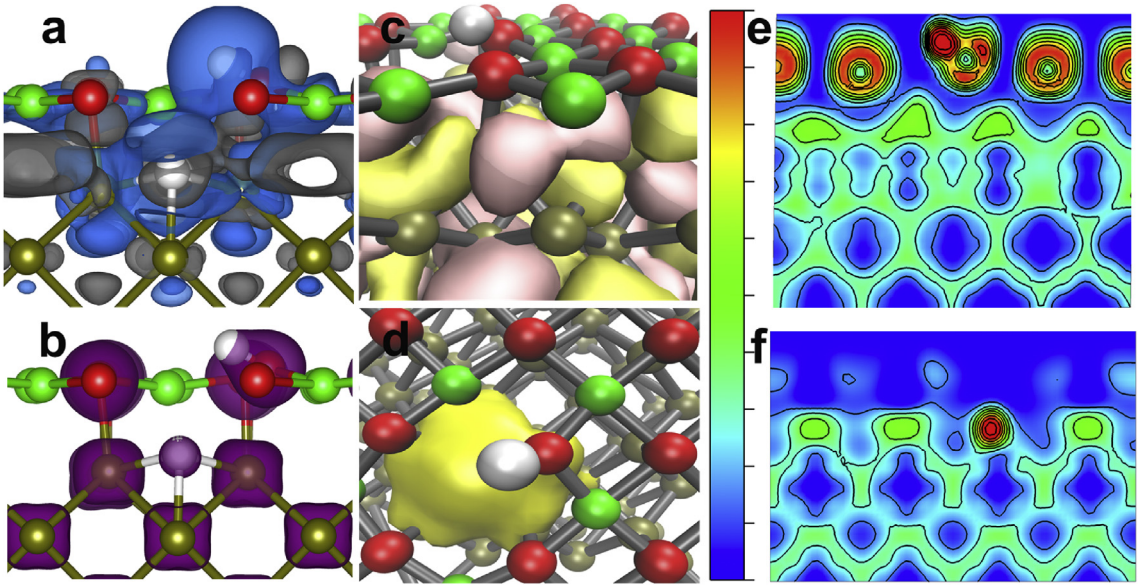

Fig. 8 – (a) Differential charge density of H_2 fragmentation at newfound D4 state, which is defined as $\Delta\rho = \rho$(Total) - ρ(adsorbate) - ρ(oxide) - ρ(substrate) (with isovalue set to be 0.002 e Bohr^{-3}). The areas withdrawing electrons and depleting electrons are indicated by blue and gray colors, respectively. (b) Contour plots of the charge density with isovalue of 0.008 e Bohr^{-3}. (c, d) Selected orbital diagrams of the highest occupied molecular orbital (HOMO, top panel) and the molecular orbital with the largest MO coefficient for H2(-Mo) (bottom panel). The isovalues are set to be ±0.08. (e, f) Slice views of the electron localization function parallel to (16.1, −18, 0.7) and (0, −1, 0) planes. Interval of the contour line is 0.1. Electron localization effect and electron delocalization effect are represented by red and blue colors, respectively. (For interpretation of the references to color in this figure legend, the reader is referred to the Web version of this article.)

states (O1-2p orbital and H1-1s orbital, Fig. S5). In case of H_2 dissociation, the magnesia film shows both oxidation ability and reduction ability. The reducibility with electron loss is the critical feature of the ultrathin magnesia. The oxidation ability obviously embodies in the gray areas between hydrogen adatom and surface oxygen, and the areas between interfacial oxygen and the molybdenum atoms beneath (Fig. 8a). The areas around dissociated product H2 show electron gain. The interfacial area between magnesia film and molybdenum slab show obvious electron accumulation, indicating the H_2 fragmentation doesn't seriously affect the strength of oxygen-molybdenum covalent bonding interaction. The inert regions of metal slab show electron accumulation feature suggesting the much higher electron affinity compared with the hydrogen adsorbates.

According to the contour plots of the charge density, the ionic bonding character of O–Mg is still robust after H_2 splitting (Fig. 8b). Evident charge density contour could be found between hydrogen adatom and the surface oxygen, indicating the formation of shared electron pair and strong covalent bonding force. Plenty charge density distribute around all the molybdenum atoms due to the richness of valence electrons of molybdenum. In the electron density contour, the regions around the hydrogen permeated into interface show non-negligible electron density. The highest occupied molecular orbital with energy level 0.808 eV higher than Fermi energy is depicted in Fig. 8c. The highest occupied orbital is mainly distributed at the substrate demonstrating that the substrate combined with the oxide film preserves typical metallic property after H_2 dissociation. The particular orbital exhibiting largest MO coefficients for H–Mo bonds demonstrates that extensive bonding interaction forms between hydrogen and the surrounding molybdenum atoms. As the s-shaped σ orbital involves more than one bonding axis, the dissociated hydrogen should form multicenter bond with adjacent molybdenum atoms (Fig. 8d). The graphical language of electron localization function is of significant practicability and importance for providing a new description of the chemical bonds in almost all classes of compounds [79]. Slice views of the electron localization function parallel to (16.1, −18, 0.7) and (0, −1, 0) planes are depicted to reveal the electron localization or delocalization effect in the interfacially defected oxide-metal hybrid structure in case of H_2 dissociation. The molybdenum mainly exhibits electron delocalization, which is consistent the maintenance of typical metallic property in the electron density analysis. The region between dissociated H1 and surface O1 shows significant electron localization, further indicating the formation of strong covalent bonding interaction. The dissociated hydrogen H2 which permeates into the interface region shows apparent electron localization effect, indicating the potential ionic bonding component in H–Mo bonds.

Conclusions

In summary, generation of molybdenum hydride species on monolayer oxide/metal composite via addition of molecular hydrogen across metal-oxygen bond is investigated for the first time utilizing periodic Van der Waals density-functional

calculations. Lewis acid-base pair constructed by the interfacially defected oxide film and the metal support provides novel active sites for activating H_2. The produced heterolytic dissociative state exhibits negative dissociative adsorption energy of −0.315 eV which thermodynamically facilitate the fragmentation process of H_2 on insulating oxide films. The obtained minimum energy pathways for splitting H_2 on interfacially defected monolayer magnesia (100) confirm the feasibility of a novel heterolytic dissociation state of H_2 from perspective of reaction dynamics. In order to better understand the nature of the unique dissociation properties of H_2 at interfacially defected monolayer oxide, the Bader charge population, differential charge density contour, electronic density plots, particular orbitals with largest MO coefficiencies and electron localization function of H_2 fragmentation are interpreted. To quantify the influence of H_2 coverage, the structural configuration, work function, surface distortion, energetics and reaction dynamics are calculated for favorable heterolytic splitting behavior with high coverages. It is anticipated that the results here could provide useful clue for enhancing the reactivity of insulating oxide toward activating H_2.

Acknowledgments

This work was financially supported by the National Natural Science Foundation of China (NSFC grants 21375092, 21976129 and 21575097), the Science and Technology Planning Project 1901GY21 (Taizhou Science and Technology Bureau), Chemical Engineering & Technology of Zhejiang Province First-Class Discipline (Taizhou University) and the Scientific Research Cultivation Project 2018PY023 (Taizhou University).

Appendix A. Supplementary data

Supplementary data to this article can be found online at https://doi.org/10.1016/j.ijhydene.2019.11.135.

REFERENCES

[1] Jia J, Qian CX, Dong YC, Li YF, Wang H, Ghoussoub M, Butler KT, Walsh A, Ozin GA. Heterogeneous catalytic hydrogenation of CO_2 by metal oxides: defect engineering - perfecting imperfection. Chem Soc Rev 2017;46:4631–44.
[2] Liu JC, Wang YG, Li J. Toward rational design of oxide-supported single-atom catalysts: atomic dispersion of gold on ceria. J Am Chem Soc 2017;139:6190–9.
[3] Di Liberto G, Tosoni S, Pacchioni G. Role of heterojunction in charge carrier separation in coexposed anatase (001)-(101) surfaces. J Phys Chem Lett 2019;10:2372–7.
[4] Freund HJ, Pacchioni G. Oxide ultra-thin films on metals: new materials for the design of supported metal catalysts. Chem Soc Rev 2008;37:2224–42.
[5] Azad UP, Singh M, Ghosh S, Singh AK, Ganesan V, Singh AK, Prakash R. Facile synthesis of BSCF perovskite oxide as an efficient bifunctional oxygen electrocatalyst. Int J Hydrogen Energy 2018;43:20671–9.
[6] Wang YG, Yoon Y, Glezakou VA, Li J, Rousseau R. The role of reducible oxide-metal cluster charge transfer in catalytic processes: new insights on the catalytic mechanism of CO oxidation on Au/TiO_2 from ab Initio molecular dynamics. J Am Chem Soc 2013;135:10673–83.
[7] Giordano L, Pacchioni G. Oxide films at the nanoscale: new structures, new functions, and new materials. Acc Chem Res 2011;44:1244–52.
[8] Pesci M, Gallino F, Di Valentin C, Pacchioni G. Nature of defect states in nitrogen-doped MgO. J Phys Chem C 2010;114:1350–6.
[9] Zhao ZJ, Li ZL, Cui YR, Zhu HY, Schneider WF, Delgass WN, Ribeiro F, Greeley J. Importance of metal-oxide interfaces in heterogeneous catalysis: a combined DFT, microkinetic, and experimental study of water-gas shift on Au/MgO. J Catal 2017;345:157–69.
[10] Wang C-M, Fan K-N, Liu Z-P. Origin of oxide sensitivity in gold-based catalysts: a first principle study of CO oxidation over Au supported on monoclinic and tetragonal ZrO_2. J Am Chem Soc 2007;129:2642–7.
[11] Wang AQ, Li J, Zhang T. Heterogeneous single-atom catalysis. Nat Rev Chem 2018;2:65–81.
[12] Liang JX, Yu Q, Yang XF, Zhang T, Li J. A systematic theoretical study on FeOx-supported single-atom catalysts: M-1/FeOx for CO oxidation. Nano Res 2018;11:1599–611.
[13] Tosoni S, Pacchioni G. Trends in adhesion energies of gold on MgO(100), rutile TiO_2(110), and CeO_2(111) surfaces: a comparative DFT study. J Phys Chem C 2017;121:28328–38.
[14] Konig T, Simon GH, Martinez U, Giordano L, Pacchioni G, Heyde M, Freund HJ. Direct measurement of the attractive interaction forces on F-0 Color centers on MgO(001) by dynamic force microscopy. ACS Nano 2010;4:2510–4.
[15] Di Valentin C, Pacchioni G, Selloni A. Electronic structure of defect states in hydroxylated and reduced rutile TiO_2(110) surfaces. Phys Rev Lett 2006;97:166803.
[16] Chanda D, Basu S. Electrochemical synthesis of Li-doped NiFeCo oxides for efficient catalysis of the oxygen evolution reaction in an alkaline environment. Int J Hydrogen Energy 2018;43:21999–2011.
[17] Damascena dos Passos RH, Pereira de Souza C, Leroux C, Arab M. Catalytic properties of $Sr_{1-x}Ce_xWO_4$: the role of mixed conduction in methane oxidation. Int J Hydrogen Energy 2018;43:15918–30.
[18] Mumtaz A, Mohamed NM, Irshad MI, Yar A, Mohamed Saheed MS. Mutual effect of extrinsic defects and electronic carbon traps of M-TiO_2 (M = V, Co, Ni) nanorod arrays on photoexcited charge extraction of CdS for superior photoelectrochemical activity of hydrogen production. Int J Hydrogen Energy 2018;43:14388–405.
[19] Tosoni S, Li C, Schlexer P, Pacchioni G. CO adsorption on graphite-like ZnO bilayers supported on Cu(111), Ag(111), and Au(111) surfaces. J Phys Chem C 2017;121:27453–61.
[20] Song Z, Zhao B, Xu H, Cheng P. Remarkably strong chemisorption of nitric oxide on insulating oxide films promoted by hybrid structure. J Phys Chem C 2017;121:21482–90.
[21] Giordano L, Ferrari AM. Modified ion pair interaction for water dimers on supported MgO ultrathin films. J Phys Chem C 2012;116:20349–55.
[22] Song ZJ, Xu H. Unusual dissociative adsorption of H-2 over stoichiometric MgO thin film supported on molybdenum. Appl Surf Sci 2016;366:166–72.
[23] Chen HYT, Giordano L, Pacchioni G. From heterolytic to homolytic H_2 dissociation on nanostructured MgO(001) films as a function of the metal support. J Phys Chem C 2013;117:10623–9.

[24] Song Z, Zhao B, Wang Q, Cheng P. Homolytic cleavage of water on magnesia film promoted by interfacial oxide-metal nanocomposite. Appl Surf Sci 2019;487:1222–32.
[25] Song Z, Zhao B, Wang Q, Cheng P. Steering reduction and decomposition of peroxide compounds by interface interactions between MgO thin film and transition-metal support. Appl Surf Sci 2018;459:812–21.
[26] Song Z, Fan J, Shan Y, Ng AMC, Xu H. Generation of highly reactive oxygen species on metal-supported MgO(100) thin films. Phys Chem Chem Phys 2016;18:25373–9.
[27] Nordio M, Rizzi F, Manzolini G, Mulder M, Raymakers L, Annaland MV, Gallucci F. Experimental and modelling study of an electrochemical hydrogen compressor. Chem Eng J 2019;369:432–42.
[28] Wang ZY, Xu L, Huang FZ, Qu LB, Li JT, Owusu KA, Liu Z, Lin ZF, Xiang BH, Liu X, Zhao KN, Liao XB, Yang W, Cheng YB, Mai LQ. Copper-nickel nitride nanosheets as efficient bifunctional catalysts for hydrazine-assisted electrolytic hydrogen production. Adv Energy Mater 2019;9:11.
[29] Numpilai T, Wattanakit C, Chareonpanich M, Limtrakul J, Witoon T. Optimization of synthesis condition for CO_2 hydrogenation to light olefins over In_2O_3 admixed with SAPO-34. Energy Convers Manag 2019;180:511–23.
[30] Lonis F, Tola V, Cau G. Renewable methanol production and use through reversible solid oxide cells and recycled CO_2 hydrogenation. Fuel 2019;246:500–15.
[31] Tosoni S, Pacchioni G. Hydrogen adsorption on free-standing and Ag-Pt supported TiO_2 thin films. J Phys Chem C 2019;123:7952–60.
[32] Vecchietti J, Baltanas MA, Gervais C, Collins SE, Blanco G, Matz O, Calatayud M, Bonivardi A. Insights on hydride formation over cerium-gallium mixed oxides: a mechanistic study for efficient H-2 dissociation. J Catal 2017;345:258–69.
[33] Henderson MA, Dahal A, Dohnalek Z, Lyubinetsky I. Strong temperature dependence in the reactivity of H-2 on RuO_2(110). J Phys Chem Lett 2016;7:2967–70.
[34] Dahal A, Mu RT, Lyubinetsky I, Dohnalek Z. Hydrogen adsorption and reaction on RuO_2(110). Surf Sci 2018;677:264–70.
[35] Li T, Kim M, Liang Z, Asthagiri A, Weaver JF. Dissociative chemisorption and oxidation of H-2 on the stoichiometric IrO_2(110) surface. Top Catal 2018;61:397–411.
[36] Wang JH, Fan CY, Sun Q, Reuter K, Jacobi K, Scheffler M, Ertl G. Surface coordination chemistry: dihydrogen versus hydride complexes on RuO_2(110). Angew Chem Int Ed 2003;42:2151–4.
[37] Jacobs R, Zheng B, Puchala B, Voyles PM, Yankovich AB, Morgan D. Counterintuitive reconstruction of the polar O-terminated ZnO surface with zinc vacancies and hydrogen. J Phys Chem Lett 2016;7:4483–7.
[38] Martins JBL, Longo E, Taft CA, Andrés J. Ab initio and semiempirical MO studies using large cluster models of CO and H_2 adsorption and dissociation on ZnO surfaces with the formation of ZnH and OH species. J Mol Struct: THEOCHEM 1997;397:147–57.
[39] Nyberg M, Nygren MA, Pettersson LGM. Hydrogen dissociation on reconstructed ZnO surfaces. J Phys Chem 1996;100:9054–63.
[40] Kim S, Lai WS. Hydrogen diffusion behavior and vacancy interaction behavior in OsO_2 and RuO_2 by ab initio calculations. Comput Mater Sci 2015;102:14–20.
[41] Huang Z-Q, Liu L-P, Qi S, Zhang S, Qu Y, Chang C-R. Understanding all-solid frustrated-lewis-pair sites on CeO_2 from theoretical Perspectives. ACS Catal 2018;8:546–54.
[42] Zhang S, Huang Z-Q, Ma Y, Gao W, Li J, Cao F, Li L, Chang C-R, Qu Y. Solid frustrated-Lewis-pair catalysts constructed by regulations on surface defects of porous nanorods of CeO_2. Nat Commun 2017;8:15266.
[43] Zhang Q, Feng XQ, Liu J, Zhao LP, Song XF, Zhang P, Gao L. Hollow hierarchical Ni/MgO-SiO2 catalyst with high activity, thermal stability and coking resistance for catalytic dry reforming of methane. Int J Hydrogen Energy 2018;43:11056–68.
[44] Coenen K, Gallucci F, Hensen E, Annaland MV. CO_2 and H_2O chemisorption mechanism on different potassium-promoted sorbents for SEWGS processes. J CO2 Util 2018;25:180–93.
[45] Zhang Y, Chen HS. Surface adsorption and encapsulated storage of H-2 molecules in a cagelike (MgO)(12) cluster. Int J Hydrogen Energy 2018;43:16609–16.
[46] Mortazavi SZ, Reyhani A, Mirershadi S. Hydrogen storage properties of multi-walled carbon nanotubes and carbon nano-onions grown on single and bi-catalysts including Fe, Mo, Co and Ni supported by MgO. Int J Hydrogen Energy 2017;42:24885–96.
[47] Jin LJ, Ma BX, Zhao S, He X, Li Y, Hu HQ, Lei Z. Ni/MgO-Al_2O_3 catalyst derived from modified Ni,Mg,Al -LDH with NaOH for CO_2 reforming of methane. Int J Hydrogen Energy 2018;43:2689–98.
[48] Thyssen VV, Georgetti F, Assaf EM. Influence of MgO content as an additive on the performance of Ni/MgO-SiO_2 catalysts for the steam reforming of glycerol. Int J Hydrogen Energy 2017;42:16979–90.
[49] Blöchl PE. Projector augmented-wave method. Phys Rev B Condens Matter Mater Phys 1994;50:17953–79.
[50] Grimme S, Antony J, Ehrlich S, Krieg H. A consistent and accurate ab Initio parametrization of density functional dispersion correction (DFT-D) for the 94 elements H-Pu. J Chem Phys 2010;132:154104.
[51] Kresse G, Joubert D. From ultrasoft pseudopotentials to the projector augmented-wave method. Phys Rev B Condens Matter Mater Phys 1999;59:1758–75.
[52] Perdew JP, Burke K, Ernzerhof M. Generalized gradient approximation made simple. Phys Rev Lett 1996;77:3865–8.
[53] Perdew JP, Burke K, Ernzerhof M. Generalized gradient approximation made simple [Phys. Rev. Lett. Phys Rev Lett 1996;77:3865. 1997;78:1396.
[54] Grimme S, Ehrlich S, Goerigk L. Effect of the damping function in dispersion corrected density functional theory. J Comput Chem 2011;32:1456–65.
[55] Karen P, Kjekshus A, Huang Q, Karen VL. The crystal structure of magnesium dicarbide. J Alloy Comp 1999;282:72–5.
[56] Stewart GR, Giorgi AL. Specific heat of bcc $Mo_{1-x}Tc_x$. Phys Rev B Condens Matter Mater Phys 1979;19:5704–10.
[57] Henkelman G, Arnaldsson A, Jónsson H. A fast and robust algorithm for Bader decomposition of charge density. Comput Mater Sci 2006;36:354–60.
[58] Sanville E, Kenny SD, Smith R, Henkelman G. Improved grid-based algorithm for Bader charge allocation. J Comput Chem 2007;28:899–908.
[59] Henkelman G, Jónsson H. Improved tangent estimate in the nudged elastic band method for finding minimum energy paths and saddle points. J Chem Phys 2000;113:9978–85.
[60] Henkelman G, Uberuaga BP, Jónsson H. A climbing image nudged elastic band method for finding saddle points and minimum energy paths. J Chem Phys 2000;113:9901–4.
[61] Kresse G, Hafner J. Ab initio molecular dynamics for liquid metals. Phys Rev B Condens Matter Mater Phys 1993;47:558–61.
[62] Kresse G, Furthmüller J. Efficient iterative schemes for ab Initio total-energy calculations using a plane-wave basis set. Phys Rev B Condens Matter Mater Phys 1996;54:11169–86.
[63] Wang Y, Lv J, Zhu L, Ma Y. Crystal structure prediction via particle-swarm optimization. Phys Rev B Condens Matter Mater Phys 2010;82:094116.

[64] Lv J, Wang Y, Zhu L, Ma Y. Particle-swarm structure prediction on clusters. J Chem Phys 2012;137:084104.
[65] Wang Y, Lv J, Zhu L, Ma Y. CALYPSO: a method for crystal structure prediction. Comput Phys Commun 2012;183:2063–70.
[66] Becke AD. Density-functional thermochemistry. III. the role of exact exchange. J Chem Phys 1993;98:5648–52.
[67] Becke AD. A new mixing of Hartree–Fock and local density-functional theories. J Chem Phys 1993;98:1372–7.
[68] Lee C, Yang W, Parr RG. Development of the colle-salvetti correlation-energy formula into a functional of the electron density. Phys Rev B Condens Matter Mater Phys 1988;37:785–9.
[69] Frisch MJ, Trucks GW, Schlegel HB, Scuseria GE, Robb MA, Cheeseman JR, Scalmani G, Barone V, Mennucci B, Petersson GA, Nakatsuji H, Caricato M, Li X, Hratchian HP, Izmaylov AF, Bloino J, Zheng G, Sonnenberg JL, Hada M, Ehara M, Toyota K, Fukuda R, Hasegawa J, Ishida M, Nakajima T, Honda Y, Kitao O, Nakai H, Vreven T, Montgomery JAJ, Peralta JE, Ogliaro F, Bearpark M, Heyd JJ, Brothers E, Kudin KN, Staroverov VN, Kobayashi R, Normand J, Raghavachari K, Rendell A, Burant JC, Iyengar SS, Tomasi J, Cossi M, Rega N, Millam JM, Klene M, Knox JE, Cross JB, Bakken V, Adamo C, Jaramillo J, Gomperts R, Stratmann RE, Yazyev O, Austin AJ, Cammi R, Pomelli C, Ochterski JW, Martin RL, Morokuma K, Zakrzewski VG, Voth GA, Salvador P, Dannenberg JJ, Dapprich S, Daniels AD, Farkas Ö, Foresman JB, Ortiz JV, Cioslowski J, Fox DJ. Gaussian 09, revision D01. Wallingford, CT: Gaussian, Inc.; 2013.
[70] Lu T, Chen F. Multiwfn: a multifunctional wavefunction analyzer. J Comput Chem 2012;33:580–92.
[71] Wang Y. VASPMO, version 031. 2016. https://sourceforge.net/projects/vaspmo/. [Accessed 24 October 2016].
[72] Momma K, Izumi F. VESTA: a three-dimensional visualization system for electronic and structural analysis. J Appl Crystallogr 2008;41:653–8.
[73] Humphrey W, Dalke A, Schulten K. VMD: visual molecular dynamics. J Mol Graph 1996;14:33–8.
[74] Wang X, Andrews L. Matrix infrared spectra and density functional theory calculations of molybdenum hydrides. J Phys Chem A 2005;109:9021–7.
[75] Perutz RN, Procacci B. Photochemistry of transition metal hydrides. Chem Rev 2016;116:8506–44.
[76] Hammond GS. A correlation of reaction rates. J Am Chem Soc 1955;77:334–8.
[77] Spreafico C, Karim W, Ekinci Y, van Bokhoven JA, VandeVondele J. Hydrogen adsorption on nanosized platinum and dynamics of spillover onto alumina and titania. J Phys Chem C 2017;121:17862–72.
[78] García-Melchor M, López N. Homolytic products from heterolytic paths in H_2 dissociation on metal oxides: the example of CeO_2. J Phys Chem C 2014;118:10921–6.
[79] Savin A, Nesper R, Wengert S, Fässler TF. ELF: the electron localization function. Angew Chem Int Ed 1997;36:1808–32.

Applied Physics Letters

Quantum-confinement-induced periodic surface states in two-dimensional metal-organic frameworks

Cite as: Appl. Phys. Lett. **117**, 191601 (2020); https://doi.org/10.1063/5.0026372
Submitted: 24 August 2020 . Accepted: 26 October 2020 . Published Online: 09 November 2020

Chun-Sheng Zhou, Xiang-Rui Liu, Yue Feng, Xiji Shao, Meng Zeng, Kedong Wang, Min Feng, and Chang Liu

Applied Physics Letters ARTICLE scitation.org/journal/apl

Quantum-confinement-induced periodic surface states in two-dimensional metal-organic frameworks

Cite as: Appl. Phys. Lett. **117**, 191601 (2020); doi: 10.1063/5.0026372
Submitted: 24 August 2020 · Accepted: 26 October 2020 ·
Published Online: 9 November 2020

Chun-Sheng Zhou,[1,2] Xiang-Rui Liu,[1] Yue Feng,[1] Xiji Shao,[1] Meng Zeng,[1] Kedong Wang,[1] Min Feng,[2] and Chang Liu[1,a)]

AFFILIATIONS

[1]Shenzhen Institute for Quantum Science and Engineering (SIQSE) and Department of Physics, Southern University of Science and Technology, Shenzhen 518055, China

[2]School of Physics and Technology and Key Laboratory of Artificial Micro- and Nano-Structures of Ministry of Education, Wuhan University, Wuhan 430072, China

[a)]Author to whom correspondence should be addressed: liuc@sustech.edu.cn

ABSTRACT

Recently, a series of single-layer metal–organic frameworks (MOFs) was theoretically predicted to be two-dimensional organic topological materials. However, the experimental evidence of their nontrivial topological states has not been found. Here, combining the use of angle-resolved photoemission spectroscopy and scanning tunneling microscopy, we report the electronic structure studies on a single-layer Cu-coordinated 2,4,6-tri(4-pyridyl)-1,3,5-triazine (Cu-T4PT) MOF supported by a Cu(111) substrate and identify periodic surface states with the period of the Cu-T4PT reciprocal lattice. These periodic surface states, which have identical features to the Cu(111) Shockley surface states, can be attributed to the quantum confinement of the surface states of the underlying Cu(111) substrate by the network lattices of the Cu-T4PT MOF. Our work indicates that the surface states of the metal substrate can be tailored in a controlled manner by the network structures of MOFs with different periodic lattices. The lack of intrinsic bands and the possible topological properties of the single-layer Cu-T4PT MOF may be attributed to the strong electronic coupling between the Cu-T4PT MOF and the Cu(111) substrates. In order to exploit organic topological materials predicted in MOFs, it is necessary to grow them on weak van der Waals interaction substrates in the future.

Over the last two decades, metal–organic frameworks (MOFs), which are architecturally robust crystalline porous materials composed of metal-containing nodes (metal ions or clusters) and organic linkers connected by coordination bonds, have attracted significant interest due to their potential applications in gas storage, gas/liquid separation and purification, catalysis, chemical sensors, luminescence, electronic devices, biomedicine, food safety, and so on.[1–12] Recently, there are many theoretical articles based on first-principles band structure calculations that predict a class of two-dimensional (2D) organic topological materials made of single-layer MOFs,[13–21] but their existence has not been confirmed by experiments so far. In contrast to the conventional inorganic topological materials,[22–31] organic topological materials have the advantages of low cost, easy fabrication, less sensitivity against oxidation, mechanical flexibility, and high tunability through functionalizing the organic components, which will greatly increase the potential for technological applications of topological materials.

The band structure of a solid material can be directly obtained by angle-resolved photoemission spectroscopy (ARPES)[32–34] in momentum space (**k**-space) or deduced from the quasi-particle interference (QPI) patterns[35–41] in scattering wave vector space (**q**-space) performed by Fourier transform of real-space (**r**-space) scanning tunneling spectroscopy (FT-STS); the former is a surface-averaging experimental technique probing only the occupied bands, whereas the latter is a local technique probing both the occupied and unoccupied bands. To date, several experimental groups have reported the band structures of substrate-supported single-layer MOFs based on ARPES[42] or QPI studies.[43,44] Using ARPES, Lobo-Checa *et al.*[42] reported a shallow dispersive 2D electronic band structure formed by electronic coupling of the trapped surface-states of the underlying Cu(111) substrate confined inside the periodic pores of the Cu-coordinated 4,9-diaminoperylene-quinone-3,10-diimine (DPDI) MOF. With the help of FT-STS, Wang *et al.*[43] investigated the

modulation of 2D electron gas of Cu(111) surface-state electrons confined in three different MOFs and found that the 2D electronic structures can be tailored by the periodicity and constituent components of MOFs. Kumar *et al.*[44] also performed QPI studies based on FT-STS and demonstrated the formation of a 2D band structure in a Co-coordinated 9,10-dicyanoanthracene (DCA) MOF synthesized on epitaxial graphene grown on an Ir(111) substrate. However, all these reports merely rely on one of the two complementary experimental techniques mentioned above. In order to provide a full understanding of the physics of a material, it is beneficial to simultaneously take advantage of these two complementary techniques. Most recently, Piquero-Zulaica *et al.*[45] study the scattering potentials and confinement properties of 2D Cu-coordinated 1,3,5-tri(4-pyridyl)-benzene (TPyB) MOFs by means of both ARPES and FT-STS. They found almost unperturbed free-electron-like states stemming from the weak electron confinement and enhanced interpore coupling, which is the combined action of the TPyB molecules acting as the dominant scatterers and the coordination metal Cu atoms acting as transmission channels for the surface electrons. Although they reported some qualitative similarities of the band dispersions between ARPES and FT-STS results, a direct and quantitative comparison is lacking, which is highly desirable for us to understand the band structure of a material.

Many theoretically proposed single-layer MOF structures have been predicted to be 2D organic topological materials,[13,14,16] but their syntheses are difficult to implement in the experiments. The experimentally synthesized Cu-coordinated 2,4,6-tri(4-pyridyl)-1,3,5-triazine (T4PT) MOF[46] has a similar honeycomb structure to the single-layer Cu-coordinated TPyB MOF, which was theoretically predicted to be a 2D organic topological material;[47] hence, the topologically nontrivial bands may also exist in the single-layer Cu-T4PT MOF. In this Letter, combining the complementary ARPES and FT-STS experimental techniques, we exploit the electronic structure of the single-layer Cu-T4PT MOF grown on a Cu(111) substrate and find quantum-confinement-induced surface-state bands with the period of the Cu-T4PT reciprocal lattice. The direct and quantitative comparison of the band dispersions extracted from these two experimental techniques shows excellent agreement, which indicates that the surface-averaging ARPES technique and the local FT-STS technique can provide consistent conclusions for probing and characterizing the surface states of the substrate-supported single-layer MOF.

The experiments were carried out in an ultrahigh vacuum (UHV) system equipped with molecular beam epitaxy (MBE), scanning tunneling microscopy (STM), and ARPES. A polished Cu(111) single crystal (99.999%, MaTecK GmbH) was used as the substrate. A clean and atomically flat Cu(111) surface was obtained by several cycles of Ar^+ sputtering and annealing in the MBE chamber with a base pressure of 3×10^{-10} mbar. T4PT molecules were deposited onto the clean Cu(111) surface by thermal evaporation from a 3-cell organic evaporator (Kentax GmbH), with the substrates at room temperature. No further annealing was carried out after the evaporation. The spontaneous growth of the room-temperature stable Cu-T4PT MOF was monitored *in situ* by low emission reflection high-energy electron diffraction (PICO-RHEED, R-DEC Co., Ltd.) in order to reduce the damage to the organic thin films from the high energy electron beam. Then, the sample was immediately transferred to the STM and ARPES chambers for further characterizations. The STM experiments were carried out with a low-temperature SPECS JT-STM operated at a pressure lower than 1×10^{-10} mbar. All the STM results shown in the present work were performed at 5 K to ensure the high quality and resolution of images and spectra. STM data were analyzed using the WSxM software.[48] The ARPES measurements were performed using a laboratory-based ARPES system consisting of a SPECS PHOIBOS 150 electron analyzer and a UVLS-600 UV lamp at a pressure lower than 1×10^{-9} mbar. The incident photon energy was 21.218 eV (He I), and the spot diameter was about 500 micrometers.

As shown in Fig. 1(a), the T4PT molecule consists of a triazine ring bonded covalently to three pyridyl rings with threefold rotational symmetry. When deposited onto a clean Cu(111) surface, T4PT molecules are prone to bond with the Cu adatoms of the substrate, forming the room-temperature stable single-layer Cu-T4PT MOF. Figure 1(b) shows a close-up STM image of the single-layer Cu-T4PT MOF with a honeycomb structure synthesized on Cu(111), which is in agreement

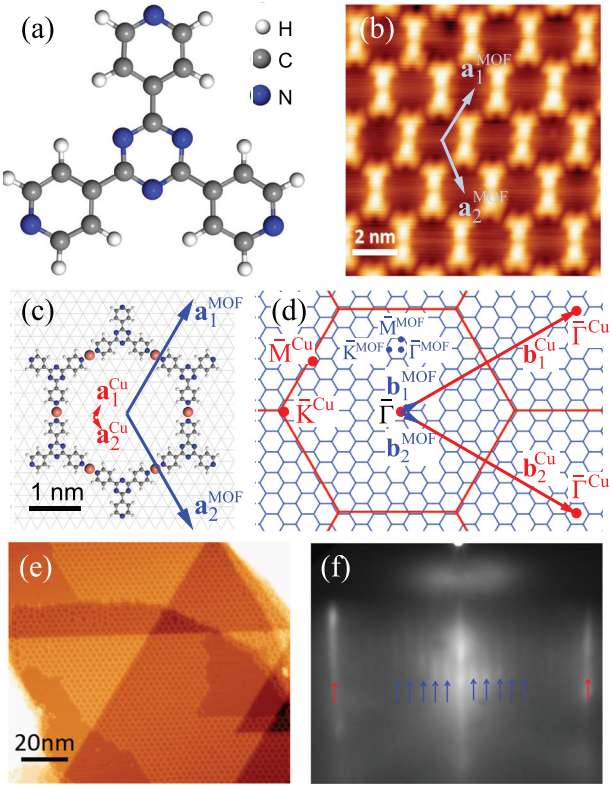

FIG. 1. (a) The molecular structure of T4PT. (b) A close-up STM image of Cu-T4PT MOFs obtained at 0.1 V. The lattice vectors $\mathbf{a}_{1,2}^{MOF}$ are marked. (c) The structure model of the Cu-T4PT MOF on a Cu(111) surface. (Reproduced with permission from Umbach *et al.*, Phys. Rev. B **89**, 235409 (2014). Copyright 2014 American Physical Society.) The lattice vectors $\mathbf{a}_{1,2}^{Cu}$ of Cu(111) are indicated by red arrows. The lattice vectors $\mathbf{a}_{1,2}^{MOF}$ of the Cu-T4PT MOF are indicated by blue arrows. Substrate Cu atoms are indicated by cross points of the gray lines. (d) The Brillouin zones of the Cu-T4PT MOF (blue hexagons) and the underlying Cu(111) substrate (red hexagon). The reciprocal lattice vectors $\mathbf{b}_{1,2}^{Cu}$ of Cu(111) and $\mathbf{b}_{1,2}^{MOF}$ of the Cu-T4PT MOF are indicated by red and blue arrows, respectively. (e) Large-scale STM image for submonolayer coverage of the Cu-T4PT MOF on Cu(111). (f) RHEED pattern of the Cu-T4PT MOF film taken after the MBE growth. The streaks of the Cu(111) substrate and Cu-T4PT MOF are marked by the red and blue arrows, respectively.

with the results reported by Umbach *et al.*[46] In Fig. 1(c), we illustrate the structural model of the Cu-T4PT MOF adapted from Ref. 46, wherein each T4PT molecule is linked to three T4PT molecules via pyridyl-Cu-pyridyl coordination bonds. The unit-cell lattice vectors of the Cu-T4PT MOF ($\mathbf{a}_{1,2}^{MOF}$) and the underlying Cu(111) substrate ($\mathbf{a}_{1,2}^{Cu}$) are indicated in Figs. 1(b) and 1(c). Here, $\mathbf{a}_1^{MOF} = \mathbf{a}_2^{MOF} = 25.3$ Å according to our measurements, which agrees well with the result in Ref. 46 where $\mathbf{a} = 25$ Å. It is clear in the structural model [Fig. 1(c)] that $\mathbf{a}_{1,2}^{MOF} = 10\,\mathbf{a}_{1,2}^{Cu}$, corresponding to a (10×10) unit cell. Figure 1(d) shows the corresponding Brillouin zones of the Cu-T4PT MOF (blue hexagons) and the Cu(111) substrate (red hexagon); the reciprocal lattice vectors ($\mathbf{b}_{1,2}^{MOF}$, $\mathbf{b}_{1,2}^{Cu}$) and high symmetry points (Γ, M, K) are also marked. In Fig. 1(e), a large-scale STM image of the Cu-T4PT MOF is shown. It is evident that a single rotational domain is present on the surface over different terraces, which is further supported by the streaky RHEED pattern shown in Fig. 1(f). Figure 1(f) shows two sets of streaks, which are associated with the Cu(111) substrate (red arrows) and the Cu-T4PT MOF (blue arrows). The streak spacing between the red arrows is about 10 times that of the blue ones, indicating that the in-plane lattice constant of the Cu-T4PT MOF is 10 times that of Cu(111), which is consistent with our STM results.

To establish the electronic structure of the single-layer Cu-T4PT MOF supported by a Cu(111) substrate, we performed ARPES measurements on a submonolayer-coverage sample similar to the one shown in Fig. 1(e). Figure 2(a) shows the room temperature ARPES constant-energy contours with different binding energies E_b. Obviously, a ring-like electron pocket with high intensity centered at the Γ point exists in all constant-energy maps, which can be mainly ascribed to the Shockley surface states of the bare Cu(111) substrate. Importantly, a series of ring-like electron pockets with low intensity uniformly distribute around the high-intensity one, which can be seen clearly in constant-energy maps at $E_b = 0.2$ eV and 0.4 eV. The ARPES measurements shown in Fig. 2(b) were performed at 80 K, which exhibits the band dispersions along the two cut directions (cut **a** at $k_x = 0$ Å^{-1} and cut **b** at $k_x = -0.34$ Å^{-1}) as defined in the lower left panel of Fig. 2(a). From cut **a**, we find that the bands with low intensity have identical features to the high-intensity one. From cut **b**, we estimate the periodicity of the low-intensity bands between the nearest-neighbor Γ point to be 0.29 Å^{-1}, which agrees well with the deduced Brillouin zone of the Cu-T4PT MOF in Fig. 1(d). Considering the periodicity of the band structure, there should be a low-intensity band centered at the Γ point, which completely overlaps with the high-intensity one. From the above discussion and considering the quantum confinement of surface-state electrons by the supported nanostructures,[42,49–55] we conclude that the periodic low-intensity bands can be attributed to quantum confinement of the surface states of the underlying Cu(111) substrate by the periodic potential of the network lattices of the Cu-T4PT MOF. The low-intensity bands arise from the weak electronic coupling between the neighboring localized-states confined by the nanopores of the Cu-T4PT MOF, whereas the strong electronic coupling between the delocalized conduction electrons of the bare Cu substrate leads to the high-intensity band of the Cu(111) surface-state.

In order to distinguish the band structure of the single-layer Cu-T4PT MOF from the bare Cu(111) substrate, which cannot be distinguished by the surface-averaging ARPES measurements, we

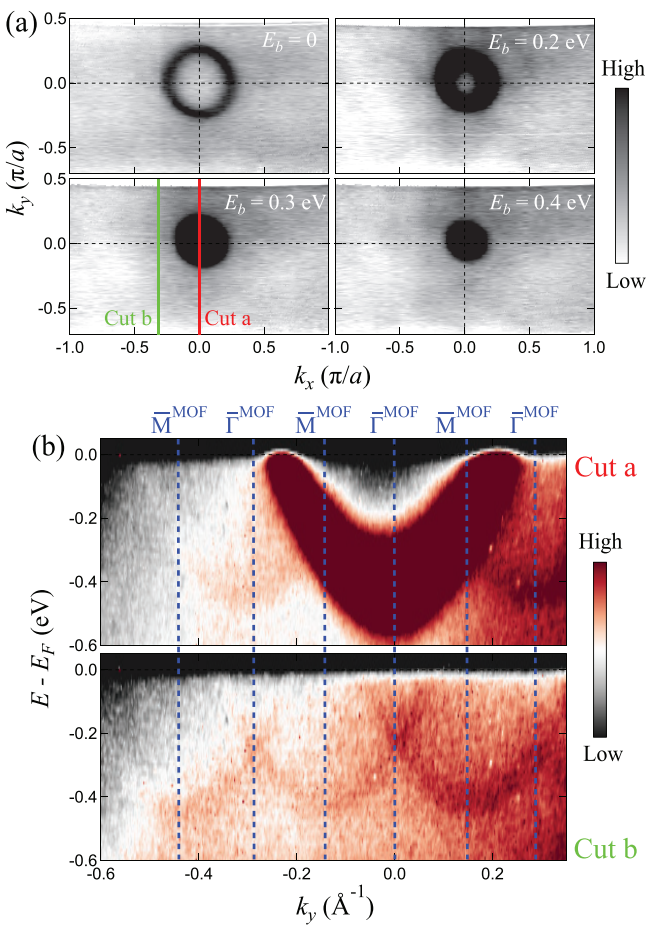

FIG. 2. (a) ARPES constant-energy contours of the band structure as a function of binding energy E_b indicated in the figure. All the data in (a) are obtained at room temperature. (b) ARPES band dispersions along cut **a** (top) and cut **b** (bottom) as defined in the lower left panel of (a). All the data in (b) are obtained at 80 K.

performed a local and area-selected FT-STS. First, we focus our measurement over the MOF-covered region without the bare Cu(111) substrate [see Fig. 3(a)] to study the band structure originating from the Cu-T4PT MOF. Figures 3(b)–3(d) show the real-space (**r**-space) dI/dV map of the same area as Fig. 3(a) acquired at 0.2 V, 0.1 V, and −0.2 V, respectively. The standing wave patterns in the vicinity of surface defects are evident in these images, especially in Fig. 3(d). The standing wave with wave vector **q** results from the quantum interference between the incident quasi-particle wave with momentum **k** and the scattered one with momentum **k**′ by surface defects and, hence, $\mathbf{q} = \mathbf{k}' - \mathbf{k}$ for elastic scattering. By Fourier transform of the dI/dV map in Figs. 3(b)–3(d), we can obtain the QPI pattern in scattering wave vector **q**-space, which displays the allowed wave vectors **q** and the relative intensities for the various scattering processes. Figures 3(e)–3(h) show a series of QPI patterns acquired at different sample bias; the six bright inner-spots correspond to the reciprocal lattice vectors $\mathbf{b}_{1,2}^{MOF}$ as indicated, and the hexagon Brillouin zone is also superimposed in the figure. The most prominent feature in these QPI patterns is the ring centered at the Γ point, whose radius varies as a

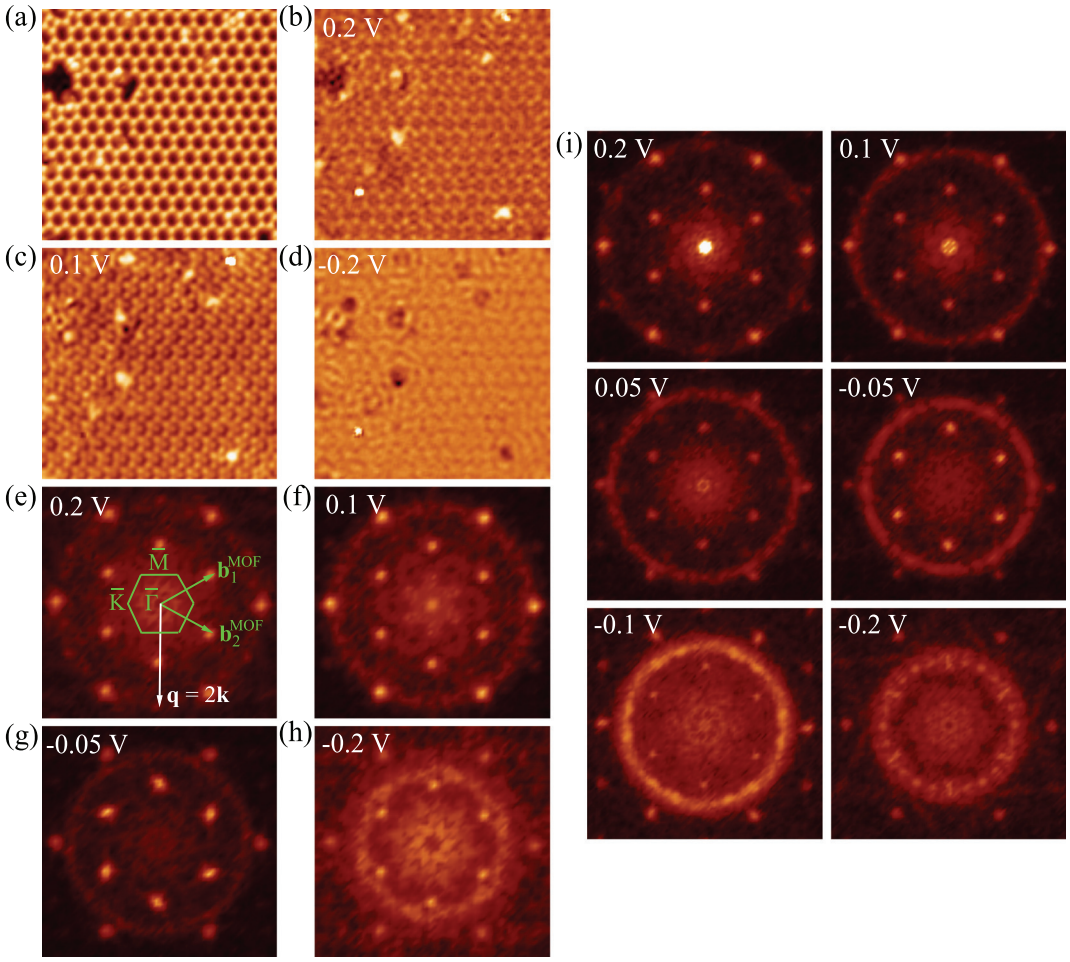

FIG. 3. (a) STM image of a region fully covered with the Cu-T4PT MOF obtained at 0.1 V. (b)–(d) The spatially resolved d*I*/d*V* maps of the same area as (a) obtained at 0.2 V, 0.1 V, and −0.2 V, as marked in the upper left corner of the figure. (e)–(h) QPI patterns obtained by Fourier transform of the d*I*/d*V* maps of the same area as (a), and the corresponding sample bias is indicated in the figure. The reciprocal lattice vectors $\mathbf{b}_{1,2}^{MOF}$ and first Brillouin zone (hexagon) are also marked in (e). (i) QPI patterns obtained by Fourier transform of the d*I*/d*V* maps over an area with both the Cu-T4PT MOF and bare Cu(111) substrate, and the corresponding sample bias is indicated in the figure. Image size: 37 nm × 37 nm for (a)–(d) and 11.3 nm^{-1} × 11.3 nm^{-1} for (e)–(i).

function of the sample bias. For noble metal surfaces, the observed standing wave-like pattern due to the interference of incoming and scattered surface electronic states around the defects is a ring in the QPI pattern, corresponding to the backscattering channel $\mathbf{k}' = -\mathbf{k}$ and, hence, $\mathbf{q} = 2\mathbf{k}$.[56,57] The rings with radius q in Figs. 3(e)–3(h) represent the allowed wave vectors $\mathbf{q}$ for the surface electrons of the Cu(111) substrate confined by the 2D Cu-T4PT MOF. Second, we focus our measurement over a region with both the Cu-T4PT MOF and bare Cu(111) substrate to simulate the ARPES measurements, and the corresponding QPI patterns are shown in Fig. 3(i). It is worth noting that there is only one ring in every QPI pattern, indicating that the standing wave patterns of the Cu(111) substrate with or without the Cu-T4PT MOF share identical wave vectors $\mathbf{q}$. Hence, the Cu-T4PT MOF grown on a Cu(111) substrate has similar band features to a Cu(111) substrate, except for the band periodicity. These area-selected FT-STS measurements agree well with the ARPES measurements and further support our explanation that the periodic surface states originate from quantum confinement of the Cu(111) surface-state electrons by the network lattices of the Cu-T4PT MOF.

The QPI patterns at different energies in Figs. 3(e)–3(i) can be used to obtain the energy-momentum dispersions of the bands, as shown in Fig. 4(a). For comparison, the ARPES results in Fig. 2 and the bands of the clean Cu(111) substrate are also shown. It is obvious that the E-k dispersions of Cu-T4PT MOFs on Cu(111) obtained from ARPES results are in good quantitative agreement with those from QPI patterns and share a similar band structure to the bare Cu(111). This further supports our conclusion that the periodic surface states in Fig. 2 originate from quantum confinement of the surface states of the underlying Cu(111) substrate by the periodic potential of the network lattices of the Cu-T4PT MOF. Our results indicate that the surface-averaging ARPES technique and the local FT-STS technique can provide consistent conclusion on this sample. Figure 4(b) illustrates the

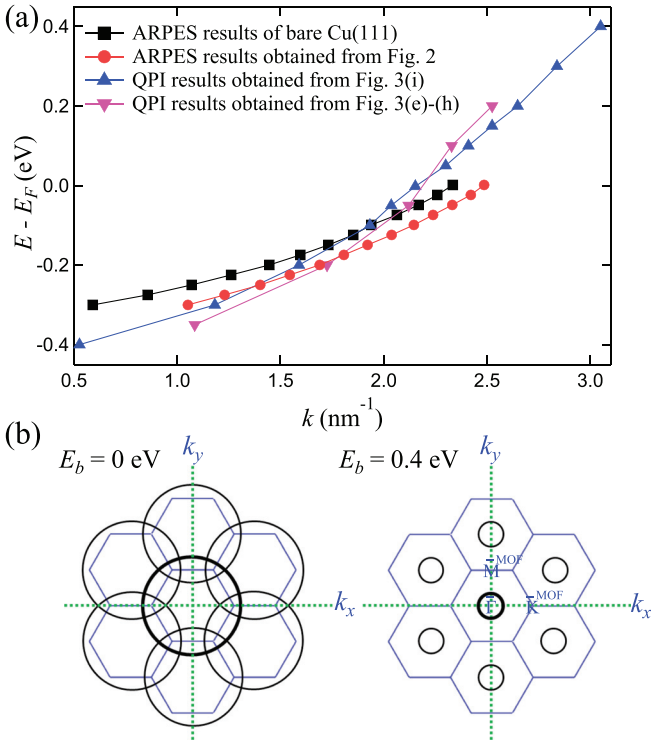

FIG. 4. (a) The band dispersions of Cu-T4PT MOFs on Cu(111) obtained by FT-STS and ARPES measurements. The bands of the clean Cu(111) substrate are also shown for comparison. (b) Schematics showing the surface-state band structure at $E_b = 0$ eV (left) and 0.4 eV (right). The blue hexagons represent the Brillouin zones of Cu-T4PT MOFs. The thick (thin) black rings represent the surface-state bands with high (low) ARPES intensity.

band structure of Cu(111)-supported single-layer Cu-T4PT MOFs at two different energies obtained by our ARPES and FT-STS measurements. The thick black ring centered at the Γ point represents the superposition of the high-intensity Shockley surface-states of the bare Cu(111) substrate and the low-intensity confined states in the first Brillouin zone originating from Cu-T4PT MOFs. The thin black rings uniformly distributed around the thick one represent the low-intensity confined states in other Brillouin zones.

Our experimentally synthesized single-layer Cu-T4PT MOF has a similar structure to the theoretically predicted organic topological material Cu-TPyB MOF[47] and may also have topologically nontrivial bands. However, our ARPES and FT-STS measurements merely captured the confined states of the two-dimensional electron gas on the Cu(111) substrate, and the intrinsic bands of single-layer Cu-T4PT MOFs and the possible nontrivial topological states were not found in the present work. The lack of these bands may be attributed to the strong electronic coupling between the Cu-T4PT MOF and the Cu(111) substrates, which may modify and even suppress the intrinsic topological properties of the metal-organic lattices. Sun *et al.*[58] investigated the dI/dV spectra obtained at the interior and boundary of the Ag-coordinated 1,4-phenylene diisocyanide (Ag-PDI) MOFs directly grown on a Ag(111) substrate and found no experimental evidence of the topological band structure theoretically predicted in this system. They explained that the electrostatic and chemical interactions between the metal substrate and the Ag-PDI MOFs quench the topological properties. In order to exploit the intrinsic bands of these MOFs, it is necessary to grow them on weak van der Waals interaction substrates in the future. Kumar *et al.*[44] demonstrated the synthesis of Co-coordinated DCA MOFs on epitaxial graphene grown on the Ir(111) substrate and found a 2D band structure in this experimental system. This is a good beginning to exploit organic topological materials predicted in MOFs.

In conclusion, with the help of the complementary ARPES and FT-STS techniques, we study the electronic structure of the single-layer Cu-T4PT MOF synthesized on a Cu(111) substrate and find periodic surface-state bands derived from quantum confinement of the two-dimensional electron gas of the Cu(111) surface state by the network structures of Cu-T4PT MOFs. The intrinsic bands and the possible topological properties of the Cu-T4PT MOF are not captured in our experiments; however, our work demonstrates that the substrate' surface states can be manipulated in a controlled manner using periodic nanostructures like surface-supported 2D MOFs, and will facilitate the engineering of electron wave functions in reduced dimensions for exploring the fundamental aspects of quantum physics.

C.-S.Z. acknowledges Hong-Jian Du for suggestions about the FT-STS experimental procedure and initial analysis. This work was supported by the National Natural Science Foundation of China (NSFC) (Nos. 11674149 and 11622437), the Guangdong Innovative and Entrepreneurial Research Team Program (No. 2016ZT06D348), the Shenzhen Key Laboratory (No. ZDSYS20170303165926217), the Science, Technology and Innovation Commission of Shenzhen Municipality (No. KYTDPT20181011104202253), and the National Key R&D Program of China (No. 2017YFA0303500).

DATA AVAILABILITY

The data that support the findings of this study are available from the corresponding author upon reasonable request.

REFERENCES

[1]H. Furukawa, K. E. Cordova, M. O'Keeffe, and O. M. Yaghi, Science **341**, 1230444 (2013).
[2]L. J. Murray, M. Dinca, and J. R. Long, Chem. Soc. Rev. **38**, 1294 (2009).
[3]J. R. Li, R. J. Kuppler, and H. C. Zhou, Chem. Soc. Rev. **38**, 1477 (2009).
[4]J. R. Li, J. Sculley, and H. C. Zhou, Chem. Rev. **112**, 869 (2012).
[5]J. Lee, O. K. Farha, J. Roberts, K. A. Scheidt, S. T. Nguyen, and J. T. Hupp, Chem. Soc. Rev. **38**, 1450 (2009).
[6]L. E. Kreno, K. Leong, O. K. Farha, M. Allendorf, R. P. Van Duyne, and J. T. Hupp, Chem. Rev. **112**, 1105 (2012).
[7]M. D. Allendorf, C. A. Bauer, R. K. Bhakta, and R. J. Houk, Chem. Soc. Rev. **38**, 1330 (2009).
[8]Y. Cui, Y. Yue, G. Qian, and B. Chen, Chem. Rev. **112**, 1126 (2012).
[9]V. Stavila, A. A. Talin, and M. D. Allendorf, Chem. Soc. Rev. **43**, 5994 (2014).
[10]I. Stassen, N. Burtch, A. Talin, P. Falcaro, M. Allendorf, and R. Ameloot, Chem. Soc. Rev. **46**, 3185 (2017).
[11]P. Horcajada, R. Gref, T. Baati, P. K. Allan, G. Maurin, P. Couvreur, G. Ferey, R. E. Morris, and C. Serre, Chem. Rev. **112**, 1232 (2012).
[12]P. L. Wang, L. H. Xie, E. A. Joseph, J. R. Li, X. O. Su, and H. C. Zhou, Chem. Rev. **119**, 10638 (2019).
[13]Z. F. Wang, Z. Liu, and F. Liu, Nat. Commun. **4**, 1471 (2013).
[14]Z. F. Wang, Z. Liu, and F. Liu, Phys. Rev. Lett. **110**, 196801 (2013).
[15]Z. F. Wang, N. Su, and F. Liu, Nano. Lett. **13**, 2842 (2013).

[16]Z. Liu, Z. F. Wang, J. W. Mei, Y. S. Wu, and F. Liu, Phys. Rev. Lett. **110**, 106804 (2013).
[17]L. Z. Zhang, Z. F. Wang, B. Huang, B. Cui, Z. Wang, S. X. Du, H. J. Gao, and F. Liu, Nano. Lett. **16**, 2072 (2016).
[18]L. Dong, Y. Kim, D. Er, A. M. Rappe, and V. B. Shenoy, Phys. Rev. Lett. **116**, 096601 (2016).
[19]M. G. Yamada, T. Soejima, N. Tsuji, D. Hirai, M. Dincă, and H. Aoki, Phys. Rev. B **94**, 081102(R) (2016).
[20]Y-p Wang, W-x Ji, C-w Zhang, P. Li, P-j Wang, B. Kong, S-s Li, S-s Yan, and K. Liang, Appl. Phys. Lett. **110**, 233107 (2017).
[21]J. Zhang, B. Zhao, Y. Xue, T. Zhou, and Z. Yang, Phys. Rev. B **97**, 125430 (2018).
[22]M. Konig, S. Wiedmann, C. Brune, A. Roth, H. Buhmann, L. W. Molenkamp, X. L. Qi, and S. C. Zhang, Science **318**, 766 (2007).
[23]I. Knez, R. R. Du, and G. Sullivan, Phys. Rev. Lett. **107**, 136603 (2011).
[24]F. Reis, G. Li, L. Dudy, M. Bauernfeind, S. Glass, W. Hanke, R. Thomale, J. Schafer, and R. Claessen, Science **357**, 287 (2017).
[25]S. Wu, V. Fatemi, Q. D. Gibson, K. Watanabe, T. Taniguchi, R. J. Cava, and P. Jarillo-Herrero, Science **359**, 76 (2018).
[26]D. Hsieh, D. Qian, L. Wray, Y. Xia, Y. S. Hor, R. J. Cava, and M. Z. Hasan, Nature **452**, 970 (2008).
[27]Y. Xia, D. Qian, D. Hsieh, L. Wray, A. Pal, H. Lin, A. Bansil, D. Grauer, Y. S. Hor, R. J. Cava, and M. Z. Hasan, Nat. Phys. **5**, 398 (2009).
[28]Y. L. Chen, J. G. Analytis, J. H. Chu, Z. K. Liu, S. K. Mo, X. L. Qi, H. J. Zhang, D. H. Lu, X. Dai, Z. Fang, S. C. Zhang, I. R. Fisher, Z. Hussain, and Z. X. Shen, Science **325**, 178 (2009).
[29]C. Z. Chang, J. Zhang, X. Feng, J. Shen, Z. Zhang, M. Guo, K. Li, Y. Ou, P. Wei, L. L. Wang, Z. Q. Ji, Y. Feng, S. Ji, X. Chen, J. Jia, X. Dai, Z. Fang, S. C. Zhang, K. He, Y. Wang, L. Lu, X. C. Ma, and Q. K. Xue, Science **340**, 167 (2013).
[30]Z. K. Liu, B. Zhou, Y. Zhang, Z. J. Wang, H. M. Weng, D. Prabhakaran, S. K. Mo, Z. X. Shen, Z. Fang, X. Dai, Z. Hussain, and Y. L. Chen, Science **343**, 864 (2014).
[31]S. Y. Xu, I. Belopolski, N. Alidoust, M. Neupane, G. Bian, C. Zhang, R. Sankar, G. Chang, Z. Yuan, C. C. Lee, S. M. Huang, H. Zheng, J. Ma, D. S. Sanchez, B. Wang, A. Bansil, F. Chou, P. P. Shibayev, H. Lin, S. Jia, and M. Z. Hasan, Science **349**, 613 (2015).
[32]A. Damascelli, Z. Hussain, and Z. X. Shen, Rev. Mod. Phys. **75**, 473 (2003).
[33]D. Lu, I. M. Vishik, M. Yi, Y. Chen, R. G. Moore, and Z.-X. Shen, Annu. Rev. Condens. Matter Phys. **3**, 129 (2012).
[34]H. Yang, A. Liang, C. Chen, C. Zhang, N. B. M. Schroeter, and Y. Chen, Nat. Rev. Mater. **3**, 341 (2018).
[35]M. F. Crommie, C. P. Lutz, and D. M. Eigler, Nature **363**, 524 (1993).
[36]J. E. Hoffman, K. McElroy, D. H. Lee, K. M. Lang, H. Eisaki, S. Uchida, and J. C. Davis, Science **297**, 1148 (2002).
[37]K. McElroy, R. W. Simmonds, J. E. Hoffman, D. H. Lee, J. Orenstein, H. Eisaki, S. Uchida, and J. C. Davis, Nature **422**, 592 (2003).
[38]G. M. Rutter, J. N. Crain, N. P. Guisinger, T. Li, P. N. First, and J. A. Stroscio, Science **317**, 219 (2007).
[39]P. Roushan, J. Seo, C. V. Parker, Y. S. Hor, D. Hsieh, D. Qian, A. Richardella, M. Z. Hasan, R. J. Cava, and A. Yazdani, Nature **460**, 1106 (2009).
[40]T. Hanaguri, S. Niitaka, K. Kuroki, and H. Takagi, Science **328**, 474 (2010).
[41]P. O. Sprau, A. Kostin, A. Kreisel, A. E. Bohmer, V. Taufour, P. C. Canfield, S. Mukherjee, P. J. Hirschfeld, B. M. Andersen, and J. C. S. Davis, Science **357**, 75 (2017).
[42]J. Lobo-Checa, M. Matena, K. Muller, J. H. Dil, F. Meier, L. H. Gade, T. A. Jung, and M. Stohr, Science **325**, 300 (2009).
[43]S. Wang, W. Wang, L. Z. Tan, X. G. Li, Z. Shi, G. Kuang, P. N. Liu, S. G. Louie, and N. Lin, Phys. Rev. B **88**, 245430 (2013).
[44]A. Kumar, K. Banerjee, A. S. Foster, and P. Liljeroth, Nano. Lett. **18**, 5596 (2018).
[45]I. Piquero-Zulaica, A. Sadeghi, M. Kherelden, M. Hua, J. Liu, G. Kuang, L. Yan, J. E. Ortega, Z. M. A. El-Fattah, B. Azizi, N. Lin, and J. Lobo-Checa, Phys. Rev. Lett. **123**, 266805 (2019).
[46]T. R. Umbach, M. Bernien, C. F. Hermanns, L. L. Sun, H. Mohrmann, K. E. Hermann, A. Krüger, N. Krane, Z. Yang, F. Nickel, Y. M. Chang, K. J. Franke, J. I. Pascual, and W. Kuch, Phys. Rev. B **89**, 235409 (2014).
[47]X. Zhang and M. Zhao, Sci. Rep. **5**, 14098 (2015).
[48]I. Horcas, R. Fernandez, J. M. Gomez-Rodriguez, J. Colchero, J. Gomez-Herrero, and A. M. Baro, Rev. Sci. Instrum. **78**, 013705 (2007).
[49]M. F. Crommie, C. P. Lutz, and D. M. Eigler, Science **262**, 218 (1993).
[50]H. C. Manoharan, C. P. Lutz, and D. M. Eigler, Nature **403**, 512 (2000).
[51]F. Klappenberger, D. Kuhne, W. Krenner, I. Silanes, A. Arnau, F. J. Garcia de Abajo, S. Klyatskaya, M. Ruben, and J. V. Barth, Phys. Rev. Lett. **106**, 026802 (2011).
[52]H. Oka, O. O. Brovko, M. Corbetta, V. S. Stepanyuk, D. Sander, and J. Kirschner, Rev. Mod. Phys. **86**, 1127 (2014).
[53]I. Piquero-Zulaica, J. Lobo-Checa, A. Sadeghi, Z. M. A. El-Fattah, C. Mitsui, T. Okamoto, R. Pawlak, T. Meier, A. Arnau, J. E. Ortega, J. Takeya, S. Goedecker, E. Meyer, and S. Kawai, Nat. Commun. **8**, 787 (2017).
[54]N. Kepčija, T.-J. Huang, F. Klappenberger, and J. V. Barth, J. Chem. Phys. **142**, 101931 (2015).
[55]K. Müller, M. Enache, and M. Stöhr, J. Phys.: Condens. Matter **28**, 153003 (2016).
[56]N. Avraham, J. Reiner, A. Kumar-Nayak, N. Morali, R. Batabyal, B. Yan, and H. Beidenkopf, Adv. Mater. **30**, 1707628 (2018).
[57]P. Sessi, V. M. Silkin, I. A. Nechaev, T. Bathon, L. El-Kareh, E. V. Chulkov, P. M. Echenique, and M. Bode, Nat. Commun. **6**, 8691 (2015).
[58]H. Sun, S. Tan, M. Feng, J. Zhao, and H. Petek, J. Phys. Chem. C **122**, 18659 (2018).

THE JOURNAL OF PHYSICAL CHEMISTRY C

pubs.acs.org/JPCC Article

Scanning Tunneling Microscopy Studies of Potassium-Doped Picene Films on Au(111) Surface

Guowei Liu, Xiji Shao, Chaoqiang Xu, Xuefeng Wu,* and Kedong Wang*

Cite This: J. Phys. Chem. C 2020, 124, 22025−22034 Read Online

ACCESS | Metrics & More | Article Recommendations

ABSTRACT: Potassium-doped picene films grown on an Au(111) surface have been investigated using low-temperature scanning tunneling microscopy. The evolution of both the morphologies and the electronic properties of the pristine and doped picene films have been carefully studied. With the increase of the K doping ratio, several novel ordered structures sequentially appear on the K_xPicene (x = 0−4) film. Meanwhile, owing to the increase of charge transferring from K atoms to picene molecules, the lowest unoccupied molecular orbital state of the films is observed to shift toward the Fermi level. In particular, for $K_{3.4}$Picene, this state splits into an upper unoccupied part and a lower occupied one when saddling the Fermi level. This may imply the presence of the electronic correlation effect.

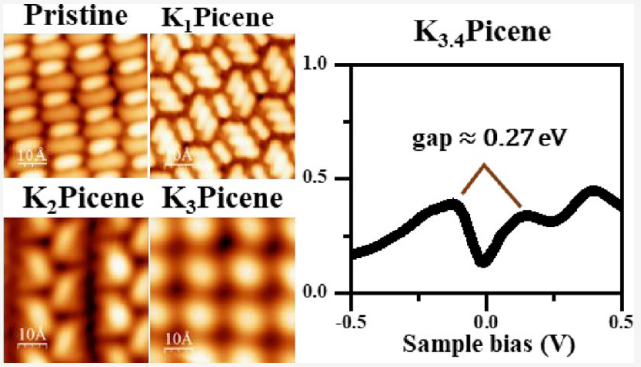

1. INTRODUCTION

Doped organic molecules provide a diverse platform to enrich the structural and electronic properties of organic materials,[1−8] which have wide applications in organic field effect transistors,[9,10] photovoltaic cells,[11,12] and so forth. Recently, doping of metal atoms, especially alkali metal atoms, into polycyclic aromatic hydrocarbon (PAH) materials attracts much attention because of the appearance of superconductivity.[6,13−15] As a typical PAH molecule, picene has an armchair aromatic molecular configuration composed of five benzene rings. This molecule has been demonstrated to be superconducting upon potassium (K) or rubidium doping.[6,16−20] The superconducting transition temperature could be as high as 18 K.[6,21,22] However, because of the very low shielding fraction (<1.2%)[6] and lack of repeatability,[23] the superconductivity in such a system is questioned by Tanigaki and co-workers,[23] Knupfer and co-workers,[24] and Ruff et al.[25] Extensive efforts have been devoted to settle this debate.[1,4,7,8,16,18−20,23,25−33] Combining photoemission spectroscopy (PES) experiments and density functional theory plus dynamical mean-field theory (DFT+DMFT) calculation, Ruff et al. found that K_xPicene was a correlated Mott insulator for x = 1, 2, 3.[25] Yokoya and co-workers performed the PES studies on the electronic structure shift of K-doped picene film on highly oriented pyrolytic graphite (HOPG).[26] Though the metallic behavior was revealed at a certain K-doping level, a superconducting gap was not observed at 4 K.[26] Kelly et al. claimed that the picene film on Ag(111) becomes amorphous after K doping.[20]Therefore, a detailed characterization of K-doped picene at various doping ratios is essential to further clarify the debate. A scanning tunneling microscope (STM) is a powerful tool to study the structural and electronic properties of surfaces[1,4,8,34] and films on substrates at the molecular level.[35] As we have known to date, picene molecules or films on surfaces have been studied by STM many times. Zhou et al. have investigated the molecular orbitals of single picene on Cu(111),[32] manipulated single picene on an Au(111) surface, and induced the accommodation of Co atoms one by one to form stable hybrid artificial structures.[33] The growth of pristine picene film on Au(111),[7,8,36] Ag(111),[31] and Ag(100)[20,37] have been studied by using STM. However, systematic observation of morphologies and corresponding electronic structures of K-doped picene films on a surface by using STM have not yet been reported.

Here, we report our investigations on the evolution of morphology and electronic structure of picene film with the increase of the K doping by means of low-temperature scanning tunneling microscopy (LT-STM). Besides, the two pristine picene phases, which are defined as Phase 1 and Phase 2,[8,20,31] three newly found dominant doped phases and some transitional phases have been observed by enhancing the K doping. Evolution of the electronic structures of corresponding

Received: April 19, 2020
Revised: September 10, 2020
Published: September 14, 2020

https://dx.doi.org/10.1021/acs.jpcc.0c03477
J. Phys. Chem. C 2020, 124, 22025−22034

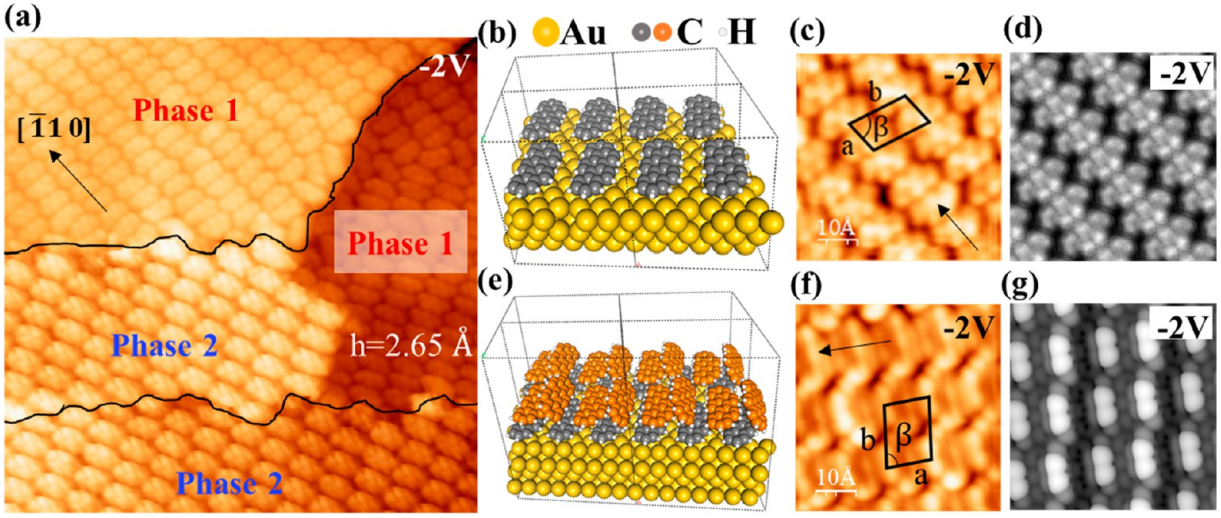

Figure 1. Two pristine picene phases on Au(111). (a) Typical topographic image of ~1.5 ML picene on Au(111)(20 × 20 nm^2, −2 V), including both Phase 1 and Phase 2. Black curves depict the steps underneath the Au(111) surface. (b) Structural model of Phase 1. (c) and (d) show the experimental and simulated STM images (5 × 5 nm^2) of Phase 1 at −2 V, respectively. (e) Structural model of Phase 2. (f) and (g) show the experimental and simulated STM images (5 × 5 nm^2) of Phase 2 at −2 V, respectively. The C atoms in the first and second picene layers are indicated by gray and orange, respectively. The unit cells of Phase 1 and Phase 2 are represented with the black parallelograms in (c) and (f), respectively. The [1̄10] directions of the Au(111) surfaces underneath are denoted by black arrows.

K-doped phases is featured with the shift of the lowest unoccupied molecular orbital (LUMO) states toward the Fermi level. Although no superconducting phase was found, our work provides a comprehensive reference for developing a deep understanding of the K-doped picene film systems.

2. METHODS

2.1. STM Experiment. Our experiments were carried out with a commercial ultrahigh vacuum (UHV) LT-STM (Unisoku Co., Ltd. USM1300, Japan). The base pressure of the STM chamber and the sample preparation chamber are all better than 1 × 10^{-10} mBar. The sample was kept at 77 K during the STM experiments. A single-crystalline Au(111) (MaTecK) was used as the substrate. It was cleaned by Ar ion sputtering and around 900 K annealing repeatedly prior to use. Picene powder (99.0%, International Laboratory USA) was loaded in an alumina crucible. It was thoroughly degassed for several hours before the deposition. The clean Au(111) substrate was kept at room temperature (RT) during the deposition of picene. A commercial potassium dispenser (SAES Getter) was then used to dope K atoms on the picene film repeatedly. The deposition amount of K was calibrated in advance by counting K atoms deposited on the Si(111)−7 × 7 surface.[1] We assume that the sticking coefficient of K atoms on picene film and Si(111)−7 × 7 surface are almost the same.[4] During the deposition of K atoms, the sample was kept at ~200 K. Then the sample was annealed moderately to improve the film quality. When the ratio of K to picene was less than 4, RT annealing for 1 h or more was enough to obtain high-quality film. As the ratio reached 4, the sample needed to be annealed at 500 K for 30 min to form ordered structures. A clean tungsten tip was used during the STM experiments. The STM images were recorded at constant tunneling current mode with a tunneling current of 100 pA. The density of states (DOS) presented by $(dI/dV)/(I/V)$ spectra were numerically calculated from the averaged multiple recorded $I-V$ curves, which were taken at different positions on the same phase.

2.2. DFT Calculation. In this work, first-principle calculations were performed by the Vienna ab initio simulation package (VASP)[38,39] based on van der Waals corrected density functional (optB88-vdW-DF),[40] where an optimized version of the B88 exchange function was adopted.[40−42] Projector-augmented wave (PAW) pseudopotential[43] was used with the PBE exchange correlation function[44] and the plane-wave cutoff of 500 eV. We used a supercell with a three atomic layer Au(111) slab and the Monkhorst−Pack Mesh of 2 × 2 × 1 k-points for Phase 1 calculations. We used four Au layers and Γ-point-only Brillouin zone sampling for other phases calculations. All models had vacuum separation of 15 Å. Structural optimizations were performed during which all adsorbed picene molecules and K atoms and the upper two layers of the Au(111) atoms were allowed to relax until the forces of each atom were below 0.02 eV/Å.

3. RESULTS AND DISCUSSION

3.1. Evolution of Structure with the Increase of K Doping. We first studied the pristine picene film on the Au(111) surface before doping. Figure 1a shows the topography of an ≈1.5 monolayer (ML) picene film on the Au(111) surface in which two kinds of ordered phases, Phase 1 and Phase 2, coexist. The picene molecular rows in Phase 1 are along the [1̄10] direction of the Au substrate.[45] Because of the symmetry of the substrate, there are three equivalent directions rotating by 120° with respect to each other. The molecular rows can be arranged along with any one of them.[29] Phase 1 has one layer of picene molecules with a flat-lying configuration on the Au(111) surface, whose structural model is shown in Figure 1b. The high-resolution image presents the picene molecule in Phase 1 as a "w" shape, whose five lobes correspond to the five benzene rings.[6] There are three kinds of intermolecular orientations in the experimental image. Thus, compared to the model in Figure 1b where all the orientations of the picene molecules are in the same direction, a model for which any two nearest picene molecules are opposite is possible. However, the former is more stable

https://dx.doi.org/10.1021/acs.jpcc.0c03477
J. Phys. Chem. C 2020, 124, 22025−22034

Table 1. Summary of K-Doped Picene Film Structures on Au(111) at Different Doping Ratios

Structure	Phase 2 (x = 0)	K_1picene	K_2picene	$K_{2.4}$picene	$K_{2.8}$picene α	$K_{2.8}$picene β
STM image	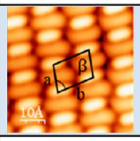	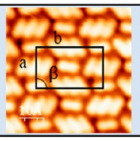	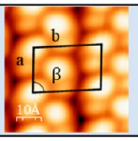	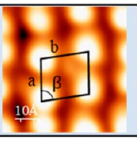	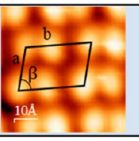	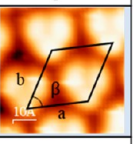
a (nm)	1.09±0.02	1.59±0.02	1.68±0.03	1.52±0.05	1.67±0.05	2.50±0.05
b (nm)	1.39±0.02	2.62±0.02	2.71±0.03	1.86±0.05	2.47±0.1	2.50±0.05
β (°)	75.5±1	90	87.5±1	75±5	77±5	60
Structure	**K_3picene**	**$K_{3.4}$picene**	**$K_{3.8}$picene α**	**$K_{3.8}$picene β**	**K_4picene α**	**K_4picene β**
STM image	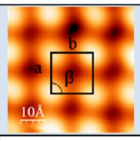	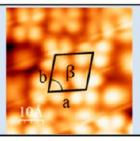	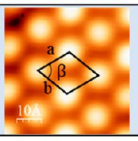	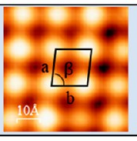	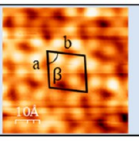	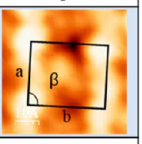
a (nm)	1.54±0.02	1.42±0.1	1.40±0.02	1.43±0.02	1.42±0.1	1.78±0.05
b (nm)	1.61±0.02	1.44±0.1	1.43±0.02	1.49±0.02	1.49±0.1	2.44±0.05
β (°)	90	74±5	71±1	84±1	79±5	90±1

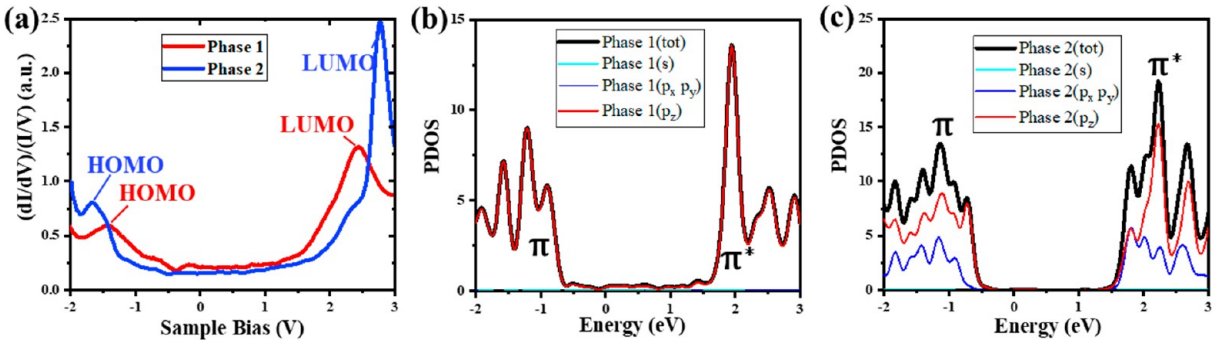

Figure 2. (a) Tunneling spectra of Phase 1 (red line) and Phase 2 (blue line). (b) Calculated PDOS of Phase 1. (c) Calculated PDOS of Phase 2.

according to our calculations. The adsorption behavior of picene molecules on Au(111) is different from that on Ag(111), where the opposite orientation dominates.[31] The randomness of picene orientation gives rise to slight meanderings of the Phase 1 rows along the $[\bar{1}10]$ direction. The unit cell of Phase 1, as marked in Figure 1c, is (0.79 ± 0.02) × (1.44 ± 0.02) nm^2 with the angle of 78.5° ± 1°. Hence, its molecule density is 0.90 ± 0.01 molecules/nm^2. The simulated STM image agrees well with the experimental image.

The structural model of Phase 2 is shown in Figure 1e. Parts (f) and (g) of Figure 1 show its experimental and simulated STM images at −2 V, respectively. However, its alternative light and dark features are observable at a sample bias of 2 V in Table 1.[31] The molecular rows are also along the $[\bar{1}10]$ directions. The unit cell of Phase 2 is (1.09 ± 0.02) × (1.39 ± 0.02) nm^2 with β of 75.5 ± 1°, which has a higher molecular density (1.36 ± 0.05 molecules/nm^2) than Phase 1. It is worth mentioning that the exact configuration of Phase 2 is controversial.[8,20,27,31,35] Some researchers believe that Phase 2 is still a one-layer structure composed of an alternative arrangement of tilted and flat-lying molecules.[31] Others proposed that Phase 2 is the result of a second layer grown on Phase 1 (see Figure 1e).[20,27] Figure 1a shows that the height difference of the two phases is 2.65 Å on the same middle stage, which corresponds to the height of one tilted picene molecule. Therefore, we prefer the latter two-layer mode. According to previous works, a tilted phase has the herringbone arrangement, which resembles the *ab*-plane of the picene bulk phase.[7,20,31,35] However, Figure 1f shows that, different from the upper, middle, and bottom rows have alternately long dim and short bright protrusions. Their difference is from the opposite orientations of the tilted picene molecules.

Figure 2 shows electronic structures of pristine picene film on Au(111). The red spectrum reveals the DOS of Phase 1, whose LUMO state is at 2.43 V and highest occupied molecular orbital (HOMO) state at −1.45 V, resulting in a band gap of 3.88 eV. The calculated PDOS spectrum interprets that the states are almost composed of the p_z orbitals, which are vertical to the picene plane forming π bonding and π^* antibonding orbitals. As for Phase 2, the LUMO and HOMO states are at 2.77 and −1.66 V, respectively, forming a band gap of 4.43 eV. Both values are larger than 3.3 eV[46] of bulk picene because of less dispersion in the direction perpendicular to the

https://dx.doi.org/10.1021/acs.jpcc.0c03477
J. Phys. Chem. C 2020, 124, 22025−22034

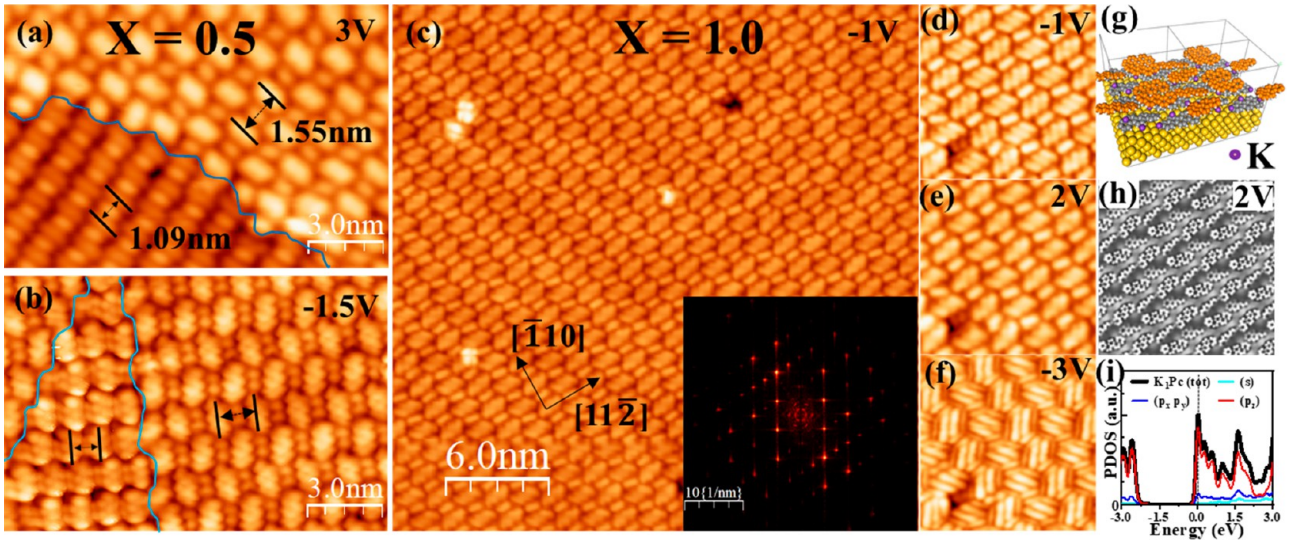

Figure 3. Sequentially dosing K onto picene/Au(111) with x = 0.5 and 1.0. (a) and (b) Coexistence of pristine Phase 2 and K_1Picene separated by blue curves (image size, 15 × 10 nm^2). (c) Typical topographic image of K_1Picene phase (image size, 30 × 30 nm^2; sample bias, V_b = −1 V). Inset shows its FFT. (d)−(f) STM images of K_1Picene at various sample biases (image size, 8 × 8 nm^2). (g) Structural model, (h) simulated STM image, and (i) calculated PDOS of K_1Picene.

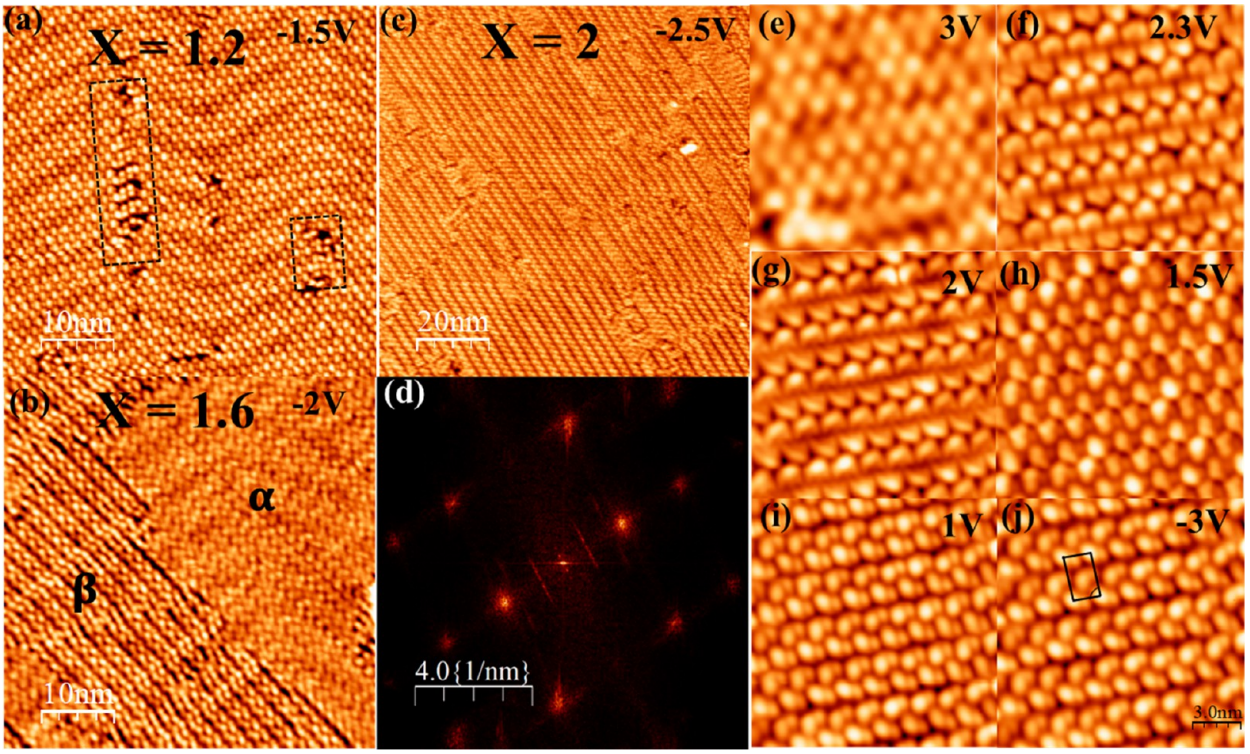

Figure 4. K_xPicene/Au(111) with doping ratio from 1 to 2. (a) Topographic image of K-doped picene at x = 1.2, in which the black dotted rectangles indicate the stripe structure (image size, 050 × 50 nm^2; sample bias, V_b = −1.5 V). (b) Topographic image shows that the stripe structure expands at x = 1.6 (image size, 50 × 50 nm^2; sample bias, V_b = −2 V) in which two different structures are noted as α and β, respectively. (c) Typical large-scale topographic image of K-doped picene phase at x = 2 (image size, 100 × 100 nm^2; sample bias, V_b = −2.5 V). (d) FFT image of (c). (e)−(j) K_2Picene phase at various sample biases (images size, 15 × 15 nm^2). The black parallelogram in (j) indicates a unit cell of K_2Picene.

substrate.[47] The LUMO state is mostly made up of p_z orbitals. The scanning tunneling spectroscopy (STS) of Phase 2 shows a shoulder at 2.4 eV, which originated from the p_x, p_y, and p_z orbitals of tilted picene molecules. Because of the existence of a Phase 1 buffer layer, it is clear in the gap and the LUMO state of Phase 2 is much stronger than that of Phase 1.[31] Thus, Phase 2 is expected to perform a more effective state shift by doping K atoms.

To make a more direct comparison with experimental results on the K-intercalated picene bulk,[6] we doped K into Phase 2, simply because this phase has more bulklike properties.[31] As the K-doping ratio increases from 0 to 1, a new phase defined as K_1Picene emerges and expands to the whole surface. The

https://dx.doi.org/10.1021/acs.jpcc.0c03477
J. Phys. Chem. C 2020, 124, 22025−22034

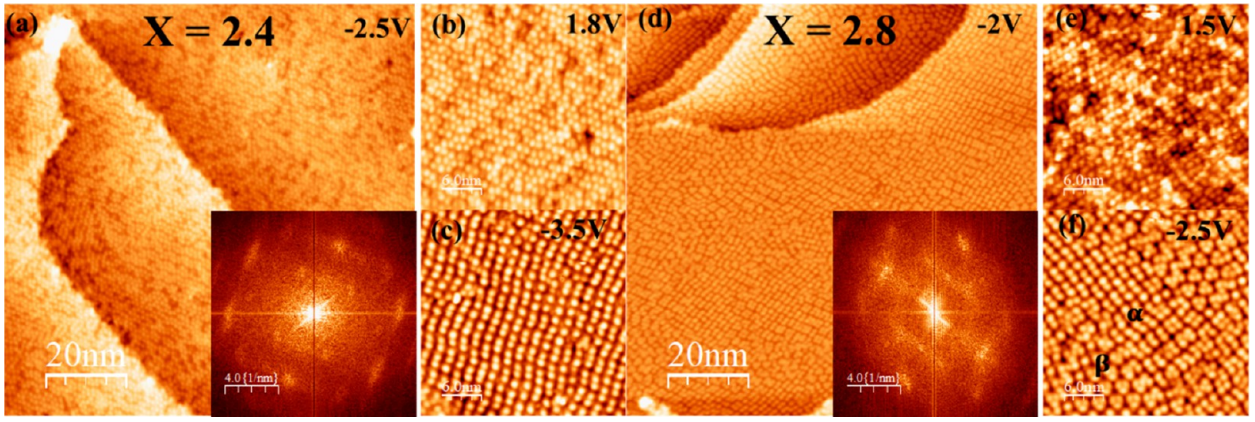

Figure 5. Topographic STM images and their FFT images of K_xPicene/Au(111) at x = 2.4 and x = 2.8. (a) Topographic image of K-doped picene at x = 2.4 (image size, 100 × 100 nm^2; sample bias, V_b = −2.5 V). Inset shows its FFT image. (b) and (c) show the zoomed-in images of (a) at 1.8 and −3.5 V, respectively. (d) and (f) show the zoomed-in images of (d) at 1.5 and −2.5 V, respectively.

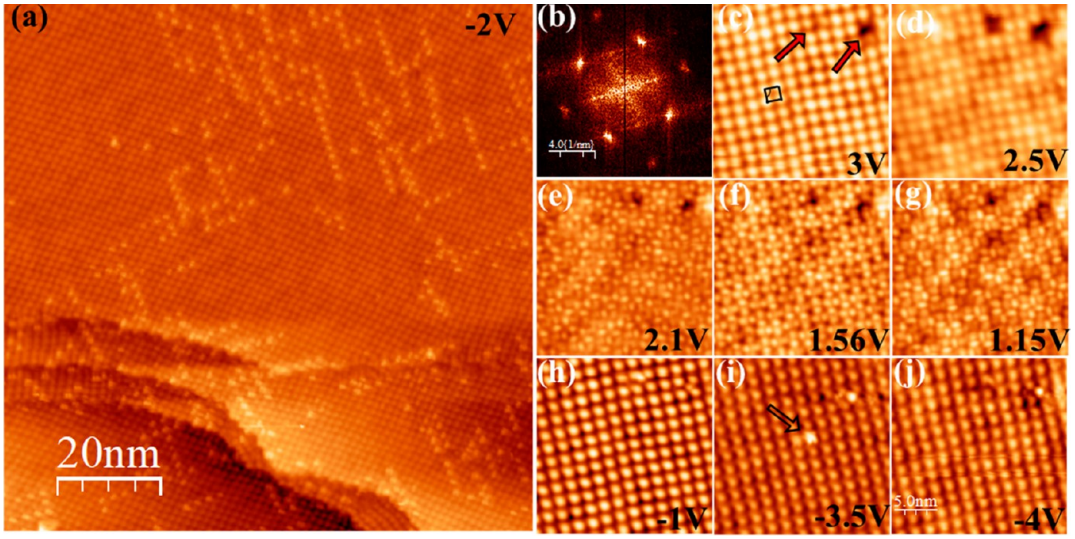

Figure 6. STM images of K_xPicene/Au(111) with x = 3 (a) Large-scale topographic STM image (image size, 100 × 100 nm^2; sample bias, V_b = −2 V) of K_3Picene/Au(111). (b) FFT image of (a). (c)−(j) Detailed STM images of K_3Picene/Au(111) at various sample biases (images size, 20 × 20 nm^2). The black rectangle denotes the unit cell of K_3Picene/Au(111).

subscript x of K_xPicene indicates the ratio of K atoms over picene molecules. Parts (a) and (b) of Figure 3 display the empty-state (3 V) and occupied-state (−1.5 V) images of two different boundary areas of Phase 2 and K_1Picene phase, respectively. The images clearly show the coexistence of the two phases as well as their different detailed structures. Apparently, molecule rows of K_1Picene and Phase 2 are along the same direction, which indicates that the K_1Picene originated from the doped Phase 2. Doping of K atoms expands the lattice constant from 1.09 to 1.55 nm. Meanwhile, the K-doped picene appears higher than Phase 2, which might result from the standing straight of the tilted picene molecules[31] and the increase of density of states that contribute to the tunneling current. Figure 3c shows that the K_1Picene expands to the whole surface when the doping ratio of K atoms reaches 1, in which herringbone reconstruction of the Au(111) surface can still be resolved. Therefore, one can find that the row direction of K_1Picene is also along the $[\bar{1}10]$ direction. Its clear FFT image demonstrates the high crystal quality of the K-doped picene film. Figure 3d−f displays the STM images of K_1Picene at different sample biases. The morphology change with the sample bias reveals the change of the density-of-state distributions around the molecules. Figure 3g displays the model of K_1Picene and Figure 3h shows the simulated STM image, which has similar features as the experimental image at 2 V (Figure 3e). The unit cell of K_1Picene is summarized in Table 1.[31]

Further increasing the doping ratio from 1 to 2, K_1Picene phase gradually evolves to a chainlike phase. Figure 4a shows that the chainlike phase emerges at the corners of the herringbones at x = 1.2. As for x = 1.6, the lower left half part of Figure 4b has been covered by the chainlike phase, which is defined as β phase. Meanwhile, the rest of the region is covered by an intermediate phase defined as α phase. With the doping ratio reaching 2, the chainlike phase has covered almost the whole surface. The direction of the chains are parallel to the $[\bar{1}10]$ direction of the Au(111) surface. Figure 4d shows a diffused FFT pattern of Figure 4c. The structure is no longer rectangular. Figure 4e−j shows the high-resolution STM images of K_2Picene in the same region at different sample biases from −3 to 3 V. K_2Picene appears differently at different

https://dx.doi.org/10.1021/acs.jpcc.0c03477
J. Phys. Chem. C 2020, 124, 22025−22034

positive sample biases, whereas the STM images of K_2Picene do not show obvious change from 1 to −3 V.

Figure 5a shows that the K-doped picene film seems to have become disordered at x = 2.4. Its FFT image displays a much more diffused centered rectangular reciprocal lattice, further demonstrating the poor crystallinity. The surface looks disordered at 1.8 V, whereas a parallelogram lattice made of chainlike structures is observed at −3.5 V. It seems that bright dots tend to pair up, though a few of them are separated alone. Because of the distortion on the surface, it is difficult to find a perfect unit cell. So, through toleration of large errors, a typical unit cell of $K_{2.4}$Picene is shown in Table 1.

With the K-doping ratio at 2.8, Figure 5d shows that the surface is composed of two phases, which can be seen more clearly in Figure 5f. The chainlike phase made of dimers is labeled as $K_{2.8}$Picene α phase and the hexagonal-like phase made of trimers is labeled as $K_{2.8}$Picene β phase. However, two phases seem disordered at a sample bias of 1.5 V (Figure 5e). The unit cells of $K_{2.8}$Picene α and $K_{2.8}$Picene β phases are listed in Table 1.

Figure 6a shows a new ordered phase that appears when x reaches 3. Some protrusive spots on the surface are the cross-shaped adsorbates (see Figure 6i). Its FFT pattern (Figure 6b) shows a rather clear rectangular reciprocal lattice, indicating an improved surface crystallinity. Figures 6c−j displays detailed images of the same area taken at various sample biases. The two defects pointed out by red arrows can be used to locate the image positions. The unit cell is labeled as a black rectangle in Figure 6c. The rectangular lattice structure is quite clear in the images taken at 3, 2.5, −1, −3.5, and −4 V. However, Figures 6e−g displays complicated structures. Such complicated patterns at different sample biases might be derived from superexchange interaction between orientational orderings and electronic states.[48]

Figure 7 shows the STM image of $K_{3.4}$Picene, where a distorted rowlike structure can be observed. The inset shows the detailed features with some clove-shaped structures at a sample bias of −2 V. The twisted molecular rows together with the new patterns indicate the emergence of a new round of structural changes with the increase of K doping.

When x = 3.8, K_xPicene displays two kinds of ordered structures together with some amorphous region, as shown in Figure 8a. The ordered phase in the right middle part of Figure 8a is labeled as $K_{3.8}$Picene α phase, which contains some round defects. While the ordered domains located in the left and bottom parts of the figure are labeled as $K_{3.8}$Picene β phase, which contains some cross-shaped defects. The two ordered phases look quite similar in the negative sample bias image (Figure 8b), yet they have different lattice constants, as shown in Table 1.

As shown in Figure 9a, as the doping ratio x reaches 4, the K_4Picene surface before annealing becomes completely amorphous, which can be verified by the inset FFT pattern. After annealing to 500 K for 30 min, the surface shows some ordered phases emerged. We label the one with a squarelike lattice as K_4Picene α phase and the striped phase as K_4Picene β phase in Figure 9d. No large and high-quality crystalline areas are found for either phase.

The structure parameters of all ordered phases mentioned before are summarized in Table 1. It is worth noting that as the K-doping concentration increases, the evolution of the unit cell shapes shows no obvious pattern. This indicates that the intercalation or doping of K atoms among picene molecules

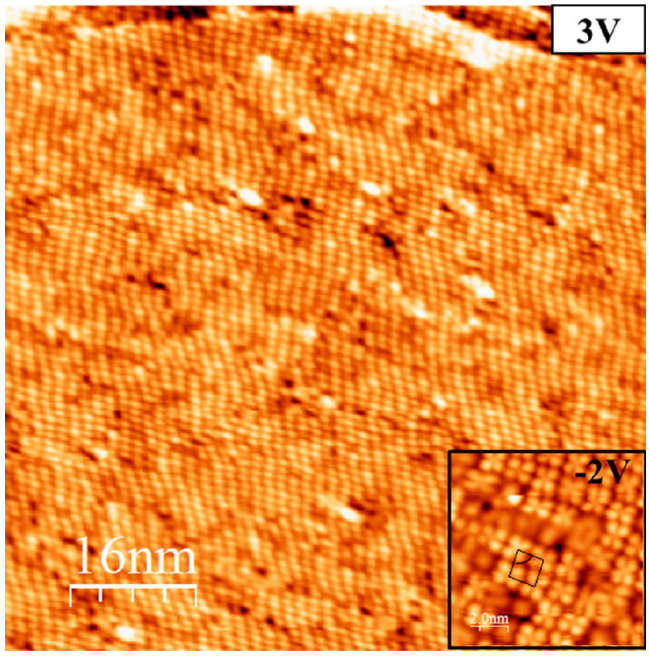

Figure 7. Topographic STM image of $K_{3.4}$Picene/Au(111) (image size, 80 × 80 nm^2; sample bias, V_b = 3 V). The inset shows a zoomed-in STM image at a sample bias of −2 V, where a black parallelogram denotes the unit cell of $K_{3.4}$Picene/Au(111) (image size, 10 × 10 nm^2).

may have rather complicated modes. During our experiments, annealing plays an important role in improving the crystallinity of K-doped picene films. One possible reason is that the annealing process may improve the uniformity of the K distribution and assist the formation of crystalline phases. Another reason is that a higher temperature may help the film overcome the possible high energy barriers between quite different unit cell structures. We should point out that RT annealing could not cause the different phases without further depositing K atoms. Therefore, the observed structural change must be caused by the increase of the K-doping ratio.

3.2. Evolution of Electronic States with K Doping.

Figure 10 shows the evolution of the electronic states of K_xPicene film on Au(111) with the increase of the doping ratio x. The curve labeled "Pristine" is taken on Phase 2 of the undoped picene film, while others are taken on the crystalline area of the corresponding sample surfaces. The STS data are representative, repeatable, and position-independent. One can see from Figure 10a that the LUMO states of K-doped picene/Au(111) are gradually shifted toward the Fermi level with the increase of K ratio from 0 to 3. Under the band-filling theory, once the electrons are doped into picene film effectively, the LUMO state will be filled partially, which leads to the Fermi level lifting into the LUMO state in principle.[49] By comparing Figure 2c and Figure 3i, one can see that K_1Picene shows similar energy gap width with the one in pristine Picene phase 2, while its Fermi level shifts upward obviously because of the K doping.[25,50] These results are consistent with the experimental observations, except for the much lower gap width and different detailed DOS structures. The application of PBE together with the complex structure may induce the underestimation of the energy gap. In our experiment, the LUMO state consecutively shifts to the Fermi level. To understand this issue, one should take into consideration the

https://dx.doi.org/10.1021/acs.jpcc.0c03477
J. Phys. Chem. C 2020, 124, 22025−22034

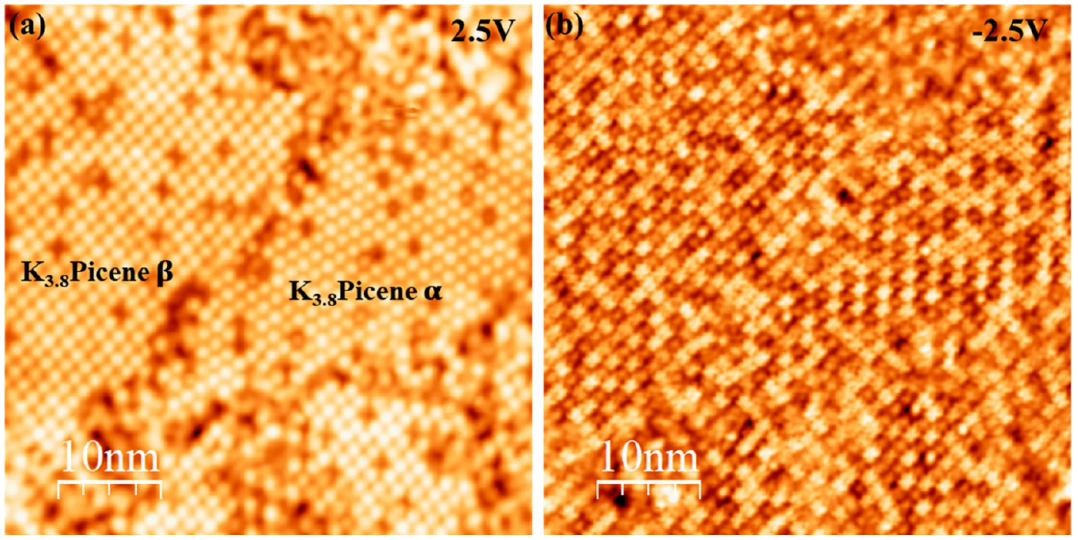

Figure 8. (a) Typical STM image of $K_{3.8}$Picene/Au(111) taken at 2.5 V, 20 pA (images size, 50 × 50 nm^2). (b) Image of the same area taken at −2.5 V, 20 pA.

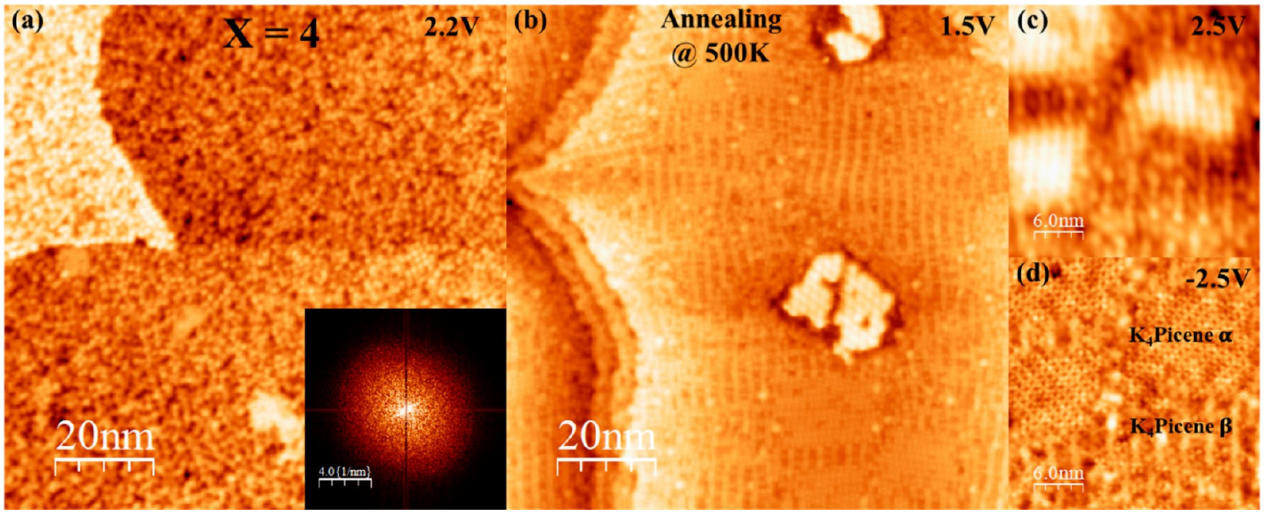

Figure 9. (a) STM image of as-grown K_4Picene/Au(111) and its FFT pattern. (b) STM image of annealed K_4Picene/Au(111). (c) and (d) Typical zoomed-in STM images of the annealed K_4Picene/Au(111) taken at sample biases of 2.5 and −2.5 V, respectively (image size, 30 × 30 nm^2). The tunneling current is set at 20 pA.

interface dipoles derived from the vacuum level difference of picene film and Au substrate.[1,51] In our sample, the substrate takes part in the charge-transfer process during the K atoms doping, resulting in less effective charge transfer into picene molecules. For K_1Picene, the LUMO state slightly shifts toward the Fermi level for about 0.2 eV, but the HOMO state shifts away from the Fermi level for about 0.5 eV. The energy gap enlarged by about 0.3 eV compared to that of the pristine film. This is caused by the changing of the molecular configuration from tilted to standing straight as well as the significant expansion of the unit cell size.[52] Further increasing the K-doping ratio, the HOMO and LUMO successively shift toward the lower energy direction. However, the LUMO state in K_3Picene does not reach the Fermi level. This could be caused by the film nature of the sample, the existence of an Au substrate, and the possible different crystal structure.[1,3,8,16,49,51,53]

Further increasing the amount of K, the previously discussed LUMO state of K_xPicene films can eventually shift across the Fermi level. Figure 10b shows the evolution of the electronic state with the K doping ratio ranging from 3.4 to 4. In the $K_{3.4}$Picene film, the LUMO state is believed to saddle right on the Fermi level and split into two states. Some additional states are found above the Fermi level, which may be caused by the inhomogeneity of the $K_{3.4}$Picene surface. The inset shows the two states with an energy gap of about 0.27 eV. Some previous works have also demonstrated similar energy gaps and proposed that strong electron-correlated effects play an important role in formation of the gap in K-doped picene systems.[7,17,18,23−25,54] The value of the energy gap in our experiment is also consistent with previous calculation results, where a Mott gap of ∼0.2 eV was obtained with a Hubbard repulsion of 0.68 eV.[55] Therefore, we speculate that the gap in our system is also caused by the electron correlation effect. The bulk samples with the K-doping ratio x = 3.3[6] or 3.5[21] are reported to have the highest superconducting transition temperature. Nevertheless, the development of the energy gap prevents the formation of a metallic state in our sample.[1,3]

https://dx.doi.org/10.1021/acs.jpcc.0c03477
J. Phys. Chem. C 2020, 124, 22025−22034

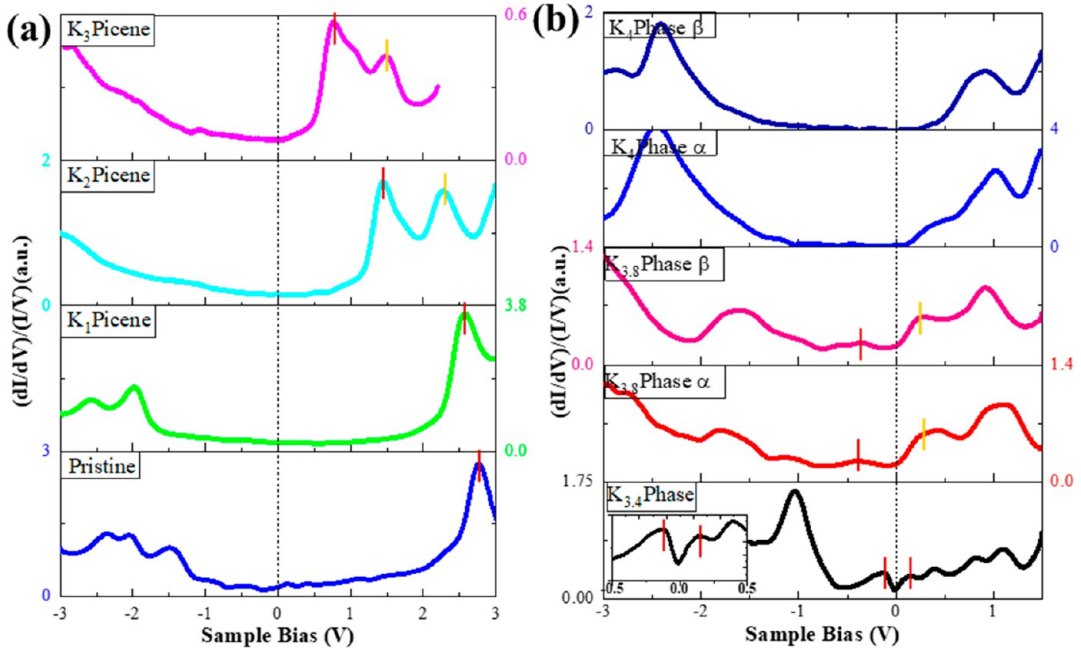

Figure 10. Evolution of electronic states of K_xPicene/Au(111). (a) $(dI/dV)/(I/V)$ spectra of K_xPicene with x from 0 to 3 and (b) from 3.4 to 4. All spectra were taken at 77 K.

More K atoms doping makes the original LUMO state shift below the Fermi level. The main states of $K_{3.8}$Picene α and $K_{3.8}$Picene β phases are almost the same (Figure 10b), even though they have different structures. The two states closest to the Fermi level are believed to originate from the LUMO and LUMO+1 states of the pristine picene film. They now form a gap of around 0.65 eV. Further doping to $x = 4$ or more shows neither high-quality crystalline structures nor metallic states.

4. CONCLUSION

In summary, a systematic study of K-doped picene film (K_xPicene) with a doping ratio ranging from 0 to 4 has been performed. Several ordered doping phases have been observed and investigated. The LUMO state of the original picene film is observed to successively shift toward the Fermi level with the increase of K doping. A gap of 0.27 eV is developed as the state saddles the Fermi level when $x = 3.4$. The state can shift below the Fermi level when $x = 3.8$, while more doping will neither generate good crystalline phases nor form metallic states. Our results rule out the possibility of superconductivity in K-doped picene on Au surfaces and provide references for future research in this area.

AUTHOR INFORMATION

Corresponding Authors

Xuefeng Wu − *Department of Physics, Southern University of Science and Technology, Shenzhen, Guangdong 518055, People's Republic of China*; Email: wuxf@mail.sustech.edu.cn

Kedong Wang − *Department of Physics, Southern University of Science and Technology, Shenzhen, Guangdong 518055, People's Republic of China*; orcid.org/0000-0003-1253-5603; Email: wangkd@sustech.edu.cn

Authors

Guowei Liu − *Harbin Institute of Technology, Harbin 150080, People's Republic of China; Department of Physics, Southern University of Science and Technology, Shenzhen, Guangdong 518055, People's Republic of China*; orcid.org/0000-0003-1283-788X

Xiji Shao − *Harbin Institute of Technology, Harbin 150080, People's Republic of China; Department of Physics, Southern University of Science and Technology, Shenzhen, Guangdong 518055, People's Republic of China*

Chaoqiang Xu − *School of Physics and Technology, Wuhan University, Wuhan, Hubei 430072, People's Republic of China*

Complete contact information is available at: https://pubs.acs.org/10.1021/acs.jpcc.0c03477

Notes

The authors declare no competing financial interest.

ACKNOWLEDGMENTS

This work was supported by the National Natural Science Foundation of China (Grant No. 11574128) and the MOST 973 Program (Grant No. 2014CB921402).

REFERENCES

(1) Wu, X. F.; Xu, C. Q.; Wang, K. D.; Xiao, X. D. Charge Transfer, Phase Separation, and Mott-Hubbard Transition in Potassium-Doped Coronene Films. *J. Phys. Chem. C* **2016**, *120*, 15446−15452.

(2) Naghavi, S. S.; Tosatti, E. Crystal Structure Search and Electronic Properties of Alkali-Doped Phenanthrene and Picene. *Phys. Rev. B: Condens. Matter Mater. Phys.* **2014**, *90*, 075143.

(3) Xu, C.; Que, Y.; Zhuang, Y.; Lin, Z.; Wu, X.; Wang, K.; Xiao, X. Growth Behavior of Pristine and Potassium Doped Coronene Thin Films on Substrates with Tuned Coupling Strength. *J. Phys. Chem. B* **2018**, *122*, 601−611.

(4) Ren, M. Q.; Chen, W.; Liu, Q.; Chen, C.; Qiao, Y. J.; Chen, Y. J.; Zhou, G.; Li, Z. H.; Zhang, T.; Yan, Y. J.; Feng, D. L. Observation of Gapped Phases in Potassium-Doped Single-Layer P-Terphenyl on Au (111). *Phys. Rev. B: Condens. Matter Mater. Phys.* **2019**, *99*, 045417.

(5) Kubozono, Y.; Eguchi, R.; Goto, H.; Hamao, S.; Kambe, T.; Terao, T.; Nishiyama, S.; Zheng, L.; Miao, X.; Okamoto, H. Recent Progress on Carbon-Based Superconductors. *J. Phys.: Condens. Matter* **2016**, *28*, 334001.

(6) Mitsuhashi, R.; Suzuki, Y.; Yamanari, Y.; Mitamura, H.; Kambe, T.; Ikeda, N.; Okamoto, H.; Fujiwara, A.; Yamaji, M.; Kawasaki, N.; Maniwa, Y.; Kubozono, Y. Superconductivity in Alkali-Metal-Doped Picene. *Nature* **2010**, *464*, 76−9.
(7) Yano, M.; Endo, M.; Hasegawa, Y.; Okada, R.; Yamada, Y.; Sasaki, M. Well-Ordered Monolayers of Alkali-Doped Coronene and Picene: Molecular Arrangements and Electronic Structures. *J. Chem. Phys.* **2014**, *141*, 034708.
(8) Shao, X. J.; Ma, X. H.; Liu, M. J.; Zhang, T.; Ma, Y. P.; Xu, C. Q.; Wu, X. F.; Lin, T.; Wang, K. D. Comparing Study of Picene Thin Films on Snse and Au(111) Surfaces. *Chem. Phys.* **2020**, *532*, 110689.
(9) Pompei, E.; Turchetti, C.; Hamao, S.; Miura, A.; Goto, H.; Okamoto, H.; Fujiwara, A.; Eguchi, R.; Kubozono, Y. Fabrication of Flexible High-Performance Organic Field-Effect Transistors Using Phenacene Molecules and Their Application toward Flexible Cmos Inverters. *J. Mater. Chem. C* **2019**, *7*, 6022−6033.
(10) Ros, E.; Puigdollers, J.; Ortega, P.; Voz, C. Origin of the Negative Differential Resistance in the Output Characteristics of a Picene-Based Thin-Film Transistor. *2019 Latin American Electron Devices Conference (LAEDC)*; IEEE: 2019; pp 53−56
(11) Rao, A.; Chow, P. C.; Gelinas, S.; Schlenker, C. W.; Li, C. Z.; Yip, H. L.; Jen, A. K.; Ginger, D. S.; Friend, R. H. The Role of Spin in the Kinetic Control of Recombination in Organic Photovoltaics. *Nature* **2013**, *500*, 435−9.
(12) Deibel, C.; Strobel, T.; Dyakonov, V. Role of the Charge Transfer State in Organic Donor-Acceptor Solar Cells. *Adv. Mater.* **2010**, *22*, 4097−111.
(13) Kubozono, Y.; Mitamura, H.; Lee, X.; He, X.; Yamanari, Y.; Takahashi, Y.; Suzuki, Y.; Kaji, Y.; Eguchi, R.; Akaike, K.; Kambe, T.; Okamoto, H.; Fujiwara, A.; Kato, T.; Kosugi, T.; Aoki, H. Metal-Intercalated Aromatic Hydrocarbons: A New Class of Carbon-Based Superconductors. *Phys. Chem. Chem. Phys.* **2011**, *13*, 16476−16493.
(14) Kim, J. S.; Kremer, R. K.; Boeri, L.; Razavi, F. S. Specific Heat of the Ca-Intercalated Graphite Superconductor Cac6. *Phys. Rev. Lett.* **2006**, *96*, 217002.
(15) Emery, N.; Herold, C.; d'Astuto, M.; Garcia, V.; Bellin, C.; Mareche, J. F.; Lagrange, P.; Loupias, G. Superconductivity of Bulk Cac6. *Phys. Rev. Lett.* **2005**, *95*, 087003.
(16) Giovannetti, G.; Capone, M. Electronic Correlation Effects in Superconducting Picene from Ab Initio Calculations. *Phys. Rev. B: Condens. Matter Mater. Phys.* **2011**, *83*, 134508.
(17) Okazaki, H.; Wakita, T.; Muro, T.; Kaji, Y.; Lee, X.; Mitamura, H.; Kawasaki, N.; Kubozono, Y.; Yamanari, Y.; Kambe, T.; Kato, T.; Hirai, M.; Muraoka, Y.; Yokoya, T. Electronic Structure of Pristine and K-Doped Solid Picene: Nonrigid Band Change and Its Implication for Electron-Intramolecular-Vibration Interaction. *Phys. Rev. B: Condens. Matter Mater. Phys.* **2010**, *82*, 195114.
(18) Caputo, M.; Di Santo, G.; Parisse, P.; Petaccia, L.; Floreano, L.; Verdini, A.; Panighel, M.; Struzzi, C.; Taleatu, B.; Lal, C.; Goldoni, A. Experimental Study of Pristine and Alkali Metal Doped Picene Layers: Confirmation of the Insulating Phase in Multilayer Doped Compounds. *J. Phys. Chem. C* **2012**, *116*, 19902−19908.
(19) Casula, M.; Calandra, M.; Profeta, G.; Mauri, F. Intercalant and Intermolecular Phonon Assisted Superconductivity in K-Doped Picene. *Phys. Rev. Lett.* **2011**, *107*, 137006.
(20) Kelly, S. J.; Sorescu, D. C.; Wang, J.; Archer, K. A.; Jordan, K. D.; Maksymovych, P. Structural and Electronic Properties of Ultrathin Picene Films on the Ag(100) Surface. *Surf. Sci.* **2016**, *652*, 67−75.
(21) Teranishi, K.; He, X. X.; Sakai, Y.; Izumi, M.; Goto, H.; Eguchi, R.; Takabayashi, Y.; Kambe, T.; Kubozono, Y. Observation of Zero Resistivity in K-Doped Picene. *Phys. Rev. B: Condens. Matter Mater. Phys.* **2013**, *87*, 060505.
(22) Kambe, T.; He, X.; Takahashi, Y.; Yamanari, Y.; Teranishi, K.; Mitamura, H.; Shibasaki, S.; Tomita, K.; Eguchi, R.; Goto, H.; Takabayashi, Y.; Kato, T.; Fujiwara, A.; Kariyado, T.; Aoki, H.; Kubozono, Y. Synthesis and Physical Properties of Metal-Doped Picene Solids. *Phys. Rev. B: Condens. Matter Mater. Phys.* **2012**, *86*, 214507.
(23) Heguri, S.; Kobayashi, M.; Tanigaki, K. Questioning the Existence of Superconducting Potassium Doped Phases for Aromatic Hydrocarbons. *Phys. Rev. B: Condens. Matter Mater. Phys.* **2015**, *92*, 014502.
(24) Mahns, B.; Roth, F.; Knupfer, M. Absence of Photoemission from the Fermi Level in Potassium Intercalated Picene and Coronene Films: Structure, Polaron, or Correlation Physics? *J. Chem. Phys.* **2012**, *136*, 134503.
(25) Ruff, A.; Sing, M.; Claessen, R.; Lee, H.; Tomic, M.; Jeschke, H. O.; Valenti, R. Absence of Metallicity in K-Doped Picene: Importance of Electronic Correlations. *Phys. Rev. Lett.* **2013**, *110*, 216403.
(26) Wakita, T.; Okazaki, H.; Jabuchi, T.; Hamada, H.; Muraoka, Y.; Yokoya, T. Electronic Structure of K-Doped Picene Film on Hopg. *J. Phys.: Condens. Matter* **2017**, *29*, 064001.
(27) Chen, S. W.; Sang, I. C.; Okamoto, H.; Hoffmann, G. Adsorption of Phenacenes on a Metallic Substrate: Revisited. *J. Phys. Chem. C* **2017**, *121*, 11390−11398.
(28) Okamoto, H.; Hamao, S.; Eguchi, R.; Goto, H.; Takabayashi, Y.; Yen, P. Y.-H.; Liang, L. U.; Chou, C.-W.; Hoffmann, G.; Gohda, S.; Sugino, H.; Liao, Y.-F.; Ishii, H.; Kubozono, Y. Synthesis of the Extended Phenacene Molecules, [10]Phenacene and [11]Phenacene, and Their Performance in a Field-Effect Transistor. *Sci. Rep.* **2019**, *9*, 4009.
(29) Okazaki, H.; Jabuchi, T.; Wakita, T.; Kato, T.; Muraoka, Y.; Yokoya, T. Evidence for Metallic States in Potassium-Intercalated Picene Film on Graphite. *Phys. Rev. B: Condens. Matter Mater. Phys.* **2013**, *88*, 245414.
(30) Wang, X. F.; Liu, R. H.; Gui, Z.; Xie, Y. L.; Yan, Y. J.; Ying, J. J.; Luo, X. G.; Chen, X. H. Superconductivity at 5 K in Alkali-Metal-Doped Phenanthrene. *Nat. Commun.* **2011**, *2*, 507.
(31) Yoshida, Y.; Yang, H.-H.; Huang, H.-S.; Guan, S.-Y.; Yanagisawa, S.; Yokosuka, T.; Lin, M.-T.; Su, W.-B.; Chang, C.-S.; Hoffmann, G.; Hasegawa, Y. Scanning Tunneling Microscopy/Spectroscopy of Picene Thin Films Formed on Ag(111). *J. Chem. Phys.* **2014**, *141*, 114701.
(32) Zhou, C. S.; Shan, H.; Li, B.; Zhao, A. D. Imaging Molecular Orbitals of Single Picene Molecules Adsorbed on Cu(111) Surface: A Combined Experimental and Theoretical Study. *Chin. J. Chem. Phys.* **2017**, *30*, 29−35.
(33) Zhou, C. S.; Shan, H.; Li, B.; Zhao, A. D.; Wang, B. Engineering Hybrid Co-Picene Structures with Variable Spin Coupling. *Appl. Phys. Lett.* **2016**, *108*, 171601.
(34) Eigler, D. M.; Lutz, C. P.; Rudge, W. E. An Atomic Switch Realized with the Scanning Tunneling Microscope. *Nature* **1991**, *352*, 600−603.
(35) Hosokai, T.; Hinderhofer, A.; Bussolotti, F.; Yonezawa, K.; Lorch, C.; Vorobiev, A.; Hasegawa, Y.; Yamada, Y.; Kubozoro, Y.; Gerlach, A.; Kera, S.; Schreiber, F.; Ueno, N. Thickness and Substrate Dependent Thin Film Growth of Picene and Impact on the Electronic Structure. *J. Phys. Chem. C* **2015**, *119*, 29027−29037.
(36) Zhang, C.; Tsuboi, H.; Hasegawa, Y.; Iwasawa, M.; Sasaki, M.; Wakayama, Y.; Ishii, H.; Yamada, Y. Fabrication of Highly Oriented Multilayer Films of Picene and Dntt on Their Bulklike Monolayer. *Acs Omega* **2019**, *4*, 8669−8673.
(37) Huempfner, T.; Hafermann, M.; Udhardt, C.; Otto, F.; Forker, R.; Fritz, T. Insight into the Unit Cell: Structure of Picene Thin Films on Ag(100) Revealed with Complementary Methods. *J. Chem. Phys.* **2016**, *145*, 174706.
(38) Kresse, G.; Furthmuller, J. Efficient Iterative Schemes for Ab Initio Total-Energy Calculations Using a Plane-Wave Basis Set. *Phys. Rev. B: Condens. Matter Mater. Phys.* **1996**, *54*, 11169−11186.
(39) Kresse, G.; Furthmuller, J. Efficiency of Ab-Initio Total Energy Calculations for Metals and Semiconductors Using a Plane-Wave Basis Set. *Comput. Mater. Sci.* **1996**, *6*, 15−50.
(40) Klimes, J.; Bowler, D. R.; Michaelides, A. Van Der Waals Density Functionals Applied to Solids. *Phys. Rev. B: Condens. Matter Mater. Phys.* **2011**, *83*, 195131.
(41) Grimme, S.; Antony, J.; Ehrlich, S.; Krieg, H. A Consistent and Accurate Ab Initio Parametrization of Density Functional Dispersion

https://dx.doi.org/10.1021/acs.jpcc.0c03477
J. Phys. Chem. C 2020, 124, 22025−22034

Correction (Dft-D) for the 94 Elements H-Pu. *J. Chem. Phys.* **2010**, *132*, 154104.
(42) Grimme, S.; Ehrlich, S.; Goerigk, L. Effect of the Damping Function in Dispersion Corrected Density Functional Theory. *J. Comput. Chem.* **2011**, *32*, 1456−1465.
(43) Blochl, P. E. Projector Augmented-Wave Method. *Phys. Rev. B: Condens. Matter Mater. Phys.* **1994**, *50*, 17953−17979.
(44) Perdew, J. P.; Burke, K.; Ernzerhof, M. Generalized Gradient Approximation Made Simple (Vol 77, Pg 3865, 1996). *Phys. Rev. Lett.* **1997**, *78*, 1396−1396.
(45) Xie, Z. X.; Huang, Z. F.; Xu, X. Influence of Reconstruction on the Structure of Self-Assembled Normal-Alkane Monolayers on Au(111) Surfaces. *Phys. Chem. Chem. Phys.* **2002**, *4*, 1486−1489.
(46) Okamoto, H.; Kawasaki, N.; Kaji, Y.; Kubozono, Y.; Fujiwara, A.; Yamaji, M. Air-Assisted High-Performance Field-Effect Transistor with Thin Films of Picene. *J. Am. Chem. Soc.* **2008**, *130*, 10470−1.
(47) Kosugi, T.; Miyake, T.; Ishibashi, S.; Arita, R.; Aoki, H. First-Principles Electronic Structure of Solid Picene. *J. Phys. Soc. Jpn.* **2009**, *78*, 113704.
(48) Wang, Y.; Yamachika, R.; Wachowiak, A.; Grobis, M.; Khoo, K. H.; Lee, D. H.; Louie, S. G.; Crommie, M. F. Novel Orientational Ordering and Reentrant Metallicity in K(X)C(60) Monolayers for 3 < or = X < or = 5. *Phys. Rev. Lett.* **2007**, *99*, 086402.
(49) Naghavi, S. S.; Fabrizio, M.; Qin, T.; Tosatti, E. Electron-Doped Organics: Charge-Disproportionate Insulators and Hubbard-Frohlich Metals. *Phys. Rev. B: Condens. Matter Mater. Phys.* **2013**, *88*, 115106.
(50) Kosugi, T.; Miyake, T.; Ishibashi, S.; Arita, R.; Aoki, H. First-Principles Structural Optimization and Electronic Structure of the Superconductor Picene for Various Potassium Doping Levels. *Phys. Rev. B: Condens. Matter Mater. Phys.* **2011**, *84*, 214506.
(51) Monti, O. L. Understanding Interfacial Electronic Structure and Charge Transfer: An Electrostatic Perspective. *J. Phys. Chem. Lett.* **2012**, *3*, 2342−51.
(52) Wang, Y.; Yamachika, R.; Wachowiak, A.; Grobis, M.; Crommie, M. F. Tuning Fulleride Electronic Structure and Molecular Ordering Via Variable Layer Index. *Nat. Mater.* **2008**, *7*, 194−7.
(53) de Andres, P. L.; Guijarro, A.; Vergés, J. A. Crystal Structure and Electronic States of Tripotassium Picene. *Phys. Rev. B: Condens. Matter Mater. Phys.* **2011**, *83*, 245113.
(54) Kim, M.; Min, B. I.; Lee, G.; Kwon, H. J.; Rhee, Y. M.; Shim, J. H. Density Functional Calculations of Electronic Structure and Magnetic Properties of the Hydrocarbon K(3)Picene Superconductor near the Metal-Insulator Transition. *Phys. Rev. B: Condens. Matter Mater. Phys.* **2011**, *83*, 214510.
(55) Giovannetti, G.; Casula, M.; Werner, P.; Mauri, F.; Capone, M. Downfolding Electron-Phonon Hamiltonians from Ab Initio Calculations: Application to K-3 Picene. *Phys. Rev. B: Condens. Matter Mater. Phys.* **2014**, *90*, 115435.

https://dx.doi.org/10.1021/acs.jpcc.0c03477
J. Phys. Chem. C 2020, 124, 22025−22034

ACS APPLIED MATERIALS & INTERFACES

www.acsami.org

Research Article

Symmetric Sodium-Ion Battery Based on Dual-Electron Reactions of NASICON-Structured $Na_3MnTi(PO_4)_3$ Material

Yu Zhou, Xiji Shao, Kwok-ho Lam, You Zheng, Lingzhi Zhao, Kedong Wang, Jinzhu Zhao,* Fuming Chen,* and Xianhua Hou*

Cite This: *ACS Appl. Mater. Interfaces* 2020, 12, 30328–30335

Read Online

ACCESS | Metrics & More | Article Recommendations | Supporting Information

ABSTRACT: Symmetric sodium-ion batteries possess promising features such as low cost, easy manufacturing process, and facile recycling post-process, which are suitable for the application of large-scale stationary energy storage. Herein, we proposed a symmetric sodium-ion battery based on dual-electron reactions of a NASICON-structured $Na_3MnTi(PO_4)_3$ material. The $Na_3MnTi(PO_4)_3$ electrode can deliver a stable capacity of up to 160 mAh g^{-1} with a Coulombic efficiency of 97% at 0.1 C by utilizing the redox reactions of $Ti^{3+/4+}$, $Mn^{2+/3+}$, and $Mn^{3+/4+}$. This is the first time to investigate the symmetric sodium-ion full cell using $Na_3MnTi(PO_4)_3$ as both cathode and anode in the organic electrolyte, demonstrating excellent reversibility and cycling performance with voltage plateaus of about 1.4 and 1.9 V. The full cell exhibits a reversible capacity of 75 mAh g^{-1} at 0.1 C and an energy density of 52 Wh kg^{-1}. In addition, both *ex situ* X-ray diffraction (XRD) analysis and first-principles calculations are employed to investigate the sodiation mechanism and structural evolution. The current research provides a feasible strategy for the symmetric sodium-ion batteries to achieve high energy density.

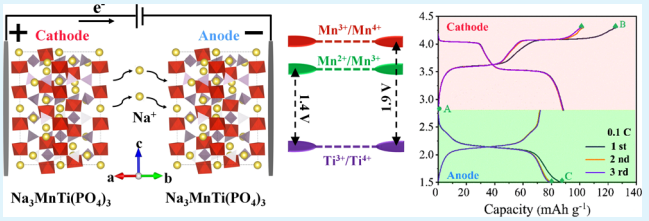

KEYWORDS: *sodium-ion batteries, symmetric full cell, $Na_3MnTi(PO_4)_3$, NASICON structure, multielectron redox reaction*

INTRODUCTION

With the consumption of oil and natural gas, the conversion of renewable energies like wind, solar, geothermal, etc. into usable energy forms is critical due to the clean and pollution-free characteristics.[1−4] In addition to energy conversion, storage is another challenge. Considerable efforts have been devoted to develop energy-storage devices, such as the lithium-ion batteries (LIBs).[5−8] Nowadays, LIBs are the most popular technology for energy storage, which are commercialized widely in various portable electronic devices, electric vehicles, etc.[9−14] However, LIBs have the drawback of high cost due to scarce availability of lithium resources. Therefore, sodium-ion batteries (SIBs) will be an emerging candidate to replace LIBs owing to the availability of sufficient raw material, safety, and low cost.[15−19] Recently, NASICON (Na superionic conductor)-structured materials are a hot research topic owing to the stable host structure, plenty of sodium-insertion interstices, and fast Na^+-ion diffusion. NASICON-structured polyanionic phosphates with a formula of $A_xMM'(PO_4)_3$ (A = Li, Na, K, etc.; M, M′ = transition-metal element) possess a robust three-dimensional framework of MO_6 and $M'O_6$ octahedral corner sharing with PO_4 tetrahedra, which delivers excellent cyclability.[20−25] Furthermore, the strong inductive effect of the phosphates endows multielectron redox reaction and higher operating potential versus Na^+/Na, compared to those of layered oxides.[26,27] $Na_3V_2(PO_4)_3$ is a typical NASICON-structured polyanionic phosphate that demonstrates two voltage plateaus at 1.6 and 3.3 V vs Na^+/Na, which correspond to the redox pairs of $V^{2+/3+}$ and $V^{3+/4+}$, resulting in dual-electron transfer.[28,29] So far, other kinds of phosphates have been synthesized via cation substitution partial or ful to develop redox reactions involving more than two electrons and excellent sodium-storage performance, including $Na_2VTi(PO_4)_3$, $Na_3V_{1.5}Cr_{0.5}(PO_4)_3$, $Na_3MnTi(PO_4)_3$, $Na_3FeV(PO_4)_3$, and $Na_2CrTi(PO_4)_3$.[26,30−33]

To date, the design of symmetric SIBs with the same electrode materials is progressively attractive compared to that of asymmetric batteries, owing to the less influence of matching design between cathode and anode materials, easy manufacturing process, facile recycling post-process, and low manufacturing cost.[34−37] In addition, symmetric SIBs based on the same intercalation-type compound are able to reduce the bulk expansion of electrode materials during Na^+ insertion/extraction because one electrode shrinks while the other electrode may expand, and vice versa.[38] At present, limited by the energy density, symmetric SIBs could be applied in storage power station, low-end electronic consumption, and low-speed

Received: March 28, 2020
Accepted: June 12, 2020
Published: June 12, 2020

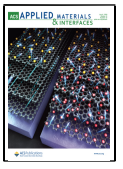

https://dx.doi.org/10.1021/acsami.0c05784
ACS Appl. Mater. Interfaces 2020, 12, 30328−30335

electric vehicles. NASICON-structured $Na_3MnTi(PO_4)_3$ has been reported recently, and its electrochemical performance is once studied in the aqueous system.[36] However, the operating voltage is limited owing to the potential window of water splitting with merely one Na^+ per formula extraction/insertion.[39] To date, symmetric sodium-ion battery in organic electrolyte with dual-electron transfer has not been reported yet.

In this work, the $Na_3MnTi(PO_4)_3$ electrode, prepared by a typical sol−gel method, delivers a reversible capacity of 160 mAh g^{-1} with a Coulombic efficiency of 97% under the voltage window of 1.5−4.3 V vs Na^+/Na at 0.1 C. This is the first time to investigate the dual-electron reactions of the symmetric sodium-ion full cell with $Na_3MnTi(PO_4)_3$ as both cathode and anode using the distinct of redox couples of $Ti^{3+/4+}$ and $Mn^{3+/4+}$. The symmetric full cell demonstrates excellent reversibility and cycling performance and exhibits a reversible capacity of 75 mAh g^{-1} at 0.1 C with energy densities of 52 Wh kg^{-1} and 60.4 mAh g^{-1} at 1 C. Moreover, theoretical investigation can be used to predict the voltage plateaus theoretically and estimate the configuration of the Na^+-site candidate under different occupation rates. Both *ex situ* X-ray diffraction (XRD) analysis and first-principles calculations are applied for studying the sodiation mechanism and structural evolution, indicating solid solution and two-phase reactions during Na^+ extraction/insertion. The proposed strategy is feasible for developing symmetric SIBs with high energy density.

EXPERIMENTAL SECTION

Preparation of $Na_3MnTi(PO_4)_3$. Carbon-coated $Na_3MnTi(PO_4)_3$ was prepared by the sol−gel method. $NaC_2H_3O_2$ (3 mmol), $MnC_4H_6O_4{\cdot}4H_2O$ (1 mmol), $NH_4H_2PO_4$ (3 mmol), and $C_6H_8O_7{\cdot}H_2O$ (3 mmol) were dissolved in 30 mL of deionized water to get Solution A. Titanium isopropoxide ($C_{12}H_{28}O_4Ti$, 1 mmol; Aladdin, 99.9% purity) was dissolved in 20 mL of absolute ethanol to obtain the transparent Solution B. Solution B was added into Solution A dropwise. The final solution was sealed and stirred in a water bath at 80 °C for 2 h and then uncovered until the moisture is completely evaporated to give a light-yellow precursor. The precursor was further kept in an oven and successively ground into powder. Finally, the precursor was sintered at 650 °C for 12 h under argon atmosphere at a heating rate of 5 °C·min^{-1} to obtain the $Na_3MnTi(PO_4)_3$ nanocomposite. The molar ratio of citric acid and transition metal (Ti and Mn) equaled 3:2, and citric acid was used as both chelating agent and carbon source.

Materials Characterization. The crystal structure of $Na_3MnTi(PO_4)_3$ was tested by X-ray diffraction (XRD) (Bruker D8 Advance with Cu/Kα radiation, λ = 0.15406 nm, 40 kV, 40 mA). Thermogravimetric (TG) analysis was employed to confirm the carbon content of materials. Raman measurements (RM) were performed on LabRAM HR Evolution with a laser wavelength of 532 nm. The morphology and distribution of elements were characterized by scanning electron microscopy (SEM, FEI Quanta 250 FEG). Energy-dispersive spectrometry (EDS) of a selected area was tested to analyze the chemical composition. Transmission electron microscopy (TEM) and selected area electron diffraction (SAED) images were obtained using a JEM-2100HR device. Cyclic voltammetry tests were carried out by a Solartron Analytical 1470E workstation. Electrochemical impedance spectroscopy (EIS) was performed under different charged/discharged states in the frequency of 1 mHz to 100 kHz.

Electrochemical Measurements. To study the electrochemical performances of the as-prepared $Na_3MnTi(PO_4)_3$, coin-type half-cells were assembled with sodium foil in a glovebox filled with argon (H_2O < 0.5 ppm, O_2 < 0.5 ppm). $Na_3MnTi(PO_4)_3$ active materials, super P conductive, and poly(vinylidene fluoride) binders with a weight ratio of 7:2:1 were dissolved in *N*-methylpyrrolidone (NMP) to obtain homogeneous slurries. The slurries were coated on aluminum foil and dried in a vacuum oven at 120 °C overnight to remove the solvent. The electrode film was then cut into a 12 mm diameter disk. The electrode loading mass was in the range of 1.2−1.5 mg cm^{-2}. Glass fiber (Whatman GF/C) was used as the separator. 1 M $NaClO_4$ dissolved in a solvent of ethylene carbonate (EC) and propylene carbonate (PC) (1:1 v/v) with 5 vol % addition of fluoroethylene carbonate (FEC) was used as the electrolyte. The electrochemical performance was tested on a Land battery analyzer within the cutoff voltage range of 1.5-4.3 V (vs Na/Na^+). Especially, without pretreatment processes, the symmetric battery with the same cathode and anode materials was directly assembled with the pristine $Na_3MnTi(PO_4)_3$ electrode. The battery was cathode-limited, and the capacity balance was controlled with the cathode/anode mass ratio of 1/1.25 (The charge specific capacity of the cathode was around 100 mA g^{-1}, and the discharge specific capacity of the anode was around 80 mA g^{-1}. Herein, the ratio of 100/80 was 1.25/1). The open-cell voltage of the symmetric full cell was approximately 0 V. 1 C corresponds to 117 mA g^{-1}.

RESULTS AND DISCUSSION

Theoretical Calculation of $Na_3MnTi(PO_4)_3$ Voltage Plateaus. The atomic structure of the supercell of $Na_xMnTi(PO_4)_3$ is shown in Figure 1a. PO_4 tetrahedron and MnO_6 (and TiO_6) octahedron share the oxygen atom at the corner. All of the possible sites are fully occupied for Na ions. To distinguish the sites of atoms, five groups are classified as colored in Figure 1b, depending on the symmetry and thermal stability of sodium ions. The calculation results are qualitatively displayed in Table S1.[40−43] Site-I is the most favorable location to occupy, and site-V is the least stable

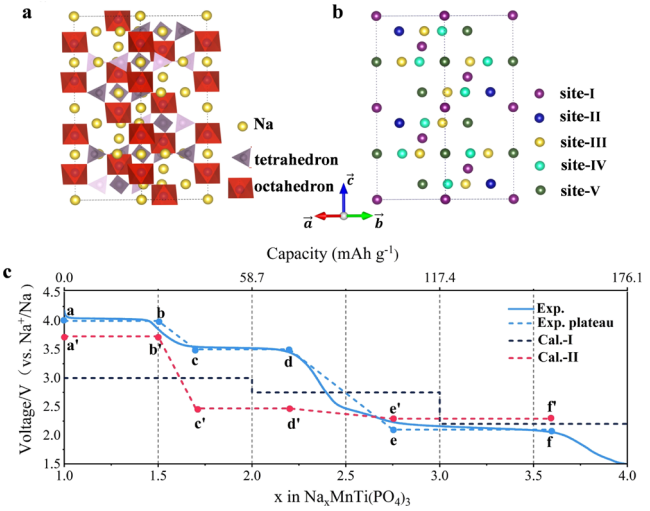

Figure 1. Theoretical calculation of voltage plateaus for $Na_3MnTi(PO_4)_3$. (a) Scheme plot of the atomic structure for the supercell of $Na_xMnTi(PO_4)_3$. Here, the fully occupied Na sites are shown (x = 5), while PO_4 tetrahedrons are highlighted with gray−purple, and MnO_6 (and TiO_6) octahedrons are highlighted with red color. (b) Five groups of Na sites are differed by colors, while the remaining sites are suppressed. (c) Calculated sodiation voltage profile (red and black dotted lines) in comparison to the experimental values (blue solid and dotted lines). The blue dotted line (exp. plateau) is simplified from the blue solid line (experimental curve). The black dotted line refers to the ideal case in which site-II, site-III, and site-IV are fully occupied one by one. The red dotted line is calculated using the experimental values of occupation rate for each plateau.

https://dx.doi.org/10.1021/acsami.0c05784
ACS Appl. Mater. Interfaces 2020, 12, 30328−30335

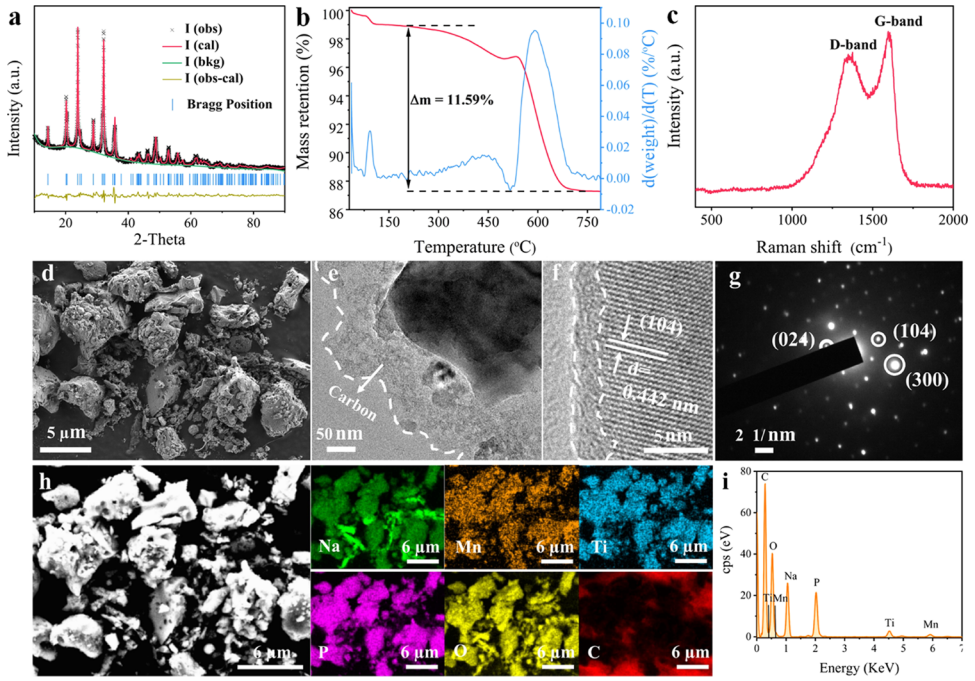

Figure 2. Crystal structure of $Na_3MnTi(PO_4)_3$ and characterization. (a) XRD pattern and Rietveld refinement, (b) TG curve, (c) Raman spectroscopy, (d) SEM image, (e) TEM image, (f) high-resolution (HR)TEM image, (g) SAED patterns, (h) elements mapping image, and (i) EDS image.

location. During the insertion/extraction process, Na ions at site-I will be immobilized to maintain the framework stability due to the most favorable energy, and Na ions at site-II, site-III, site-IV, and site-V are able to be inserted/extracted for electrochemical energy storage.[44] In our experiments, the occupation of site-V is not considered due to the least priority in the investigation.

During the discharging process from $Na_1MnTi(PO_4)_3$ to $Na_4MnTi(PO_4)_3$, three voltage plateaus are displayed at 4.0, 3.5, and 2.1 V vs Na^+/Na. Starting from the configuration $Na_1MnTi(PO_4)_3$ (x = 1), the occupation will follow the theoretical order, i.e., site-II, site-III, and then site-IV in sequence. Three ideal plateaus can be obtained as shown by the black dotted line (Cal.-I) in Figure 1c. When the current group is fully occupied, Na ions will go to the next group. However, there are still partial deviations on voltage plateaus, and their difference between the calculation and experimental results is shown by the blue solid line (Exp.). The main reasons can be given as follows: (1) The calculated group of sites is not fully occupied at voltage plateaus in practical experiments. When Na ions start to occupy a new site with different on-site energies, the voltage will shift to the next plateau like the plateau c,d for site-III and the plateau e,f for site-IV. (2) In the practical discharge process, the voltage moves from one plateau to another gradually, i.e., the ranges of b,c and d,e. It is contrary to the ideal calculated case in which the voltage jumps from one plateau to another discontinuously. In the intermediate region, Na ions would occupy sites with different on-site energies, while the experimental values are the dynamic average of them.

To further analyze the voltage evolution, the experimental value of x for each plateau is selected for re-simulation. The updated result, see the red dotted line (Cal.-II), fits better the trend of experimental results. It is worth to point out that the calculated voltage value strongly depends on the value of x and the corresponding configurations. At this stage, it is relatively easy to estimate the configurations at two ends such as Points a, b, e, and f. Nevertheless, the calculated voltage of the c′,d′ plateau is still far less than the experimental one, which requires a substantial detailed study to give the accurate atomic structures of Points c and d. Theoretical studies do not only predict the voltage plateaus but also provide valuable clues to qualitatively understand the mechanism of charge/discharge process in $Na_xMnTi(PO_4)_3$.

Crystal Structure of $Na_3MnTi(PO_4)_3$ and Characterizations. The crystal structure analysis and characterization of $Na_3MnTi(PO_4)_3$ are demonstrated in Figure 2. Rietveld refinement of the X-ray diffraction (XRD) pattern shows the successful preparation of $Na_3MnTi(PO_4)_3$ by a facile sol−gel method in Figure 2a. The pattern can be indexed to the rhombohedral structure with lattice parameters of a = 8.73352 Å and c = 21.84703 Å and a reliable result of R = 4.32%, exhibiting little discrepancy to that of $Na_3V_2(PO_4)_3$.[45] $Na_3MnTi(PO_4)_3$ possesses a typical rhombohedral NASICON-type structure with space group $R\bar{3}c$.[46] The detailed structural information including lattice parameters and site occupancy factor is presented in Table S2 (Supporting Information). The carbon amount of 11.59% is confirmed by the thermogravimetric (TG) analysis (Figure 2b). A slight increase in weight around 500 °C is attributed to the oxidation of low-valence-state metal species during the combustion of carbon. Raman spectroscopy (Figure 2c) is utilized to qualitatively study the degree of graphitization in $Na_3MnTi(PO_4)_3$. The G-band and D-band of carbon materials are located at 1594.7 and 1348.3 cm^{-1}, respectively. The ratio of I_G/I_D = 1.14 (the intensity ratio of 2394/2090) indicates the existence of amorphous carbon in pristine $Na_3MnTi(PO_4)_3$.[26,46]

The morphology of $Na_3MnTi(PO_4)_3$ is obtained by SEM, as shown in Figure 2d. $Na_3MnTi(PO_4)_3$ has a wide range of

https://dx.doi.org/10.1021/acsami.0c05784
ACS Appl. Mater. Interfaces 2020, 12, 30328−30335

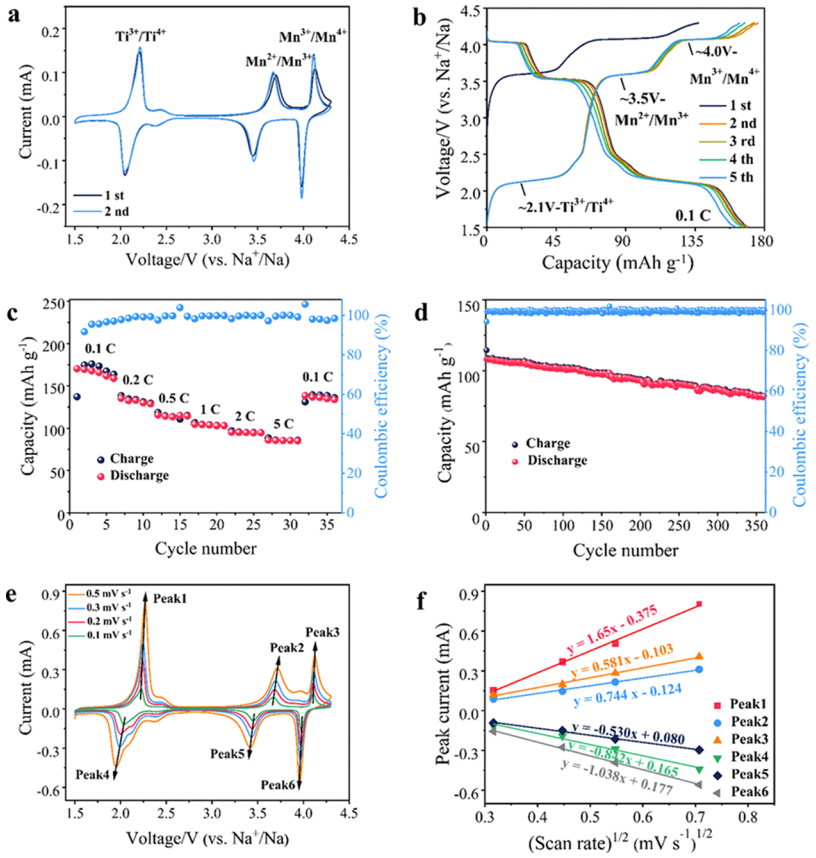

Figure 3. Sodium-ion storage performance and kinetic properties of $Na_3MnTi(PO_4)_3$ with Na counter. (a) Cyclic voltammogram curves between 1.5 and 4.3 V at a scan rate of 0.1 mV s^{-1}. (b) Galvanostatic charge−discharge profiles in the initial five cycles between 1.5 and 4.3 V at 0.1 C (1 C = 117 mA g^{-1}). (c) Rate capability from 0.1 to 5 C. (d) Cycling performance at 5 C. (e) Cyclic voltammogram curves at different scanning rates. (f) Relationship between the peak current (I_p) and the square root of the scan rate ($v^{1/2}$).

particle size from few nanometers to micrometer. The matching of different particle sizes is beneficial to the physical contact between particles, resulting in high density. TEM analysis is conducted to further confirm the composition of the amorphous carbon and $Na_3MnTi(PO_4)_3$. As shown in Figure 2e, $Na_3MnTi(PO_4)_3$ particles are embedded in an amorphous carbon matrix. The high-resolution HRTEM (Figure 2f) image manifests that the surface of well-crystallized $Na_3MnTi(PO_4)_3$ is coated by a thin layer of uniform amorphous carbon with ∼3 nm thickness from the pyrolysis of critic acid. The observed lattice fringe of 0.442 nm is consistent with the interplanar spacing plane (104). Selected area electron diffraction (SAED) in Figure 2g is employed to further explore the structure of $Na_3MnTi(PO_4)_3$, which exhibits (024), (104), and (300) planes for the rhombohedral structure. These agree with the XRD results. Element mapping in Figure 2h and energy-dispersive spectra (EDS) in Figure 2i of selected area are tested to analyze the chemical composition. The distribution of homogeneous elements of Na, Mn, Ti, P, and O can be observed as displayed. Based on the EDS results, no other elements are detected and the atomic ratio of Na:Mn:Ti is equal to 3.5:1.06:1. The amorphous carbon layer on the surface of $Na_3MnTi(PO_4)_3$ particles will promote the electron transfer owing to the low electrical conductivity of NASICON-structured phosphates.[23,31,47]

Sodium-Ion Storage Performance and Kinetic Properties of $Na_3MnTi(PO_4)_3$. The electrochemical performance of the as-prepared $Na_3MnTi(PO_4)_3$ is evaluated by assembling the CR2032-type half-cell with sodium counter. Cyclic voltammogram (CV) tests are carried out to investigate the redox activities of $Na_3MnTi(PO_4)_3$. As shown in Figure 3a, the initial three CV cycles are recorded with a scan rate of 0.1 mV s^{-1} between 4.3 and 1.5 V. Three pairs of redox couples are located at around 2.04/2.22, 3.46/3.66, and 3.99/4.10 V, respectively, which also correspond to a three-step transition of the Na^+ extraction/insertion due to the redox reactions of $Ti^{3+/4+}$, $Mn^{2+/3+}$, and $Mn^{3+/4+}$. The electrochemical impedance spectra (EIS) are tested to understand the difference in different voltage conditions. As represented in Figure S1 and Table S3 (Supporting Information), according to the equivalent circuit, the charge-transfer resistances (R_{ct}) do not change a lot at different charged/discharged states, which can be attributed to the physical properties of carbon-coated NASICON structure, particularly the better conductivity. The evolution processes are further analyzed in detail using *ex situ* XRD with different charge/discharge states between 4.3 and 1.5 V, as shown in Figure S2 (Supporting Information). The whole Na^+ extraction or insertion process refers to two-phase evolution and solid solution reactions (single-phase evolution).[46,48] As depicted in Figure 3b, in the first charge process, two plateaus are displayed, corresponding to dual-electron reactions. This low capacity may be attributed to the high initial open-circuit voltage of up to 2.6−2.8 V. Afterward, in the following charge cycles, three charge voltage plateaus are located at 2.1, 3.5, and 4.0 V vs Na^+/Na, which are consistent with three oxidation couples of Ti^{3+} to Ti^{4+}, Mn^{2+} to Mn^{3+}, and

https://dx.doi.org/10.1021/acsami.0c05784
ACS Appl. Mater. Interfaces 2020, 12, 30328−30335

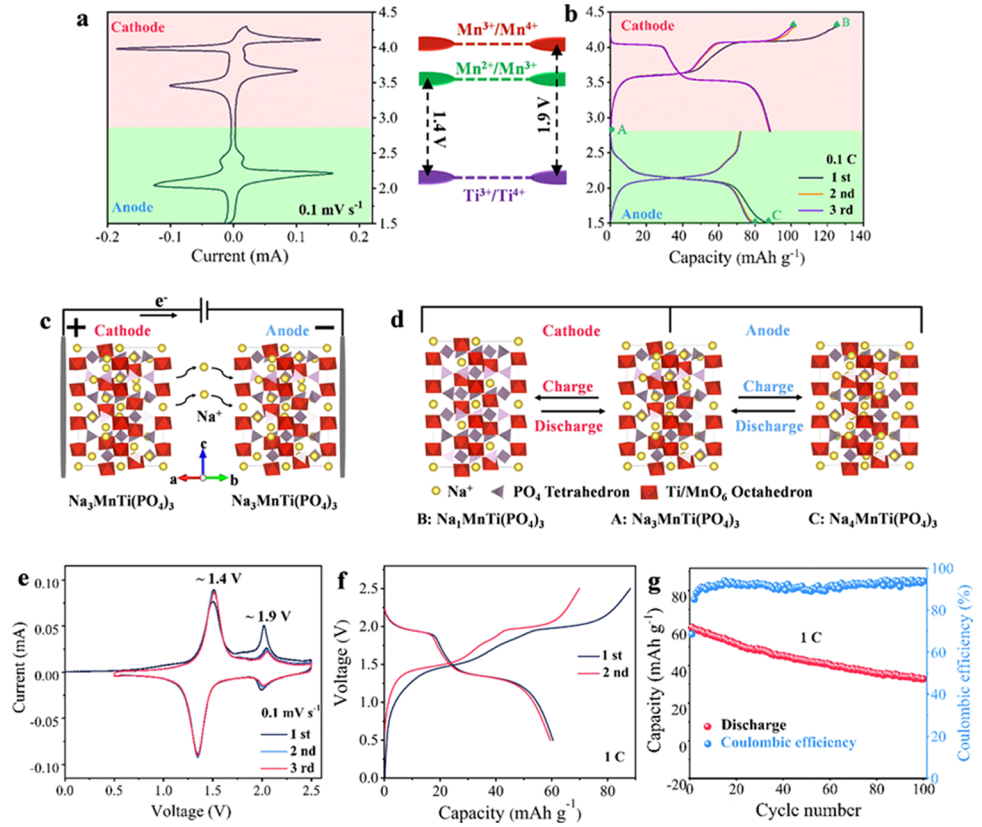

Figure 4. (a) Half-cell charge/discharge voltage curves and (b) voltage capacity profiles within different potential regions (A: pristine $Na_3MnTi(PO_4)_3$; B: charge to 4.3 V, $Na_1MnTi(PO_4)_3$; C: discharge to 1.5 V, $Na_4MnTi(PO_4)_3$). (c) Schematic illustration of $Na_3MnTi(PO_4)_3$||$Na_3MnTi(PO_4)_3$ symmetric SIBs. (d) Schematic diagram of unit cells of cathode and anode during the charge/discharge process. (e) Cyclic voltammogram curves of symmetric sodium-ion battery, (f) charge/discharge curves, and (g) cycling performance at 1 C for the symmetric batteries.

Mn^{3+} to Mn^{4+}, respectively. $Na_3MnTi(PO_4)_3$ delivers an initial charge specific capacity of 137.2 mAh g^{-1}, and the initial discharge specific capacity is 170.3 mAh g^{-1}. In the subsequent cycles, a stable discharge specific capacity of 160 mAh g^{-1} can be obtained with a Coulombic efficiency (CE) of 97%, indicating the superior reversible stability. The results are in good agreement with the voltage plateaus in Figure 3a. The rate capability in Figure 3c demonstrates the reversible capacities of 169.4, 135.4, 115.7, 104.7, 95.3, and 86.0 mAh g^{-1} at 0.1, 0.2, 0.5, 1, 2, and 5 C, respectively. The corresponding charge and discharge profiles are shown in Figure S3 (Supporting Information), and all curves exhibit three voltage plateaus. Both the highest-voltage plateau and capacity decay with the rate increase, possibly resulting from the polarization. When the rate returns to 0.1 C, the discharge capacity of 138.5 mAh g^{-1} is obtained with capacity retentions of 82% and ~100% CE, indicating the excellent rate capability. Long-term stability is demonstrated in Figure 3d. The discharge capacity of 107.9 mAh g^{-1} is delivered at 5 C with a capacity retention of 76.2% after 360 cycles. Figure S4 (Supporting Information) displays the corresponding charge and discharge profiles at different cycles.

To get an insight into the kinetic behaviors, CV tests with different scanning rates from 0.1 to 0.5 mV s^{-1} are conducted, as shown in Figure 3e. The peak current increases with the increasing scan rate, in which the linear relationship between the peak currents (I_p) and the square root of the scanning rate ($v^{1/2}$) is plotted to estimate the diffusion coefficient (D_{Na^+}) in Figure 3f using the following equation[49]

$$I_p = 2.69 \times 10^5 n^{3/2} A D_{Na^+}^{1/2} C_{Na} v^{1/2} \quad (1)$$

where I_p, n, A, C_{Na}, and v are the peak current, number of exchanged electrons per formula during the reactions, effective reaction area (1.13 cm^2), Na^+ concentration in the electrode, and scan rate, respectively. During the anodic scan, D_{Na^+} values for peak 1, peak 2, and peak 3 are 3.86×10^{-11}, 3.14×10^{-11}, and 7.66×10^{-11} cm^2 s^{-1}, respectively. During the cathodic scan, D_{Na^+} values for peak 4, peak 5, and peak 6 are 1.00×10^{-11}, 1.59×10^{-11}, and 2.44×10^{-10} cm^2 s^{-1}, respectively. Peak 3 and peak 6 show the largest D_{Na^+} values in anodic and cathodic scans, indicating that the structural evolution of $Na_2MnTi(PO_4)_3 \leftrightarrow Na_1MnTi(PO_4)_3$ is the most favorable with the fastest ion diffusion compared to other two evolution processes. The results agree well with the Na^+ insertion/extraction energy results in density functional theory (DFT) calculation, which indicates that the site-I and site-II are the most favorable sites for sodium ions to diffuse, relating to the configurations $Na_1MnTi(PO_4)_3$ and $Na_2MnTi(PO_4)_3$ (Table S1, Supporting Information).

Sodium-ion storage can be defined as two processes: diffusion reactions of faradic contribution and redox process of pseudocapacitance. The effect of the pseudocapacitance for the battery reaction system can be explored by the following equations[30,50]

https://dx.doi.org/10.1021/acsami.0c05784
ACS Appl. Mater. Interfaces 2020, 12, 30328−30335

$$I_p = av^b \quad (2)$$

$$\log I_p = \log a + b \log v \quad (3)$$

where a and b are adjustable parameters, I_p is the peak current, and v is the scan rate. For a pesudocapacitance-controlled process, the b-value is close to or above 1, while for the electrochemical diffusion-dominated process, the b-value is around 0.5. In Figure S5 (Supporting Information), all b-values are above 0.5, indicating the coexistent behaviors of diffusion and pesudocapacitance within the $Na_3MnTi(PO_4)_3$ electrode. It should be noted that the pseudocapacitance reaction is conducive to the rate capability and cycling performance.

Electrochemical Performance of the Symmetric Sodium-Ion Battery in Organic Electrolyte. The charge/discharge voltage plots and voltage matchup of $Na_3MnTi(PO_4)_3$ half-cell within different voltage regions are shown in Figure 4a,b. The $Ti^{3+/4+}$ redox pair at 2.1 V and $Mn^{2+/3+}$ and $Mn^{3+/4+}$ pairs at 3.5 and 4.0 V indicate that $Na_3MnTi(PO_4)_3$ is able to serve as both anode and cathode materials. For the cathode part, it exhibits the extraction/insertion of two Na^+ (A ↔ B = $Na_3MnTi(PO_4)_3$ ↔ $Na_1MnTi(PO_4)_3$) and delivers an initial charge capacity of 125.6 mAh g^{-1} with a stable charge capacity of about 100 mAh g^{-1}. As for the anode part, it relates to the reversible one Na^+ insertion into $Na_3MnTi(PO_4)_3$, leading to the phase of $Na_4MnTi(PO_4)_3$ (C) at 2.1 V with an initial discharge capacity of 87.4 mAh g^{-1} and a stable discharge capacity of about 80 mAh g^{-1}.

Benefiting from the potential difference between $Mn^{3+/4+}$, $Mn^{2+/3+}$, and $Ti^{3+/4+}$ redox pairs, a symmetric battery based on the dual-electron reactions is constructed with $Na_3MnTi(PO_4)_3$||$NaClO_4$ (1 M)||$Na_3MnTi(PO_4)_3$. The schematic illustration of symmetric SIBs is demonstrated in Figure 4a. There is no pretreatment for both cathode and anode electrodes during the fabrication of symmetric battery. Figure 4b illustrates the respective reactions and evolution of cathode (A ↔ B) and anode (A ↔ C) during the charge/discharge process. Herein, the reactions of cathode and anode during the charging ↔ discharging process can be identified as follows

$$\text{Cathode: } Na_3MnTi(PO_4)_3 \leftrightarrow Na_1MnTi(PO_4)_3 + 2Na^+ + 2e^- \quad (4)$$

$$\text{Anode: } Na_3MnTi(PO_4)_3 + Na^+ + e^- \leftrightarrow Na_4MnTi(PO_4)_3 \quad (5)$$

Cyclic voltammogram curves (Figure 4e) exhibit two pairs of obvious redox peaks at ∼1.4 and ∼1.9 V, confirming the dual-electron redox reactions for the $Na_3MnTi(PO_4)_3$ symmetric battery, which are consistent with the voltage gaps in Figure 4a,b. The low-voltage plateau is derived from the voltage gap of 2.1 V ($Ti^{3+/4+}$) and 3.5 V ($Mn^{2+/3+}$), and the high voltage plateau of ∼1.9 V is dominantly originated from the contribution of 2.1 V ($Ti^{3+/4+}$) and $Mn^{3+/4+}$ (4.0 V), which is relatively high compared to the reported values in various types of symmetric batteries with the NASCION-structured material (Table S4, Supporting Information). The first two charge−discharge profiles and the corresponding cycling performance at 1 C are illustrated in Figures 4f,g and S6 (Supporting Information), which deliver an initial discharge capacity of 60.4 mAh g^{-1} and a capacity retention of 54.5% after 100 cycles. The cycling stability at 1 C is not very high, which is mainly attributed to the polarization and slightly low Columbic efficiency. The capacity−voltage profiles of the $Na_3MnTi(PO_4)_3$ symmetric battery at 0.1 C are shown in Figure S7 (Supporting Information). The initial charge and discharge capacities are 116.3 and 72.9 mAh g^{-1}, respectively. The energy density is 52 Wh kg^{-1}. Except the first cycle, the subsequent neighbor cycles can be overlapped well, indicating the excellent reversibility. Figure S8 (Supporting Information) demonstrates the charge/discharge curves at different rates. The discharge capacities of 76.1, 67.0, 58.9, 51.7, 44.4, and 34.5 mAh g^{-1} can be obtained of 0.1, 0.2, 0.5, 1, 2, and 5 C, respectively. The promising performance is mainly attributed to the symmetric nature, abating the volume expansion of electrodes during the sodiation/desodiation process. Besides, the characters of fast electron and ionic conductivity of carbon-coated NASICON-structured materials strongly generate a positive impact on sodium-storage performance. Furthermore, based on the transition-metal multivalence status, NASICON-structured symmetric batteries with a higher energy density could be achieved by matching higher and lower transition-metal redox couples.

CONCLUSIONS

A NASICON-structured $Na_3MnTi(PO_4)_3$ is prepared through a facile sol−gel method and displays a stable capacity of 160 mAh g^{-1} with a Coulombic efficiency of 97% at 0.1 C. The three voltage plateaus of 2.1, 3.5, and 4.0 V vs Na^+/Na correspond to the redox pairs of $Ti^{3+/4+}$, $Mn^{2+/3+}$, and $Mn^{3+/4+}$, respectively. By utilizing the voltage difference between three redox pairs, the current symmetric sodium-ion full cell with $Na_3MnTi(PO_4)_3$ as both cathode and anode achieves dual-electron reactions and a high operating voltage, leading to a high energy density. It exhibits a stable discharge capacity of about 75 mAh g^{-1} at 0.1 C and 60.4 mAh g^{-1} at 1 C, indicating the good reversibility and cycling performance. The operating voltage of 1.9 V and an improved energy density of 52 Wh kg^{-1} are obtained. Moreover, the agreement between experimental and DFT investigations does not only provide better understanding of the sodiation mechanism but also show the potential pathway of designing the voltage plateaus by tuning the occupation of carriers. Our research highlights the prospect of NASICON-structured symmetric batteries based on multi-electron reactions to improve sodium-storage performance for high energy density.

ASSOCIATED CONTENT

Supporting Information

The Supporting Information is available free of charge at https://pubs.acs.org/doi/10.1021/acsami.0c05784.

DFT details; detailed crystal structure; EIS results; and capacity−voltage profiles of $Na_3MnTi(PO_4)_3$ half-cell and symmetric full cell (PDF)

AUTHOR INFORMATION

Corresponding Authors

Jinzhu Zhao − *Guangdong Provincial Key Laboratory of Quantum Engineering and Quantum Materials, Guangdong Engineering Technology Research Center of Efficient Green Energy and Environment Protection Materials, School of Physics and Telecommunication Engineering, South China Normal University, Guangzhou 510006, P. R. China; Center for Computational Science and Engineering, Southern University of Science and Technology, Shenzhen 518055, China;*

https://dx.doi.org/10.1021/acsami.0c05784
ACS Appl. Mater. Interfaces 2020, 12, 30328−30335

orcid.org/0000-0003-1841-1302;
Phone: +862039318011; Email: zhaojz@m.scnu.edu.cn

Fuming Chen − *Guangdong Provincial Key Laboratory of Quantum Engineering and Quantum Materials, Guangdong Engineering Technology Research Center of Efficient Green Energy and Environment Protection Materials, School of Physics and Telecommunication Engineering and National and Local Joint Engineering Research Center of Key Materials and Technologies for High Energy and Safety Batteries. Engineering Research Center of MTEES (Ministry of Education), South China Normal University, Guangzhou 510006, P. R. China;* orcid.org/0000-0002-0108-9831; Email: fmchen@m.scnu.edu.cn

Xianhua Hou − *Guangdong Provincial Key Laboratory of Quantum Engineering and Quantum Materials, Guangdong Engineering Technology Research Center of Efficient Green Energy and Environment Protection Materials, School of Physics and Telecommunication Engineering and National and Local Joint Engineering Research Center of Key Materials and Technologies for High Energy and Safety Batteries. Engineering Research Center of MTEES (Ministry of Education), South China Normal University, Guangzhou 510006, P. R. China;* orcid.org/0000-0003-4305-5143; Email: houxianhua@m.scnu.edu.cn

Authors

Yu Zhou − *Guangdong Provincial Key Laboratory of Quantum Engineering and Quantum Materials, Guangdong Engineering Technology Research Center of Efficient Green Energy and Environment Protection Materials, School of Physics and Telecommunication Engineering and National and Local Joint Engineering Research Center of Key Materials and Technologies for High Energy and Safety Batteries. Engineering Research Center of MTEES (Ministry of Education), South China Normal University, Guangzhou 510006, P. R. China*

Xiji Shao − *Department of Physics, Southern University of Science and Technology, Shenzhen 518055, China; Harbin Institute of Technology, Harbin 150080, China*

Kwok-ho Lam − *Department of Electrical Engineering, The Hong Kong Polytechnic University, Hung Hom, Kowloon, Hong Kong*

You Zheng − *Guangdong Provincial Key Laboratory of Quantum Engineering and Quantum Materials, Guangdong Engineering Technology Research Center of Efficient Green Energy and Environment Protection Materials, School of Physics and Telecommunication Engineering, South China Normal University, Guangzhou 510006, P. R. China*

Lingzhi Zhao − *SCNU Qingyuan Institute of Science and Technology Innovation Co., Ltd., Qingyuan 511517, China*

Kedong Wang − *National and Local Joint Engineering Research Center of Key Materials and Technologies for High Energy and Safety Batteries. Engineering Research Center of MTEES (Ministry of Education), South China Normal University, Guangzhou 510006, P. R. China;* orcid.org/0000-0003-1253-5603

Complete contact information is available at: https://pubs.acs.org/10.1021/acsami.0c05784

Author Contributions

○Y.Z. and X.S. contributed equally to this work.

Notes

The authors declare no competing financial interest.

ACKNOWLEDGMENTS

This work was financially supported by the union project of National Natural Science Foundation of China and Guangdong Province (U1601214), National Natural Science Foundation of China (NSFC, grant nos. 11404159 and 11704177), the Science and Technology Planning Project of Guangdong Province (2018B050502010, 2018A050506078, 2017B090901027, 2019B090905005), the Challenge Cup Gold Seed cultivation Project of South China Normal University (19WDKB01) and the Pearl River Talent Program (2019QN01L951).

REFERENCES

(1) Chen, F.; Huang, Y.; Guo, L.; Sun, L.; Wang, Y.; Yang, H. Y. Dual-ions Electrochemical Deionization: a Desalination Generator. *Energy Environ. Sci.* **2017**, *10*, 2081−2089.

(2) Zhang, W.; Li, Y.; Zhou, L.; Zheng, Q.; Xie, F.; Lam, K. H.; Lin, D. Ultrathin Amorphous CoFeP Nanosheets Derived from CoFe LDHs by Partial Phosphating as Excellent Bifunctional Catalysts for Overall Water Splitting. *Electrochim. Acta* **2019**, *323*, No. 134595.

(3) Fan, L.; Ma, R.; Zhang, Q.; Jia, X.; Lu, B. Graphite Anode for a Potassium-Ion Battery with Unprecedented Performance. *Angew. Chem., Int. Ed.* **2019**, *58*, 10500−10505.

(4) Liu, J. Addressing the Grand Challenges in Energy Storage. *Adv. Funct. Mater.* **2013**, *23*, 924−928.

(5) Hu, Q.; Jiang, X.; He, M.; Zheng, Q.; Lam, K. H.; Lin, D. Core-shell Nanostructured MnO_2@Co_9S_8 Arrays for High-performance Supercapacitors. *Electrochim. Acta* **2020**, *338*, No. 135896.

(6) Fan, L.; Chen, S.; Zhu, J.; Ma, R.; Li, S.; Podila, R.; Rao, A. M.; Yang, G.; Wang, C.; Liu, Q.; Xu, Z.; Yuan, L.; Huang, Y.; Lu, B. Simultaneous Suppression of the Dendrite Formation and Shuttle Effect in a Lithium-Sulfur Battery by Bilateral Solid Electrolyte Interface. *Adv. Sci.* **2018**, *5*, No. 1700934.

(7) Zhang, Z.; Hu, X.; Zhou, Y.; Wang, S.; Yao, L.; Pan, H.; Su, C.-Y.; Chen, F.; Hou, X. Aqueous Rechargeable Dual-ion Battery Based on Fluoride Ion and Sodium Ion Electrochemistry. *J. Mater. Chem. A* **2018**, *6*, 8244−8250.

(8) Li, S.; Dong, Y.; Xu, L.; Xu, X.; He, L.; Mai, L. Effect of Carbon Matrix Dimensions on the Electrochemical Properties of $Na_3V_2(PO_4)_3$ Nanograins for High-Performance Symmetric Sodium-Ion Batteries. *Adv. Mater.* **2014**, *26*, 3545−3553.

(9) He, Z.; Jiang, Y.; Zhu, J.; Li, Y.; Jiang, Z.; Zhou, H.; Meng, W.; Wang, L.; Dai, L. Boosting the Performance of $LiTi_2(PO_4)_3$/C Anode for Aqueous Lithium Ion Battery by Sn Doping on Ti Sites. *J. Alloys Compd.* **2018**, *731*, 32−38.

(10) Zhou, Y.; Hou, X.; Shen, K.; Wang, S.; Chen, F.; Li, Y.; Chen, H.; Wang, B. $Li_{1.1}Na_{0.1}Mn_{0.534}Ni_{0.133}Co_{0.133}O_2$ as Cathode with Ameliorated Electrochemical Performance Based on Dual Li^+/Na^+ Electrolyte. *Ionics* **2019**, *25*, 51−59.

(11) Shi, L.; Zeng, F.; Cheng, X.; Lam, K. H.; Wang, W.; Wang, A.; Jin, Z.; Wu, F.; Yang, Y. Enhanced Performance of Lithium-Sulfur Batteries with High Sulfur Loading Utilizing Ion Selective MWCNT/SPANI Modified Separator. *Chem. Eng. J.* **2018**, *334*, 305−312.

(12) Luo, J. Y.; Xia, Y. Y. Aqueous Lithium-ion Battery $LiTi_2(PO_4)_3$/$LiMn_2O_4$ with High Power and Energy Densities as well as Superior Cycling Stability. *Adv. Funct. Mater.* **2007**, *17*, 3877−3884.

(13) Li, Y.; Hou, X.; Zhou, Y.; Han, W.; Liang, C.; Wu, X.; Wang, S.; Ru, Q. Electrochemical Performance of Structure-Dependent $LiNi_{1/3}Co_{1/3}Mn_{1/3}O_2$ in Aqueous Rechargeable Lithium-Ion Batteries. *Energy Technol.* **2018**, *6*, 391−396.

(14) Hu, Y.; Ding, H.; Bai, Y.; Liu, Z.; Chen, S.; Wu, Y.; Yu, X.; Fan, L.; Lu, B. Rational Design of a Polyimide Cathode for a Stable and High-Rate Potassium-Ion Battery. *ACS Appl. Mater. Interfaces* **2019**, *11*, 42078−42085.

(15) Senguttuvan, P.; Rousse, G.; Arroyo y de Dompablo, M. E.; Vezin, H.; Tarascon, J. M.; Palacin, M. R. Low-Potential Sodium

Insertion in a NASICON-Type Structure through the Ti(III)/Ti(II) Redox Couple. *J. Am. Chem. Soc.* **2013**, *135*, 3897−3903.
(16) Liu, T.; Zhang, Y.; Chen, C.; Lin, Z.; Zhang, S.; Lu, J. Sustainability-Inspired Cell Design for a Fully Recyclable Sodium Ion Battery. *Nat. Commun.* **2019**, *10*, No. 1965.
(17) Wang, X.; Wang, S.; Shen, K.; He, S.; Hou, X.; Chen, F. Phosphorus-Doped Porous Hollow Carbon Nanorods for High-Performance Sodium-Based Dual-Ion batteries. *J. Mater. Chem. A* **2020**, *8*, 4007−4016.
(18) Li, H.; Jin, T.; Chen, X.; Lai, Y.; Zhang, Z.; Bao, W.; Jiao, L. Rational Architecture Design Enables Superior Na Storage in Greener NASICON-$Na_4MnV(PO_4)_3$ Cathode. *Adv. Energy Mater.* **2018**, *8*, No. 1801418.
(19) Niu, Y. B.; Yin, Y. X.; Guo, Y. G. Nonaqueous Sodium-Ion Full Cells: Status, Strategies, and Prospects. *Small* **2019**, *15*, No. e1900233.
(20) Zhao, L.; Zhao, H.; Du, Z.; Wang, J.; Long, X.; Li, Z.; Świerczek, K. Delicate Lattice Modulation Enables Superior Na Storage Performance of $Na_3V_2(PO_4)_3$ as both an Anode and Cathode Material for Sodium-Ion Batteries: Understanding the Role of Calcium Substitution for Vanadium. *J. Mater. Chem. A* **2019**, *7*, 9807−9814.
(21) Zhao, W.; Guo, L.; Ding, M.; Huang, Y.; Yang, H. Y. Ultrahigh-Desalination-Capacity Dual-Ion Electrochemical Deionization Device Based on $Na_3V_2(PO_4)_3$@C-AgCl Electrodes. *ACS Appl. Mater. Interfaces* **2018**, *10*, 40540−40548.
(22) Kawai, K.; Asakura, D.; Nishimura, S. I.; Yamada, A. Stabilization of a 4.5 V $Cr^{(4+)}/Cr^{(3+)}$ Redox Reaction in NASICON-Type $Na_3Cr_2(PO_4)_3$ by Ti Substitution. *Chem. Commun.* **2019**, *55*, 13717−13720.
(23) Ramesh Kumar, P.; Kheireddine, A.; Nisar, U.; Shakoor, R. A.; Essehli, R.; Amin, R.; Belharouak, I. $Na_4MnV(PO_4)_3$-rGO as Advanced Cathode for Aqueous and Non-Aqueous Sodium Ion Batteries. *J. Power Sources* **2019**, *429*, 149−155.
(24) Kawai, K.; Zhao, W.; Nishimura, S.-i.; Yamada, A. High-Voltage Cr^{4+}/Cr^{3+} Redox Couple in Polyanion Compounds. *ACS Appl. Energy Mater.* **2018**, *1*, 928−931.
(25) Zhang, L.; Zhang, B.; Wang, C.; Dou, Y.; Zhang, Q.; Liu, Y.; Gao, H.; Al-Mamun, M.; Pang, W. K.; Guo, Z.; Dou, S. X.; Liu, H. K. Constructing the Best Symmetric Full K-ion Battery with the NASICON-Type $K_3V_2(PO_4)_3$. *Nano Energy* **2019**, *60*, 432−439.
(26) Wang, D.; Bie, X.; Fu, Q.; Dixon, D.; Bramnik, N.; Hu, Y. S.; Fauth, F.; Wei, Y.; Ehrenberg, H.; Chen, G.; Du, F. Sodium Vanadium Titanium Phosphate Electrode for Symmetric Sodium-Ion Batteries with High Power and Long Lifespan. *Nat. Commun.* **2017**, *8*, No. 15888.
(27) Wang, P.-F.; You, Y.; Yin, Y.-X.; Guo, Y.-G. Layered Oxide Cathodes for Sodium-Ion Batteries: Phase Transition, Air Stability, and Performance. *Adv. Energy Mater.* **2018**, No. 1701912.
(28) Yao, X.; Zhu, Z.; Li, Q.; Wang, X.; Xu, X.; Meng, J.; Ren, W.; Zhang, X.; Huang, Y.; Mai, L. 3.0 V High Energy Density Symmetric Sodium-Ion Battery: $Na_4V_2(PO_4)_3$ parallel $Na_3V_2(PO_4)_3$. *ACS Appl. Mater. Interfaces* **2018**, *10*, 10022−10028.
(29) Guo, J. Z.; Wang, P. F.; Wu, X. L.; Zhang, X. H.; Yan, Q.; Chen, H.; Zhang, J. P.; Guo, Y. G. High-Energy/Power and Low-Temperature Cathode for Sodium-Ion Batteries: In Situ XRD Study and Superior Full-Cell Performance. *Adv. Mater.* **2017**, *29*, No. 1701968.
(30) Zhao, Y.; Gao, X.; Gao, H.; Jin, H.; Goodenough, J. B. Three Electron Reversible Redox Reaction in Sodium Vanadium Chromium Phosphate as a High-Energy-Density Cathode for Sodium-Ion Batteries. *Adv. Funct. Mater.* **2020**, *30*, No. 1908680.
(31) Zhu, T.; Hu, P.; Cai, C.; Liu, Z.; Hu, G.; Kuang, Q.; Mai, L.; Zhou, L. Dual Carbon Decorated $Na_3MnTi(PO_4)_3$: A high-Energy-Density Cathode Material for Sodium-Ion Batteries. *Nano Energy* **2020**, *70*, No. 104548.
(32) Zhou, W.; Xue, L.; Lu, X.; Gao, H.; Li, Y.; Xin, S.; Fu, G.; Cui, Z.; Zhu, Y.; Goodenough, J. B. $Na_xMV(PO_4)_3$ (M = Mn, Fe, Ni) Structure and Properties for Sodium Extraction. *Nano Lett.* **2016**, *16*, 7836−7841.
(33) Wang, D.; Wei, Z.; Lin, Y.; Chen, N.; Gao, Y.; Chen, G.; Song, L.; Du, F. Intercalation Pseudocapacitance in a NASICON-Structured $Na_2CrTi(PO_4)_3$@Carbon Nanocomposite: towards High-Rate and Long-Lifespan Sodium-Ion-Based Energy Storage. *J. Mater. Chem. A* **2019**, *7*, 20604−20613.
(34) Liu, X.; Jiang, X.; Zhong, F.; Feng, X.; Chen, W.; Ai, X.; Yang, H.; Cao, Y. High-Safety Symmetric Sodium-Ion Batteries Based on Nonflammable Phosphate Electrolyte and Double $Na_3V_2(PO_4)_3$ Electrodes. *ACS Appl. Mater. Interfaces* **2019**, *11*, 27833−27838.
(35) Dong, J.; Zhang, G.; Wang, X.; Zhang, S.; Deng, C. Cross-Linked $Na_2VTi(PO_4)_3$@C Hierarchical Nanofibers as High-Performance Bi-Functional Electrodes for Symmetric Aqueous Rechargeable Sodium Batteries. *J. Mater. Chem. A* **2017**, *5*, 18725−18736.
(36) Gao, H.; Goodenough, J. B. An Aqueous Symmetric Sodium-Ion Battery with NASICON-Structured $Na_3MnTi(PO_4)_3$. *Angew. Chem., Int. Ed.* **2016**, *55*, 12768−12772.
(37) Feng, Y.; Chen, S.; Wang, J.; Lu, B. Carbon Foam with Microporous Structure for High Performance Symmetric Potassium Dual-Ion Capacitor. *J. Energy Chem.* **2020**, *43*, 129−138.
(38) Wang, H.; Zhang, T.; Chen, C.; Ling, M.; Lin, Z.; Zhang, S.; Pan, F.; Liang, C. High-Performance Aqueous Symmetric Sodium-Ion Battery using NASICON-Structured $Na_2VTi(PO_4)_3$. *Nano Res.* **2018**, *11*, 490−498.
(39) Li, C.; Wu, W.; Wang, P.; Zhou, W.; Wang, J.; Chen, Y.; Fu, L.; Zhu, Y.; Wu, Y.; Huang, W. Fabricating an Aqueous Symmetric Supercapacitor with a Stable High Working Voltage of 2 V by Using an Alkaline-Acidic Electrolyte. *Adv. Sci.* **2019**, *6*, No. 1801665.
(40) Monkhorst, H. J.; Pack, J. D. Special Points for Brillouin-Zone Integrations. *Phys. Rev. B: Condens. Matter Mater. Phys.* **1976**, *13*, 5188−5192.
(41) Liechtenstein, A. I.; Anisimov, V. V.; Zaanen, J. Density-Functional Theory and Strong Interactions: Orbital Ordering in Mott-Hubbard Insulators. *Phys. Rev. B* **1995**, *52*, R5467−R5470.
(42) Jian, Z.; Sun, Y.; Ji, X. A New Low-Voltage Plateau of $Na_3V_2(PO_4)_3$ as an Anode for Na-ion Batteries. *Chem. Commun.* **2015**, *51*, 6381−6383.
(43) He, Q.; Yu, B.; Li, Z.; Zhao, Y. Density Functional Theory for Battery Materials. *Energy Environ. Mater.* **2019**, *2*, 264−279.
(44) Gao, H.; Li, Y.; Park, K.; Goodenough, J. B. Sodium Extraction from NASICON-Structured $Na_3MnTi(PO_4)_3$ through Mn(III)/Mn(II) and Mn(IV)/Mn(III) Redox Couples. *Chem. Mater.* **2016**, *28*, 6553−6559.
(45) Jian, Z.; Yuan, C.; Han, W.; Lu, X.; Gu, L.; Xi, X.; Hu, Y.-S.; Li, H.; Chen, W.; Chen, D.; Ikuhara, Y.; Chen, L. Atomic Structure and Kinetics of NASICON $Na_xV_2(PO_4)_3$ Cathode for Sodium-Ion Batteries. *Adv. Funct. Mater.* **2014**, *24*, 4265−4272.
(46) Zhu, T.; Hu, P.; Wang, X.; Liu, Z.; Luo, W.; Owusu, K. A.; Cao, W.; Shi, C.; Li, J.; Zhou, L.; Mai, L. Realizing Three-Electron Redox Reactions in NASICON-Structured $Na_3MnTi(PO_4)_3$ for Sodium-Ion Batteries. *Adv. Energy Mater.* **2019**, *9*, No. 1803436.
(47) Zhang, W.; Zhang, Z.; Li, H.; Wang, D.; Wang, T.; Sun, X.; Zheng, J.; Lai, Y. Engineering 3D Well-Interconnected $Na_4MnV(PO_4)_3$ Facilitates Ultrafast and Ultrastable Sodium Storage. *ACS Appl. Mater. Interfaces* **2019**, *11*, 35746−35754.
(48) Li, H.; Xu, M.; Gao, C.; Zhang, W.; Zhang, Z.; Lai, Y.; Jiao, L. Highly Efficient, Fast and Reversible Multi-Electron Reaction of $Na_3MnTi(PO_4)_3$ Cathode for Sodium-Ion Batteries. *Energy Storage Mater.* **2020**, *26*, 325−333.
(49) Xu, Y.; Wei, Q.; Xu, C.; Li, Q.; An, Q.; Zhang, P.; Sheng, J.; Zhou, L.; Mai, L. Layer-by-Layer $Na_3V_2(PO_4)_3$ Embedded in Reduced Graphene Oxide as Superior Rate and Ultralong-Life Sodium-Ion Battery Cathode. *Adv. Energy Mater.* **2016**, *6*, No. 1600389.
(50) He, S.; Wang, S.; Chen, H.; Hou, X.; Shao, Z. A New Dual-Ion Hybrid Energy Storage System with Energy Density Comparable to that of Ternary Lithium Ion Batteries. *J. Mater. Chem. A* **2020**, *8*, 2571−2580.

https://dx.doi.org/10.1021/acsami.0c05784
ACS Appl. Mater. Interfaces 2020, 12, 30328−30335

Nanoscale

PAPER

View Article Online
View Journal | View Issue

Cite this: *Nanoscale*, 2019, **11**, 6228

The shielding effects of a C_{60} cage on the magnetic moments of transition metal atoms inside the corner holes of Si(111)-(7 × 7)†

Xiji Shao,[a,b,c] Lin Li,[d] Xingqiang Shi,[b] Yaping Ma,[e] Xuefeng Wu[b] and Kedong Wang*[b,c]

The strong interaction between transition metal (TM) atoms and semiconductor surface atoms may diminish the magnetic moments of the TM atoms and prevent them from being used as single atom spin-based devices. A carbon cage that can encapsulate TM atoms and isolate them from interacting with surface atoms is considered to protect the magnetic moments of the TM atoms. We have studied the magnetic moments of Fe, Co, and Ni atoms adsorbed inside the corner hole of Si(111)-(7 × 7) by using first-principles calculations based on the density functional theory. The results show that when Co and Ni atoms are directly adsorbed inside the corner hole, the magnetic moments are 1.353μ_B and 0, respectively. However when a C_{60} cage is used to encapsulate the atoms, the magnetic moments increase to 1.849μ_B and 0.884μ_B, respectively. The results show a clear protecting effect of a carbon cage. For Fe with and without C_{60}, the magnetic moments are 2.909μ_B and 2.825μ_B, respectively. The presence of a C_{60} cage can also maintain their magnetic moments. Further analysis shows that the TM atoms possess magnetic moments when the conduction electrons are localized around them. All the results can be well understood in the framework of the Anderson impurity model. Our results demonstrate that a carbon cage may effectively protect the magnetic moments of TM atoms. This provides a new strategy for developing single atom spin-based devices on semiconductors.

Received 6th February 2019,
Accepted 6th March 2019

DOI: 10.1039/c9nr01177c

rsc.li/nanoscale

Introduction

In the last few decades, the performance of microelectronic devices has been significantly promoted by the development of the design and fabrication technology. However, the performance of the devices is limited by the dissipation and quantum effects in miniaturization. To solve these problems, molecular and quantum electronics[1–3] and spintronics[4] are intensively investigated in the field of science and technology. Spintronics is an active area of research, in which information processing and storage are based on the spins of nuclei, atoms or molecules,[5–7] rather than electronic charges.[8] To make spin devices, magnetic-based materials are very important on account of the relatively large anisotropy. Therefore, 3d transition metals (TMs), including iron (Fe), cobalt (Co), and nickel (Ni) atoms, can be good candidates. The spin anisotropy of atoms has been experimentally demonstrated on various surfaces. Khajetoorians *et al.* demonstrated the feasibility of nanoscale spintronic devices on nonmagnetic metallic surfaces based on single magnetic atoms.[4] The adsorption of nonmagnetic atoms on surfaces and some 2D magnetic materials have been widely studied.[9–16] However, the magnetic properties of single TM atoms on semiconductor surfaces need to be further clarified. Because the current applicable devices are all made on semiconductor surfaces, the devices consisting of single magnetic atoms are also required to be fabricated on the surface of a semiconductor. Silicon is particularly an intriguing material for spin devices. The research of Co atoms adsorbing on silicon shows the properties of remnant spins and spin states, making this system applicable for implementation in those atomic-scale spin-based devices.[17–24] However, due to the strong interaction between the atom and the semiconductor surface, the magnetic moment of magnetic atoms usually cannot be maintained. Therefore, how to retain the magnetism of the magnetic

[a]Harbin Institute of Technology, Harbin 150080, China
[b]Department of Physics, Southern University of Science and Technology, Shenzhen 518055, China. E-mail: wangkd@sustech.edu.cn
[c]Shenzhen Key Laboratory of Quantum Science and Engineering, SUSTech, Shenzhen 518055, China
[d]College of Physics and Electronic Engineering, and Center for Computational Sciences, Sichuan Normal University, Chengdu 610068, China
[e]SZU-NUS Collaborative Innovation Center for Optoelectronic Science & Technology, Shenzhen University, Shenzhen 518060, China

†Electronic supplementary information (ESI) available. See DOI: 10.1039/c9nr01177c

atom on a semiconductor surface is of critical importance in this field.

One simple method is to protect the magnetism of TM atoms by using a shielding shell. The shells must satisfy two requirements. Firstly, the interaction between the TM atoms and the shell is relatively weak. Secondly, the shell has a stable structure and sufficient interior volume. Fullerenes are highly symmetric hollow structure molecules that can encapsulate atoms in their interior.[25] It is also found that fullerenes are good containers to encapsulate atoms whilst the encapsulated atoms can retain some of their atomic characters.[26,27] The existence of a carbon cage may protect the TM atoms from interacting with substrate atoms and with other surrounding adsorbates.[28]

Experimentally, metal atoms encapsulated inside carbon cages ($M@C_n$) adsorbed on surfaces have been extensively studied by using scanning tunnelling microscopy. For example, the structures, electronic properties and even local metal–cage hybrid states in $Dy@C_{82}$ molecules adsorbed on Si(111)-(7 × 7) surfaces have been revealed at various temperatures.[29,30] Although the compounds of C_{60} and TM have already been found to be promising as functional materials,[31–33] the magnetic moments of the $TM@C_n$-Si(111)-(7 × 7) composites have been scarcely studied by either experimental or theoretical calculation. For the further development of novel materials for atomic-scale spin-based devices, theoretical study has become an important premise.

In the present work, we compare the magnetic properties of TM atoms and $TM@C_{60}$ adsorbed in the corner hole of the Si(111)-(7 × 7) surface to evaluate the shielding effect of a C_{60} cage. Density functional theory (DFT) calculations are used to determine the structures, electronic properties and magnetic moments. All the results can be well understood in the framework of the Anderson impurity model. Our results show that carbon cages are good candidates for protecting the magnetic moments of TM atoms.

Calculation methods

To study the shielding effect of a C_{60} cage, we have studied several related constructions in our calculations, including single TM atoms or $TM@C_{60}$ molecules adsorbed inside the corner hole of Si(111)-(7 × 7) and free TM atoms and free $TM@C_{60}$ molecules for comparison. The Si(111)-(7 × 7) surface provides natural patterns for the arrangement of adsorbates. However, when atoms or molecules are adsorbed on top of the adatoms of the Si(111)-(7 × 7) surface, they may have several different adsorption sites and can be removed easily, especially at room temperature. In contrast, when the adsorbates are adsorbed inside the corner holes of the Si(111)-(7 × 7) surface, their positions are much more stable and accurate. This is very important for possible applications in devices. In fact, the corner hole is the most stable site for both the TM atoms and $TM@C_{60}$ compared with other sites outside the corner hole (see the ESI†). So the adsorbates in the following discussions are restricted inside the corner hole of the Si(111)-(7 × 7) surface.

All simulations presented in this study have been performed using the Vienna *ab initio* simulation package (VASP).[34] The projector augmented wave (PAW) potentials[35] are used to describe the core electrons. The generalized gradient approximation (GGA) of the Perdew–Burke–Ernzerhof (PBE) functional[36] is employed to describe the electron exchange and correlation. For the 3d electrons of Fe, Co and Ni, the Hubbard-U correction term is used, which is 5 eV, 5 eV and 5.4 eV, respectively.[5,37,38] A plane wave cutoff energy of 450 eV is used for the wave function expansion, and a convergence criterion of 1×10^{-4} eV is applied for the total energy in supercells. In the geometry optimization, a vacuum separation of 15 Å is adopted and all the atoms are relaxed until the force on each atom is less than 0.01 eV $Å^{-1}$. Only the Γ point is used for all calculations of the Brillouin zone sampling. These values are chosen to ensure energy convergence and reduce the computational time and memory requirements. Each supercell of Si(111)-(7 × 7) contains 298 Si atoms and 49 H atoms in the bottom Si layer which terminate the dangling bonds, as shown in Fig. 1. Bader charge analysis[39] is used to determine the amount of charge transfer between TM (Fe, Co, Ni) and C_{60}-Si(111)-(7 × 7).

The binding energy (E_b) is the key parameter for describing the stability of a system. The binding energies of TM-Si(111)-(7 × 7) (E_{b1}), $TM@C_{60}$ (E_{b2}) and $TM@C_{60}$-Si(111)-(7 × 7) (E_{b3}) can be calculated from the following expressions respectively:

$$E_{b1} = E_{TM} + E_{Si(111)\text{-}(7\times7)} - E_{TM\text{-}Si(111)\text{-}(7\times7)}$$

$$E_{b2} = E_{TM} + E_{C_{60}} - E_{TM@C_{60}}$$

$$E_{b3} = E_{TM} + E_{C_{60}} + E_{Si(111)\text{-}(7\times7)} - E_{TM@C_{60}-Si(111)\text{-}(7\times7)}$$

where $E_{TM@C_{60}}$-Si(111)-(7 × 7) is the total energy of TM (Fe, Co, Ni) in the C_{60}-Si(111)-(7 × 7) system, and E_{TM}, $E_{C_{60}}$, and

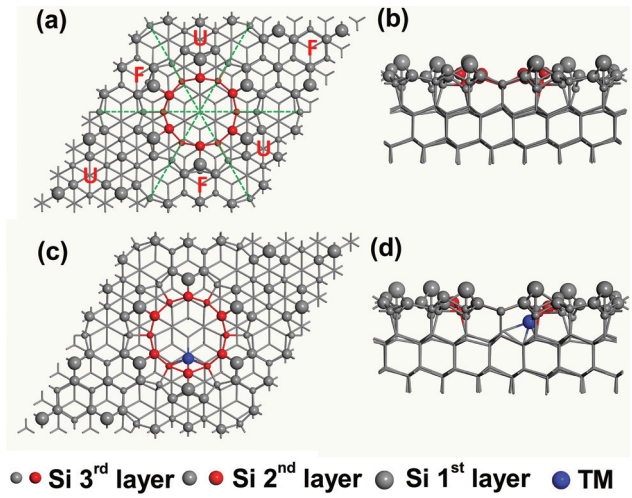

Fig. 1 Top view (a) and side view (b) of the structure of Si(111)-(7 × 7); "U" and "F" represent part of the unfaulted and faulted half unit cells, respectively. Top view (c) and side view (d) of the structure of TM atoms adsorbed in the corner hole of Si(111)-(7 × 7). The red Si atoms in the figures illustrate the hole of Si(111)-(7 × 7).

$E_{Si(111)-(77)}$ are the energies of the isolated transition atoms, C_{60} molecule, and Si(111)-(7 × 7) supercell, respectively.

Results and discussion

The calculations show that the C–C bond lengths in the C_{60} cage are 1.451 Å and 1.402 Å for the 6–5 edge and the 6–6 edge, respectively, which are consistent with the previous experimental[40,41] and theoretical values.[42]

To find the most stable adsorption sites for TM atoms or C_{60} molecules inside the corner hole of Si(111)-(7 × 7), random initial adsorption sites are selected and compared. When adsorbed inside the corner hole, single TM atoms or C_{60} molecules form chemical bonds with some of the surrounding Si atoms, indicating chemical adsorption.

The calculation results show that Fe, Co, and Ni atoms have very similar stable adsorption sites as shown in Fig. 1. The TM atoms are close to the edge of the hole. Seven bonds between TM and Si atoms are formed, with average bond lengths of 2.513 Å (Fe–Si), 2.455 Å (Co–Si) and 2.492 Å (Ni–Si). The binding energies are 3.78 eV, 4.58 eV, and 4.36 eV, for Fe, Co and Ni atoms, respectively. These binding energies are larger than the corresponding binding energies when they are adsorbed on the other sites of Si(111)-(7 × 7) (see the ESI†). The results indicate that the corner hole is the most stable adsorption site for these atoms, although seldom mentioned.[43]

For a TM atom enclosed inside the C_{60} cage, we calculated the binding energies at several possible adsorption sites and the TM–C bond lengths (see the ESI†). We found that the most stable structure is similar for all the three TM atoms where the TM is located on one three-fold rotation axis of C_{60} and close to the center of the one six-membered ring, resulting in the formation of six bonds between the TM atom and six C atoms nearby (Fig. 2). This result can be understood by the following reasons. Firstly, the electron density on the six-membered rings of the C_{60} cage is relatively higher than that on the five-membered rings. Secondly, more chemical bonds can be formed when the TM atom is close to the six-membered rings. The average bonding lengths of Fe–C, Co–C and Ni–C are 2.037 Å, 2.018 Å and 2.061 Å in TM@C_{60} structures, respectively, while the binding energies are 0.62 eV, 1.11 eV and 0.95 eV for Fe, Co, and Ni in TM@C_{60}, respectively.

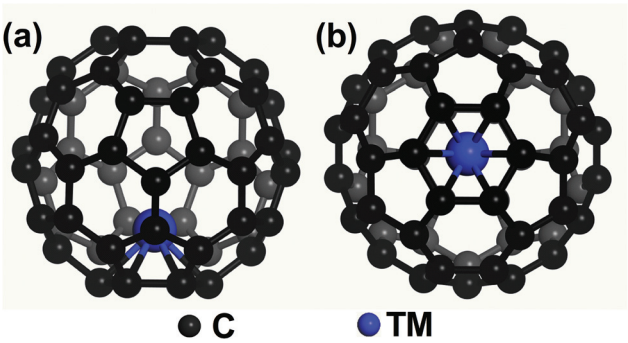

Fig. 2 Side view (a) and top view (b) of the structure of TM atoms adsorbed inside the C_{60} cage near a six-membered ring.

For TM (Fe, Co, Ni)@C_{60} adsorbed in the corner hole of Si(111)-(7 × 7), several possible orientations have been considered. The detailed data can be found in the ESI.† We found that the most stable configurations are very similar for all the three TM atoms (Fig. 3). Inside the C_{60} cage, the TM atoms are still bonded with the six C atoms. Meanwhile, the most stable orientation of the C_{60} cage is different from that of an empty cage.[44] The six-membered ring with the TM atom close to it is likely to stay in the bottom and retain the 3-fold symmetry of the structure along the surface normal direction (see Fig. 3). When the C_{60} cage binds with Si(111)-(7 × 7), the height is 1.683 Å between the bottom of the C_{60} cage and the Si rest atom at the center of the hole for Si(111)-(7 × 7). The binding energies are 0.92 eV, 1.61 eV and 1.43 eV for Fe@C_{60}, Co@C_{60}, and Ni@C_{60}, respectively.

The calculated magnetic moments of the Fe, Co and Ni atoms in various situations are shown in Table 1. The magnetic moments of free Fe, Co and Ni atoms are 3.895μ_B, 2.939μ_B and 1.937μ_B, respectively. However, when the atoms are adsorbed in the corner hole of Si(111)-(7 × 7), the magnetic moment of the Ni atom vanished. The magnetic moment of Fe and Co atoms changed to 2.909μ_B and 1.353μ_B, respectively. These results indicate a strong interaction between the TM atoms and the Si substrate. When the TM atoms are trapped in the C_{60} cage, the magnetic moments of the Fe, Co and Ni atoms are 2.920μ_B, 1.939μ_B and 0.136μ_B, respectively. When TM@C_{60} are adsorbed in the corner hole of Si(111)-(7 × 7), the magnetic moments become 2.825μ_B, 1.849μ_B and 0.884μ_B for Fe, Co and Ni atoms, respectively. These data clearly show that the presence of a carbon cage can maintain or protect the magnetic moment of TM atoms on the Si(111)-(7 × 7) surface.

To better understand the details of the changes of the magnetic moments of TM atoms, we calculated the total density of

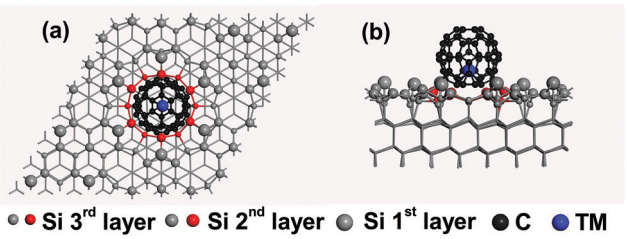

Fig. 3 Top view (a) and side view (b) of the structure of TM@C_{60}-Si(111)-(7 × 7).

Table 1 The magnetic moments for the different systems of the TM atoms (μ_B)

Systems	Free atoms	TM-Si(111)	TM@C_{60}	TM@C_{60}-Si(111)
Fe	3.895	2.909	2.920	2.825
Co	2.939	1.353	1.939	1.849
Ni	1.937	0.000	0.136	0.884

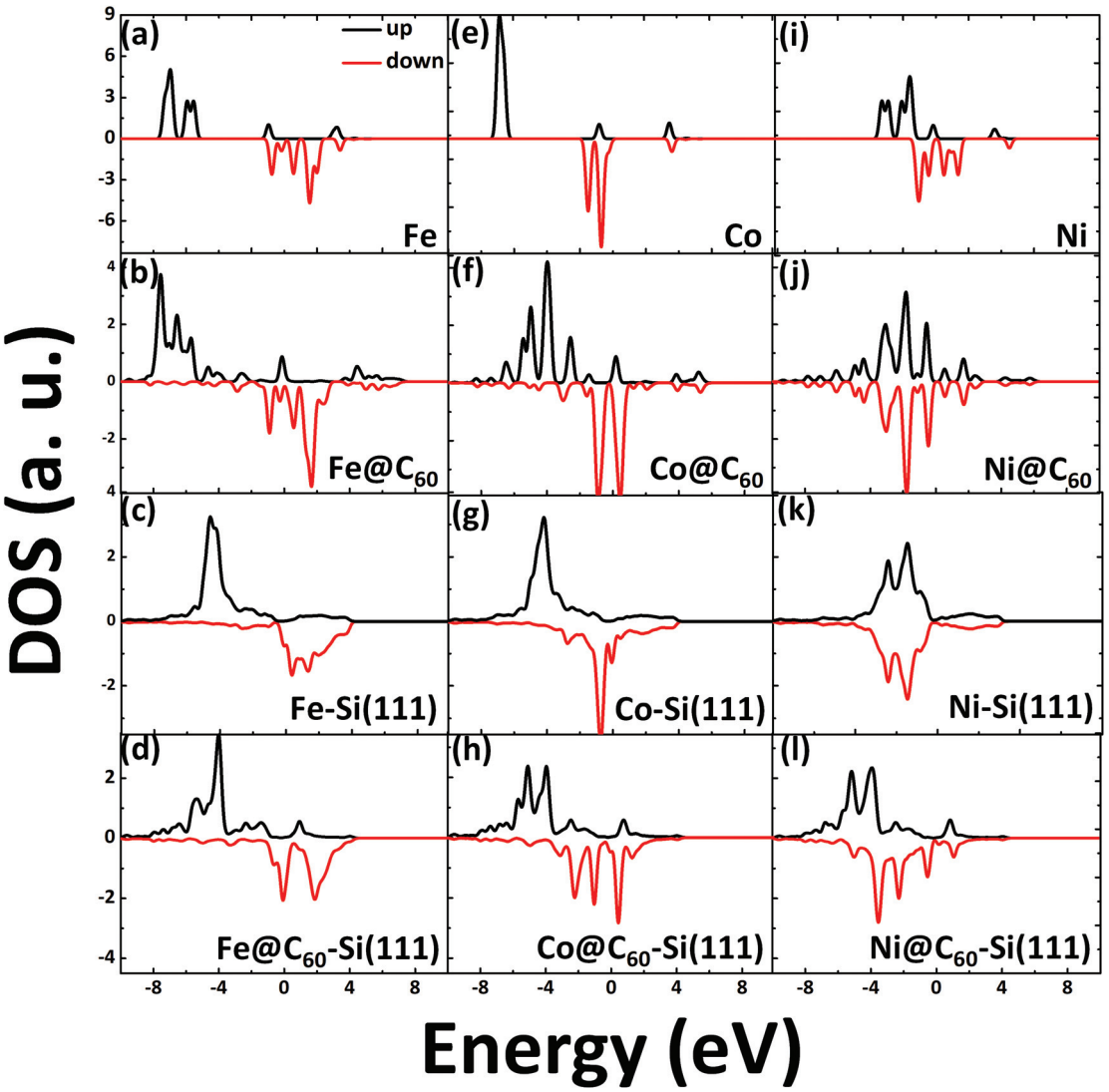

Fig. 4 The total DOS of TM atoms in different configurations. The Fermi level is set to zero.

states (DOS) of TM atoms in different systems, as shown in Fig. 4. We only considered the s, p, and d orbitals of TM atoms in different systems. The PDOS is illustrated in the ESI (Fig. S5†). For free TM atoms, they have different magnetic moments as can be seen in Fig. 4(a), (e) and (i). For Fe and Co atoms, the magnetic moments are always nonzero in different configurations, as shown in Fig. 4(b)–(d) and (f)–(h). However, the magnetic moment of Ni–Si(111)-(7 × 7) is zero, because the total DOSs of the spin up and spin down states are equal, as can be seen in Fig. 4(k). For Co@C_{60}, the magnetic moment of the Co atom is 1.939μ_B, where the PDOS is mainly rooted in d_{z^2}, d_{xz}, d_{yz} and $d_{x^2-y^2}$ at the Fermi level, as shown in Fig. S5(f).† For Co@C_{60}-Si(111)-(7 × 7), the magnetic moment is 1.849μ_B, increased by 0.496μ_B, compared with Co–Si(111), and the PDOS is mainly from d_{z^2} and $d_{x^2-y^2}$ near the Fermi level (Fig. S5g and h†). The magnetic moment of the Ni atom is 0.136μ_B and 0.884μ_B in Ni@C_{60} and Ni@C_{60}-Si(111)-(7 × 7), respectively. These values are quite small. The reason is that the total DOS of the spin up state is almost equal to that of the spin down state, as shown in Fig. 4(j) and (l). The PDOS is from the same orbitals of the Ni atom (Fig. S5j and l†). It is clear that for all the TM@C_{60} adsorbed inside the Si(111)-(7 × 7) corner hole, the magnetic moments are nonzero. The results show a clear protecting effect of a carbon cage. Even for Fe, the presence of a C_{60} cage can also maintain its magnetic moment.

From previous discussions one can find that although the Fe, Co and Ni atoms are similar magnetic atoms and the PDOSs are all mainly contributed by the d orbitals, they have different magnetic moments when they are in similar systems. To further explore the underlying mechanisms, we calculated the charge transfer of TM atoms in different systems (Table 2). For Fe atoms in the systems of Fe–Si(111)-(7 × 7), Fe@C_{60}, and Fe@C_{60}-Si(111)-(7 × 7), they lose 0.3495e, 0.7431e and 0.8143e, respectively. However, the Co(Ni) atom obtained 0.0789e(0.2868e) when it was adsorbed in the hole of Si(111)-

Table 2 The charge transfer of the TM atoms in different systems

Systems	TM-Si(111)	TM@C_{60}	TM@C_{60}-Si(111)
Fe	−0.3495*e*	−0.7431*e*	−0.8143*e*
Co	0.0789*e*	−0.8939*e*	−0.7408*e*
Ni	0.2868*e*	−1.1063*e*	−0.6245*e*

(7 × 7). Meanwhile, for the systems of Co(Ni)@C_{60} and Co(Ni)@C_{60}-Si(111)-(7 × 7), the Co(Ni) atom loses 0.8939*e*(1.1063*e*) and 0.7408*e*(0.6245*e*), respectively. On comparing with the magnetic moment data shown in Table 1, one can find that the TM atoms possess magnetic moments when the conduction electrons are localized around them.

To understand the localized magnetic moments of the TM atoms in different situations, we employ the Anderson impurity model to clarify the underlying physics.[45–47] The Hamiltonian of a magnetic impurity in the hosts is

$$H = \sum_{k\sigma} \varepsilon_{k\sigma} c_{k\sigma}{}^{+} c_{k\sigma} + \sum_{\sigma} E_{d\sigma} d_{\sigma}{}^{+} d_{\sigma} + U n_{\sigma} n_{\bar{\sigma}} + \sum_{k\sigma} (V_{k\sigma} c_{k\sigma}{}^{+} d_{\sigma} + \text{h.c.}) \quad (1)$$

where the operator $c_{k\sigma}{}^{+}$ ($c_{k\sigma}$) denotes the creation (annihilation) of an electron in the conduction band, and $d_{\sigma}{}^{+}$ (d_{σ}) is the create (annihilate) operator of the d-electron on the impurity level. $\varepsilon_{k\sigma}$ denotes the energy of the conduction electrons, $E_{d\sigma}$ is the impurity level, and U is the Coulomb repulsion. $V_{k\sigma}$ is the coupling amplitude between the magnetic atom and the conduction electrons. In the present work, the localized magnetic moment of the TM atoms in different cases is determined by the parameters in the Hamiltonian in eqn (1).

Based on the equation of motion of the impurity Green's function, the phase diagram of the localized magnetic states can be obtained in the framework of Hartree–Fock approximation.[45–47] The impurity Green's function can be written as:

$$G_{d\sigma}(\omega) = \frac{1}{\omega - E_{d\sigma} - U n_{\bar{\sigma}} + i\Gamma},$$

where the occupation of the impurity level is $n_{\bar{\sigma}} = -\frac{1}{\pi}\int f(\omega)\mathrm{Im}[G_{d\sigma}(\omega)]\mathrm{d}\omega$, $f(\omega) = \frac{1}{1+e^{-(\omega-E_f)/K_B T}}$ is the Fermi function of the conduction electrons, $\Gamma = \pi|V_{k\sigma}|^2\rho(\omega)$ is the coupling strength, and $\rho(\omega)$ is the density of states of the conduction electrons in the hosts. Then, the Green's function and the occupation of the impurity level can be calculated self-consistently. By tuning the parameters, such as the impurity level $E_d = E_{d\sigma}$, the onset interaction, and the coupling strength Γ, the local magnetic moment of the impurities can be discussed and predicted from numerical calculations. In Fig. 5, we show the phase diagram of the magnetic and nonmagnetic states of the TM atoms. The parameters we used in the Anderson impurity model for the current study are listed in Table 3. The data are either taken from ref. 48 and 49 or obtained by DFT+U calculations. The positions of the TM atoms in different situations in the phase diagram are plotted in Fig. 5. As can be seen when they are adsorbed on Si(111)-(7 × 7) without C_{60}, Fe and Co atoms tend to preserve the local moment since the points ($\pi\Gamma/U$ = 0.84, $(E_f - E_d)/U$ = 0.25) and ($\pi\Gamma/U$ = 0.32, $(E_f - E_d)/U$ = 0.17) are located inside the magnetic region, while the point for the Ni atom ($\pi\Gamma/U$ = 0.70, $(E_f - E_d)/U$ = 0.11) is in the nonmagnetic region. The points for TM@C_{60}-Si(111)-(7 × 7) are then all located inside the magnetic region in the phase diagram (Fig. 5). These results agree with all our first principles calculations. The change of coupling strength (Γ) plays vital roles in the change of the magnetic properties of the TM atoms in different situations. Although the binding energy and the coupling strength have different origins, they both reflect the interaction strength between the TM atoms and the hosts. The dramatic changes in E_b for the TM atoms in different situations already indicate possible changes in Γ, especially for Fe and Ni.

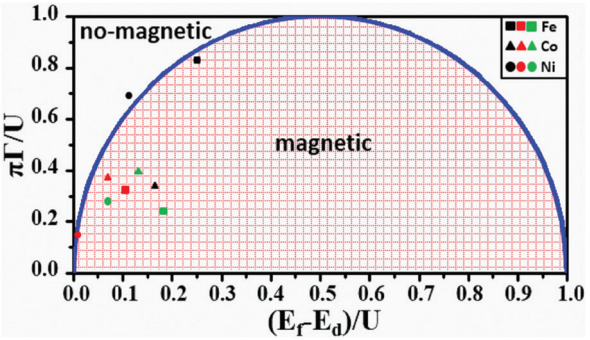

Fig. 5 The phase diagram of the Anderson impurity model.[45] The positions of TM-Si(111)-(7 × 7) (black), TM@C_{60} (red) and TM@C_{60}-Si(111)-(7 × 7) (green) are plotted.

Table 3 The parameters used in the Anderson impurity model

Systems	U (eV)[48]	E_d (eV)[49]	E_f (eV)	Γ (eV)	$\pi\Gamma/U$
Fe–Si(111)	5.00	−1.80	−0.56	1.34	0.84
Co–Si(111)	5.00	−1.53	−0.66	0.51	0.32
Ni–Si(111)	5.40	−1.28	−0.67	1.20	0.70
Fe@C_{60}	5.00	−1.80	−1.26	0.50	0.31
Co@C_{60}	5.00	−1.53	−1.17	0.58	0.36
Ni@C_{60}	5.40	−1.28	−1.21	0.25	0.14
Fe@C_{60}-Si(111)	5.00	−1.80	−0.92	0.39	0.24
Co@C_{60}-Si(111)	5.00	−1.53	−0.88	0.62	0.40
Ni@C_{60}-Si(111)	5.40	−1.28	−0.89	0.50	0.29

Therefore, from the point of view of the protection of the magnetic moment of TM atoms on the surface of Si(111)-(7 × 7), a C_{60} cage is a good choice. The relatively weak coupling parameters ensure relatively strong magnetic moments for adsorbed magnetic atoms.

Conclusions

Through detailed density functional calculations combined with theoretical analysis, the magnetic moments of transition

metal atoms in various configurations are studied and compared. When TM atoms are directly adsorbed inside the corner hole of Si(111)-(7 × 7), the magnetic moments of Ni atoms vanished, while the magnetic moments of single Fe and Co atoms are $2.909\mu_B$ and $1.353\mu_B$. When TM atoms are trapped inside the C_{60} cage, they will form 6 bonds with the six carbon atoms nearby. The magnetic moments then become $2.920\mu_B$, $1.939\mu_B$ and $0.136\mu_B$ for Fe, Co and Ni atoms, respectively. When TM@C_{60} were adsorbed inside the corner hole of Si(111)-(7 × 7), the magnetic moments change to $2.825\mu_B$, $1.849\mu_B$ and $0.884\mu_B$, respectively. These results indicate that the C_{60} cage can effectively protect the magnetic moments of the TM atoms, especially for Co and Ni atoms. By studying the charge transfer, it was found that the TM atoms possess magnetic moments when the conduction electrons are localized around them. An Anderson impurity model can be employed to understand our results. Our findings provide a new strategy for developing single atom spin-based devices on semiconductors.

Conflicts of interest

There are no conflicts to declare.

Acknowledgements

This work was supported by the MOST 973 Program (Grants No. 2014CB921402) and the National Natural Science Foundation of China (Grants No. 11574128, 11604138, and 11474145) and financially supported by the Shenzhen Fundamental Research Foundation (Grants No. JCYJ20170817105007999). This work was also supported by the Science, Technology and Innovation Commission of Shenzhen Municipality (No. ZDSYS20170303165926217).

References

1 S. Sanvito, *Chem. Soc. Rev.*, 2011, **40**, 3336–3355.
2 M. Shiraishi and T. Ikoma, *Phys. E*, 2011, **43**, 1295–1317.
3 F. A. Zwanenburg, A. S. Dzurak, A. Morello, M. Y. Simmons, L. C. L. Hollenberg, G. Klimeck, S. Rogge, S. N. Coppersmith and M. A. Eriksson, *Rev. Mod. Phys.*, 2013, **85**, 961–1019.
4 A. A. Khajetoorians, J. Wiebe, B. Chilian and R. Wiesendanger, *Science*, 2011, **332**, 1062–1064.
5 W. Jiang, M. Zhou, Z. Liu, D. Sun, Z. V. Vardeny and F. Liu, *J. Phys.: Condens. Matter*, 2016, **28**, 176004.
6 D. L. Sun, C. M. Kareis, K. J. van Schooten, W. Jiang, G. Siegel, M. Kavand, R. A. Davidson, W. W. Shum, C. Zhang, H. L. Liu, A. Tiwari, C. Boehme, F. Liu, P. W. Stephens, J. S. Miller and Z. V. Vardeny, *Phys. Rev. B: Condens. Matter Mater. Phys.*, 2017, **95**, 054423.
7 J. Y. Wang, A. Deloach, W. Jiang, C. M. Papa, M. Myahkostupov, F. N. Castellano, F. Liu and D. B. Dougherty, *Phys. Rev. B: Condens. Matter Mater. Phys.*, 2017, **95**, 241410.
8 J. F. Gregg, I. Petej, E. Jouguelet and C. Dennis, *J. Phys. D: Appl. Phys.*, 2002, **35**, R121–R155.
9 C. W. Zhang and S. S. Yan, *J. Phys. Chem. C*, 2012, **116**, 4163–4166.
10 M. H. Zhang, C. W. Zhang, P. J. Wang and S. S. Li, *Nanoscale*, 2018, **10**, 20226–20233.
11 S. S. Li, W. X. Ji, S. J. Hu, C. W. Zhang and S. S. Yan, *ACS Appl. Mater. Interfaces*, 2017, **9**, 41443.
12 S. J. Zhang, C. W. Zhang, S. F. Zhang, W. X. Ji, P. Li, P. J. Wang, S. S. Li and S. S. Yan, *Phys. Rev. B: Condens. Matter Mater. Phys.*, 2017, **96**, 205433.
13 L. Zhang, S. F. Zhang, W. X. Ji, C. W. Zhang, P. Li, P. J. Wang, S. S. Li and S. S. Yan, *Nanoscale*, 2018, **10**, 20748–20153.
14 Y. P. Wang, W. X. Ji, C. W. Zhang, P. Li, S. F. Zhang, P. J. Wang, S. S. Li and S. S. Yan, *Appl. Phys. Lett.*, 2017, **110**, 213101.
15 W. Jiang, Z. Liu, J. W. Mei, B. Cui and F. Liu, *Nanoscale*, 2019, **11**, 955–961.
16 X. J. Ni, W. Jiang, H. Q. Huang, K. H. Jin and F. Liu, *Nanoscale*, 2018, **10**, 11901–11906.
17 B. E. Kane, *Nature*, 1998, **393**, 133–137.
18 M. Fuechsle, J. A. Miwa, S. Mahapatra, H. Ryu, S. Lee, O. Warschkow, L. C. L. Hollenberg, G. Klimeck and M. Y. Simmons, *Nat. Nanotechnol.*, 2012, **7**, 242–246.
19 S. Mahapatra, H. Büch and M. Y. Simmons, *Nano Lett.*, 2011, **11**, 4376–4381.
20 E. Hamid, D. Moraru, Y. Kuzuya, T. Mizuno, L. T. Anh, H. Mizuta and M. Tabe, *Phys. Rev. B: Condens. Matter Mater. Phys.*, 2013, **87**, 085420.
21 J. H. Cole, A. D. Greentree, C. J. Wellard, L. C. L. Hollenberg and S. Prawer, *Phys. Rev. B: Condens. Matter Mater. Phys.*, 2005, **71**, 115302.
22 P. M. Koenraad and M. E. Flatté, *Nat. Mater.*, 2011, **10**, 91–100.
23 M. Pierre, R. Wacquez, X. Jehl, M. Sanquer, M. Vinet and O. Cueto, *Nat. Nanotechnol.*, 2009, **5**, 133–137.
24 T. D. Ladd, F. Jelezko, R. Laflamme, Y. Nakamura, C. Monroe and J. L. O'Brien, *Nature*, 2010, **464**, 45–53.
25 H. Shinohara, *Rep. Prog. Phys.*, 2000, **63**, 843–892.
26 K. Lips, M. Waiblinger, B. Pietzak and A. Weidinger, *Phys. Status SolidiA*, 2000, **177**, 81–91.
27 B. Cui, B. Huang, C. Li, X. M. Zhang, K. H. Jin, L. Z. Zhang, W. Jiang, D. S. Liu and F. Liu, *Phys. Rev. B: Condens. Matter Mater. Phys.*, 2017, **96**, 085134.
28 X. X. Zhang, G. H. Wen, S. M. Huang, L. M. Dai, R. P. Gao and Z. L. Wang, *J. Magn. Magn. Mater.*, 2001, **231**, L9–L12.
29 F. Satoshi, K. Yoshihiro, H. Tomoko, K. Takayoshi, F. Akihiko, N. Youichi and U. Tsuneo, *Phys. Rev. B: Condens. Matter Mater. Phys.*, 2004, **69**, 045415.
30 K. D. Wang, J. Zhao, S. F. Yang, L. Chen, Q. X. Li, B. Wang, S. H. Yang, J. L. Yang, J. G. Hou and Q. S. Zhu, *Phys. Rev. Lett.*, 2003, **91**, 185504.
31 H. Högberg, J.-O. Malm, A. Talyzin, L. Norin, J. Lu and U. Jansson, *J. Electrochem. Soc.*, 2000, **147**, 3361–3369.

32 M. Pedio, K. Hevesti, N. Zema, M. Capozi, P. Perfetti, R. Goutebaron, J.-J. Pireaux, R. Caudano and P. Rudolf, *Surf. Sci.*, 1999, **437**, 249–260.
33 S. Sakai, K. Yakushiji, S. Mitani, K. Takanashi, H. Naramoto, P. V. Avramov, K. Narumi and V. I. Lavrentiev, *Appl. Phys. Lett.*, 2006, **89**, 113118.
34 G. Kresse and J. Furthmüller, *Phys. Rev. B: Condens. Matter Mater. Phys.*, 1996, **54**, 11169–11186.
35 G. Kresse and D. Joubert, *Phys. Rev. B: Condens. Matter Mater. Phys.*, 1999, **59**, 1758–1775.
36 J. P. Perdew, K. Burke and M. Ernzerhof, *Phys. Rev. Lett.*, 1996, **77**, 3865–3968.
37 A. I. Liechtenstein, V. I. Anisimov and J. Zaanen, *Phys. Rev. B: Condens. Matter Mater. Phys.*, 1995, **52**, 5467.
38 V. I. Anisimov, J. Zaanen and O. K. Andersen, *Phys. Rev. B: Condens. Matter Mater. Phys.*, 1991, **44**, 943.
39 W. Tang, E. Sanville and G. Henkelman, *J. Phys.: Condens. Matter*, 2009, **21**, 084204.
40 O. V. Pupysheva, A. A. Farajian and B. I. Yakobson, *Nano Lett.*, 2008, **8**, 767–774.
41 A. V. Nikolaev, T. J. S. Dennis, K. Prassides and A. K. Soper, *Chem. Phys. Lett.*, 1994, **223**, 143–148.
42 M. B. Javan, N. Tajabor, M. Behdani and M. R. Rokn-Abadi, *Physica B Condens. Matter.*, 2010, **405**, 4937–4942.
43 F. F. Ming, K. D. Wang, S. Pan, J. P. Liu, X. Q. Zhang, J. L. Yang and X. D. Xiao, *ACS Nano*, 2011, **5**, 7608–7616.
44 O. Gunnarsson, *Rev. Mod. Phys.*, 1997, **69**, 575–606.
45 P. W. Anderson, *Phys. Rev.*, 1961, **124**, 41–53.
46 B. Uchoa, V. N. Kotov, N. M. R. Peres and A. H. Castro Neto, *Phys. Rev. Lett.*, 2008, **101**, 026805.
47 L. Li, J. H. Sun, Z. H. Wang, D. H. Xu, H. G. Luo and W. Q. Chen, *Phys. Rev. B: Condens. Matter Mater. Phys.*, 2018, **98**, 175110.
48 M. M. Steiner, R. C. Albers and L. J. Sham, *Phys. Rev. B: Condens. Matter Mater. Phys.*, 1992, **45**, 23.
49 P. J. Hay, *J. Chem. Phys.*, 1977, **66**, 4377–4384.

Journal: ACS Applied Nano Materials
Manuscript ID: an-2021-028275
Title: "Magnetic moment modulation of 3d transition metal atoms on Si (100) surface"
Author(s): Shao, Xiji; Li, Lin; Huang, Sizhao; Song, Zhenjun; Wang, Kedong

COVID-19 Support: Please visit the following website to access important information for ACS authors and reviewers during the COVID-19 crisis: https://axial.acs.org/2020/03/25/chemists-covid-19-coronavirus/

We are flexible in these unprecedented times affecting the global research community. If you need more time to complete authoring or reviewing tasks, please contact the editorial office and request an extension.

Dear Dr. Wang:

Thank you for submitting your manuscript for publication in ACS Applied Nano Materials. The reviewer comments for the above-referenced manuscript are enclosed for your information. The reviewers indicate that the manuscript requires major revision to address a number of specific points before it can be published.

On the basis of the reviewer comments and my own assessment of the manuscript, I am willing to consider a revised version of this paper for publication in ACS Applied Nano Materials pending a second round of external review. In preparing the revision, carefully consider all of the comments made by the reviewers.

We would like to receive your revision as soon as possible, by 25-Oct-2021 at the latest.